Study of the Gas and Dust Activity of Recent Comets

vorgelegt von
Diplom-Physiker
Michael Weiler
aus Andernach

Von der Fakultät II - Mathematik und Naturwissenschaften
der Technischen Universität Berlin
zur Erlangung des akademischen Grades
Doktor der Naturwissenschaften
Dr. rer. nat.

genehmigte Dissertation

Promotionsausschuss:

Vorsitzender: Prof. Dr.-Ing. Hans Joachim Eichler
Berichter/Gutachter: Prof. Dr. rer. nat. Heike Rauer
Berichter/Gutachter: Prof. Dr. rer. nat. Erwin Sedlmayr

Tag der wissenschaftlichen Aussprache: 18.12.2006

Berlin 2007

D 83

Contents

0 Zusammenfassung

Kometen gehören zu den seit seiner Entstehung am wenigsten veränderten Objekten im Sonnensystem. Ihre Untersuchung ermöglicht daher Rückschlüsse auf die physikalischen und chemischen Bedingungen im präsolaren Nebel.

In dieser Arbeit wurde ein eindimensionales vereinfachtes Multi-Fluid-Model zur Beschreibung der Chemie in der Kometenkoma aufgebaut. Dieses Modell wurde verwendet, um die Entstehung der Radikale C_3 und C_2 in zu untersuchen. Dazu wurden radiale Profile der optischen Emissionen von C_3 und C_2 der Kometen C/2001 Q4 NEAT, C/2002 T7 LINEAR und 9P/Tempel 1 bei heliozentrischen Abständen zwischen 1,0 AE und 1,5 AE verwendet. Diese wurden mittels Langspaltspektroskopie erhalten. Ein Reaktionsnetzwerk zur Erklärung der Bildung von C_3 und C_2 bei größeren heliozentrischen Abständen (Helbert, 2002) wurde aktualisiert und erweitert. Es wurden Moleküle und Radikale identifiziert, deren Photoreaktionsraten vor einer Erklärung der C_3- und C_2-Bildung genauer bestimmt werden müssen.

Als Kometen von besonderem Interesse wurden 67P/Churyumov-Gerasimenko und 9P/Tempel 1 detaillierter untersucht. Beide Kometen sind Ziele von Weltraummissionen.

Archivbeobachtungen des Kometen 67P/Churyumov-Gerasimenko sowie Bilder der Staubkoma wurden analysiert. Die Daten wurden verwendet, um die Langzeitaktivität des Kometen zu untersuchen. Daten zur Staub- und Gasaktivität wurden verwendet, um den Staubfluß in der inneren Koma abzuschätzen. Diese Analysen dienen der Vorbereitung der europäischen Weltraummission Rosetta, die im Jahr 2014 den Kometen erreichen wird.

Komet 9P/Tempel 1 war das Ziel der amerikanischen Mission Deep Impact, in deren Rahmen am 4. Juli 2005 ein Projektil in den Kometenkern eingeschlug und dabei eine Energie von ca. 19,3 GJ freigesetzte (A'Hearn *et al.*, 2005). Die Auswirkungen des Einschlags wurden unter anderem im Rahmen einer Beobachtungskampagne der Europäischen Südsternwarte beobachtet. Langspaltspektren, die während dieser Kampagne gewonnen wurden, wurden verwendet, um die Einschlagwolke und die Änderungen der kometaren Aktivität nach dem Einschlag zu untersuchen. Es wurden Hinweise auf eine chemische Inhomogenität des Kometenkerns gefunden.

Da sich während dieser Arbeit zeigte, daß nur wenige Informationen über die Größe von Kernen langperiodischer Kometen verfügbar sind, wurde die Möglichkeit untersucht, Kernradien von Kometen aus Beobachtungen von Monitorprogrammen des Himmels zu bestimmen. Mit diesem Verfahren abgeleitete Kernradien von langperiodischen Kometen und Jupiterfamilienkometen legen Unterschiede in den Größenverteilung beider Populationen nahe. Nicht alle Auswahleffekte, die in die Kerngrößenbestimmung eingehen, können im Rahmen dieser Arbeit eliminiert werden. Zielkometen wurden ausgewählt, deren Beobachtung die Ergebnisse dieser Arbeit bestätigen kann.

1 Introduction

1.1 Historical Development of Comet Science in Brief

All through the history of mankind, comets with naked eye brightness have been observed with interest in the sky. Therefore, comets belong to the oldest-known phenomena in astronomy. The first records of comet apparitions reach back to the early days of writing. For example, a document from the 2nd centrury BC reports of a comet as early as in the 11th century BC saying "When King Wu-Wang waged a punitive war against King Chou a comet appeared with its tail pointing towards the people of Yin."[1] (Ho, 1962). Such early reports indicate the importance that comets had for early civilisations. The sometimes spectacular and unpredictable appearence of comets may have caused the often strong and emotional reactions to comet discoveries in history. Rational explanations for comets have been rare, e.g. the idea of Aristoteles (384–322 BC), that comets are a kind of vapour rising up from the Earth and are therefore part of Earth's atmosphere. This theory was overthrown by Tycho Brahe, whose attempts to measure the parallax of a comet in 1577 AD failed and thus gave the Moon's distance as a lower limit for the comet's distance from the Earth. Shortly after the formulation of the gravitational law by Isaac Newton, which made the solar system a subject of physical research, Edmund Halley in 1705 was the first person to determine the orbital elements of a comet, now named 1P/Halley. This success made comets acknowledged members of the solar system and showed the periodicity of comet passages.

The model of comets that is still valid up to modern days goes back to Fred Whipple and was developed in the 1950s (Whipple, 1950, 1951, 1955). According to this model, comets consist of a nucleus built up of different ices and embedded dust grains. These ices sublimate while a comet is approaching the Sun and the solar irradiation is increasing. The dust and the gas ionised by the solar radiation form the dust tail and the plasma tail of the comet, respectively. As an example Fig. 1 shows comet C/2001 Q4 NEAT where the coma and the different tails are indicated. Comets move on strongly eccentric orbits so that their heliocentric distance changes strongly during one orbital revolution. Therefore they are at distances far from the Sun and the Earth during the major part of their orbits, so most comets are not observable during large parts of their orbits.

1.2 Short Overview of the Present Picture of Comets

The following sections give a short introduction to the cometary structures and effects important for this work.

---

[1] The year of the mentioned war remains very uncertain, most probably it was in 1055 BC (Chang Hung-Chhiao, 1958)

Figure 1: Picture of comet C/2001 Q4 NEAT, taken on June 8, 2004, by Michael Jäger and Gerald Rhemann. The almost symmetric neutral coma, an extended plasma tail, and a faint dust tail can be seen.

1.2.1 The Cometary Nucleus

According to the present idea, the cometary nucleus consists of a mixture of volatile material and silicates. The known sizes of cometary nuclei range from radii of a few hundred meters to several tens of km (Lamy *et al.*, 2004). The physical structure of cometary nuclei is however still very uncertain, even nowadays. A few estimates on nuclear densities exist that indicate low values below the density of water ice (e.g. Sagdeev *et al.* (1988), Davidsson and Gutiérrez (2004a), Davidsson and Gutiérrez (2004b)). The low densities suggest a fluffy, porous structure. This is consistent with a low tensile strength that could be estimated from the break-up of comet D/1993 F2 Shoemaker-Levy 9 under the tidal forces of Jupiter (Greenberg *et al.*, 1995). The thermal inertia of cometary nuclei also seems to be very low, as derived from temperature maps of the surface of comet 9P/Tempel 1 obtained from the Deep Impact fly-by spacecraft (Groussin *et al.*, 2006). The production of CN by comet C/1995 O1 Hale-Bopp, that could be derived over a wide range of heliocentric distances, also indicates a low heat conductivity of its nucleus (Rauer *et al.*, 2003). Therefore, a porous, soft mixture of ices and silicate dust or rocks is the favoured idea for the nucleus structure.

Images of cometary nuclei obtained during spacecraft missions revealed only on the nucleus of comet 9P/Tempel 1 areas on the surface that contain water ice. These areas are small compared to the whole surface area of the nucleus and cannot explain the observed water production rate of comet 9P/Tempel 1 (Sunshine *et al.*, 2006). Production rates for water determined for a variety of comets also indicate quite a large fraction of the nucleus surface material does not consist of ice. Typically, a few percent of the nucleus surface covered with ice would be sufficient to release the observed quantity of water in the cometary coma (A'Hearn *et al.*, 1995). These observations lead to the idea of active surface areas within a nucleus that is in most parts not or only weakly active.

One proposed mechanism that causes the surface of a nucleus to become inactive is the formation of a crust consisting of non-volatile material. Due to the sublimation of ices, the surface of volatiles retracts and mineral particles too large to be lifted off the nucleus by the gas flow remain and cover the ices below the surface. When the underlying ices are no more reached by the orbital heat wave due to the covering by dust, the surface becomes inactive.

The sublimation of ices may also alter the volatile composition in the near-surface layers of the nucleus. The sublimation enthalpy for different ices in the nucleus is different, which causes differences in the sublimation rates for the different ices with changing heliocentric distances. E.g. the effective sublimation of water ice stops at a heliocentric distance of approximately 3 AU, while carbon monoxide sublimates up to heliocentric distances of 30 AU. Therefore the relative abundances of different ices could change in the layers affected by the orbital heat wave. Some sublimation models for cometary nuclei predict a complete depletion of the layers close to the surface of highly volatile materials and the formation of differentiated sub-surface sublimation fronts for various volatile species (Prialnik *et al.*, 2004). The poorly known heat conductivity of the nucleus material has a strong influence on the formation of such sublimation fronts. While a high heat conductivity would allow the orbital heat wave to penetrate deeply into the nucleus and leads to differentiation, a very low heat conductivity would prohibit external heating from influencing material below a thin surface layer.

An opportunity to reveal material from deeper surface layers was provided by the Deep Impact space mission. Within this mission, on July 4, 2005, an impactor hit the nucleus of comet 9P/Tempel 1, releasing an impact energy of about 19.3 GJ (A'Hearn *et al.*, 2005). The consequences of that experiment were observable with ground-based instruments and opened the opportunity to study the impact ejecta and material potentially originating from below the surface of a cometary nucleus.

1.2.2 The Dust Coma and Tail

The presence of dust particles in comets is confirmed by the observation of the dust coma and the dust tails of comets. As an example, Fig. 1 shows a faint dust tail. When ices sublimate from the nucleus, the resulting gas flow can carry dust particles off the nucleus. The particles are accelerated by the gas flow as long as its density is high enough, which is usually the case within some hundreds of kilometers above the nucleus surface. From the decoupling of the dust from the gas onwards, the dust particles move with a constant nucleocentric velocity. The volume around a cometary nucleus which is dominated by an approximately radial movement of the dust grains is named the dust coma. The long-term dynamics of the dust grains is determined by solar gravity and radiation pressure, which causes the dust to move on Keplerian orbits in a heliocentric frame of reference. The recently-released dust then forms the dust tail, whereas dust emitted during earlier perihelion passages of the comet forms structures like dust trails (Fulle, 2004). The dust becomes observable in the optical and near infrared wavelength range by the scattering of sunlight.

The main constituent of the dust grains is believed to be silicates, since their thermal infrared spectra, showing various features, can be reproduced by spectra from mixtures of amorphous and cristalline silicates (Hanner *et al.*, 1999). Nevertheless, measurements with the mass spectrometer aboard the comet mission Giotto showed the presence of grains in the coma of comet 1P/Halley that were rich in the chemical elements carbon, hydrogen, oxygen, and nitrogen (Jessberger and Kissel, 1991). These elements are typical for the composition of organic substances and thus, the presence of organic material in or on dust grains is possible.

1.2.3 The Neutral Coma

When ice sublimates on the surface or shortly below the surface of a cometary nucleus, the resulting gas flows into space. These molecules are called the parent species. Under the influence of solar irradiation or due to collisions these molecules undergo chemical reactions. The resulting molecules, radicals or ions are called the daughter species. Typical extensions of the neutral coma are some 10^5 km to 10^6 km. The neutral hydrogen coma is even more extended and can be observed for very active comets up to several millions of kilometers from the nucleus. The neutral hydrogen coma of a very active comet can fill a significant fraction of the night sky on Earth (Combi *et al.*, 2000).

The neutral coma is close to rotational symmetry. Fig. 1 indicates a neutral coma with almost circular shape. Day-side to night-side asymmetries in activity are smoothed out on the large spatial scales of the neutral coma. Furthermore, most neutral species are only slightly sensitive to solar radiation pressure. The most prominent exception to this is sodium, which has a high fluorescence efficiency and therefore gets highly accelerated by the solar radiation field. This leads to an asymmetric sodium distribution and to the formation of a neutral sodium tail (Cremonese *et al.*, 2002).

1.2.4 The Plasma Environment

Cometary comae represent obstacles for the solar wind, which carries with it the solar magnetic field. Daughter species that get ionized by solar irradiation or electron impact reactions become sensitive to the magnetic field. Inside an ionopause, formed by a pressure balance between the solar wind and the outflowing cometary ions, no magnetic fields are present. Within this field-free cavity, the distribution of ions is expected to be close to symmetric. Outside the ionopause the cometary ions get accelerated approximately in the antisolar direction. This effect results in a strongly asymmetric density distribution and in the formation of the cometary plasma tail. Fig. 1 shows an extendend plasma tail. A detailed overview of the cometary plasma environment is presented by Neubauer (1991).

1.2.5 Dynamical Classification of Comets

The most detailed classification of comets is based on their heliocentric orbits. The earliest division of comets into classes makes use of their orbital periods. Comets with periods less than 200 years are called short-period comets, those with periods larger than 200 years are called long-period comets. Short-period comets having periods of less than 20 years were called comets of the Jupiter family. This taxonomy was based on the repeated observability of comets and has no deeper theoretical background. Furthermore, cometary orbits change often during close encounters with planets, and thus comets can become members of the Jupiter family and leave this family several times during the time they spend in the inner solar system. A more systematical classification was therefore introduced by Levison (1996) and is used in this work. This classification is based on the Tisserand parameter with respect to Jupiter, T_J. This is the only conserved quantity in the restricted three body problem, describing the movement of a massless body in the gravitational field of two other bodies orbiting on circular orbits around their common center of mass. The movement of a comet in the gravitational field of the Sun and Jupiter can be approximated by this situation. For a comet, the Tisserand parameter with respect to Jupiter is then (Murray and Dermott, 2000):

$$T = a_J/a_c + 2 \cdot [a_c/a_J \cdot (1 - e^2)]^{1/2} \cdot \cos(i) \ . \tag{1}$$

Here, a_J and a_c denote the semi-major axes of Jupiter and the comet respectively, e denotes the eccentricity of the comet's orbit and i its inclination. T_J varies only slightly even during major orbital changes due to close encounters with Jupiter and is therefore suitable for the classification of comets. Jupiter as the most massive planet has the major influence on the evolution of cometary orbits, so the Tisserand parameter with respect to Jupiter is the most suitable choice.

Long-period comets are comets having a T_J less than two. Small Tisserand parameters are especially caused by large eccentricities. If a long period comet has a semi-major axis larger than 10^4 AU, it is called dynamically new, otherwise the comet is regarded as dynamically old. Comets with a Tisserand parameter smaller than two and a semi-major axis up to 40 AU are called comets of Halley type.

If the Tisserand parameter of a comet is larger than three, a crossing of Jupiter's orbit is not possible. Such comets orbiting the Sun outside the orbit of Jupiter are called comets of Chiron type. Comets that are inside the orbit of Jupiter at all times are called comets of Encke type.

All comets having a Tisserand parameter between two and three are called the Jupiter family of comets. Comets of this family have aphelion distances close to the orbit of Jupiter, and their orbital periods are typically in the range of 5 to 7 years.

1.2.6 Cometary Source Regions

The lifetime of activity of a comet (the time within which the activity of a comet fades) and the dynamical lifetime of comets (time until ejection of a comet from the inner solar system) is short compared to the age of the solar system. Therefore, there have to exist reservoirs that supply new comets to the observable population. Two such reservoirs are known in the solar system.

The most distant one is the Oort cloud. This is a spherical volume, extending from a presently unknown inner edge out to the end of the space dominated by the solar gravity, and containing cometary nuclei. From this reservoir, a flux of comets is delivered to the inner solar system by disturbances of their orbits due to galactic tides or the gravitational effects of passing stars or molecular clouds. The Oort cloud is divided into a so-called inner Oort cloud and an outer Oort cloud. The boundary between the two subcategories is usually assumed to be around a semi-major axis of 10^4 AU, but can vary depending on the source of literature. Comets from the inner Oort cloud are assumed to be unobservable in the inner solar system, since objects from the inner Oort cloud cannot cross the so-called *Jupiter barrier*. The change of perihelion distance between two orbits around the Sun is a strong function of the semi-major axis ($\sim a^{7/2}$, Hills (1981)). Comets from the Oort cloud having a semi-major axis smaller than approximately 1 to $2 \cdot 10^4$ AU so cannot cross the area of the orbits of the giant planets in the solar system (especially Jupiter) within one revolution around the Sun. Therefore, these relatively weakly bounded objects spend a relatively long time close to the giant planets and suffer strong orbital disturbances leading to ejection from the solar system. A more detailed discussion of this effect is presented by Hills (1981). Long-period comets observed, having a semi-major axis smaller than 10^4 AU, are therefore thought to originate from the outer Oort cloud and have undergone several passages through the inner solar system, hence suffered a reduction in their semi-major axis. They are therefore called dynamically old. For an accurate classification of a long-period comet as dynamically old, a backward integration of the comet's movement over one orbit is required to include the effect of recent perturbations upon the orbital parameters (Dybczyński, 2001). In the following, the term "Oort cloud" refers to the outer Oort cloud.

Another source of comets are the transneptunian objects (TNOs). TNOs are objects in a belt around the Sun ($i < 30°$) defined by a semi-major axis larger than 30 AU (Morbidelli *et al.*, 2003). The TNOs are divided into two groups, called the scattered disc and the Kuiper belt. The scattered disc population consists of objects with orbital elements that allow at least one close passage with Neptune inside its Hill sphere within the lifetime of the solar system. The Kuiper belt population is the corresponding complement. The scattered disc is therefore populated by objects whose dynamics is strongly influenced by Neptune, while objects of the Kuiper belt are on more stable orbits, because they are either in a mean motion resonance with Neptune (e.g. the so called ”Plutinos” in the 2:3 mean motion resonance), or they are on an arbitrary orbit with small eccentricity ($e < 0.1$).

Both the scattered disc and the Kuiper belt are possible source regions of comets. In the case of the Kuiper belt, objects have to be delivered to the inner solar system by gravitational instabilities or collisions. Objects from the scattered disc population can reach the inner solar system after a close encounter with Neptune. The Chiron-type objects are believed to evolve from the TNO population into Jupiter family comets. (2060) Chiron, discovered in 1977, was the first object of this type and also shows cometary activity (Romon-Martin *et al.*, 2003).

The Oort cloud population and the TNO population are not independent. Fernández *et al.* (2004) point out that up to 10% of the loss of objects from the Oort cloud to the long-period comets could be replenished by scattered disc objects injected into the Oort cloud by Neptune. Furthermore, Emel'yanenko *et al.* (2005) suggest that the Oort cloud is contributing about 50% to the Chiron-type population, which can evolve into Jupiter family comets. The contributions of the different source regions to the different dynamical classes of comets mean that deducing the source region given the dynamical class is not a simple task.

A third reservoir of comets is the main asteroid belt. This region between the orbits of Mars and Jupiter was assumed to contain a large number of asteroids only until the recent discovery of cometary objects among the bodies in the main belt (Hsieh and Jewitt, 2006). However, since the main belt objects are on stable orbits with low eccentricities, they do not contribute to the observed flux of comets in the inner solar system.

1.2.7 Classification according to the Coma Composition

The largest statistical study of comets to date using a homogeneous dataset was published by A'Hearn *et al.* (1995). This work includes observations of 85 comets. This dataset was analysed with respect to the ratios of the parent production rates of C_2, C_3, CN, and NH with respect to OH, determined using the Haser model (Haser (1957), see section 4.7 for more details). It was found that comets can be divided into two classes, differing in their C_3, and even more in their C_2 production with respect to the OH production. According to A'Hearn *et al.* (1995), the comets regarded as ”typical” have $\log(Q(\mathrm{C_2})/Q(\mathrm{OH})) = -2.44 \pm 0.20$ and $\log(Q(\mathrm{C_3})/Q(\mathrm{OH})) = -3.59 \pm 0.29$, where Q denotes the production rate of the parent species. Comets that are members of a group denoted ”depleted” have $\log(Q(\mathrm{C_2})/Q(\mathrm{OH})) = -3.30 \pm 0.35$ and $\log(Q(\mathrm{C_3})/Q(\mathrm{OH})) = -4.18 \pm 0.28$. For the other gaseous species studied, CN and NH however, no significant difference between the comets of the depleted and the typical class was found in the production rate ratios with respect to OH. Therefore, the classification can also be done by using the ratios of the C_2 and C_3 production rates with respect to the CN production rate. Typical comets are then defined by having $\log(Q(C_2)/Q(CN)) < -0.18$. This classification as typical or depleted is to date the only spectroscopically-based classification method.

1.2.8 Correlations between Taxonomy, Source Regions, and Formation Regions of Comets

The Oort cloud and the TNO region do not represent the formation region of the objects they contain. According to the current model, cometary nuclei represent planetesimals that did not contribute to planet formation and survived up to the present. Planetesimals formed in the region of the orbits of Jupiter to Neptune were scattered by the giant planets into the Oort cloud. A fraction of planetesimals that were formed outside the orbit of Neptune could remain there up to the present and make up the TNO population. It has to be taken into account that Neptune migrated outwards after its formation due to scattering of planetesimals. During its migration to its present position of about 30 AU, Neptune also shifted outwards the population of planetesimals outside its own orbit. The formation region of TNOs therefore lies outside Neptune's orbit before its migration, which was around 23 AU from the Sun (Levison and Morbidelli, 2003; Gomes *et al.*, 2004).

Models of the Oort cloud formation by Dones *et al.* (2004) indeed showed that the present population can be expected to be dominated by planetesimals that were formed in the region of Uranus and Neptune, and a smaller fraction which has its origin in the Jupiter and Saturn region. However, planetesimals from the transneptunian region of the early solar system are also injected into the Oort cloud. A simple correlation between the formation region of a comet and its source region is therefore not possible.

It was found by A'Hearn *et al.* (1995) that the depletion in C_2 is correlated with the dynamical type of the comet. From 41 comets of a restricted dataset analysed by them, 12 were found to be depleted. From these depleted comets, 9 of them belong to the Jupiter family, one is of Halley type, and two are long-period comets. Furthermore, not all the Jupiter family comets studied are depleted. From these results, A'Hearn *et al.* (1995) suggested a scenario according to which the depletion is a primordial characteristic of comets originating in the Kuiper belt. This reservoir provides the depleted comets to the Jupiter family, while the typical population of Jupiter family comets originate in the Oort cloud.

Theoretical considerations suggest there may be variations in the relative abundance of C_2 and C_3 parent hydrocarbons depending on where the comet formed. Models of the carbon chemistry in the protoplanetary disc (Gail, 2002) predict variations in the concentrations of C_2H_2, C_2H_3, C_2H_4, and C_2H_6 with heliocentric distance, while the individual distribution of these species depends on parameters of the protoplanetary disc, such as the degree of radial mixing. This could lead to varying contents of these species in cometary nuclei formed at different heliocentric distances. Therefore, a study of the relative contents of hydrocarbons in cometary nuclei from different formation regions could be used in principle to constrain the conditions in the protoplanetary disc.

Due to the complex interplay between the formation region, the source region, and the dynamical type of an observed comet, reliable conclusions as to a correleation between the chemical composition of a comet and its formation region can only be drawn if a large number of comets is studied. Since optical observations provide the largest database of comets, it would be desirable to apply them to constrain the relative abundances of various hydrocarbons in comets.

1.3 The Formation Chemistry of C_2 and C_3

The classification of comets based on the C_2 parent production rates was derived using the Haser model, which simplifies the formation and destruction processes of an observed daughter radical to a two-step chemical process (see chapter 4). From the work by Helbert (2002) it is known that the chemical reaction network that leads to the formation of C_2 and C_3 is more complicated. As the main parent of C_2, C_2H_2 (acetylene) was identified. C_2H_6 (ethane) represents an additional minor parent. Furthermore, the C_3 radical also contributes to the formation of C_2. For the parent of C_3 suggested by Helbert (2002), C_3H_4, two isomers exist, H_2CCCH_2 (allene) and CH_3C_2H (propyne). The formation of C_3 from both isomers of C_3H_4 takes place via the same intermediate steps, and thus it is not possible to discriminate between the two isomers from comet observations. In the following, C_3H_4 therefore refers to the sum of both isomers.

A scheme for the formation chemistry of C_3 and C_2 according to Helbert *et al.* (2005) is shown in Figure 2. The main reaction mechanisms are photoreactions and electron impact reactions, leading to the decay of the parent species C_3H_4, C_2H_2, and C_2H_6.

This formation scheme can reproduce the observed radial column density profiles of C_3 and C_2 in comet C/1995 O1 (Hale-Bopp) at heliocentric distances beyond 2.9 AU. Observations of comets at such larger heliocentric distances tend to have a lower spatial resolution due to the also larger geocentric distance. Therefore, new influences upon the formation of C_3 and C_2 especially in the inner coma can become observable in radial column density profiles obtained at smaller heliocentric and thus also smaller geocentric distances.

Furthermore, a simple scaling of chemical processes from heliocentric distances of about 3 AU and beyond to heliocentric distances around 1 AU is not possible. Photoreactions for example scale with the incident solar radiation, thus with r_h^{-2}. Electron impact reactions strongly depend on the density of water in the cometary coma, since the electron temperature is coupled to the temperature of neutral species in the inner coma by inelastic electron−water collisions (see chapter 4). Since water sublimation becomes ineffective at heliocentric distances larger than about 3 AU, the dependency of the electron impact reaction rates show a different dependency on the heliocentric distance than the photoreaction rates. As will be shown in this work, in the innermost coma, neutral−ion reactions of hydrocarbon species with H_3O^+ are important for the formation of C_3. The formation of H_3O^+ depend on the water densities in the cometary coma, thus the formation of C_3 by this mechanism also shows a different dependency on the heliocentric distance than photoreaction rates.

Therefore, the formation of C_2 and C_3 at smaller heliocentric distances has to be studied in detail. Furthermore, other species than the parent species included in the work by Helbert (2002) may become important at smaller heliocentric distances. For the formation of C_3, Swings (1965) suggested C_4H_2 (diacetylene) as a parent species, forming C_3 via the photodissociation reaction

$$\mathrm{C_4H_2} + \gamma \rightarrow \mathrm{C_3} + \mathrm{CH} + \mathrm{H} \ . \tag{2}$$

Here, γ denotes a photon. Krasnopol'Skii (1991) suggested C_3H_2O (propynal) to produce C_3 via the reaction

$$\mathrm{C_3H_2O} + \gamma \rightarrow \mathrm{C_3} + \mathrm{H_2} + \mathrm{O} \ . \tag{3}$$

For the formation of C_2, beside the parent species C_2H_2 and C_2H_6 also HC_3N (cyanoacetylene) can contribute by the reactions (Halpern *et al.*, 1988):

$$\mathrm{HC_3N} + \gamma \rightarrow \mathrm{CN} + \mathrm{C_2H} \tag{4}$$

$$\mathrm{HC_3N} + \gamma \rightarrow \mathrm{C_3N} + \mathrm{H} \ . \tag{5}$$

The radicals C_2H and C_3N then undergo the photodissociation reactions

$$\mathrm{C_2H} + \gamma \rightarrow \mathrm{C_2} + \mathrm{H} \tag{6}$$

$$\mathrm{C_3N} + \gamma \rightarrow \mathrm{C_2} + \mathrm{CN} \ . \tag{7}$$

An analysis of the formation chemistry of C_2 and C_3 at small heliocentric distances therefore should also include a study of the importance of these additional potential parent species.

1.4 Goals of this work

One goal of this work is the study of the formation of the C_3 and C_2 radical in the comae of comets at heliocentric distances between 1.0 AU and 1.5 AU. For this study, data of the three comets C/2001 Q4 NEAT, C/2002 T7 LINEAR, and 9P/Tempel 1 are analysed. Potential parent species are identified and their production rates are estimated. For this purpose an easy-to-handle model of the chemistry of cometary comae is presented.

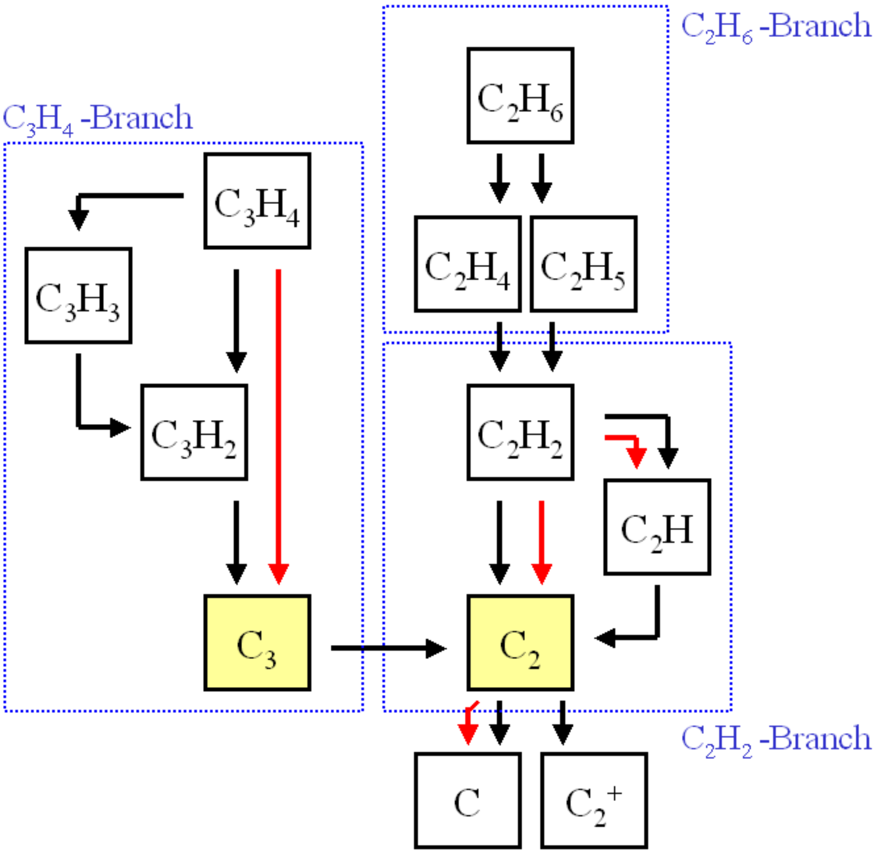

Figure 2: Scheme of reactions leading to the formation of C_3 and C_2, adapted from Helbert et al. *(2005). Black arrows indicate photoreactions, red arrows indicate electron impact reactions. Loss reactions, leading to species being removed from the formation pathways of C_2 and C_3, are not shown.*

The model has to take a complex chemical reaction network including various classes of reactions (i.e. photoreactions, electron impact reactions) into account. The reaction network for the formation of C_3 and C_2 derived by Helbert (2002) for comet C/1995 O1 Hale-Bopp at heliocentric distances larger than 2.8 AU is tested at smaller heliocentric distances and adapted.

As comets of special interest, the two spacecraft target comets 67P/Churyumov-Gerasimenko and 9P/Tempel 1 are studied in more detail.

Archive observations of comet 67P/Churyumov-Gerasimenko are compared with observations obtained during other perihelion passages and published in literature. The goal of this study is to investigate the long-term variability of the activity of 67P/Churyumov-Gerasimenko. Images obtained during the preparation of this work are used to study the morphology of the dust coma. The dust production rate of the comet is estimated. These studies help to characterize the environment the Rosetta spacecraft will be exposed to after its arrival at comet 67P/Churyumov-Gerasimenko in 2014.

Optical spectroscopic observations of comet 9P/Tempel 1 from two days before the Deep Impact event on July 04, 2005, to eight days after impact are analysed. From the observations, the amount of material released by the impact event is estimated. The influence of the impact upon the gas activity of comet 9P/Tempel 1 on timescales of days is determined and the spectra are used to search for new optical emission bands in the post-impact coma compared to the pre-impact coma.

Since the goals of this work as described so far require information on the size of cometary nuclei and it turned out that the available information on the size of especially long-period comets is very poor, a method for deriving the size of cometary nuclei based on survey observations is presented in this work. This method makes use of the apparent absence of cometary activity on parts of the heliocentric orbits of a number of comets and allows to estimate nuclear sizes of comets from all dynamical classes. The available observations of comets suitable for such a study between the years 1998 and 2004 are analysed. The nucleus size frequency distributions of Jupiter family comets and long-period comets are determined and compared. The limitations of the presented method are evaluated.

2 Optical Comet Observations

This chapter describes the principles of light emission from comets and the techniques applied in the observations analysed in this work. The dataset analysed within this work is presented.

2.1 Optical Emissions from Comets

2.1.1 Gas Emissions

Electromagnetic emissions from molecules and radicals are related to changes in the quantum numbers for the rotational, vibrational or electronic state. The different types of transitions mean energy changes in typical orders of magnitude. Therefore, the wavelengths of the electromagnetic radiation correlated with one of the three transition types lie in different regimes. Purely rotational transitions (only the quantum numbers of rotation change) correspond to emissions in the radio wavelength regime. Vibrational-rotational transitions (the vibration quantum numbers and possibly the rotational quantum numbers change) have energies corresponding to radiation in the infrared region of the electromagnetic spectrum. Transitions were all three quantum numbers, including the electronic state change have emissions from the near infrared over the optical to the ultraviolet regime.

For ground-based observations, the optical emissions are easily accessible due to the high transparency of the Earth's atmosphere and available sensitive detectors at optical wavelengths. Ultraviolet radiation is effectively blocked by the atmosphere, while transmission windows suitable for observations exist in the infrared and radio region of the electromagnetic spectrum. Only relatively bright comets can be observed in these windows with a sufficient signal-to-noise ratio, excluding the majority of comets from beeing targets of observations. A study of a large number of comets is therefore restricted to optical observations.

Intact molecules, such as the cometary parent species, do not show observable emissions in the optical wavelength range. The electronic transitions that result in such emissions require the electronic excitation of a binding electron. Such excitation in a molecule usually leads to its dissociation and the formation of radicals. Thefore, parent species can only be observed by their vibrational and rotational transitions. The radicals resulting from dissociation on the other hand have an unpaired electron which is available for electronic transitions without significant influence on the binding state of the radical. Therefore, such radicals show emissions in the optical wavelength range. Since the binding potential of a radical is not significantly modified by such electronic exitation, a typical group spectrum results (Haken and Wolf, 2006). This means for transitions between two electronic states transitions between vibrational states with the same quantum number are most probable. The strongest emission therefore is a band of lines which correspond to $\Delta v = 0$, if v denotes the vibrational quantum number, and that contains lines from all transitions between different vibrational and rotational states. Other bands, e.g. with $\Delta v = \pm 1$, occur with a lower intensity.

The excitation within a radical in the cometary coma is caused by the absorption of a photon from the solar radiation field. The de-excitation of radicals in the cometary coma is achived by isotropic emission of photons of the same wavelength as absorbed before. This process is called resonant fluorescence. Due to the low densities, excitation and deexcitation due to collisions between molecules, radicals, or electrons, and thus without emission of radiation is unlikely.

If the exitation is done by absorption of photons of a wavelength that lies in the vicinity of a strong solar absorption line, a Doppler shift can influence the effectivity of excitation of the radicals. The potentially largest contribution of the radial component to the heliocentric velocity of a radical arises from the orbital velocity of the comet. Close to perihelion of a comet, its radial velocity component is close to zero, but it can reach values up to the order of several tens of kilometers per second along its orbit. If the Doppler shift due to that velocity component significantly influences the efficiency of excitation of a molecule, atom or radical, one speaks of the *Swings effect*. The Swings effect e.g. is important for the CN $\Delta v = 0$ emission band analysed in this work. For typical radial heliocentric velocities at which comets were observed, the efficiency of resonant fluorescence varies up to a factor of three (Schleicher, 1983).

The resolution of the different lines within a band requires a high spectral resolution, in the order of several 10^4 to 10^5. Observations of the different lines are for example of interest to study the isotopic ratios in comets (Hutsemékers *et al.*, 2005). For the determination of abundances of a particular radical in the cometary coma, a resolution of the structure of an emission band is not required and spectra of lower resolution ($< 10^3$) can be used, where the bands can be seen as apparently continuous broad features. Spectroscopy with a low resolution has the advantage to provide a sufficient signal-to-noise ratio even for fainter comets. As an example, with an 8-m telescope a sufficient signal-to-noise ratio for the analysis done in this work within an integration time of 15 minutes could be obtained for a comet with a visual brightness around 10^{mag}.

Fig. 3 shows a comet spectrum covering the whole optical wavelength range as an example. The most prominent emission bands are identified there. Furthermore, Tab. 1 summarizes the most important radical emissions that were analysed within this work.

2.1.2 Light Scattering by Dust Particles

The cometary nucleus sets dust particles free. These particles scatter sunlight and thus become visible as a diffuse source of light. The scattering properties depend on the material that build up the dust grains, their size distribution, and their shape. Smaller

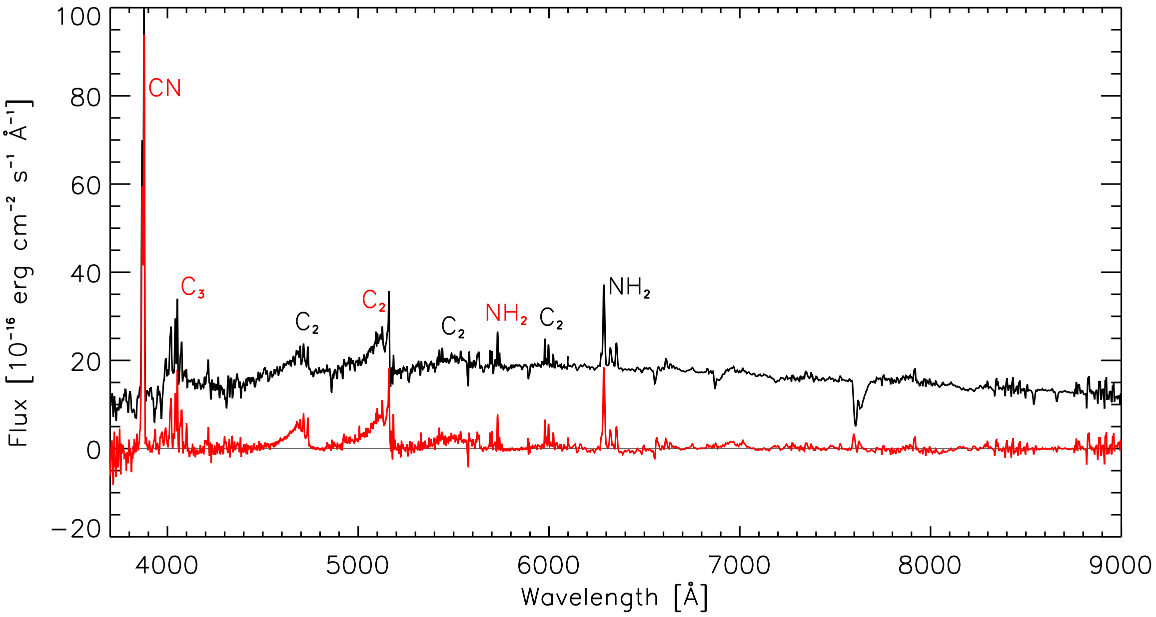

Figure 3: Spectrum of comet 9P/Tempel 1, obtained on July 3, 2005, and covering the whole optical wavelength range. The spectrum is integrated $1.5 \cdot 10^4$ km around the nucleus position in the sunward-tailward direction. The red curve shows the spectrum after subtraction of the sunlight scattered by dust particles (see chapter 3). The main gaseous emissions are indicated with the radicals causing them. The emissions labeled in red are the emissions used for further analysis in this work: the CN ($\Delta v = 0$) band, the C_3 emission, the $C_2(\Delta v = 0)$ band, and the NH_2 (0,10,0) band.

particles are thought to scatter more efficiently at shorter wavelength compared to larger grains. The spectral energy distribution of the scattered light is the one of the solar spectrum, with some tendencies over wider wavelegth ranges. These tendencies are refered to as the colour of the cometary dust. The colour is usually neutral to slightly red, which means that the scattering efficiency of the dust ranges from wavelength-independent to slightly increased for larger wavelengths compared to the shorter.

Different from the emissions originating from the gasous species, the scattering is not isotropically but follows a phase function, describing the dependency of intensity of scattered light from the scattering angle. The scattering is enhanced in the backward and foreward direction. A detailed overview on the study of cometary dust by light scattering is presented by Jockers (1997).

2.1.3 Optical Observations of the Nucleus

The nucleus of a comet becomes in principle observable by reflecting the sunlight. For active comets, the light originating from the nucleus is conterminated to overlayed by light scattered by the dust in the cometary coma. The nucleus brightness can therefore

Table 1: Overwiew of the most prominent radical emissions in the cometary coma (Feldman et al.*, 2004b). The emissions correlated with the given transitions were analysed within the framework of this work.*

Species	Electronic Transition	System Name
CN	$\mathrm{B}^2\Sigma^+ \rightarrow \mathrm{X}^2\Sigma^+(0,0)$	Violet System
C_2	$d^3\Pi_g \rightarrow a^3\Pi_u(0,0)$	Swan System
C_3	$\tilde{\mathrm{A}}^1\Pi_\mathrm{u} \rightarrow \mathrm{X}^1\Sigma_\mathrm{g}^+$	Comet Head Group
NH_2	$\tilde{\mathrm{A}}^2\mathrm{A}_1 \rightarrow \tilde{\mathrm{X}}^2\mathrm{B}_1$	–

be determined only for inactive comets or by subtraction the coma contribution.

Observations of inactive comets are only possible at relatively large heliocentric and with it geocentric distances where sublimation of ices becomes ineffective. This means that the nucleus itself becomes a faint source (typically below 20^{mag}), too, which makes detailed spectroscopic observations impossible. Ground-based spectroscopic observations of cometary nuclei are therefore only available for comets that show no permanent activity but that are only active on parts of their orbit in the inner solar system for reasons that are not completely understood by now. An example of such a comet is C/2001 OG_{108} LONEOS, for which a detailed optical and infrared study was published by Abell *et al.* (2005). Groundbased studies of distant inactive comets restrict on photometry in filters with a broad bandpass for reaching a sufficiently high signal-to-noise ratio.

The contribution of light from the dust coma to the nucleus signal can be estimated by modeling the brightness distribution in the coma and the point spread function of the nucleus. This can be done only if a high spatial resolution of the inner coma can be obtained and in case of a relatively symmetric coma brightness distribution. A summary of these method is given by Lamy *et al.* (2004).

2.2 Overview of Observational Techniques

Within this work, two methods for the observation of comets were applied, the low resolution long-slit spectroscopy and the imaging in broadband filters. Both techniques are described in the following.

2.2.1 Long-Slit Spectroscopy

In long-slit spectroscopy, a slit is placed before the cometary coma and the light passing the slit is dispersed to obtain a spectrum. From long-slit spectra it is possible to study both, the gaseous species in the coma and the dust, since the emissions and the dust continuum are obtained at once. The disadvantage is that a long-slit spectrum only contains information on one spatial dimension within the coma. The slit widths used for observations analysed in this work are 1" and 2" in the plane of sky. The broader slit was used for fainter comets, since more light can pass on the cost of spectral resolution. The length of the slit depends on the instrument used and is typically in the order of a few arcminutes. The slit was always placed within the coma that it contained the photocenter of the coma, which is assumed to be the position of the cometary nucleus. Different position angles of the slit were applied during observations. The projected direction of the Sun in the sky was the prefered setting, but also other position angles were used.

The spectra were produced with the help of a grism, which represents a combination of a prism and grating and can be inserted into the optical path. The typical resolution of the spectra analysed in this work is between 600 and 800. As a detector, CCDs were used by all instruments from which data were used in this work. The procedures for reduction of the long-slit spectra obtained is described in chapter 3 of this work.

2.2.2 Imaging

Images of the cometary coma make it possible to study the two-dimensional structure of the coma. If the images are photometrically calibrated, the gas or dust production rates can be determined from images. However, no images were used within this work for the determination of production rates since the accuracy in calibration remains poor compared to long-slit spectra. Furthermore, long-slit spectroscopic observations make it possible to obtain information on several species in the coma at the same time.

Images of comets were taken for this work using broadband filters. The filters of different instruments used for observations differ in their transmission curves. Nevertheless, they follow the usual sequence of B,V and R, which means that their transmission lies within the blue, visible (yellow) or red part of the optical spectrum. Since the bandpass of these filters is relatively wide, usually around 100 nm, the filters can also be used for observations of relatively faint sources. The major disadvantage of these filters is that their transmission curves include light from both, continuum of scattered sunlight and gaseous emissions. It is therefore not possible to distinguish between dust and gas within the images.

2.3 Observational Dataset of this Work

Within this work, observations of the four comets 67P/Churyumov-Gerasimenko, 9P/Tempel 1, C/2002 T7 LINEAR, and C/2001 Q4 NEAT are analysed. The basic parameters of these comets are summarized in Tab. 2. While the comets 67P/Churyumov-Gerasimenko and 9P/Tempel 1 belong to the Jupiter family, the comets C/2002 T7 LINEAR and C/2001 Q4 NEAT are of long period. Comet 67P/Churyumov-Gerasimenko is classified as depleted in C_2 (A'Hearn *et al.*, 1995). Different telescopes and instruments were used for the observations, detailed information on the technical and observational circumstances are given in the following subsections.

For the three comets 9P/Tempel 1, C/2002 T7 LINEAR, and C/2001 Q4 NEAT, optical long-slit spectra that cover the emissions of C_3 and C_2 are available. These three comets are therefore used to study the formation chemistry of C_3 and C_2. The three comets were observed at similar heliocentric distances between about 1 AU and 1.5 AU. Furthermore, they range from low water production rate (9P/Tempel 1, $3.4 \cdot 10^{27}\,\mathrm{s}^{-1}$, Küppers *et al.* (2005)) over a medium range water production rate (C/2002 T7, $6.9 \cdot 10^{28}\,\mathrm{s}^{-1}$, Howell *et al.* (2004)) to a relatively high water production rate (C/2001 Q4, $1.9 \cdot 10^{29}\,\mathrm{s}^{-1}$, Weaver *et al.* (2004)). Therefore, the three comets provide a good sample for the study of chemical processes in the coma.

2.3.1 Observations of Comet 67P/Churyumov-Gerasimenko

For this work, long-slit spectra of comet 67P/Churyumov-Gerasimenko obtained at the Observatoire de Haute-Provence (OHP), France, in February 1996 were available. Using the 1.93-m telescope at OHP, the medium resolution long-slit spectrograph CARELEC (Lemaitre *et al.*, 1990) was used for the observations. The instrument was equipped with a 512 × 512 pixel CCD, providing a slit length of 5.5 arcminutes and a spatial scale of 1.1" /pixel. The slit width used is 2.1". The slit was aligned along the projected solar direction. The CARELEC instrument set-up is summarized in Tab. 3. During the three nights of observations, different wavelength ranges have been chosen to cover various emission bands in the optical spectrum of the comet. The wavelength ranges and observational details are given in Tab. 4. Unfortunately, the sky conditions were only photometric on February 10/11, 1996.

In March and May, 2003, B, V and R-filter images of comet 67P/Churyumov-Gerasimenko were obtained in collaboration with Dr. Silvio Klose and Dr. Jochen Eislöffel using the 2-m-telescope of the Thüringer Landessternwarte. The observations are listed in Tab. 5. For the technical parameters of the instrument see Tab. 3.

All those images taken in one of the six time intervals presented in Tab. 5 were co-added after shifting the images to compensate the comet's movement. Images obtained on May 30, 2003 could not be used for coma analysis. The comet faded significantly from the previous observations in March, so only an insufficient signal-to-noise ratio could be achieved. The strong loss in brightness was caused in part by the increase of the geocentric distance by approximately a factor of two and an increase of the phase angle from 4.3° to 19.3° between the beginning of March, and the end of May. Since no absolute measure of the comet's gas or dust activity during these observations is available, it cannot be quantified how much of the brightness decrease is due to decreasing cometary activity.

During the observation period the Earth crossed the orbital plane of comet 67P/Chury-

Table 2: Summary of the basic parameters of the comets studied in this work. T *denotes the time of the perihelion passage (for short-period comets, the time of the last perihelion passage is displayed),* q *denotes the perihelion distance, e the excentricity, i the inclination, and ω and Ω denote the argument of perihelion and the longitude of the ascending node, respectively. T_J is the Tisserand parameter with respect to Jupiter.*

C/2001 Q4 NEAT	
Date of Discovery:	2001 August 24.4
Orbital elements:	T = 2004 May 15.97
(MPC 52163)	q = 0.962 AU
	$e = 1.000664$, $i = 99.643°$
	$\omega = 1.204°$, $\Omega = 210.279°$
Orbital Period:	–
Mean Nuclear Radius:	2.5–5 km (Tozzi *et al.*, 2003) estimate only
T_J:	–
C/2002 T7 LINEAR	
Date of Discovery:	2002 October 14.4
Orbital elements:	T = 2004 April 23.06
(MPC 52164)	q = 0.615 AU
	$e = 1.000561$, $i = 160.583°$
	$\omega = 157.736°$, $\Omega = 94.859°$
Orbital Period:	–
Mean Nuclear Radius:	44.2 km (this work) upper limit
T_J:	–
9P/Tempel 1	
Date of Discovery:	1867 April 3.9
Orbital elements:	T = 2005 July 5.32
(MPC 45657)	q = 1.506 AU
	$e = 0.517491$, $i = 10.530°$
	$\omega = 178.839°$, $\Omega = 68.937°$
Orbital Period:	5.52 a
Mean Nuclear Radius:	3.0 ± 0.1 km (A'Hearn *et al.*, 2005)
T_J:	2.97
67P/Churyumov-Gerasimenko	
Date of Discovery:	1969 Septemper 11.9
Orbital elements:	T = 2002 August 18.31
(Kinochita, 2004)	q = 1.292 AU
	$e = 0.631529$, $i = 7.121°$
	$\omega = 11.451°$, $\Omega = 50.969°$
Orbital Period:	6.57 a
Mean Nuclear Radius:	1.98 ± 0.02 km (Lamy *et al.*, 2003)
T_J:	2.75

umov-Gerasimenko, moving from 4.3° South of the plane on March 7 to 0.8° North of the plane on May 30, as measured from the comet's nucleus. This means, the dust tail of

Table 3: Technical parameters for the observations of comet 67P/Churyumov-Gerasimenko done with the instrument CARELEC at the 1.93-m telescope at OHP and the CCD camera at the 2-m telescope of the TLS. Δx *and* $\Delta\lambda$ *show the spatial scale and wavelength scale, respectively, and FOV shows the field of view.* $\Delta x'$ *is the spatial scale in the plane of the comet's nucleus.*

Instrument	Date	Δx ["/pix.]	$\Delta x'$ [km/pix.]	$\Delta\lambda$ [Å/pix.]	FOV [']
CARELEC	Feb., 1996	1.1	941	1.8	–
TLS-CCD 1	Mar. 6/7, 2003	1.5	1621	–	52.6 & 28.9*
TLS-CCD 2	other	1.2	1480 – 2454	–	38.2 & 21.0*

* CCD area reduced to save readout time in some exposures

Table 4: Spectroscopic observations of comet 67P/Churyumov-Gerasimenko from OHP. All observations were performed at the 1.93-m telescope using the CARELEC spectrograph. r_h *and* Δ *denote the heliocentric and the geocentric distance, respectively, and* β *denotes the phase angle. N is the number of spectra obtained in one night, T is the total exposure time during the night, and* $\Delta\lambda$ *is the wavelength range of the spectra.*

Date	r_h [AU]	Δ [AU]	β [°]	N	T [min]	$\Delta\lambda$
09/10.02.1996*	1.33	1.18	45.9	2	20	5817 Å – 6731 Å
10/11.02.1996	1.33	1.18	45.7	3	50	3751 Å – 4666 Å
11/12.02.1996*	1.34	1.19	45.6	4	50	6034 Å – 6944 Å

* non-photometric night

Table 5: Overview of the broadband filter observations of comet 67P/Churyumov-Gerasimenko performed with the 2-m telescope/CCD camera at the TLS. Observation dates and time intervals of the observations are presented. r_h *and* Δ *denote the heliocentric and the geocentric distance,* β *denotes the phase angle, N is the number of images and T is the exposure time of each frame. None of the observations were obtained under photometric conditions.*

Date	Time [UT]	r_h [AU]	Δ [AU]	β [°]	N	Filter	T [min]
07.03.2003	01:52 – 02:47	2.47	1.49	4.3	14	B + R	2
27.03.2003	20:36 – 21:41	2.62	1.69	10.0	19	R	2
28.03.2003	00:26 – 00:53	2.62	1.70	10.1	10	R	2
28.03.2003	20:17 – 21:03	2.63	1.71	10.4	15	R	2
31.03.2003	21:41 – 22:27	2.65	1.75	11.4	15	R	2
30.05.2003	21:00 – 22:26	3.06	2.82	19.3	17	V + R	2

comet 67/Churyumov-Gerasimenko is seen nearly edge-on in the observations. At the same time comet 67P/Churyumov-Gerasimenko was at a high elongation (169° on March 7, decreasing to 94° at the end of May). This leads to unusual position angles of the projected solar direction with respect to the dust tail direction (see Fig. 41). The projected Sun direction moved towards the extended tail structure during the observations analysed in this work while the position of the tail changed only a few degrees with respect to the equatorial coordinates. When the Earth was in the orbital plane of the comet on May 10/11, the tail structure should have pointed directly along the projected Sun direction. Because of its strong variations during the observations, the projected Sun direction is not a suitable reference direction in observations analysed in this work.

2.3.2 Observations of Comet 9P/Tempel 1

The observations of comet 9P/Tempel 1 started on the night of July 02/03, 2005, and lasted until July 10 at UT1 of the VLT, ESO, with the FORS 2 instrument. During two additional nights, measurements were then performed by using FORS 1 at UT2. This time period includes the impact of the Deep Impact projectile spacecraft on July 4, 2005. An overview of the observations is presented in Tab. 6. During the observations, 9P/Tempel 1 was at a heliocentric distance of 1.51 AU and a geocentric distance of 0.88 AU − 0.94 AU. Two grisms were used at UT1, covering in total 370−920 nm. However, the red part of the spectral range (610−920 nm) was covered only once per night, whereas the blue range (370−620 nm) was the standard setting. The resolving power is 780 for the 370−620 nm range and 660 for the 610−920 nm range while using FORS 2. For the spectra taken with FORS 1, the resolving power is 780, too. The FORS instruments provide a field-of-view of 6.8' × 6.8'. The slit length was 6.8' and a slit width of 1" was used to observe the comet. The pixel scale is 0.252" pixel^{-1} (after a 2×2 binning) in the spatial and 1.5 Å pixel^{-1} in the wavelength direction for FORS 2. For FORS 1, the corresponding values are 0.20" pixel^{-1} and 1.2 Å pixel^{-1}. These values correspond to a pixel scale from 162.3 km pixel^{-1} to 129.2 km pixel^{-1} for FORS 2 and from 135.2 km pixel^{-1} to 135.9 km pixel^{-1} for FORS 1, respectively. The detector of the FORS 2 instrument consists of two individual 2048 × 4096 pixel CCDs, which are separated by a gap of 480 μm, corresponding to 4.03". The gap is oriented parallel to the wavelength direction. The FORS 1 instrument uses a single CCD with 2048 × 2048 pixels.

The position angle of the projected solar direction ranges from 291.7° on the evening of July 2, 2005, to 290.3° on the morning of July 12. The slit was oriented at four different position angles, the reference position being along the projected Sun-comet line. The additional spectra were taken perpendicular to the projected Sun-comet line and at the 45° angles in between. In addition to the spectra, images were made at the beginning of each night in broadband filters to study the dust coma of the comet. Tab. 6 provides an overview of the spectroscopic observing sequence for each night.

2.3.3 Observations of Comets C/2002 T7 LINEAR and C/2001 Q4 NEAT

The comets C/2002 T7 LINEAR and C/2001 Q4 NEAT were the two bright comets of the year 2004. Both comets reached naked-eye visibility and were targets of observing campaigns carried out at the ESO La Silla observatory.

Long-slit spectroscopic observations of comet C/2002 T7 were done using the EFOSC2 instrument at the ESO 3.6-m telescope. The observations were performed in the night of June 12/13, 2004. Long-slit spectra of comet C/2001 Q4 were obtained with the same instrument during the night of April 29/30, 2004. The instrument set-up and the observing conditions during that nights are summarized in Tab. 7. The sky conditions were photometric in both nights. Long-slit spectra of both comets were taken with the slit aligned along the projected solar-antisolar direction.

Comet C/2001 Q4 was observed at a relatively small geocentric distance of only 0.39 AU. Therefore, observations with a high spatial resolution were possible.

2.3.4 Reference Observations of Comet C/1995 O1 Hale-Bopp

In order to validate the model of coma chemistry introduced in this work, long-slit spectroscopic observations of comet C/1995 O1 Hale-Bopp obtained on December 19, 1997 were analysed. The observations were done within the Hale-Bopp long-term monitoring programme (Rauer *et al.*, 2003) and the reduction of the data was performed by J. Helbert. The observations and their reduction are described in detail by Helbert (2002). The spectra were taken with the Boller & Chivens spectrograph mounted at the ESO 1.5-m telescope at the La Silla observatory. At the time of observation, comet Hale-Bopp was at a heliocentric distance of 3.78 AU and a geocentric distance of 3.60 AU. The instrument set-up used for the observations is summarized in Tab. 8. For the validation of the model, only one spectrum obtained on December 19, centered on the nucleus position and with the slit oriented along the projected solar-antisolar direction, is used. A spectrum with good signal-to-noise ratio and not affected by star traces was selected. In order to increase the signal-to-noise ratio, the spectrum was rebined along the spatial direction by a factor of 9.

*Table 6: Observing log including all long-slit spectra of comet 9P/Tempel 1. The Table provides the date and time of each observation, the exposure time, exp, and the wavelength range, $\Delta\lambda$, covered in each spectrum. The position angle of the slit, p.a., is measured from the projected solar direction towards the North. Observations marked with * were done using FORS 1, the others were done with FORS 2. The symbol † indicates that the night was not photometric.*

Time [UT]	*exp* [s]	$\Delta\lambda$ [nm]	p.a. [°]	r_h [AU]	v_r [km s^{-1}]	Δ [AU]	solar p.a.
July 3, 00:09	600	370 – 620	0, 180	1.51	−0.38	0.88	291.7°
July 3, 00:21	900	370 – 620	0, 180				
July 3, 00:40	900	610 – 920	0, 180				
July 3, 01:19	900	370 – 620	90, 270				
July 3, 01:43	900	370 – 620	135, 315				
July 3, 02:14	900	370 – 620	45, 225				
July 3, 02:36	900	370 – 620	0, 180				
July 3, 02:49	900	370 – 620	0, 180				
July 3, 03:11	900	370 – 620	90, 270				
July 3, 03:40	900	370 – 620	0, 180				
July 3, 23:31	900	370 – 620	0, 180	1.51	−0.15	0.89	291.4°
July 3, 23:49	900	610 – 920	0, 180				
July 4, 00:40	900	370 – 920	90, 270				
July 4, 01:00	900	370 – 620	0, 180				
July 4, 01:21	900	370 – 620	90, 270				
July 4, 01:42	900	370 – 620	0, 180				
July 4, 02:07	900	370 – 620	90, 270				
July 4, 02:28	900	370 – 620	0, 180				
July 4, 02:50	900	370 – 620	90, 270				
July 4, 03:11	900	370 – 620	0, 180				
July 4, 03:27	600	370 – 620	0, 180				
July 4, 23:50	900	370 – 620	0, 180	1.51	−0.03	0.90	291.3°
July 5, 00:07	900	610 – 920	0, 180				
July 5, 00:48	900	370 – 620	90, 270				
July 5, 01:13	900	370 – 620	135, 315				
July 5, 01:36	900	370 – 620	45, 225				
July 5, 01:58	900	370 – 620	0, 180				
July 5, 02:22	900	370 – 620	135, 315				
July 5, 03:22	900	370 – 620	135, 315				
July 5, 03:46	900	370 – 620	0, 180				
July 6, 00:32	900	370 – 620	0, 180	1.51	0.09	0.90	291.1° †
July 6, 00:53	900	610 – 920	0, 180				
July 6, 01:36	900	370 – 620	90, 270				
July 6, 02:00	900	370 – 620	135, 315				
July 6, 02:30	606	370 – 620	45, 225				
July 6, 02:57	600	370 – 620	45, 225				

Time [UT]	*exp* [s]	$\Delta\lambda$ [nm]	p.a. [°]	r_h [AU]	v_r [km s^{-1}]	Δ [AU]	solar p.a. [°]
July 7, 00:32	900	370 – 620	0, 180	1.51	0.20	0.91	291.0°
July 7, 00:53	900	370 – 620	90, 270				
July 7, 01:17	900	370 – 620	135, 315				
July 7, 01:39	900	370 – 620	45, 225				
July 7, 02:20	900	370 – 620	0, 180				
July 7, 02:39	900	610 – 920	0, 180				
July 7, 03:01	900	370 – 620	90, 270				
July 7, 03:24	900	370 – 620	135, 315				
July 7, 23:33	900	370 – 620	0, 180	1.51	0.32	0.91	290.9°
July 7, 23:52	900	610 – 920	0, 180				
July 8, 00:34	900	370 – 620	90, 270				
July 8, 00:58	900	370 – 620	135, 315				
July 8, 01:24	900	370 – 620	45, 225				
July 8, 01:46	900	370 – 620	0, 180				
July 8, 02:30	900	370 – 620	90, 270				
July 8, 02:53	900	370 – 620	135, 315				
July 8, 03:18	900	370 – 620	45, 225				
July 8, 03:41	900	370 – 620	0, 180				
July 8, 23:44	900	370 – 620	0, 180	1.51	0.44	0.92	290.7°
July 9, 00:03	900	610 – 920	0, 180				
July 9, 00:45	900	370 – 620	90, 270				
July 9, 01:11	900	370 – 620	135, 315				
July 9, 01:32	900	370 – 620	45, 225				
July 9, 01:56	900	370 – 620	0, 180				
July 9, 02:19	900	370 – 620	90, 270				
July 9, 02:42	900	370 – 620	135, 315				
July 9, 03:03	900	370 – 620	45, 225				
July 9, 03:36	900	370 – 620	0, 180				
July 9, 23:34	900	370 – 620	0, 180	1.51	0.55	0.93	290.5°
July 9, 23:54	900	610 – 920	0, 180				
July 10, 00:34	900	370 – 620	90, 270				
July 10, 00:56	900	370 – 620	135, 315				
July 10, 01:20	900	370 – 620	45, 225				
July 10, 01:42	900	370 – 620	0, 180				
July 10, 02:05	900	370 – 620	90, 270				
July 10, 02:28	900	370 – 620	135, 315				
July 10, 02:50	900	370 – 620	45, 225				
July 10, 03:22	900	370 – 620	0, 180				
July 11, 03:20*	900	370 – 580	0, 180	1.51	0.67	0.93	290.5°
July 12, 03:16*	900	370 – 580	0, 180	1.51	0.78	0.94	290.3°
July 12, 03:40*	600	370 – 580	90, 270				

Table 7: Summary of the instrumental set-up and the observing conditions during the observations of comet C/2002 T7 LINEAR and C/2001 Q4 NEAT with EFOSC2. r_h *and* Δ *denote the heliocentic and geocentric distance, respectively.* β *denotes the phase angle and w.r. means the wavelength range covered by the spectra.* Δx *and* $\Delta\lambda$ *denote the spatial scale and the wavelength increment, respectively.* $\Delta x'$ *is the spatial scale in the plane of the comet's nucleus.*

Parameter	C/2002 T7	C/2001 Q4
slit length [']	5.0	5.0
slit width ["]	2.0	2.0
w.r. [Å]	3700−6100	3700−6100
Δx ["/pixel]	0.316	0.158
$\Delta x'$ [km/pixel]	236	44.7
$\Delta\lambda$ [Å/pixel]	3.0	1.5
r_h [AU]	1.20	1.00
Δ [AU]	1.03	0.39
β	53.6°	79.7°

Table 8: Overview of the set-up of the Boller & Chivens spectrograph used for observations of comet C/1995 O1 Hale-Bopp on December 19, 1997.

Parameter	Value	Remark
Slit length	4.5'	
Slit width	2.36"	
Pixel size	0.82"/pixel	unbinned
	7.38"/pixel	binned
Spatial scale	2158.8 km/pixel	unbinned
	19429.2 km/pixel	binned
Wavelength scale	1.89 Å/pixel	
Wavelength range	3600 Å– 6800 Å	

3 Data Reduction

The purpose of this chapter is to provide an overview of the reduction procedures applied to the data used in this work. First, the basic reduction steps for images and long-slit spectra are presented in brief in the order in which they were applied. It is noted in the beginning of each subsection whether the procedures described apply to images, long-slit spectra, or both. From the section discussing extinction correction onwards, however, only the reduction of long-slit spectra is discussed since all images used in this work were only calibrated up to this step.

Reduction steps specific to a particular telescope or instrument will also be discussed. These reduction steps have to be applied to single observations only.

3.1 Basic Reduction Steps

3.1.1 Removal of Cosmic Ray Events

This reduction step applies to both images and long-slit spectra.
The CCD chip is affected by irradiation due to the natural background radiation, caused by cosmic radiation and terrestrial radioactive isotopes. The radiation can produce charge inside the CCD if they penetrate the chip. The pixels of the CCD where this occurs can be recognized by their high counting rate in ADU[2], compared to the surrounding area of the CCD. These isolated areas with strongly enhanced counting rates due to cosmic ray events are called *cosmics*. Typical rates for cosmic events depend on the geographical location and physical properties of the detector. As an example, for the FORS 2 spectrograph at the ESO Paranal Observatory, the cosmic event rate is 2.4 per minute per square centimeter (FORS1 + 2 User Manual, Issue 2.8, 2004). Since the cosmics disturb the further reduction and analysis of the data, they have to be removed. For sequences of exposures of the same type (e.g. a number of flatfield frames or bias frames), this can be done by creating a median frame. In this median frame, every pixel has the median value determined from the same pixel on the CCD in all frames of one sequence. Different from taking the mean value, median filtering is suitable for removing cosmics, because the median filter is not sensitive to single values in a sequence which may have a value very different from the other values in the sequence.

In exposures where such a procedure is not applicable (e.g. single comet or standard star exposures), the values of the pixels affected by the cosmic have to be interpolated from the surrounding pixels in the CCD frame. This can by done by fitting a polynomial of low order to both sides of the area of which the pixel values are to be replaced. The direction of fitting (along the rows or columns of the CCD) should be chosen for which

---

[2] ADU stands for *Analog-to-Digital-Unit* and is the discrete unit into which the signal in a CCD pixel is converted after read-out.

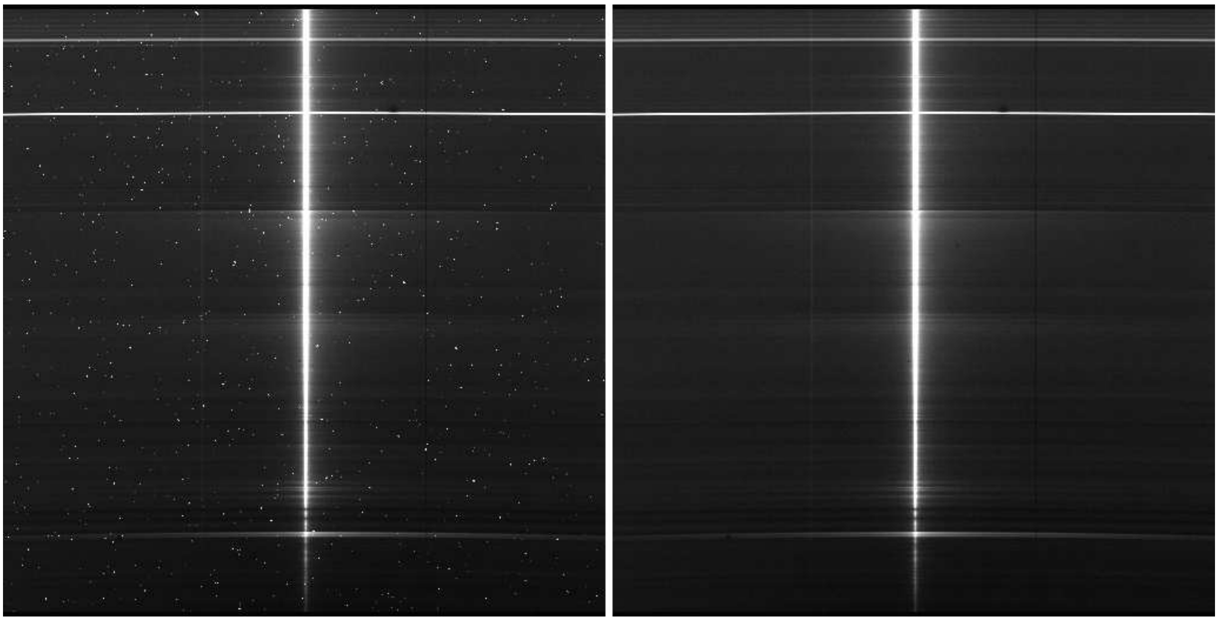

Figure 4: Long-slit spectrum of comet 9P/Tempel 1 taken with the FORS 1 instrument on July 10/11, 2005, before (left) and after (right) the removal of the cosmics. The exposure time was 15 minutes. The spatial axis is in the horizontal direction, the wavelength is increasing from the bottom to the top of the image. In the bottom, the prominent cometary CN emission line at 3875 Å can be seen, in the top the two bright night sky lines at 5577 Å and 5893 Å are visible.

the change in pixel values is most smooth. As an example, for frames of long-slit spectra in some distance from the photocenter this is usually the case along the spatial direction. In the vicinity of the photocenter in long-slit spectra or images of comets, the gradient is usually too large to allow a good interpolation of pixel values from the neighbouring pixels.

Fig. 4 shows a long-slit spectrum of comet 9P/Tempel 1 before and after the removal of the cosmics for comparison. The brightness scaling is the same in both cases.

3.1.2 Bias Subtraction

This reduction step applies for both images and long-slit spectra.
In order to avoid negative numbers when converting the charge collected within one CCD pixel to digital units (ADU), an (ideally) constant voltage is applied in the read-out mechanism of the CCD. This voltage results in an (ideally) constant number of ADUs added to each pixel in the image obtained after the read-out. In order to quantitatively analyse CCD frames, this value has to be subtracted from all CCD exposures.

The value of the bias voltage in ADU, or simply the *bias* value, is determined by taking a sequence of images produced by simply reading out the CCD detector without any exposure or time delay. These images should then contain only the bias value in each pixel. Furthermore, the images can be used to check the degree to which the bias value remains constant. If no variable structures are present in the single images, the median filtered bias frame can be created, as explained for the cosmic removal previously. If the median filtered bias frame shows no variation along its rows and columns, its mean value can be determined and subtracted from other frames. If a systematic variation of the bias value is present, the frame itself has to be subtracted from other frames. If however the possible variations are of a large scale, the bias frame can be smoothed to suppress its noise before subtraction from other frames.

In most cases, bias frames are obtained at the beginning and at the end of an observing night. Only in a few observations bias frames were obtained only once a night or only once for a number of consecutive nights.

3.1.3 Correction for Dark Current

With time charges accumulate in the CCD pixels even without exposure to light. This charges result in an additional value in ADU added to the pixel values. This additional value, increasing linearly with time, is called *dark current*. However, for most modern instruments, this value is small and can be neglected for typical exposure times. In this work, the longest exposure time applied is 20 minutes. Within this time, the dark current remains smaller than the CCD read-out noise. Therefore, the dark current is neglected in this work.

3.1.4 Flatfield Correction

This reduction step has to be done in a different way for images compared with long-slit spectra.

Pixels of a CCD detector show different sensitivity to light and thus systematic differences in their ADU values after read-out. Furthermore, optical effects, e.g. due to vignetting or dirt particles within the light path, lead to the appearence of structures in CCD images on a medium to large scale. In order to remove the influence of all these effects from an exposure, additional exposures of a field of (ideally) homogeneous brightness are taken. These frames are called *flatfield exposures* and reveal variations in the counting rates of different pixels due to the effects mentioned afore. To obtain the field with a homogeneous brightness, one may use a canvas with a homogeneous illumination, or the approximately homogeneous sky during dusk or dawn. In the latter case, the telescope has to be slightly moved between single flatfield exposures to make possible the removal of star images within the exposures. Flatfield frames have to be obtained separately for all instrumental set-ups used for observations. Usually, all flatfield frames of a sequence for the same instrumental set-up are median filtered to remove cosmics and to reduce the noise level. The median filtered flatfield frame (after bias subtraction) is normalized, and other images are divided by the median filtered and normalized flatfield frame.

For images, the normalization is simply achieved by dividing the frame by its mean value. For long-slit spectra, the wavelength dependency of brightness along the dispersion direction has to be taken into account. This is done by taking the average spectrum along the spatial direction of the CCD frame and dividing every CCD line along the spatial direction by the mean spectrum.

3.1.5 Wavelength Calibration

This reduction step only applies to long-slit spectra.
To obtain a wavelength calibration of long-slit spectra, emission spectra of calibration lamps are taken. These lamps provide line spectra of noble gases (usually Helium, Neon, and Argon), for which the wavelengths of certain lines are provided by catalogues. By comparing the position of the lines on the CCD with the corresponding wavelengths from the catalogue, every pixel position along the dispersion direction of the CCD frame can be related to a wavelength. Two effects complicate this process:

Usually, the wavelength for a given pixel position in dispersion direction is not constant along the spatial direction of the CCD frame. This effect makes a separate wavelength calibration of every column of the CCD frame along the slit direction necessary.

The dispersion is usually not strictly linear with wavelength. Therefore, a binomial is fitted to the relation of the pixel position of spectral lines and the corresponding wavelength.

A resampling of the spectra is then performed to obtain one linear wavelength axis for all columns of the CCD along the spatial direction.

3.1.6 Sky Background Subtraction

This reduction step has to be done in a different way for images compared with long-slit spectra.
The background of ground-based optical observations is dominated by fluorescent emissions from the Earth's atmosphere. This telluric background, called *airglow*, consists of both, a continuum as well as much stronger emission lines (Lena *et al.*, 1998; Patat, 2003). At poor observational sites, artificial light from surrounding infrastructure can also contribute to the night sky background mainly in the form of emissions from mercury and sodium. Fig. 5 shows spectra of the night sky for the Paranal observatory, obtained with the FORS 2 instrument. The displayed wavelength range includes the most prominent and thus most important cometary gas emissions. The spectra were taken at different times during the night which revealed a temporal variation in the brightness of the emission lines.

For images, the determination of the sky background level to be subtracted from the

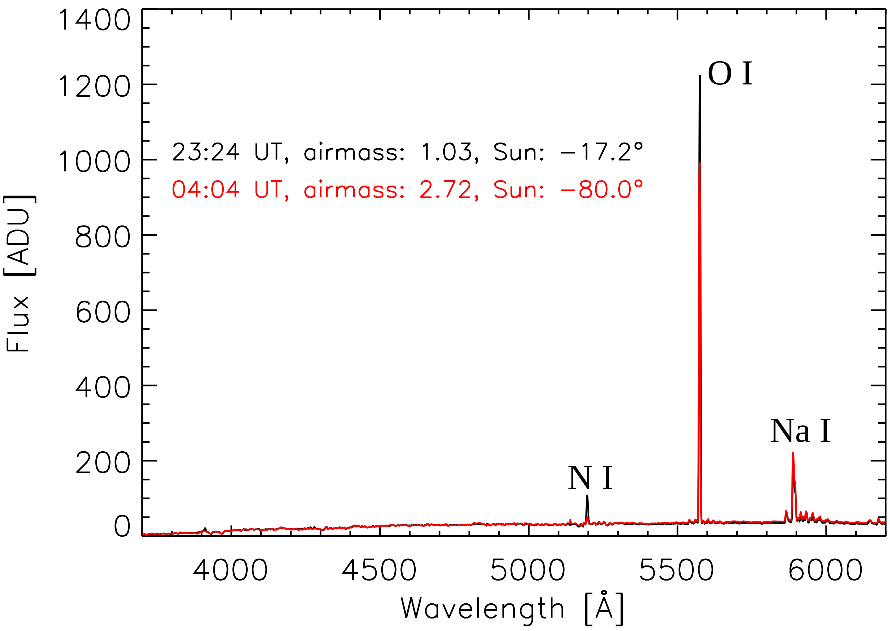

Figure 5: Spectra of the night sky at the Paranal observatory, taken in the night of July 7/8, 2005, with the FORS 2 instrument. The observing times, airmass, and solar altitudes are displayed. The spectra were taken under photometric conditions while the Moon was below the horizon. The most prominent emission lines are marked with the atoms causing them, using spectroscopic notation.

comet images and calibration frames can be done in three different ways, depending on the observational situation:

(1) In the case of standard star exposures or exposures of comets without activity (i.e. all point-like sources), the sky background brightness can best be determined from an annulus around the source of interest, whereby a two-dimensional Gaussian profile is fitted to the point-spread function of the source. By doing so, the position of the center and the width of the point-spread funcion on the CCD frame can be determined. The sky background brightness is obtained as the mean value of all pixels fulfilling the condition $\mathrm{n}_1 \cdot \sigma < \mathrm{r} < \mathrm{n}_2 \cdot \sigma$. Here, r denotes the distance of a particular pixel to the center of the point spread function of the source (measured in pixels), and σ denotes the width of the Gaussian. The values of n_1 and n_2 are chosen in such a way that the brightness contribution of the source to the annulus is negligible and that no other stars are included. The actual values can vary for different observations, but typical values are for example $\mathrm{n}_1 = 5$ and $\mathrm{n}_2 = 15$.

(2) In the case of observations of comets which do not fill the whole field of view with their comae, areas at the edge of the frame containing no cometary brightness and no stars can be chosen. The sky background brightness is then given by the mean value of

all pixels from the areas chosen.

(3) In the case of observations of comets whose comae fill the instrument's entire field of view, separate sky background exposures have to be taken. For this purpose, the telescope has to be trained upon a position close to that of the comet (typically around 30 to 40 arcminutes away from the nucleus position), where an exposure of the sky without contributions from the cometary coma is taken. In this exposure, areas without stars are chosen, and the sky background brightness is given by the mean value of all pixels in the chosen areas. The adjustment of the telescope should be done roughly towards the projected solar direction to make sure that the cometary tail is not influencing the sky background determination. Since the sky background brightness changes, a number of sky exposures has to be taken during the night, more often while the solar altitude is changing quickly (after dusk and before dawn), and less often during the middle of the night. Since a larger area of the sky background frame can be averaged, a shorter exposure time of the sky frames than the exposure time of the science frames can in principle be used in order to safe time. This requires very stable bias conditions and an accurate determination of the bias level, since the low counting rate in ADU of the sky background makes it very sensitive to errors or variations in the bias level. Unfortunately, it turned out that most instruments used for observations in this work did not provide sufficiently stable conditions to allow for a shorter exposure time for the sky frames.

In the case of long-slit spectroscopic observations, the sky background depends on the wavelength. Therefore, a sky background spectrum has to be subtracted from the data.

If the cometary coma does not fulfil the whole slit length, the sky background can be determined from the edges of the slit. Therefore, sections of the data frame taken along the spatial direction, which are free of cometary coma and star traces, are averaged to a one-dimensional spectrum of the sky background. This spectrum is subtracted from the whole data frame.

In the case of a coma that fills the entire slit length, additional sky spectra have to be taken, analogous to the case of images as described above. The sky background spectrum is then determined from these separate sky exposures and subtracted from the comet long-slit frame.

For the reduction of the spectroscopic observations of the comets C/2001 Q4 and C/2002 T7 analysed in this work, no suitable sky backgroud measurements are available. Therefore, no sky background subtraction could be done.

3.1.7 Extinction Correction

In order to correct spectra for extinction, the ESO standard extinction curve was used (Burki *et al.*, 1995). The wavelength-dependent extinction coefficients were linearly interpolated to the wavelength axis of the long-slit specta, and the extinction correction of the flux $F(\lambda)$, as measured in one pixel, was done according to

$$F_c(\lambda) = F(\lambda) \cdot 10^{0.4\,\beta(\lambda)\,z} \,, \tag{8}$$

where $F_c(\lambda)$ is the extinction-corrected flux, $\beta(\lambda)$ is the wavelength-dependent extinction coefficient, and z is the airmass at which the observation was done.

3.1.8 Flux Calibration

The conversion of the comet spectra from arbitrary units to physical units is done by comparison with standard star spectra. Standard stars, for which flux-calibrated catalogue spectra are available, were observed before or after the observations of the comet. By dividing the observed spectrum by the catalogue spectrum, the response curve of the detector is obtained, which makes a conversion from arbitrary units to physical units possible. For this purpose, the observed spectrum and the catalogue spectrum are brought to the same wavelength resolution by rebinning, and the observed flux of the star is determined by summation over the point-spread function along the long-slit.

If more than one standard star was observed in one night, the response curves obtained from the different stars can be averaged to improve the accuracy of the calibration. Fig. 6 shows flux-calibrated spectra of observed standards, LTT 7379 (Hamuy *et al.*, 1992, 1994) and NGC 7293 (Oke, 1990), compared with their catalogue spectra. The calibration of the observed spectra was done with a spectrum of a third standard star (LTT 6248, Hamuy *et al.* (1992, 1994)). For LTT 7379, the observed spectrum is slightly below the corresponding catalogue spectrum, while for NGC 7293 the observed spectrum and the catalogue spectrum are in a good agreement. For the calibration of the comet spectra, the response curves from all three standards were averaged.

3.1.9 Gas Emission - Continuum Separation

In order to analyse the gas emissions of a cometary coma, one must separate the signal from the gas emissions from that of the continuum of sunlight scattered by the dust particles in the coma. This is done by fitting a solar spectrum to the cometary spectrum in wavelength regions where no gas emissions are present. Therefore, the comet spectrum is divided by the solar spectrum and a polynomial is fitted to the result. The degree of the polynomial and the regarded wavelength range can be varied until a satisfying fit is obtained. Then, the solar spectrum is multiplied by the fitted polynomial and the result is subtracted from the cometary spectrum. The pure gas emission spectrum is obtained after subtraction. The solar spectrum multiplied with the polynomial can be used as an approximation of the continuum spectrum. This procedure has to be applied to each position of the CCD along the spatial direction. Fig. 3 shows a flux calibrated cometary spectrum, and the gas emission spectrum obtained from it.

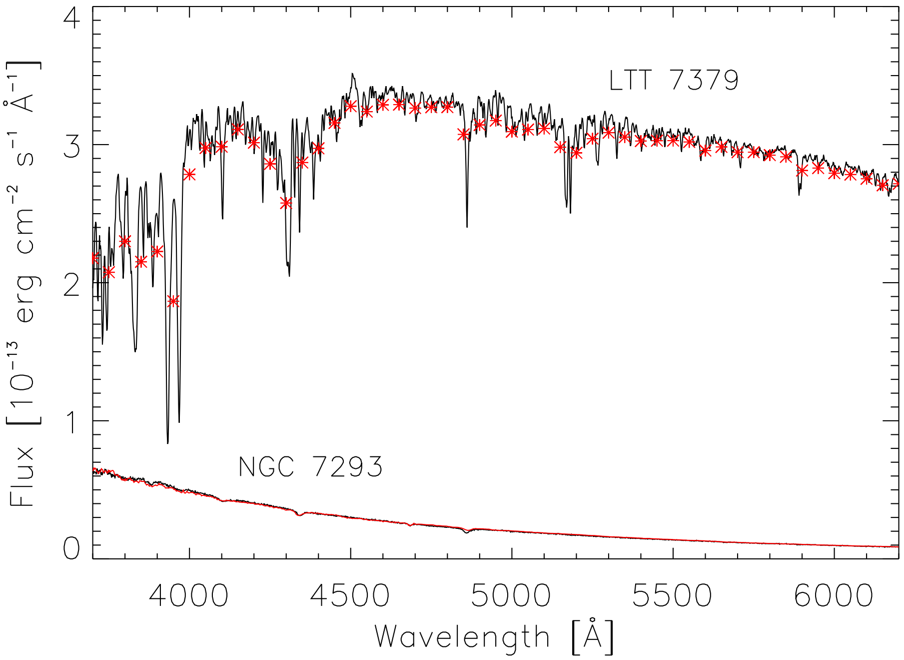

Figure 6: Comparison of the catalogue spectra and spectra observed with FORS 2 on July 3/4, 2005, of the two spectrophotometric standards LTT 7379 and NGC 7293. The catalogue values are displayed in red, the observed spectra are shown in black. Note that the wavelength bins of the catalogue spectrum of LTT 7379 are larger than the wavelength bins for NGC 7293. The observed spectra were calibrated using a third spectrophotometric standard (LTT 6248).

For the solar spectrum, a spectrum of a solar analogue star or a solar system object (e.g. the Moon, a planet), observed with the same instrumental set-up as the comet, can be used. If no such spectrum is available, a high-resolution solar catalogue spectrum (e.g. Kurucz *et al.* (1984)) can be convolved with a Gaussian of adjustable width until it matches the resolution of the comet spectrum. The catalogue spectrum with the same resolution as the comet spectra can then be used for continuum separation.

In the long-slit spectra of comets C/2001 Q4 and C/2002 T7, the sky background could not be subtracted. When subtracting the continuum from the gas emission spectrum, the major contribution of the night sky continuum spectrum can be expected to be removed from the gas emission spectrum, too. Therefore, the gas emission spectra of these two comets can still be used for further analysis.

3.2 Specific Reduction Steps

3.2.1 Removal of Coherent Noise

All data used in this work that were obtained with the FORS 2 spectrograph at the VLT UT1 in July 2005 are affected by a coherent noise, which has a low frequency in the spatial

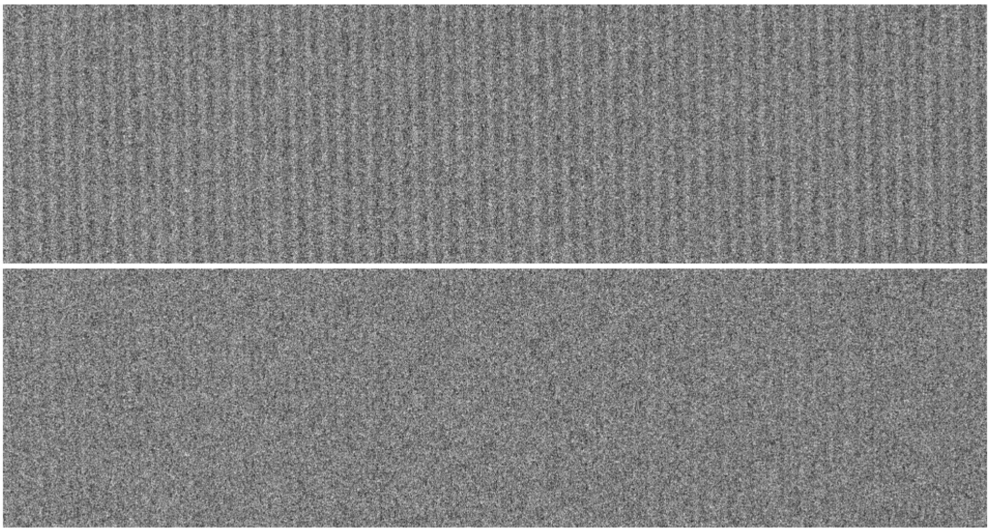

Figure 7: Subsection (950 × 250 pixels) of a bias frame taken with FORS 2 on July 3/4, 2005, before (top) and after (below) correction for the coherent noise. The brightness is scaled ± 8% around the mean value of 188.6 ADU.

direction of long-slit spectra, and a high frequency along the dispersion direction. The low-frequency component was basically constant over each night and could be determined well from bias frames, where it was clearly visible. For the high-frequency component, the investigations showed, however, a slight variation in frequency during the night. This noise component was determined by the use of unexposed edges of the CCDs of FORS 2 in each single exposure. A Fourier filter method was applied for both noise components to identify and remove them. A discrete Fast Fourier Transformation was applied to the full bias frames or to the unexposed edges of the other frames. Then, all signals above a given threshold were included in an inverse Fourier transformation to produce a noise frame. This noise frame was then subtracted from the original. The threshold value was chosen in such a way that a good removal of the coherent noise by visual inspection could be obtained. The noise frame included one frequency for the low-frequency contribution and one or two frequencies (in rare cases three frequencies) for the high-frequency contribution.

This reduction step was applied after the removal of cosmics and before the bias subtraction. Fig. 7 shows a section of a bias frame before and after removal of the coherent noise for illustration. In this Figure, the dispersion direction is in the horizontal direction, and the spatial direction is along the vertical direction. On the left edge of the image, it can be seen that the noise patterns are not perfectly parallel to the edge of the images, showing the low-frequency noise pattern in the spatial direction.

3.2.2 Correction for Straylight

In the spectroscopic frames taken with the FORS 2 instrument in July 2005, there featured a poor matching of the sky background spectra with the cometary spectra. As a possible explanation, straylight on the detector was considered. Since the slit of this instrument does not cover the full width of the two CCDs[3], unexposed edges remain on each side of the individual CCD frames that can be used for an evaluation of possible straylight. Fig. 8 shows the counting rate level of the unexposed edge along the dispersion direction for different types of observations. It can be seen that the level of the unexposed edge of a standard star frame (green), taken with the shortest exposure time and thus having a very low background exposure level (red), is in a good agreement with the mean bias level. In the sky background exposures (blue) an enhancement can be seen in the unexposed edges. This enhancement becomes stronger in comet frames (black) which are taken with longer exposure times and have a higher background level. The enhancement of the ADU values in the unexposed edges of the comet frames also show a dependency on the wavelength. A likely explanation is straylight in the case of a fully illuminated field of view. Since the two-dimensional structure and the temporal stability of the straylight contribution remains unknown, only a crude correction is possible. Several rows along the unexposed edges were binned and then smoothed over a wide smoothing window (30 pixels). The result of that procedure was then subtracted from each row of the CCD as an approximation for the straylight contribution. This was done for the two CCDs independently.

This reduction step was done after the bias subtraction and the flatfield correction. No significant change in the final spectra was detectable if the straylight correction was done before the flatfield correction.

Since for the data taken with the FORS 1 instrument, the sky background spectra only poorly matched the comet spectra, the presence of a straylight contribution is likely in the data from that instrument, too. Since no ”unexposed edges” are available in the data taken with FORS 1, a straylight correction cannot be done for FORS 1 spectra.

3.2.3 Correction for Differential Movement of a Comet

The 2-m telescope of the Thüringer Landessternwarte Tautenburg does not have the capability to track a comet with its velocity relative to the background stars. Therefore, only short exposure times were possible without noticeable smearing of the comet image. In order to improve the image quality, sequences of images of a comet were taken with exposure times within which the comet's movement in the sky is less than the pixel size of the CCD (in arcseconds in the sky). Then, the images were shifted to compensate for the comet's movement and finally co-added.

In order to determine the required shift of an image relative to another in the x- and y-directions, measured in number of pixels along the perpendicular egdes of the comet frames, between three and five stars detectable in both images were selected. The point-

---

[3] The detector of the FORS 2 instrument uses two individual CCD chips that are separated by a small gap.

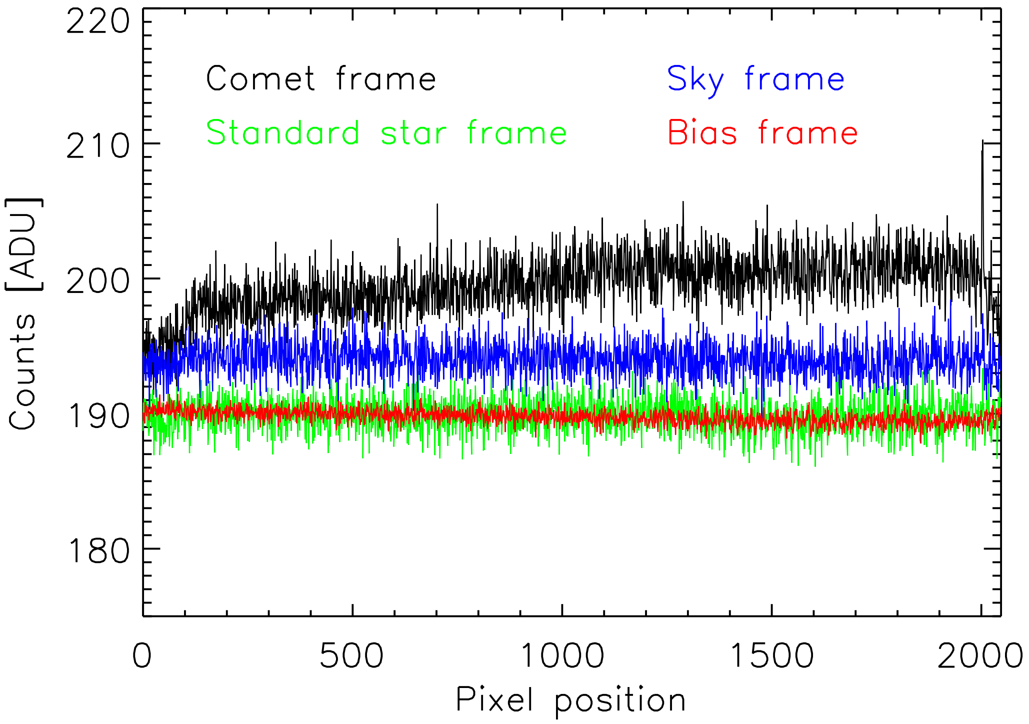

Figure 8: Comparison of the counting rates within the unexposed edges for four different types of FORS 2 exposures. The counting rate levels for the mean bias frame, a standard star frame (5 s exposure time), a sky background frame (180 s exposure time) and a comet frame (900 s exposure time) are shown in different colours. All frames were taken on July 3/4, 2005. 15 rows in each unexposed edge were binned together to increase the signal-to-noise ratio, the displayed pixel position follows the dispersion direction on the CCD with increasing wavelength.

spread functions of these stars were fitted by a two-dimensional Gaussian to determine the position of the center of the stars in both images. From this procedure, the relative shift of the star background in the two images due to poor guiding of the star movement can be determined. From the ephemeris, the mean velocity of the comet in the sky in declination and right ascension is known. By knowing the time between the two exposures, the movement of the comet in arcseconds between the two images can be computed in both directions. Since the pixel size of the CCD in arcseconds in the sky is known, the movement of the comet in declination and right ascension can be computed in number of pixels. The orientation of the images relative to the equatorial reference frame (i.e. the North and East direction in the images) is also known. Together with the guiding error relative to the stars, the total shift between two images that puts the comet's nucleus position on the same pixel position in both images can be computed.

This procedure can be applied to the full sequence of images obtained. The images are then co-added. The major disadvantage of this method is the increasing flatfield error if a larger number of images is added. Weak systematic tendencies in the flatfield-corrected frames add up with the images, too, and cause artificial features to arise. When adding more than approximately 16 to 18 images, such features become so prominent that no more improvement of the quality of the comet image is obtained.

3.2.4 Removal of Detector Effects

Observations done with the CCD camera at the 2-m telescope of the Thüringer Landessternwarte Tautenburg on March 06/07, 27/28 and 29/30, 2003, were affected by a large number of "dead" pixels within the images, having a value of zero ADU. The positions of these "bad pixels" appear to be random, and their density in the images is so high that a detailed analysis of the cometary coma after the co-adding of several images is impossible. Interpolating the values of the disturbed pixels from the surrounding area of the same image is not suitable in the inner coma of the comet since the brightness gradient is large, making it difficult to obtain a good fit. Therefore, other images obtained in the same night were used for correction of the "bad pixels". The bias- and flatfield-corrected images were shifted to compensate for the comet's movement in a way that the optocenter of the coma always corresponded to the same pixel on the CCD, as described above. The positions of the disturbed pixels were then detected by applying a threshold level in each image. The pixel values were replaced by values of the same pixel from another (in most cases the next) image of the observing sequence. In order to take the changing weather conditions into account (the sky conditions were non-photometric in all cases), the values from the image used for replacing the disturbed pixels were multiplied by a correction factor. This factor was derived from the ratios of fluxes of a number of stars (in ADU), determined in both the image to be corrected and the image used for the replacement. Due to the shifting of the images on a sub-pixel level to compensate the comet's movement, the pixels neighbouring a disturbed pixel could be affected as well. Therefore, all pixels of an image surrounding a detected 'bad' pixel were also replaced.

4 Model of the Coma Chemistry

As summarized in chapter 1, the gas in the cometary coma is subject to a number of influences, such as solar irradiation, magnetic fields, and solar gravity. In this chapter a coma model is presented that includes a gas flow from the nucleus surface into space. Within that gas flow, chemical reactions of different types occur, and causing the chemical composition of the gas flow to vary with nucleocentric distance. The goal of the model is to obtain radial column density profiles for various species. The presented model makes use of a number of simplifications that are also discussed in this chapter.

For the species that can be observed by optical long-slit spectroscopy, the computed column density profiles as a function of nucleocentric distance can be compared with observed column density profiles to constrain the initial composition of the gas flow at the nucleus surface.

4.1 Hydrodynamics of the Coma

4.1.1 Basic Equations

The fundamental equations to describe the cometary coma are the continuity equation for particle number, and the conservation equations for mass, momentum, and energy. First only one inviscid fluid is regarded. For the particle flux, $n\vec{v}$ where n is the particle number density in a fluid and $\vec{v}$ is the velocity of the fluid, the continuity equation is:

$$\frac{\partial n}{\partial t} + \operatorname{div}(n\vec{v}) = N_s \; . \tag{9}$$

Here, N_s denotes the source term for n. For the conservation of mass, the corresponding equation is:

$$\frac{\partial \rho}{\partial t} + \operatorname{div}(\rho\vec{v}) = M_s \; , \tag{10}$$

with the mass density ρ and the mass source term, M_s. However, the mass density can be computed from the number density n by $\rho = \mu \cdot n$, where μ is the molecular mass. The energy flux density is given by $\rho\vec{v}\,(v^2/2 + w)$, where w is the enthalpy per mass. It is related to the specific internal energy of the fluid element, ϵ, by $w = \epsilon + pV$ (Landau and Lifschitz, 1991). The energy conservation equation therefore becomes:

$$\frac{\partial}{\partial t}\left(\frac{\rho v^2}{2} + \rho\epsilon\right) + \operatorname{div}\left(\rho\vec{v}\left(\frac{v^2}{2} + w\right)\right) = Q_s \; , \tag{11}$$

where Q_s denotes the energy source term. The conservation equation for the momentum is complicated by its vector nature. The momentum flux density is given by the expression:

$$\frac{\partial}{\partial t}(\rho\vec{v}) + \vec{\nabla}\Pi = \vec{F}_s \; . \tag{12}$$

Here, Π is the momentum flux tensor, which is in cartesian coordinates $\Pi_{ik} = p\delta_{ik} + \rho v_i v_k$ (Landau and Lifschitz, 1991). p denotes the gas pressure and $\vec{F_s}$ is the momentum source term.

In the following, a steady-state and spherically symmetric gas flow is assumed. With these assumptions, the equations (9) to (12) can be simplified. The steady-state flow causes the partial deviation with respect to time, t, to become zero. The divergence can be written in spherical coordinates and the symmetry causes only the radial component of the divergence to be non-zero. The conservation equations then become (Rodgers and Charnley, 2002):

$$\begin{aligned}
\frac{1}{r^2}\frac{\mathrm{d}}{\mathrm{d}r}\left(r^2 n v\right) &= N_s && (13)\\
\frac{1}{r^2}\frac{\mathrm{d}}{\mathrm{d}r}\left(r^2 \rho v\right) &= M_s && (14)\\
\frac{1}{r^2}\frac{\mathrm{d}}{\mathrm{d}r}\left(r^2 \rho v\left(\frac{v^2}{2} + \frac{\gamma}{\gamma-1}\frac{k_B T}{\mu}\right)\right) &= Q_s && (15)\\
\frac{1}{r^2}\frac{\mathrm{d}}{\mathrm{d}r}\left(r^2 \rho v^2\right) + \frac{\mathrm{d}}{\mathrm{d}r}\left(n k_B T\right) &= F_s\ . && (16)
\end{aligned}$$

In the energy equation (15), w was replaced by using the relation

$$w = \gamma/(\gamma-1)pV = \gamma/(\gamma-1)k_B T/\mu\ , \tag{17}$$

with the Boltzmann constant k_B, the adiabatic exponent γ, and the molecular mass μ. In the equation for the momentum conservation (16), the pressure p was replaced by using the ideal gas law, $p = n k_B T$.

From the equations (13) to (16), differential equations for the number density n, the velocity v, and the temperature T can be obtained. Equation (13) directly leads to

$$\frac{\mathrm{d}n}{\mathrm{d}r} = \frac{N_s}{v} - \frac{n}{v}\frac{\mathrm{d}v}{r} - \frac{2n}{r}\ . \tag{18}$$

From equations (14) to (16), one obtains after some re-arrangement (Rodgers and Charnley, 2002):

$$\begin{aligned}
\frac{\mathrm{d}v}{\mathrm{d}r} &= \frac{1}{\rho v^2 - \gamma n k_B T}\left(F_s v - (\gamma-1)G - M_s v^2 + \frac{2v}{r}\gamma n k_B T\right) && (19)\\
\frac{\mathrm{d}T}{\mathrm{d}r} &= \frac{(\gamma-1)T}{v}\left(\frac{G}{n k_B T} - \frac{2v}{r} - \frac{\mathrm{d}v}{\mathrm{d}r} - \frac{N_s}{(\gamma-1)n}\right)\ , && (20)
\end{aligned}$$

where $G = Q_s - F_s v + 1/2 M_s v^2$.

4.1.2 Generalization to a Simplified Multi-Fluid Model

The cometary coma contains a variety of chemical species. In principle, every single species has to fulfil a set of differential equations given by equations (18) to (20). These equations are coupled by the source terms, since members of a species are created or destroyed by chemical reactions, and the energy and momentum can be exchanged between the different species. In order to reduce the number of equations to be solved, not all species are treated as individual fluids. In the following, three fluids consisting of the neutral species, the ionic species, and the electrons are considered. For the computation of the expansion velocity v, all species are assumed to move with the same velocity. Since the ions and the electrons are coupled by Coulomb forces, charge neutrality results. The assumption of the ion and electron fluid moving with the same hydrodynamic velocity, hereafter called the plasma velocity, is therefore reasonable. When computing the plasma velocity from equation (19), numerical problems occur since the plasma fluid can become subsonic when moving outwards from the nucleus. The sonic speed c_p of the plasma, containing ions of a mean ion mass μ_i, is given by (Rodgers and Charnley, 2002):

$$c_p = \sqrt{\frac{k_B(\gamma_i T_i + \gamma_e T_e)}{\mu_i}} \ . \tag{21}$$

Since the electron temperature can become high in the outer coma (to the order of 10^4 K), c_p can increase until it reaches the hydrodynamic plasma velocity. At the sonic point, equation (19) becomes singular, as becomes obvious if equation (19) is combined with equation (21) (Rodgers and Charnley, 2002):

$$\frac{\mathrm{d}\,v_i}{\mathrm{d}r} = \rho_i^{-1}\left((F_i + F_e)v_i - (\gamma_i - 1)G_i - (\gamma_e - 1)G_e - M_i v_i^2 + 2v_i\rho_i c_p^2/r\right) / \left(v_i^2 - c_p^2\right) \ . \tag{22}$$

A smooth transition through the singularity in equation (22) would occur if the numerator also tended to zero in a similar manner to $(v_i^2 - v_p^2)$. But for reasonable initial conditions, this is not the case (Rodgers and Charnley, 2002). An exact numerical treatment of the plasma velocity would therefore require a solution of a set of partial differential equations. To avoid this, in the following the same velocity for all three fluids is assumed. Such an approximation was also made in other, previous models of the cometary coma (Marconi and Mendis, 1986; Rodgers and Charnley, 2002). In the case of Marconi and Mendis (1986) it was possible, with the assumption of a single bulk velocity to reproduce within an uncertainty of a factor of two the electron temperature and densities, as measured in comet Giacobini-Zinner during the ICE flyby. Since other uncertainties, e.g. the rates for a large number of reactions, are of a similar magnitude, calculating one bulk velocity is acceptable within the scope of the presented model. Equation (19) then becomes:

$$\frac{\mathrm{d}\,v}{\mathrm{d}r} = \frac{1}{\sum \rho_k v^2 - \sum(\gamma_k n_k k_B T_k)}\left(-\sum(\gamma_k - 1)G_k + \frac{2v}{r}\sum(\gamma_k n_k k_B T_k)\right) \ . \tag{23}$$

All summations are done over the corresponding values for the three fluids k, neutral, ionic and electrons. The temperature T is computed for three bulk fluids. To take the chemistry into account, equation (18) has to be solved for each species individually. Each of the three fluids has an individual temperature T_k, obtained from equation (20) with γ_k and n_k, the adiabatic exponent and the number density for fluid k (the neutrals, ions, and electrons), and G_k and N_k, the source terms for the fluid k.

For the three fluids, the adiabatic exponents γ_n, γ_i, and γ_e are required. For the neutral and the ionic species, the adiabatic exponent of 4/3 is applied, as it is valid for water at low temperatures. A change of the adiabatic coefficient with temperature is neglected. For the electron fluid, consisting of point-like particles, the adiabatic exponent of 5/3 is used. Equation (20) is written for each fluid:

$$\frac{\mathrm{d}\,T_k}{\mathrm{d}r} = \frac{(\gamma_k - 1)T_k}{v}\left(\frac{G_k}{n_k k_B T_k} - \frac{2v}{r} - \frac{\mathrm{d}\,v}{\mathrm{d}r} - \frac{N_k}{(\gamma_k - 1)n_k}\right) . \tag{24}$$

Since the gas undergoes a steep geometric dilution when streaming off the nucleus, equation (18) is rewritten in the form:

$$\frac{\mathrm{d}\,(n_j r^2)}{\mathrm{d}r} = \frac{N_j r^2}{v} - \frac{n_j r^2}{v}\frac{\mathrm{d}\,v}{\mathrm{d}r} . \tag{25}$$

The index j runs over all species included in the chemical reaction network. The quantity $(n_j r^2)$ has a weaker variation with nucleocentric distance than the number density n_j has, and is thus more suitable for computation.

The equations (23), (24) and (25) are the final set of equations solved by the presented model.

4.1.3 Initial Conditions

The initial conditions for the equations are

$$n_j(r = R_N) = n_{j,0} \tag{26}$$

$$\rho_k(r = R_N) = \rho_{k,0} \tag{27}$$

$$v(r = R_N) = v_0 \tag{28}$$

$$T_k(r = R_N) = T_{k,0} , \tag{29}$$

where the index j runs over all species and the index k runs over all three fluids.

The values for $n_{j,0}$ are the input parameters to be constrained by comparison with observations. The initial densities for the three fluids, $\rho_{k,0}$, follow from the $n_{j,0}$ by the summation:

$$\rho_{k,0} = \sum_i \mu_i \cdot n_{i,0} . \tag{30}$$

The index i runs over all species that belong to fluid k.

The initial value for the temperature can be obtained from a simple sublimation model (Knollenberg, 1993). In this model, a pure ice surface exposed to solar irradation is considered. For this surface, the energy balance, including solar irradiation, thermal emission, and sublimation of ice, can be formulated:

$$\frac{F_\odot (1-A)}{r_h^2} \cos(\phi) = \epsilon \sigma T^4 + H \, z_{gas} \; . \tag{31}$$

In this equation, $F_\odot$ is the incident solar flux, A is the albedo, ϵ is the emissivity of the surface, and H denotes the sublimation heat of the ice. z_{gas} is the gas flux resulting from sublimation and ϕ is the solar zenith angle. Using the Clausius-Clapeyron equation for the correlation between the vapour pressure and the temperature for the sublimating ice (Fanale and Salvail, 1984), an implicit equation for the ice temperature, T is obtained. This equation is solved numerically by interval enclosure.

From the temperature of the ice surface, the gas temperature can be computed. Here, it has to be taken into account that the gas flow when leaving the surface does not have a Maxwellian velocity distribution, since the gas expansion above the nucleus surface is only possible in a half space, away from the nucleus. After several molecular collisions, a Maxwellian velocity distribution is reached. The temperature of the ice surface can then be correlated to the gas temperature after reaching a Maxwellian velocity distribution by using a reservoir outflow analogy (Knollenberg, 1993):

$$T_0 = \frac{T_S}{1 + \frac{1}{2}(\gamma - 1)} \; . \tag{32}$$

Here, T_S is the surface temperature and T_0 is the initial gas temperature. Initially, all three fluids are set to the gas temperature computed in this way. The gas temperature was computed for a mean zenith angle of 60°, an albedo and emissivity of 0.04 and 0.9, respectively, and the thermodynamical constants for water (Fanale and Salvail, 1984; Kührt, 1999).

The initial velocities then follow by assuming that the gas velocity at the nucleus surface is equal to the local sonic speed. This assumption is a consequence from observations which imply that the cometary coma extends to very large distances, assumed to be infinity. This implies a supersonic stationary flow. If the initial flow velocity would be subsonic, the expansion of the fluid would be restricted, since the fluid velocity would then decrease with nucleocentric distance, approaching zero. If a stationary flow is supersonic, the local sonic velocity (i.e. the local Mach number $M = 1$) is reached at the position where the fluid flux density has its maximum (Landau and Lifschitz, 1991). For the case of a spherical symmetric flow from a comet nucleus surface, this is the case at the surface of the nucleus.

4.1.4 General Source Terms

The equations (18) to (20) contain the source terms N_s, F_s, M_s and G. The equations are coupled by these terms. The term N_s for each species can be computed by including a chemical reaction network. This network is described in more detail in section 4.2. For each fluid, the overall particle source terms can then be computed by summing the loss and the gain terms for one fluid over all species. E.g., neutrals undergoing ionisation, represent a loss for the neutral fluid and a gain for the ionic species. From the summation, the fluid source terms N_n, N_i, and N_e for the neutrals, ions and electrons are obtained, respectively. Since no particles are subject to removal within the coma, the condition

$$N_n + N_i = 0 \tag{33}$$

is fulfilled. The same is true for the mass and momentum source terms for the three fluids:

$$\begin{aligned} M_n + M_i + M_e &= 0 \quad (34) \\ F_n + F_i + F_e &= 0 \,. \quad (35) \end{aligned}$$

For the energy source term, no such conservation is valid, since energy can be injected or removed from all three fluids by exothermic or endothermic chemical reactions. The energy source term is discussed in detail in section 4.3.

4.2 Chemical Reactions in the Coma

4.2.1 Reaction Types

Gas flowing from the cometary nucleus into space is subject to several types of chemical reactions. The solar ultraviolet radiation field provides photons with sufficient energy to trigger photochemical reactions. Furthermore, collisions between neutrals, ions, and electrons can result in chemical reactions. In the following, the different types of chemical reactions included in the model are shown, together with general reaction equations and example reactions. In the reaction equations, γ indicates a photon.

Photodissociation
General reaction equation:

$$\mathrm{A} + \gamma \rightarrow \mathrm{B} + \mathrm{C} \tag{36}$$

Example reaction:

$$\mathrm{H_2O} + \gamma \rightarrow \mathrm{H} + \mathrm{OH} \tag{37}$$

Photoionisation

General reaction equation:

$$A + \gamma \rightarrow A^+ + e^- \tag{38}$$

Example reaction:

$$CH_4 + \gamma \rightarrow CH_4^+ + e^- \tag{39}$$

Photodissociative Ionisation

General reaction equation:

$$A + \gamma \rightarrow B + C^+ + e^- \tag{40}$$
$$A + \gamma \rightarrow B + C + D^+ + e^- \tag{41}$$

Example reactions:

$$CH_4 + \gamma \rightarrow H_2 + CH_2^+ + e^- \tag{42}$$
$$CH_4 + \gamma \rightarrow H_2 + H + CH^+ + e^- \tag{43}$$

Neutral-Neutral Rearrangement

General reaction equations:

$$A + B \rightarrow C + D \tag{44}$$
$$A + B \rightarrow C + D + E \tag{45}$$

Example reactions:

$$CH_3 + CH_2 \rightarrow C_2H_4 + H \tag{46}$$
$$CH_4 + H_2 \rightarrow CH_3 + H_2 + H \tag{47}$$

Neutral-Ion Rearrangement

General reaction equations:

$$A + B^+ \rightarrow C + D^+ \tag{48}$$
$$A + B^+ \rightarrow C + D + E^+ \tag{49}$$
$$A + B^+ \rightarrow C + D + E + F^+ \tag{50}$$

Example reactions:

$$H_2O + CH^+ \rightarrow H_2 + HCO^+ \tag{51}$$
$$CH_4 + CH_2^+ \rightarrow H_2 + H + C_2H_3^+ \tag{52}$$
$$C_2H_6 + H_2^+ \rightarrow H_2 + H_2 + H_2 + C_2H_2^+ \tag{53}$$

Charge Exchange Reactions
General reaction equation:

$$A + B^+ \rightarrow A^+ + B \tag{54}$$

Example reaction:

$$H_2O + OH^+ \rightarrow H_2O^+ + OH \tag{55}$$

Electron Impact Dissociation
General reaction equation:

$$A + e^- \rightarrow B + C + e^- \tag{56}$$

Example reaction:

$$CO_2 + e^- \rightarrow CO + O + e^- \tag{57}$$

Electron Impact Ionisation
General reaction equation:

$$A + e^- \rightarrow A^+ + e^- + e^- \tag{58}$$

Example reaction:

$$H_2O + e^- \rightarrow H_2O^+ + e^- + e^- \tag{59}$$

Recombination
General reaction equation:

$$A^+ + e^- \rightarrow A + \gamma \tag{60}$$

Example reaction:

$$H^+ + e^- \rightarrow H + \gamma \tag{61}$$

Dissociative Recombination
General reaction equations:

$$\begin{aligned} A^+ + e^- &\rightarrow B + C && (62) \\ A^+ + e^- &\rightarrow B + C + D && (63) \\ A^+ + e^- &\rightarrow B + C + D + E && (64) \end{aligned}$$

Example reactions:

$$\begin{aligned} H_2O^+ + e^- &\rightarrow H + OH && (65) \\ CH_4^+ + e^- &\rightarrow CH + H_2 + H && (66) \\ CH_4^+ + e^- &\rightarrow CH + H + H + H && (67) \end{aligned}$$

Ionisative Association
General reaction equation:

$$\mathrm{A} + \mathrm{B} \rightarrow \mathrm{C}^+ + \mathrm{e}^- \tag{68}$$

Example reaction:

$$\mathrm{CH} + \mathrm{O} \rightarrow \mathrm{CHO}^+ + \mathrm{e}^- \tag{69}$$

Dissociative Electron Impact Ionisation
General reaction equation:

$$\mathrm{A} + \mathrm{e}^- \rightarrow \mathrm{B} + \mathrm{C}^+ + \mathrm{e}^- + \mathrm{e}^- \tag{70}$$

Example reaction:

$$\mathrm{H_2O} + \mathrm{e}^- \rightarrow \mathrm{H} + \mathrm{OH}^+ + \mathrm{e}^- + \mathrm{e}^- \tag{71}$$

Electron Impact Excitation
General reaction equation:

$$\mathrm{A} + \mathrm{e}^- \rightarrow \mathrm{A}^* + \mathrm{e}^- \tag{72}$$

Example reaction:

$$\mathrm{CO} + \mathrm{e}^- \rightarrow \mathrm{CO}^* + \mathrm{e}^- \tag{73}$$

Radiative De-Excitation
General reaction equation:

$$\mathrm{A}^* \rightarrow \mathrm{A} + \gamma \tag{74}$$

Example reaction:

$$\mathrm{CO}^* \rightarrow \mathrm{CO} + \gamma \tag{75}$$

4.2.2 Mathematical Description of Chemical Reactions

The change in the number density of one species in the cometary coma follows from a system of differential equations. If the number density of a certain species is denoted by n_i, where the index i is running over all species regarded, the change of n_i is given by (Schmidt *et al.*, 1988):

$$N_i = \frac{\mathrm{d}n_i}{\mathrm{d}t} = \sum_{j=1}^{q} \nu_{ij} k_j \prod_{l=1}^{s} n_l^{m_{ij}} \; . \tag{76}$$

In this equation, the indices i and l run over all species, numbered from 1 to s, and j over all reactions, numbered from 1 to q. k_j is the rate coefficient of reaction j, determining the reaction velocity, and ν_{ij} is the stoichiometric coefficient of species i in reaction j. m_{ij}

denotes the reaction order. This equation simply expresses that a particular reaction rate depends on the product of the number densities of the reactants, and that the change in the number density of species i is determined by the sum over all reactions producing or destroying species i.

The rate coefficient contains the information on the probability of a reaction to occur. In the model, it is parameterized in the so called Arrhenius form to describe its dependency on the temperature, T:

$$k_j = A_j \left(\frac{T}{300K} \right)^{B_j} e^{-C_j/T} \ . \tag{77}$$

The three free parameters, A_j, B_j, and C_j are tabulated in the literature for various reactions. The Arrhenius form has no strict theoretical background[4] but nevertheless is suitable for fitting the variation of k_j with T. The term $\left(\frac{T}{300K}\right)^{B_j}$ describes the dependency of the reaction rate from an impact energy (energy $\sim$ $\mathrm{T}^{1/2}$). The term $e^{-C_j/T}$ takes into account the possible existence of an activation energy, since for a Maxwellian velocity distribution, the fraction $e^{-C_j/T}$ of all molecules has a kinetic energy above a level given by $C_j \cdot k_B$. From this it becomes clear that photoreactions have B_j and C_j equal to zero, since these reactions have no dependency on impact energies.

Since the different fluids regarded in this work have different temperatures, for the collisional reactions an effective temperature was computed according to (Flower *et al.*, 1985):

$$T = \frac{m_k T_l + m_l T_k}{m_l + m_k} \ . \tag{78}$$

T_k and T_l indicate the temperatures of the fluids to which the reactants with masses m_k and m_l belong. Since the electron mass m_e is much smaller than the mass of all other species in the reaction network, for electron collision reactions, $T = T_e$.

The Arrhenius coefficients used in this work were taken from Schmidt *et al.* (1988), Huebner *et al.* (1992)[5] and Helbert (2002). Coefficients were updated if necessary from the UMIST RATE05 database (Woodall *et al.*, 2006). Since this database provides photochemical reaction rate coefficients only for the interstellar ultraviolet radiation field, they are not suitable for the study of cometary comae. Therefore, only impact reaction rate coefficients could be updated using the UMIST database. All photo rate coefficients used in this work were computed for solar minimum conditions. A detailed discussion on this assumption is presented in section 9.1. The photo rate coefficients are listed for a heliocentric distance of 1 AU and scaled with r_h^{-2}. For some reactions, the rate coefficients were estimated in this work, as described in chapter 8.

---

[4] In the hard-sphere collision theory, two reactants with the molecular radii r_A and r_B react when they collide with a kinetic energy above a threshold of E, assuming a Maxwellian velocity distribution. The reaction rate coefficient is then given by $k = (r_A + r_B)^2 \left(\frac{8\pi k_B T}{\mu}\right)^{1/2} e^{-E/k_B T}$ (Connors, 1990), thus having the Arrhenius form. μ is the reduced molecular mass.

[5] Photochemical data from this source is also available online at `www.atmo.swri.edu`

Table 9: Typical range of rate coefficients for different types of reactions important in cometary comae. The values are computed at 1 AU heliocentric distance and for a neutral and ion temperature of 300 K and an electron temperature of 10^4 K.

Type of Reaction	Rate Coefficient
Photo Reactions	10^{-3} to $10^{-7}\mathrm{s}^{-1}$
Electron Impact Reactions	10^{-10} to $10^{-13}\,\mathrm{cm}^3\,\mathrm{s}^{-1}$
Neutral-Neutral Rearrangements	10^{-10} to $10^{-11}\,\mathrm{cm}^3\,\mathrm{s}^{-1}$
Neutral-Ion Rearrangements	10^{-9} to $10^{-10}\,\mathrm{cm}^3\,\mathrm{s}^{-1}$
Radiative De-excitation	10^2 to $10^7\,\mathrm{s}^{-1}$

The typical ranges of the k_j for various reactions in a cometary coma at 1 AU heliocentric distance are shown in Tab. 9. It can be seen that the values of k_j cover many orders of magnitude for the different types of reactions.

The chemical reaction network used in this work includes 167 different species and 1054 chemical reactions. All chemical reactions are tabulated in Appendix A, together with their Arrhenius coefficients.

4.2.3 Optical Density Effects

Ultraviolet radiation has to pass through the outer cometary coma before it can lead to photochemical reactions in the inner coma. If the cometary coma is sufficiently dense (i.e. if the cometary gas production is large enough), the solar ultraviolet radiation is significantly reduced on passing through the coma. This effect causes the photoreactions in the inner coma to be slowed compared to the outer coma. Since the photo cross sections depend on the wavelength, and this dependency is different for different reactions, the influence of optical depth has to be computed as a function of wavelength for each reaction. A photo rate coefficient $k(r)$ (identical to A_j in the Arrhenius parametrization), at a nucleocentric distance r and integrated over all wavelengths λ, is given by (Schmidt *et al.*, 1988):

$$k(r) = \int_0^\infty F_\odot(\lambda)\sigma'(\lambda)e^{-\tau(\lambda,r)}\mathrm{d}\lambda\ . \tag{79}$$

In this equation, $F_\odot(\lambda)$ denotes the solar flux as a function of wavelength, and $\sigma'(\lambda)$ is the wavelength-dependent photo cross section of the regarded reaction. $\tau(\lambda, r)$ is the wavelength-dependent optical depth of the coma. This quantity depends on the amount of material between the place where the reaction occurs and the light source, i.e. the Sun. Therefore, τ is a function of the nucleocentric distance and, along the nucleus−Sun line, is given by (Schmidt *et al.*, 1988):

$$\tau(\lambda, r) = \sum_i \left(\int_r^\infty n_i(r')\,\sigma_i(\lambda)\,\mathrm{d}r' \right)\ . \tag{80}$$

The sum in this equation runs over all species i in the cometary coma, and $n_i(r)$ is the number density of species i. σ_i denotes the total photo cross section, i.e. the sum of the photo cross sections of all reactions leading to a species destruction.

The dependency of $\tau(\lambda, r)$ upon $n_i(r)$ makes, strictly speaking an iteration in the computation of the n_i necessary. Such a procedure would however significantly increase the computation time. Therefore, as a simplified approach it is assumed that the number density $n_i(r)$ decreases outwards with r'^{-2}. Now, equation (80) becomes (Schmidt *et al.*, 1988):

$$\tau(\lambda, r) = \sum_i n_i(r)\, \sigma_i(\lambda) \cdot r\,, \tag{81}$$

and such an iteration is avoided. Since the influence of the optical density is small for all comets regarded in this work, so the iterative approach leads to only slight deviations from the simplified approach used here (G. Papoutsis, pers. com.).

The sum over all species, i is in this work reduced to a sum over the three molecules H_2O, CO, and CO_2, since these species are by far the most abundant in the cometary coma. The values of $\sigma_i(\lambda)$ and $F_\odot(\lambda) \cdot \sigma'(\lambda)$ are available online in tabulated form for a number of photoreactions discussed by Huebner *et al.* (1992). For a total of 71 photoreactions from 16 parent species, the wavelength-dependent optical density is included in the model. These reactions are marked in Appendix A. The integration over wavelength in equation (79) is replaced by a summation over 175 wavelength bins between 1 Å to 3525 Å.

For photoreactions where the required wavelength-dependent cross sections are not available, the optical depth is computed without taking the wavelength-dependency into account. In this case, equation (79) becomes

$$k(r) = k_0\, e^{-\tau(r)}\,, \tag{82}$$

where k_0 is the photo rate coefficient in the unshielded solar radiation field. To determine τ, the photo cross sections σ_i of H_2O, CO, and CO_2, were averaged over the wavelength interval from 1 Å to 3525 Å, which led to $9.45 \cdot 10^{-22}\,\mathrm{m}^2$ for H_2O, $1.78 \cdot 10^{-21}\,\mathrm{m}^2$ for CO, and $2.09 \cdot 10^{-21}\,\mathrm{m}^2$ for CO_2.

The influence of the optical depth becomes significant only in the innermost coma for comets with modest to high gas production rates. For comet 9P/Tempel 1 at perihelion, the photoreactions of hydrocarbon species at the nucleus surface are reduced to about 61% of the unshielded rates. At 2.2 km above the surface, the reaction rates have risen to 85%, and at 37 km above the surface, the photo reaction rates proceed at 99% of the unshielded rates. The influence of the optical depth upon the observed radial emission profiles is therefore negligible.

The optical density of the coma also has to be taken into account when regarding the infrared emissions of species. Inelastic collisions in the coma can cause rotational and vibrational excitation of species. The de-excitation of the excited states by emission of infrared photons causes loss of energy from the coma. If however the coma is optically thick to infrared radiation, energy is re-absorbed and the energy loss is reduced. This effect is called *radiative trapping*. To compute the infrared optical thickness of the coma, τ_{IR}, a value for the infrared cross section σ_{IR} of $4 \cdot 10^{-19}\,\mathrm{m}^2$ (Schmidt *et al.*, 1988) is used. Again, a dependency of the number densities according to r^{-2} is assumed to avoid iterations.

4.3 Treatment of the Energy Source Terms

The energy source terms G_n, G_i and G_e, as required in equations (23) and (24), consist of several contributions (Rodgers and Charnley, 2002):

$$\begin{aligned} G_n &= G_n^{chem} + G_n^{e} - G_n^{rad} + G_n^{inel} && (83)\\ G_i &= G_i^{chem} - G_e^{ion} && (84)\\ G_e &= G_e^{chem} + G_e^{ion} - G_e^{inel} - G_n^{e}\ . && (85) \end{aligned}$$

The indices n, i, and e stand for the neutral fluid, the ion fluid, and the electron fluid, respectively. The single contributions to G_n, G_i, and G_e are discussed in the following.

4.3.1 $\mathbf{G_n^{chem}}$, $\mathbf{G_i^{chem}}$, and $\mathbf{G_e^{chem}}$

The terms G_n^{chem}, G_i^{chem}, and G_e^{chem} contain the contribution arising from the chemical reactions to the energy budget of the three fluids. If particles of one species are produced or destroyed, the kinetic energy of that particle is added to or removed from the fluid. The rate per volume of energy added to species A by a reaction α is given by (Draine, 1986):

$$G_{A,\alpha} = R_{A,\alpha}\,(1/2\,|\vec{v}_A - \vec{w}_{A,\alpha}|^2 + 1/2 m_A \zeta^2)\ . \tag{86}$$

Here, $R_{A,\alpha}$ is the rate of creation or destruction of species A in reaction α. $\vec{v}_A$ and $\vec{w}_{A,\alpha}$ are the hydrodynamic velocity vectors of the species A and the particles of A emerging from reaction α or being destroyed by reaction α. ζ is the random velocity of the particles A involved in reaction α. Since all species in the described model have the same bulk velocity, here $\vec{v}_A - \vec{w}_{A,\alpha} = \vec{0}$. The source term ${}^{i}G_{A,\alpha}$, denoting the rate of thermal energy per volume and reaction, is in this case determined by the internal energy, $1/2 m_A \zeta^2$ only. This can be computed for the different types of chemical reactions included in the reaction network.

In addition to the thermal energy of the reactants and products, chemical reactions can add energy to (if the reaction is exothermic) or subtract energy from (if the reaction is endothermic) the system. This energy is called *excess energy*, ΔE. If excess energy is set free by a reaction, the fraction of ΔE each product species obtains is calculated from the energy and momentum conservation in the center of momentum reference frame of the reactants. If electrons are among the product species of a reaction, they therefore obtain the full excess energy due to their negligible mass compared to the mass of all other species.

For reactions where the excess energies are available (given by Schmidt *et al.* (1988) and Huebner *et al.* (1992)), they are included in the reaction network. The values of ΔE employed are tabulated together with the reactions in Appendix A.

Tab. 10 lists the total energy source terms ${}^{i}G_k^{chem}$ per reaction for the reaction types included in the reaction network. The terms G_k^{chem}, $k = n, i, e$, are then obtained by summing over the ${}^{i}G_k^{chem}$ times the reaction rate over all reactions.

For the neutral-ion rearrangement, and derived from it for the charge exchange reactions, it is assumed for the expressions in Tab. 10 that no foreward-backward asymmetry in the scattering occurs. This assumptions corresponds to the existance of a relatively long-lived intermediate state for the reaction, so that "memory" of the direction of the reacting particles is lost. See Draine (1986) for a more detailed discussion on this assumption.

4.3.2 Electron Scattering

Electrons can undergo elastic collisions with the neutrals and ions within the cometary coma. Since the electron fluid may have a temperature that is different from the temperatures of the neutral and ionic fluids, such processes can lead to an exchange of energy between the electrons and the neutrals and ions.

For elastic electron-neutral scattering, only water is taken into account in this work, since water is the dominant neutral species in the coma. Rodgers and Charnley (2002) give an equation to calculate the energy exchange by electron-water scattering, based on a measured scattering cross section:

$$G_n^e = 1.1 \cdot 10^{-25} n(water) n(electron) T_e^{-1/2} (2T_e - 3T_n) \quad \left[\mathrm{erg\ cm^{-3}\ s^{-1}}\right] . \tag{87}$$

For elastic electron-ion scattering, the heat transfer between the electron and the ionic fluid was derived by Draine (1980) and is also used in this work:

$$G_e^{ion} = 1.37 \cdot 10^{-42} \frac{n_i^2}{\mu_i} T_e^{-1.5} (T_i - T_e) \ln \left(1.24 \cdot 10^4 \sqrt{\frac{T_e^3}{n_i}} \right) \quad \left[\mathrm{erg\ cm^{-3}\ s^{-1}}\right] . \tag{88}$$

Here, n_i denotes the number density of the ions and μ_i their mean mass. In inelastic electron scattering, internal excitation of the neutral collision partner occurs. Since de-excitation is achieved by emission of a photon, which can escape from the cometary coma, inelastic scattering provides a cooling mechanism for the coma that is affected by radiation trapping.

For inelastic electron-neutral scattering, water is the only neutral species taken into account. This approach is not only justified by water beeing the most abundant species in the coma, but also since the electron collision cross section of the water molecule is about

Table 10: The thermal energy source terms arising from the chemical reactions, ${}^{i}G_{k}^{chem}$, per reaction. The column denoted with 'General Equation' gives the number of the general reaction equation. Θ_k is the thermal energy of one particle of fluid k: $\Theta_n = 3/2 k_B T_n$, $\Theta_i = 3/2 k_B T_i$, and $\Theta_e = k_B T_e$. M is the sum of the masses of the reactants, m_{ijk} refers to $m_i + m_j + m_k$. The small numbers next to the equation number indicate the references: (1) – Draine (1986), (2) – Rodgers and Charnley (2002), (3) – this work.

Reaction type	General Equation	${}^{i}G_{n}^{chem}$	${}^{i}G_{i}^{chem}$	${}^{i}G_{e}^{chem}$
Photodissociation	$(36)^1$	ΔE	0	0
Photoionisation	$(38)^2$	$-\Theta_n$	Θ_n	ΔE
Photodissociative Ionisation	$(40)^2$	$-\frac{m_{\mathrm{C}}}{m_{\mathrm{A}}}\Theta_n$	$\frac{m_{\mathrm{C}}}{m_{\mathrm{A}}}\Theta_n$	ΔE
	$(41)^3$	$-\frac{m_{\mathrm{D}}}{m_{\mathrm{A}}}\Theta_n$	$\frac{m_{\mathrm{D}}}{m_{\mathrm{A}}}\Theta_n$	ΔE
Neutral – Neutral Rearrangement	$(44)^2$	ΔE	0	0
	$(45)^3$	ΔE	0	0
Neutral – Ion Rearrangement	$(48)^1$	$\frac{m_{\mathrm{A}}m_{\mathrm{D}}+m_{\mathrm{B}}m_{\mathrm{C}}}{M^2}\cdot(\Theta_i-\Theta_n)+\frac{m_{\mathrm{D}}}{M}\Delta E$	$-\frac{m_{\mathrm{A}}m_{\mathrm{D}}+m_{\mathrm{B}}m_{\mathrm{C}}}{M^2}\cdot(\Theta_i-\Theta_n)+\frac{m_{\mathrm{C}}}{M}\Delta E$	0
	$(49)^3$	$\frac{m_{\mathrm{A}}m_{\mathrm{E}}+m_{\mathrm{B}}m_{\mathrm{CD}}}{M^2}\cdot(\Theta_i-\Theta_n)+\frac{m_{\mathrm{E}}}{M}\Delta E$	$-\frac{m_{\mathrm{A}}m_{\mathrm{E}}+m_{\mathrm{B}}m_{\mathrm{CD}}}{M^2}\cdot(\Theta_i-\Theta_n)+\frac{m_{\mathrm{CD}}}{M}\Delta E$	0
	$(50)^3$	$\frac{m_{\mathrm{A}}m_{\mathrm{E}}+m_{\mathrm{B}}m_{\mathrm{CDE}}}{M^2}\cdot(\Theta_i-\Theta_n)+\frac{m_{\mathrm{F}}}{M}\Delta E$	$-\frac{m_{\mathrm{A}}m_{\mathrm{F}}+m_{\mathrm{B}}m_{\mathrm{CDE}}}{M^2}\cdot(\Theta_i-\Theta_n)+\frac{m_{\mathrm{CDE}}}{M}\Delta E$	0
Charge Exchange	$(54)^1$	$\frac{m_{\mathrm{A}}^2+m_{\mathrm{B}}^2}{M^2}\cdot(\Theta_i-\Theta_n)+\frac{m_{\mathrm{A}}}{M}\Delta E$	$-\frac{m_{\mathrm{A}}^2+m_{\mathrm{B}}^2}{M^2}\cdot(\Theta_i-\Theta_n)+\frac{m_{\mathrm{B}}}{M}\Delta E$	0
e^--Impact Dissociation	$(56)^2$	0	0	ΔE
e^--Impact Ionisation	$(58)^2$	$-\Theta_n$	Θ_n	ΔE
Recombination	$(60)^1$	Θ_i	$-\Theta_i$	$-\Theta_e$
Dissociative Recombination	$(62)^1$	$\Theta_i+\Theta_e+\Delta E$	$-\Theta_i$	$-\Theta_e$
	$(63)^3$	$\Theta_i+\Theta_e+\Delta E$	$-\Theta_i$	$-\Theta_e$
	$(64)^3$	$\Theta_i+\Theta_e+\Delta E$	$-\Theta_i$	$-\Theta_e$
Ionisative Association	$(68)^3$	$-2\ \Theta_n$	$2\ \Theta_n$	ΔE
Dissociative e^--Impact Ionisation	$(70)^3$	$-\frac{m_{\mathrm{C}}}{m_{\mathrm{A}}}\Theta_n$	$\frac{m_{\mathrm{C}}}{m_{\mathrm{A}}}\Theta_n$	ΔE
e^--Impact Excitation	$(72)^3$	0	0	ΔE
Radiative De-Excitation	$(74)^3$	0	0	0

four magnitudes larger than that of the next abundant molecule, CO (Ashihara, 1975). Cravens and Korosmezey (1986) give analytical parametrisations for the cooling rates of electrons by rotational and vibrational excitation of water molecules. For rotational excitation, the cooling rate is given by:

$$G_{rot} = \left[a + b\ln\left(\frac{T_e}{T_n}\right)\right]\left[(T_e - T_n)\,T_e^{-5/4}\right] n(water)n(electron) \quad \left[\mathrm{eV\ cm^{-3}\ s^{-1}}\right], \qquad (89)$$

where

$$a = 1.052\cdot 10^{-8} + 6.043\cdot 10^{-10}\ln(T_n) \qquad (90)$$

$$b = 4.180\cdot 10^{-9} + 2.026\cdot 10^{-10}\ln(T_n)\ . \qquad (91)$$

Table 11: Values of the parameters W_j, A_j, B_j, C_j, and D_j, $j = 1, 2$, as presented by Cravens and Korosmezey (1986) and required in equations (92) and (93).

$W_1 =$	0.198 eV	$W_2 =$	0.460 eV
$A_1 =$	-35.62	$A_2 =$	-33.91
$B_1 =$	-215.0	$B_2 =$	-297.0
$C_1 =$	$-1.75 \cdot 10^4$	$C_2 =$	$-6.11 \cdot 10^4$
$D_1 =$	$5.25 \cdot 10^4$	$D_2 =$	$2.66 \cdot 10^5$

For vibrational excitation, the cooling rate, $G_{\nu j}$ is

$$\begin{aligned} G_{\nu j} = & \left[8.37 \cdot 10^{13}\, W_j T_e^{-3/2} \right] \left[1 - \exp\left\{ W_j / k_B (T_e^{-1} - T_n^{-1}) \right\} \right] \\ & \cdot I_j(T_e)\, n(water) n(electron) \qquad \left[\text{eV cm}^{-3}\,\text{s}^{-1} \right] . \end{aligned} \tag{92}$$

In this equation, k_B is the Boltzmann constant in *cgs* -units. The index $j = 1, 2$ indicates the vibrational transition, where $j = 1$ is the (000) → (010) transition[6] of water, $j = 2$ represents the sum of the (000) → (100) and (000) → (001) transition. $I_j(T_e)$ is given by:

$$I_j = \exp\left\{ A_j + B_j / T_e^{1/2} + C_j / T_e^{3/2} + D_j / T_e^2 \right\} . \tag{93}$$

The values of the remaining parameters in equations (92) and (93) are summarized in Tab. 11.

The total inelastic electronic scattering source term is the sum of the rotational and the vibrational contributions:

$$G_e^{inel} = G_{rot} + G_{\nu\,1} + G_{\nu\,2} . \tag{94}$$

In case of non-negligible optical density of the coma, which could be the case in the innermost coma, not all photons emitted during de-excitation of the water escape from the coma, but may be re-absorbed. Therefore, not all the thermal energy transferred from electrons to excitation is lost from the coma, but a part can be re-absorbed and thus heats the neutral fluid. If τ_{IR} is the optical depth of the coma, the heating term of the neutral fluid from inelastic electron scattering is:

$$G_n^{inel} = G_e^{inel} \left[1 - \exp(-\tau_{IR}) \right] , \tag{95}$$

with

$$\tau(r) = \sigma_{IR}\, n(r)\, r , \tag{96}$$

where σ_{IR} is the absorption cross section for the infrared radiation emitted by de-excitation.

---

[6] The nomenclature (000) gives the quantum numbers for the fundamental vibrations (ν_1 ν_2 ν_3) of a water molecule.

A cooling by inelastic collisions of electrons with CO molecules is not included in G_n^{inel}. However, a cooling mechanism by electronic excitation of CO due to electron impacts is included in the chemical reaction network by the reactions listed in Tab. 12. Since Arrhenius coefficients for these reaction are available, they can be included in the reaction network directly instead of parameterising the cooling process as a function of nucleocentric distance. Tab. 12 shows four electron impact reactions with negative excess energy that transfer thermal energy from the electron fluid to the CO molecules by electronic excitation. The six de-excitation reactions by photon emission lead to a loss of energy from the cometary coma.

Table 12: Reactions causing a cooling of the coma by inelastic electron-CO-collisions. The upper four reactions are the excitation reactions, the lower six reactions are the de-excitation reactions by emission of photons. A, B, and C show the Arrhenius coefficients of the reactions, ΔE is the excess energy per reaction. The subscripts indicate the electronic state of the excited CO molecule. The parameters A, B, and C are taken from Schmidt et al. *(1988).*

Reaction			A [cm^3 s^{-1}]	B	C	ΔE [eV]
$CO + e^-$	$\rightarrow$	$CO_{1p} + e^-$	$4.46 \cdot 10^{-9}$	0.203	94940.0	-8.1
$CO + e^-$	$\rightarrow$	$CO_{3p} + e^-$	$1.36 \cdot 10^{-7}$	-0.418	83840.0	-6.0
$CO + e^-$	$\rightarrow$	$CO_{3s} + e^-$	$2.89 \cdot 10^{-9}$	0.107	91000.0	-6.9
$CO + e^-$	$\rightarrow$	$CO_{3d} + e^-$	$8.22 \cdot 10^{-10}$	-0.040	99850.0	-7.7
Reaction			A [s^{-1}]	B	C	ΔE [eV]
CO_{1p}	$\rightarrow$	$CO + \gamma$	$9.79 \cdot 10^{7}$	0	0	0
CO_{3p}	$\rightarrow$	$CO + \gamma$	$1.26 \cdot 10^{2}$	0	0	0
CO_{3s}	$\rightarrow$	$CO + \gamma$	$1.00 \cdot 10^{5}$	0	0	0
CO_{3d}	$\rightarrow$	$CO + \gamma$	$1.00 \cdot 10^{-5}$	0	0	0
CO_{3s}	$\rightarrow$	$CO_{3p} + \gamma$	$1.00 \cdot 10^{5}$	0	0	0
CO_{3d}	$\rightarrow$	$CO_{3p} + \gamma$	$2.37 \cdot 10^{5}$	0	0	0

4.3.3 Neutral Scattering

Elastic scattering between two particles of the same fluid does not affect the energy balance. But elastic scattering between neutrals and ions can cause an exchange of thermal energy between the neutral and the ionic fluid.

Inelastic scattering between two neutrals can also cool the cometary coma if the de-excitation occurs via photon emission. In this work, only inelasic water-water scattering is taken into account. The thermal energy loss of this process is described by the semiempirical relation (Schmidt *et al.*, 1988):

$$G_n^{rad} = \frac{8.5 \cdot 10^{-19}\, T_n^2\, n(water)^2}{n(water) + (2.7 \cdot 10^7\, T_n)} \exp(-\tau_{IR}) \quad \left[\mathrm{erg\ cm^{-3}\, s^{-1}}\right] . \tag{97}$$

Here, τ_{IR} again is the optical depth of the coma at infrared wavelengths.

4.3.4 Neutral – Ion Scattering

Elastic collisions between neutrals and ions cause a heat exchange between the two fluids. This effect is taken into account within the reaction network. Reactions of the type

$$\mathrm{A} + \mathrm{B}^+ \rightarrow \mathrm{A} + \mathrm{B}^+ \tag{98}$$

are included and treated with respect to energy exchange as regular neutral—ion reactions. For heat exchange, the most abundant neutral species H_2O, CO, and CO_2, and the ions H_3O^+, NH_4^+, and H_2CO^+ are taken into account. These ions do not undergo chemical reactions with the listed neutral species. To compute the rate coefficients for the elastic collisions, hard-sphere collision theory was used, providing an expression for the rate (Connors, 1990):

$$k = (r_A + r_B)^2 \left(\frac{8\pi k_B T}{\mu}\right)^{1/2} e^{-E/k_B T} \tag{99}$$

In this equation, μ denotes the reduced mass of the reactants. The energy threshold E is assumed to be zero. Using typical molecular and ion radii, one obtains the Arrhenius coefficients of the elastic collision rates of $B_j = 0.5$ and $C_j = 0$, and $A_j \approx 10^{-10}\ cm^3\ s^{-1}$, as applied in this work.

4.4 Numerical Integration

4.4.1 Stiff Systems of Ordinary Differential Equations

The chemical reaction network, as given by equation (76), involves rate coefficients of very different orders of magnitude. This makes the system of ordinary differential equations given by equation (25) *stiff* [7]. In numerical integration of stiff systems of differential equations, the step size for explicit integration schemes (integration schemes for which the approximate solution for integration step $i+1$, η_{i+1}, is a function of the step size h and η_i) is determined by the reaction with the smallest rate coefficient, although the corresponding rate for that rate coefficient may deliver a negligible contribution to the total change of the number density n_i of a species i. Therefore, explicit integration schemes are not appropriate for such problems. Two other numerical approaches exist for solving

---

[7] No strict mathematical definition for *stiffness* exists. A system of ordinary differential equations, $y' = f(x, y)$, is regarded as stiff if the Jacobian of that system, f_y, has Eigenvalues λ with $\mathrm{Re}(\lambda) << 0$ (Stoer and Bulirsch, 2000).

stiff systems of differential equations. In the following, we regard an initial value problem of a set of first-order ordinary differential equations in the generalised form $y' = f(x, y)$, $y(x_0) = y_0$. The first approach is the use of implicit integration schemes. In such schemes, $\eta_{i+1} = f(h, x_{i+1}, \eta_i, \eta_{i+1})$, which requires iterations. Widely used, also in modelling of the chemistry in cometary comae, is the implicit Gear method (Gear, 1971).

The second approach is the use of semi-implicit integration schemes. Here, the stiff part of the system of differential equations $y' = f(y)$ is separated by introducing an auxiliary function $c(t) := e^{-A(t-x)}y(t)$ around $t = x$, with $A := f_y(y(x))$. For the function $c(t)$, explicit integration schemes can be formally applied, and then $c(t)$ can be eliminated to obtain an integration scheme for $y(x)$. This is shown in the following in which the explicit mid-point rule is applied to $c(t)$ (Stoer and Bulirsch, 2000).

With $c'(x) = \bar{f}(y(x))$, $\bar{f}(y) := f(y) - Ay$, one obtains with the mid-point rule:

$$c(x + h) \approx c(x - h) + 2h\bar{f}(y(x)) \ . \tag{100}$$

Using $c(x \pm h) = e^{\mp Ah}y(x \pm h)$, and taking only the leading term of the development of the exponential function into account, $c(x \pm h) \approx (I - \mp Ah)y(x \pm h)$, where I is the unity matrix, one obtains a semi-implicit mid-point rule for $y(x)$, $y(x_0) = y_0$:

$$\begin{aligned} \eta(x_0), h) &:= y_0 && (101) \\ \eta(x_0 + h, h) &:= (I - hA)^{-1}\left[y_0 + f\bar{f}(y_0)\right] && (102) \\ \eta(x + h, h) &:= (I - hA)^{-1}\left[(I + hA)\eta(x - h, h) + 2h\bar{f}(\eta(x, h))\right] \ . && (103) \end{aligned}$$

The above integration scheme is incorporated in the integrator `METAN1` by Bader and Deuflhard (1983) and has been successfully applied to problems in the field of chemical kinetics (Stoer and Bulirsch, 2000) and is used in this work.

4.4.2 The `METAN1` Integrator

The integrator `METAN1` by Bader and Deuflhard (1983) applies the semi-implicit mid-point rule as given above. The double precision fortran 77 code is provided by the online library of the Konrad-Zuse-Zentrum für Informationstechnologie Berlin[8]. `METAN1` is equipped with an integrated step size control (Deuflhard, 1983).

The use of `METAN1` is not common in the modeling of the chemistry in cometary comae since other models, like Schmidt *et al.* (1988) and Rodgers and Charnley (2002), use the Gear method (Gear, 1971), incorporated in the `LSODE` package (Hindmarsh, 1983). Nevertheless, a detailed comparison of the `METAN1` integrator with the Gear integrator (Bader and Deuflhard, 1983) showed that the two routines have comparable performance in terms of computer time. In order to enhance the variety in numerical methods applied to the modelling of cometary comae, the `METAN1` integrator was used in this work.

---

[8] `http://www.zib.de`

Table 13: The input parameters used for a Hyakutake-like comet as used by Rodgers and Charnley (2002), and the input values for the same comet used in this work. Q is the production rate, M is the ratio of the production rate of a species with respect to water ($M(H_2O) = 1$).

Parameter	Value (Rodgers and Charnley, 2002)	Value (this work)
$Q(H_2O)$	$1.7 \cdot 10^{29}$ s^{-1}	$1.7 \cdot 10^{29}$ s^{-1}
M(CO)	0.20	0.20
$M(CO_2)$	0.06	0.06
$M(CH_3OH)$	0.02	0.02
$M(H_2CO)$	0.01	0.01
$M(CH_4)$	0.007	0.007
$M(C_2H_6)$	0.004	0.004
$M(C_2H_2)$	0.001	0.001
$M(NH_3)$	0.01	0.01
M(HCN)	0.001	0.001
$M(N_2)$	0.0004	0.0
r_h	1 AU	1 AU
R_N	2.2 km	2.2 km
T_e, T_i, T_e	100 K	171.6 K
$v(r = R_N)$	250 m s^{-1}	325.1 m s^{-1}

`METAN1` solves simultaneously the 167 equations for the number densities of the species included in the reaction network (equation (25)), plus one equation for the bulk velocity (equation (23)) and three equations for the temperatures of the three fluids (equation (24)).

4.4.3 Numerical Tests for Consistency

Several tests were performed to check the reliability of the model outputs, described in the following subsections.

Tests for Input Errors

The chemical reaction network is automatically checked to find out whether the conservation of mass for all reactions involved in the network is ensured, and whether no chemical reaction appears twice in the network. Furthermore, the charge conservation for all reactions in the network is checked. This procedure helps to rule out trivial errors in the model input.

Comparison of Different Numerical Methods

Since the `METAN1` integrator has not been used in previous coma chemistry models, a comparison of the output for a test case obtained by using `METAN1` and `LSODE` was performed. In Fig. 9, the results of the computation of the temperatures of the neutrals, ions, and electrons are shown. Exept for the innermost few meters in the coma, both integrators lead to the same results to a level better than 10^{-4}. In the following discussion, all computations were performed by `METAN1`.

The initial values used for the computation shown in Fig. 9 are summarized in Tab. 13. The nucleus size, the heliocentric distance, and the initial gas composition match the corresponding initial values applied in the computation by Rodgers and Charnley (2002), chosen for a Hyakutake-like comet. Only for the initial temperature of the three fluids at the nucleus surface and the initial gas velocity the results obtained from the model of this work were used instead the corresponding values from Rodgers and Charnley (2002). The results obtained for the temperatures of the three fluids by Rodgers and Charnley (2002) are displayed in Fig. 10. The general results from the model of the present work and Rodgers and Charnley (2002) are similar. Nevertheless, some deviations between the ion temperatures and the neutral temperatures at large nucleocentric distances can be seen. In the case of the neutral temperatures, the difference might be caused by the negligence of the superthermal fluid in the present work. Since no loss of energy due to the escape of fast hydrogen is included in the presented model, the temperature of the neutral fluid (and, with it, the bulk velocity) is overestimated at large nucleocentric distances. A possible reason for slight differences between the ion temperatures obtained with the two models may result from differences in the reaction networks employed. Since the ion temperature is dominated by the chemical source term, as will be shown in section 4.5, different reactions included in the network may result in differences in the ion temperatures. Since the ion chemistry is not of importance for the formation of C_2 and C_3, which is the main purpose of the model in this work, the differences in the ion temperature are not of importance in this work.

Test of the Mass Conservation

The model has to ensure the conservation of mass. As a check, the total mass of all species included in the reaction network can be computed for each nucleocentric position where the model output is obtained. An example for the change in the total mass is shown in Fig. 11, computed by using the initial values presented in Tab. 13. The change of the total mass with respect to the initial mass is displayed for a calculation done with the `METAN1` code and with the `LSODE`. It can be seen that mass conservation is ensured down to a level of 10^{-7}, which is the typical degree of accuracy of all computations performed in this work.

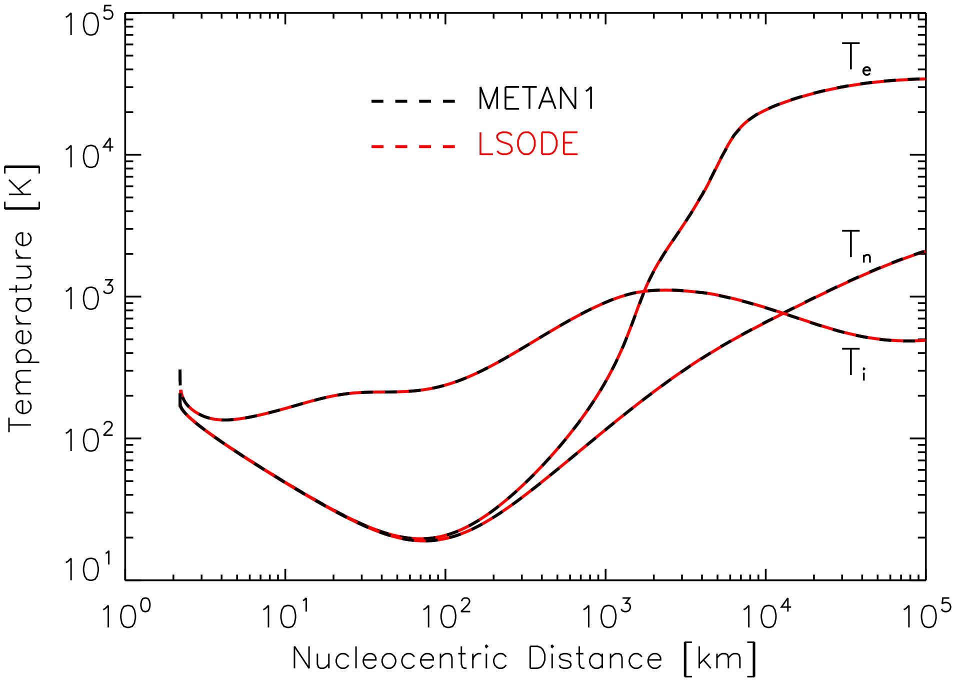

Figure 9: Neutral (T_n), ion (T_i), and electron (T_e) temperatures computed for the case of a Hyakutake-like comet by Rodgers and Charnley (2002). The computation was done by using the `METAN1` *integrator and the* `LSODE` *integrator, and showed very good agreement.*

4.5 Relative Importance of the Different Source Terms

Fig. 12 analyses the importance of the different energy source terms at different nucleocentric distances for the case of the Hyakutake-like comet discussed before. It can be seen that for all three fluids the chemical energy source term is the dominant energy input at all nucleocentric distances. At small nucleocentric distances, inelastic electron-water scattering is very efficient, removing all energy input from the electron fluid. Therefore, the electron temperature is strongly coupled to the neutral temperature at small nucleocentric distances. When the inelastic electron-water scattering becomes less effective, the electron temperature rises above the neutral temperature. Due to radiation trapping, a significant amount of the energy loss of the electron fluid to the neutral-water scattering is transfered to the neutral fluid. For the ion fluid, the energy loss due to the electron-ion scattering becomes significant within a small range of nucleocentric distances. This effect causes a temporary decrease of the ion temperature at small nucleocentric distances. The radiative energy loss due to neutral-neutral scattering becomes noticeable only in the intermediate coma.

For comets with lower activity, the density-dependent source terms are important at even smaller nucleocentric distances. This can be seen in Fig. 13, where the source terms are plotted versus nucleocentric distances for comet 9P/Tempel 1 at perihelion

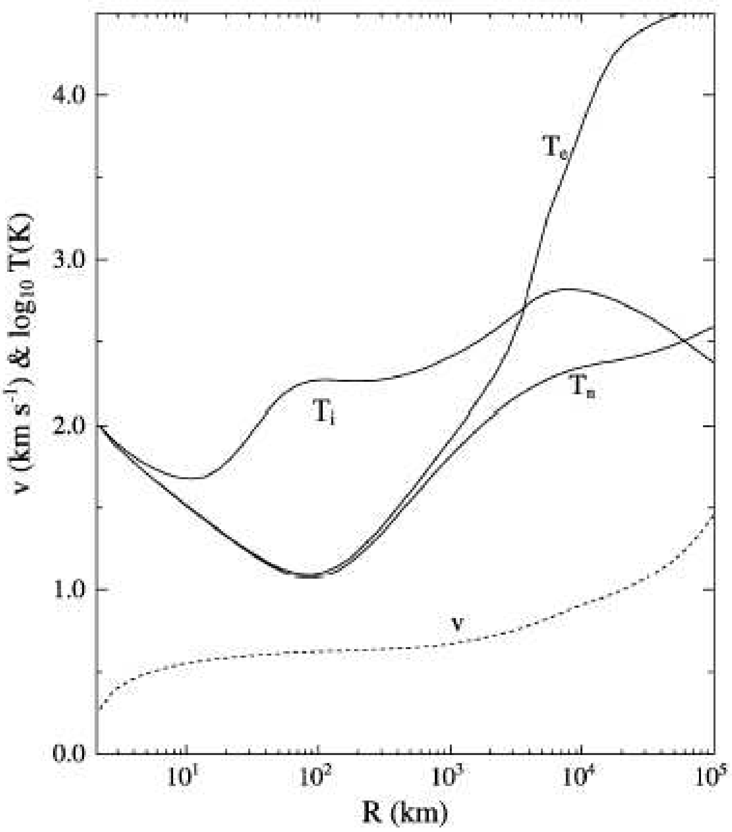

Figure 10: Result of the model by Rodgers and Charnley (2002) for the neutral, ion, and electron temperature and the gas velocity for a Hyakutake-like comet.

(r_h = 1.51 AU). This comet has a water production rate of only $3.4 \cdot 10^{27}$ s^{-1} (see Tab. 17).

4.6 Discussion of the Simplifications

The described model for the chemistry in the cometary coma makes a number of simplifying assumptions which are now discussed.

4.6.1 Hydrodynamic Flow

The model assumes a hydrodynamic flow throughout the cometary coma. This is only true so long as the coma is collisionally dominated, so that a Maxwellian velocity distribution can be developed. Since the gas dilutes strongly when expanding into space, a collisionally dominated gas flow exists only in the inner coma. In the outer coma, the gas is subject to a free molecular flow. The transition regime is typically at nucleocentric distances around 10^4 km for a Halley-type comet at a heliocentric distance of 1 AU (Rodgers *et al.*, 2004). In the free molecular flow regime, a Monte-Carlo simulation of the movement of the gas particles is required for a physically correct description of the coma. Nevertheless,

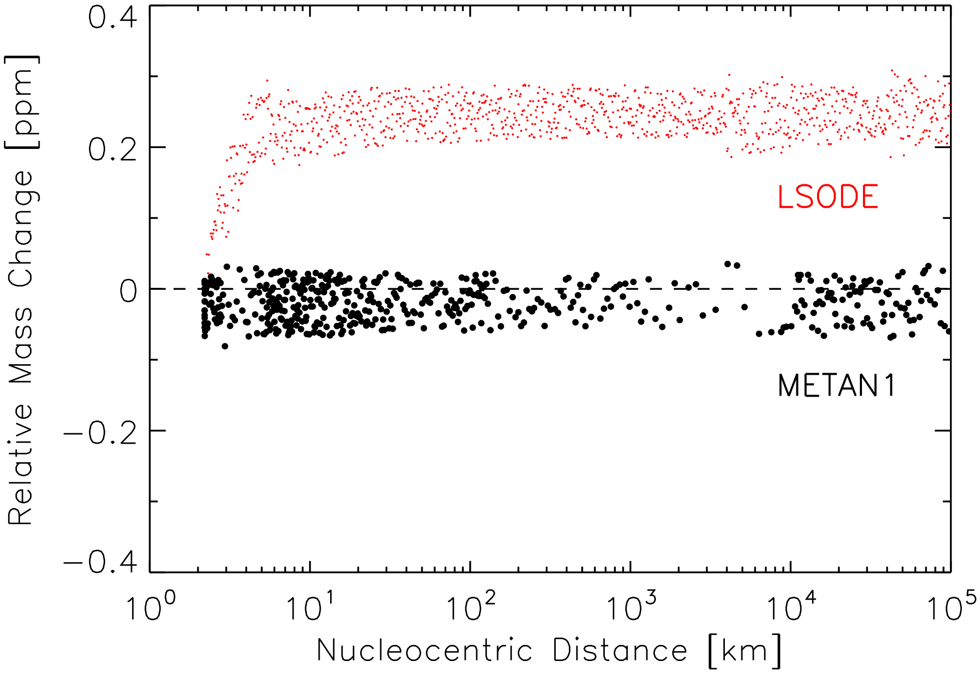

Figure 11: Relative change in the total mass for each computational step, normalized to the initial mass. The results for a Hyakutake-like comet obtained with the integrators `METAN1` *and* `LSODE` *are displayed.*

a number of studies of cometary comae have shown that a hydrodynamical description of the coma even in the free molecular flow regime can reasonable reproduce the observations of number densities and temperatures (Marconi and Mendis, 1986). Therefore, the use of the hydrodynamic model seems appropriate for the calculation of radial number densities.

4.6.2 Steady State Flow

The model as described above is valid only for a steady state coma. Transient phenomena, such as a sudden release of additional gas (e.g. by the Deep Impact event, see chapter 12), or periodic variations in activity (e.g. by active surface areas on a rotating nucleus), cannot be taken into account. Variations in activity due to changes in heliocentric distance typically occur on a timescale much longer than the timescale on which a fluid element of gas stays within the regarded range of nucleocentric distances. With a gas expansion velocity of 1 km s^{-1} and a radius of 10^5 km for the observable gas coma, a fluid element stays for about 28 hours in the coma. Within that time, the change in heliocentric distance of a comet is negligible.

4.6.3 Spherical Symmetry and the Negligence of Magnetic Fields

Since the cometary nucleus is expected to be only active on the sunward hemisphere (the heat conduction of cometary nuclei is very low, see chapter 1.2.1), an asymmetry in the number densities of parent species is introduced. A detailed modelling of the gas coma would therefore require a multi-dimensional approach. However, the shape of the cometary nucleus and the distribution of ices on the nucleus is from ground-based observations in general unknown. From spacecraft missions and the study of nuclear lightcurves it is known that cometary nuclei tend to have shapes very different from spherical (Lamy *et al.*, 2004). The shape of the nucleus strongly influences the distribution of gas in the coma (Crifo *et al.*, 2004). Due to the lack of knowledge on the detailed properties of the cometary nucleus, a simplified approach assuming a spherically symmetric coma is the only one practicable.

For the ions in the coma at nucleocentric distances beyond approximately 10^4 km an additional asymmetry is introduced, since they interact with the solar wind, taking the solar magnetic field with it. This leads to a strong asymmetry in the distribution of ionic species, as can be seen from the formation of the ion tail. An accurate description of this processes requires a 3-dimensional magnetohydrodynamic model, which is beyond the scope of this work. The introduction of magnetic fields into the model increases the number of input parameters. These parameters, describing the conditions of the magnetic field at the position of a comet, are generally not known from ground-based observations.

Therefore, a more detailed model including magnetic fields would not necessarily increase the accuracy of the modelling of the chemistry in the cometary coma. And since the main purpose of this study is not to simulate the observed ion densities but to derive estimates on the mean number densities of neutral species in the cometary coma, the assumption of spherical symmetry is an acceptable simplification.

4.6.4 Negligence of Superthermal Species

A number of reactions occurring in cometary comae produce neutral hydrogen atoms or molecules. Since the mass of these species is low, they receive the major part of the excess energies during formation. In a free molecular flow, a significant fraction of these fast hydrogen atoms and molecules can escape from the coma before they transfer their excess energy to the bulk fluid by collisions. Therefore, the loss of fast hydrogen represents a cooling mechanism for the coma at larger nucleocentric distances. Since this cooling process is not included in the presented model, the temperatures and the velocity of the fluids are overestimated in the outer coma. However, since radial column densities of C_3 and C_2 with a sufficient signal-to-noise ratio can only be obtained at projected nucleocentric distances less than about 10^5 km, where the overestimation of the gas velocity and temperature is not significant, neglecting the superthermal species is expected to be a reasonable assumption as far as the hydrodynamics of the coma is concerned.

Due to their high kinetic energy, the hydrogen atoms and molecules are in principle able to trigger chemical reactions that are expected to be prohibited in the coma due to the low temperatures. Due to their high energy, they can activate reactions that possess activation energies that are too high to be reached by a significant fraction of molecules in the coma at the given temperature. However, a detailed study of this effect by Rodgers and Charnley (2005) showed that the influence of fast species on the chemistry in the coma is only weak. Therefore, the negligence of superthermal species is reasonable also as far as the chemistry in the coma is concerned.

4.6.5 Negligence of Dust

The presented model is free of dust, although significant amounts of dust grains are observed in numerous comets. As shown for comet 67P/Churyumov-Gerasimenko in chapter 11, even dust-to-gas mass ratios as high as 8.5 (assuming typical dust size distributions) have only negligible influence upon the gas flow. Therefore, a dust-free model is a reasonable assumption.

For some species, such as H_2CO and HCN, it is assumed that dust grains provide a significant extended source in the coma. This effect is not included in this model.

4.7 Relation to the Haser Model

An early model for the correlation of observed daughter species and their parent species production rates was introduced by Haser (1957). This model makes use of a number of strong simplifications of the hydrodynamics and chemistry in the coma, but provides simple analytic expressions for the parent species number densities as a function of nucleocentric distance. Because of its simplicity, it is still widely used nowadays. For easy comparison of the results of this work with publications of parent production rates, the Haser model is also used in this work for the determination of parent production rates.

The dynamics of the gas is simplified in a way that an isotropical emission of gas with a constant gas expansion velocity, u, is assumed all through the cometary coma. This assumption simplifies the number density continuity equation (18), for a species i, to

$$\frac{\partial n_i}{\partial r} + 2\frac{n_i}{r} = \frac{1}{u}\frac{\mathrm{d}n_i}{\mathrm{d}t} \tag{104}$$

Furthermore, in the Haser model only two chemical reactions are considered, leading to the production and destruction of a species denoted by B:

$$A \rightarrow B \tag{105}$$

$$B \rightarrow C \tag{106}$$

In this case, the parent species A is destroyed by one chemical reaction only. The intermediate product B decays into a species C, which is assumed in the Haser model to be not of interest. The species B is assumed to be observable due to its optical emissions, e.g. if B is a radical. The equations (76) for the two-step reaction network become:

$$\begin{aligned} \frac{\mathrm{d}n_A}{\mathrm{d}t} &= -k_A n_A && (107) \\ \frac{\mathrm{d}n_B}{\mathrm{d}t} &= k_A n_A - k_B n_B && (108) \end{aligned}$$

The system of differential equations (104) (with $i = A, B, C$), (107), and (108), to be solved with the initial conditions $n_A(t = t_0) = n_{A,0}$ and $n_B(t = t_0) = 0$, then leads to the number density n_B:

$$n_B = \frac{k_A}{k_B - k_A} n_{A,0} \left(\frac{r_0}{r}\right)^2 \left[e^{-k_A/u\,(r-r_0)} - e^{-k_B/u\,(r-r_0)}\right] \qquad (109)$$

Here, r_0 is the nucleus radius. The number densities n_B can be converted into column densities if spherical symmetry of the coma is assumed (see section 5.1), and be compared with observed column density profiles. From such a comparison, $n_{A,0}$ can be constrained. With the gas expansion velocity u and the nuclear radius r_0, this quantity can be converted into a production rate:

$$Q(A) = 4\pi r_0^2\, u \cdot n_{A,0}\ . \qquad (110)$$

The quantities $l_p = u/k_A$ and $l_d = u/k_B$ are referred to as the parent and daughter scale lengths. When fitting an observed column density profile, these quantities can be varied until a reasonable fit is obtained. Together with an assumption on the gas expansion velocity, the determination of l_p and l_d from the fit to observations allows to put constraints on the photoreaction rates involved. The Haser model makes use of strong simplifications. Nevertheless, for some species it delivers a good result. An example for a subset of simple reactions as in equations (105) and (106) is the photodissociation of HCN, for which two reactions are dominant at least at large heliocentric distances (Rauer *et al.*, 2003):

$$\begin{aligned} \mathrm{HCN} + \gamma &\rightarrow \mathrm{CN} + \mathrm{H} && (111) \\ \mathrm{CN} + \gamma &\rightarrow \mathrm{C} + \mathrm{H} && (112) \end{aligned}$$

The species HCN, C and H cannot be observed in the optical wavelength range, but CN has strong optical emissions.

4.8 Comparison of Current Coma Models

A number of models for the chemistry in the cometary coma exist today. The different models have different degrees of complexity and focus on different aspects of the processes

Table 14: Comparison of the properties of some widely-used coma chemical models with the model presented in this work. Ref. 1 is Haser (1957), Ref. 2 is Schmidt et al. *(1988), and Ref. 3 is Rodgers and Charnley (2002). + means the effect is included in the model, − means the effect is not included.*

Effect	Ref. 1	Ref. 2	Ref. 3	This work
Spherical symmetry of the gas flow	+	+	+	+
Inclusion of magnetic fields	−	+	−	−
Variable gas expansion velocity	−	+	+	+
Multiple Fluids	−	+	+	+
Inclusion of superthermal species	−	+	+	−
Complex chemical pathways	−	+	+	+
Wavelength-dependent optical density	−	+	−	+
Initial conditions from sublimation model	−	−	−	+

in the coma. In the following, the main properties of the three most common models, the Haser model, the model of Schmidt *et al.* (1988), and the model of Rodgers and Charnley (2002), are compared with the model described in this work. The Haser model is used because of its simplicity, which makes it very easy to handle. On the other hand, it is oversimplified for an analysis of the formation of species with complex formation chemistry, e.g. the C_2 and C_3 chemistry. The model of Schmidt *et al.* (1988) is the most advanced model so far. Since the model includes a three-dimensional magnetohydrodynamic module, it is especially suitable for the study of ion chemistry. The model of Rodgers and Charnley (2002) was applied mainly for the study of deuterium chemisty (Rodgers and Charnley, 2002) and for the reactions of superthermal species (Rodgers and Charnley, 2005). In Tab. 14, the main processes included in the four models are compared.

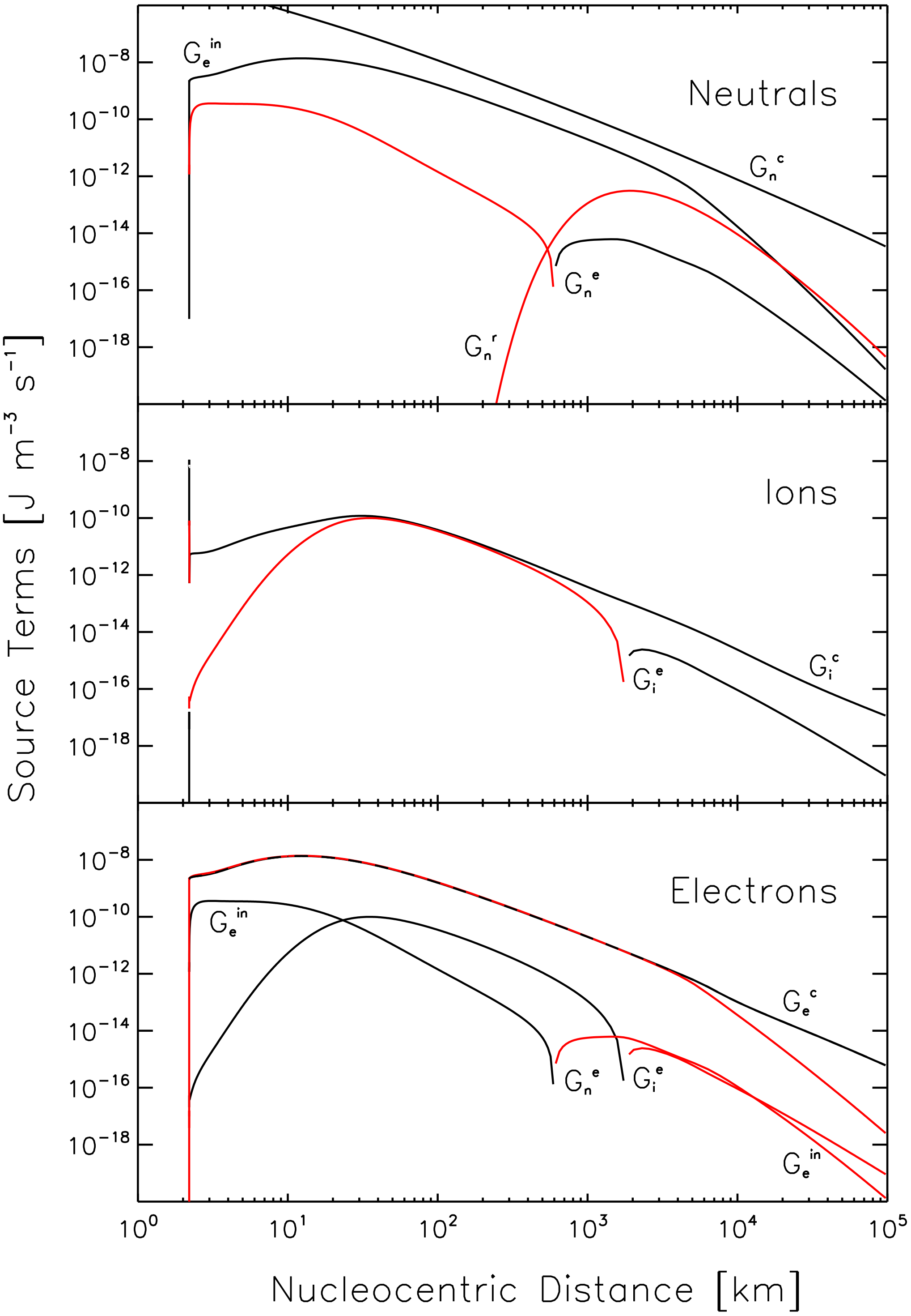

Figure 12: Energy source terms for a Hyakutake-like comet as a function of nucleocentric distance, shown for the neutral, ion, and electron fluids. Black lines indicate gains in energy, whereas red lines indicate energy loss.

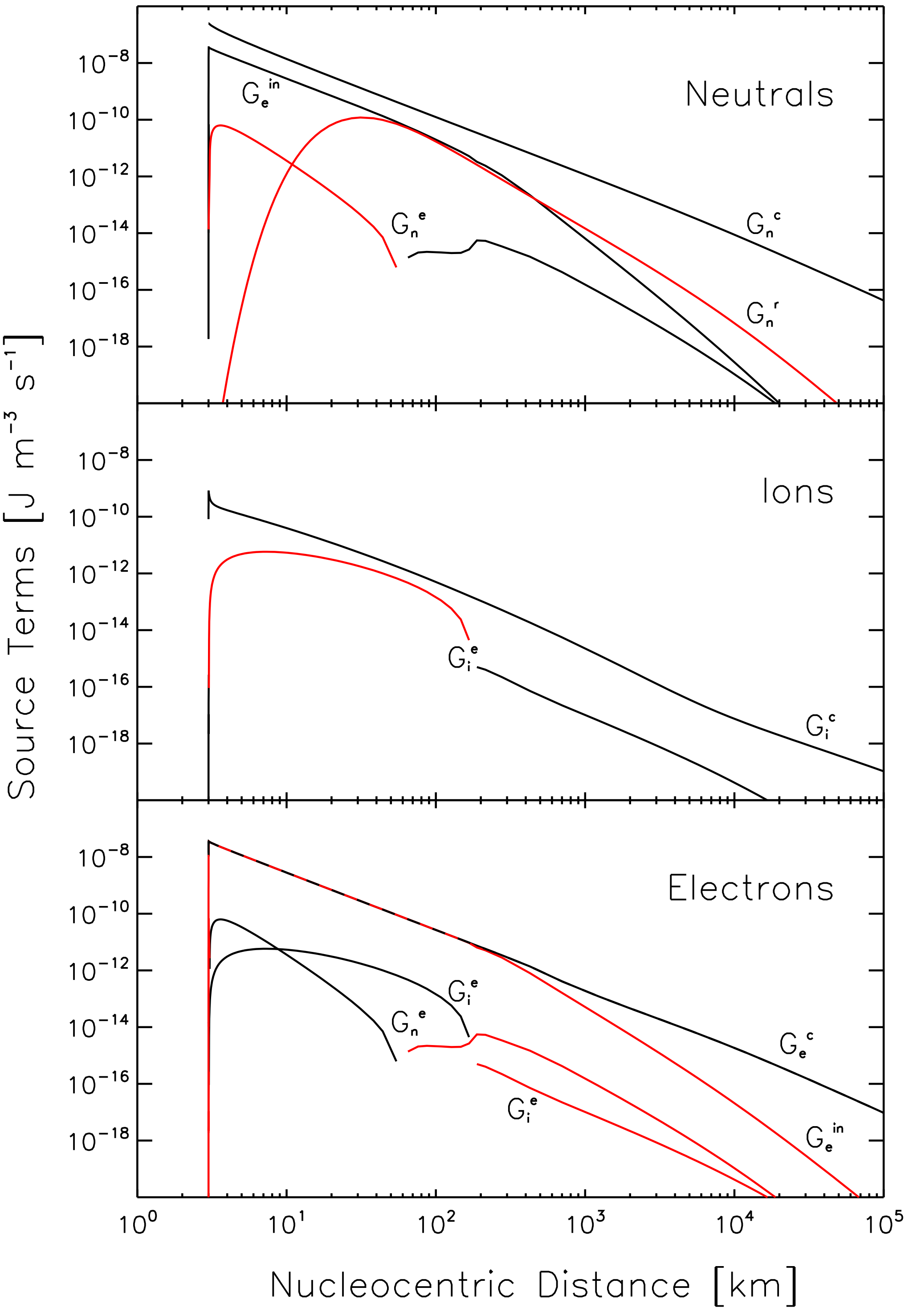

Figure 13: Same as Fig. 12, but for comet 9P/Tempel 1.

5 Comparison between Chemical Model Output and Observations

For a comparison of the chemical model output with the observed radial emission profiles, both the computed number densities and the observed emission profiles have to be converted into column densities. The radial column density profiles derived with the chemistry model have to be fitted to the column density profiles derived from the observed radial emission profiles, which is complicated by the potential importance of more than one parent species. The procedures applied to achieve are described in this chapter.

5.1 Conversion from Number Density to Column Density

For this work, long-slit spectra of cometary comae containing emissions from radicals are available. The long-slit spectra contain information on line brightness as a function of projected nucleocentric distance for those species that have sufficiently strong emissions in the optical wavelength range. In this work, emissions from CN, C_2, C_3 and NH_2 are studied.

From a model of the chemistry in the cometary coma (e.g. the model presented in this work, or the Haser model), the number densities as a function of the nucleocentric distance for the regarded species are obtained. In order to correlate the model output for the number density with an observed radial emission profile of the same species, the number densities and the observed radial emission profiles are converted into column densities as a function of the projected nucleocentric distance.

The conversion from number densities to column densities can be done if spherical symmetry of the coma is assumed and an integration of the number density along the line of sight is performed. Therefore, the function $n_i(r)$ in spherical coordinates is converted into cylindrical coordinates with the origin in the center of the comet's nucleus and the symmetry axis of the cylinder (the z axis) along the line of sight. Due to the assumed spherical symmetry, the function $n_i(r)$ is independent from the angles θ and ϕ in spherical coordinates, and $n_i(\rho, z)$ is independent from ϕ in cylindrical coordinates. For a given projected distance ρ from the nucleus, the coordinate transformation is done by using the relation $r^2 = \rho^2 + z^2$. The column density, N_i^c is then given by:

$$N_i^c(\rho) = \int_{-\infty}^{\infty} n_i(\rho, z)\, dz \; . \tag{113}$$

Since this integral has to be computed for various functions n_i for the species i included in the chemical reaction network, equation (113) is analysed only numerically. The integration is done along paths that have discrete projected distances ρ_j from the nucleus center. Each integration path, which should run from $-\infty$ to ∞, is restricted from a minimum to a maximum value. A specified number of discrete points (200 as the default number) is chosen over this interval in a way that the cosine of the angle between the line defined by ρ_j and the line connecting the origin (the center of the comet's nucleus) and each point in the interval, is equally spaced on the interval $[\,0.01, 1\,]$. The density n_i at each point is computed by a linear interpolation of the values of n_i computed at given discrete distances r_k from the nucleus center. Then, a five-point Newton-Cotes code is used for the integration over the chosen interval. Library routines were available for the conversion of the number densities into column densities.

5.2 Conversion from Line Flux to Column Density

In order to convert the radial emission brightness obtained from long-slit spectra into column densities, the fluorescence efficencies, also called g-factors, are required. These give the energy emitted by one radical per unit of time for a given emission and is taken from the literature. The g-factors applied in this work for the radicals observed are listed in Table 15. The g-factors depend on the heliocentric distance and the values in Tab. 15 are valid for $r_h = 1$ AU. The g-factors for C_2 and C_3 are assumed to scale with r_h^{-2}. The g-factors for NH_2 were taken directly from Kawakita and Watanabe (2002) for the heliocentric distance where required.

Due to the Swings effect, the g-factor for CN also depends on the temporal deviation of r_h. The value listed in Tab. 15 is valid for radial component of the heliocentric velocity of zero. The g-factors for CN for each observation of a comet were calculated based on g-factors given by Schleicher (1983). In this work, g-factors are tabulated for the heliocentric distances of 0.25 AU, 0.5 AU, 1.0 AU, 2.0 AU, and 4.0 AU. For each of these distances, the g-factors are given for radial heliocentric velocities from -60 km s^{-1} to 60 km s^{-1} in steps of 1 km s^{-1}. The interpolation to the heliocentric distances and radial heliocentric velocities of the observations analysed in this work was done linearly between the velocity steps and according to r_h^{-2} between the heliocentric distance steps.

After conversion from line brightness to number densities, the results of a coma chemistry model can be compared with long-slit observations. The computed radial column density profiles can be fitted to column density profiles derived from observations to determine the production rate of the parent species of observed radicals.

5.3 Simultaneous Fitting of the C_3 and C_2 Radial Emission Profiles

5.3.1 Fitting of Multiple Parent Species

For the analysis of the production rates of the C_3 and C_2 parent species, the observed radial column density profiles can be fitted individually when using the Haser model.

Table 15: Summary of the g-factors used for the analysis of the data of this work. All g-factors are valid for r_h =1 AU and are scaled according to r_h^{-2}. The presented g-factor for CN was taken from Schleicher (1983) for a radial component of the heliocentric velocity of zero.

emission	g-factor [erg s^{-1} molecule^{-1}]	Reference
CN (0,0)	$2.38 \cdot 10^{-13}$	Schleicher (1983)
C_2 (Δv = 0)	$4.47 \cdot 10^{-13}$	Cochran et al. (1992)
C_3	$3.80 \cdot 10^{-13}$	Cochran et al. (1992)
NH_2 (0,10,0)	$8.89 \cdot 10^{-15}$	Kawakita and Watanabe (2002)

This is possible since the simple two-step formation and destruction mechanism allows no coupling of different reaction pathways leading to the formation of an observable daughter species.

In a more realistic approach, the formation of C_3 and C_2 is coupled (see Fig. 2). Furthermore, several parent species are believed to contribute to the observed radial emission profiles of C_3 and C_2. Therefore, a simultaneous fitting of the radial emission profiles of C_3 and C_2 with the output of the coma chemistry model of this work is required. Helbert (2002) suggested the following procedure to determine the production rates of C_3H_4, C_2H_2, and C_2H_6 from the observations:

Since the influence of the C_2H_2 and C_2H_6 upon the radial C_3 densities is negligible, the production rate of C_3H_4 is determined by fitting the C_3 radial emission profiles. Once the C_3H_4 production rate is determined, its value is kept fixed. Since the ratio of the production rates of C_2H_6 and C_2H_2 influences the shape of the radial C_2 emission profile, the production rates of both parent species can be determined. This is done by choosing a fixed ratio of the production rates, $Q(C_2H_6)/Q(C_2H_2)$, then fitting the observed C_2 emission line profile. This procedure is repeated for a number of fixed ratios. For each production rate ratio, the value of χ^2 of the best fit is obtained. The global best fit is then defined by the triple $[\,Q(C_2H_6), Q(C_2H_2), \chi^2\,]$ with the minimum value of χ^2.

The fitting of a single computed column density profile to an observed one is done iteratively. The profile of one step is scaled with a parameter k, so that it best matches the observed profile. Then, the parent molecule production rate is multiplied by the resulting k, and a new emission line profile is computed and again fitted to the observation by varying k. This procedure converges quickly, typically after three to five iterations the parent production rate varies by less than 5%, equivalent to $0.95 < k < 1.05$. This condition for k was used as the abort condition for the iteration. The initial value of the parent production rate has to be estimated. Typically, initial values around 1% of the water production rate were applied. The resulting parent production rate turned out to

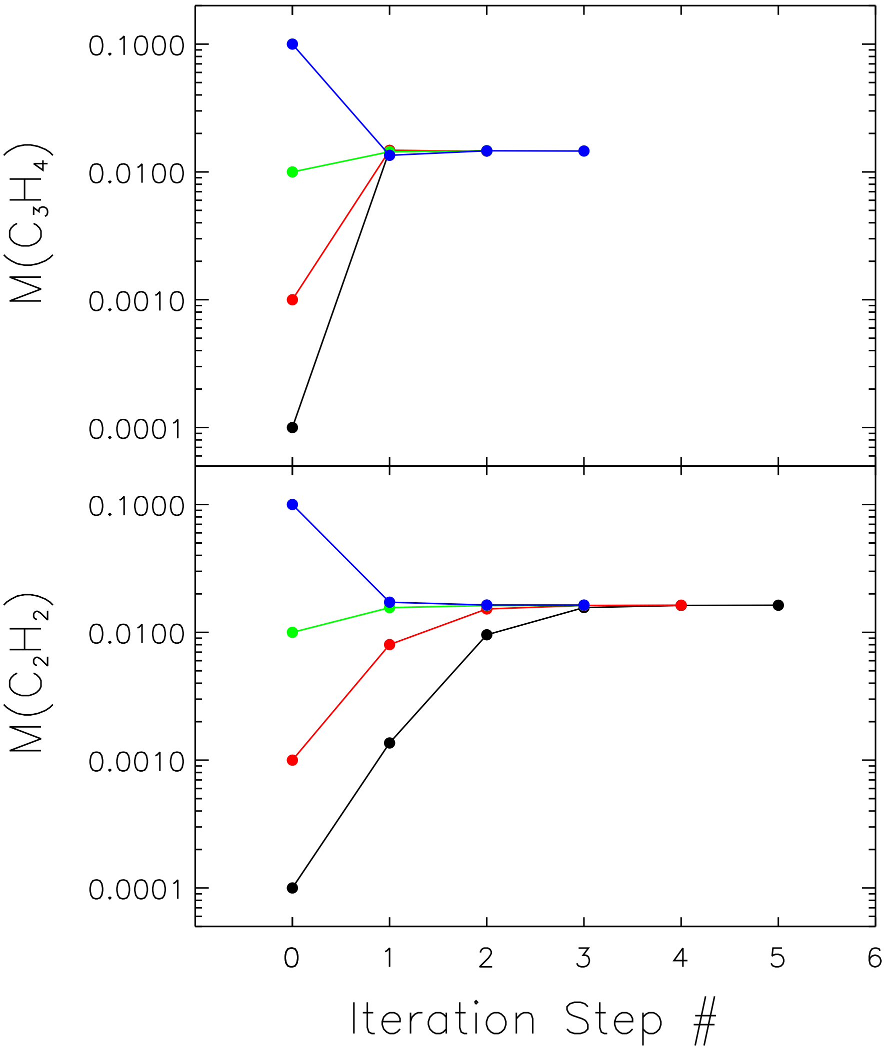

Figure 14: Mixing ratios of C_3H_4 and C_2H_2 relative to water versus the iteration step. This examle was obtained from fitting the C_3 and C_2 column density profiles of comet 9P/Tempel 1 on the tailward side with the C_3 parent species C_3H_4 and the additional C_2 parent species C_2H_2 and C_2H_6 in the fixed ratio of 10. The iteration was stopped in this example when the change in the mixing ratio between two iteration steps became smaller than 2%.

be independent from the chosen initial value. As an example, the mixing ratios for C_3H_4 and C_2H_2 obtained for each iteration step are shown in Fig. 14. It can be seen that for a wide range of initial mixing ratios this procedure converges fast to the same value.

The described method was used in all cases where an observed radial column density profile was fitted with two contributing parent species.

5.3.2 Influence of the Seeing

As a further effect, the influence of seeing has to be considered. While passing the Earth's atmosphere, wavefronts of light are disturbed (Lena *et al.*, 1998). This effect causes the point spread function of a point-like astronomical source of light to be broader than expected from diffraction by the telescope aperture. The full-width-half-maximum (FWHM) of the point spread function is called *seeing* and measured in arcseconds. Due to this effect, also the radial emission profiles of the cometary comae can be expected to be "smeared". This effect is more prominent in the innermost coma with its steep decrease in brightness, compared to the outer coma. In order to obtain a crude estimate of up to which projected nucleocentric distances the seeing effect can significantly affect the emission profiles, the computed best fitting C_3 column density profiles were interpolated to the projected nucleocentric distance axes of the observations and then convolved with a Gaussian having a FWHM corresponding to two arcseconds. Since all observations analysed in this work were obtained under good seeing conditions (around 1 arcsecond in the zenith), this value represents an upper limit. The convolved column density profiles were compared to the unconvolved ones in order to estimate the nucleocentric distance up to which the difference is significant compared to the uncertainty of the measured column density profiles. For the comets C/2001 Q4, C/2002 T7, and 9P/Tempel 1, the values of 1500 km, 4000 km, and 3000 km were obtained, respectively. In the following, the observed column density profiles were fitted only from the given lower limits outwards.

5.3.3 Weighting of the Data Points

The fit to an observed column density profile should match the profile at all heliocentric distances. By simply fitting the profiles, the large number of datapoints at large projected nucleocentric distances dominate the value of χ^2. Therefore, the fit is only determined by the outermost part of the radial column density profiles, and changes in the innermost coma when using different input parameters hardly influence the χ^2 value. To avoid this problem, each datapoint of the measured column density profile is not only weighted by its uncertainty but by the product of its uncertainty and its projected nucleocentric distance. The datapoints at small projected nucleocentric distance thus have a higher weight than datapoints at larger projected nucleocentric distances, which are instead more numerous. This procedure ensures a good fit to the observed column density profiles at all projected distances from the nucleus.

6 Model Validation

In order to validate the model described in this work, two reference cases were regarded in detail. Rodgers and Charnley (1998) give abundances of several species as a function of nucleocentric distance as computed by their model for comet C/1996 B2 Hyakutake. The same input parameters as used by them were applied for a computation with the model of this work, and the results are compared.

Furthermore, the C_3 and C_2 column density profiles from a spectrum of comet C/1995 O1 Hale-Bopp that was analysed within the work of Helbert (2002) were fitted by using the model of this work. From the best-fitting profiles, the production rates of the parent species C_3H_4, C_2H_2, and C_2H_6 are constrained and the results are compared with the results by Helbert (2002).

6.1 Test Computation for Comet Hyakutake

In the work by Rodgers and Charnley (1998) the fluxes of the nine species H_2O, OH, H, HCN, HNC, H_3O^+, $CH_3OH_2^+$, NH_4^+, and $HCNH^+$ are presented as a function of nucleocentric distance. The initial values used for the computation are summarized in Tab. 16. The species H_2O, OH, H, HCN, HNC, H_3O^+, and NH_4^+ are also included in the reaction network used in this work. Therefore, the same initial values as used by Rodgers and Charnley (1998) were applied in a computation with the model described in this work, and the fluxes of the seven common species are compared. If n is the number density of a particular species, r is the nucleocentric distance, and $v(r)$ is the gas velocity, the flux f of the species is given by:

$$f = 4\pi r^2 v\, n\ . \tag{114}$$

Fig. 15 shows the fluxes as determined by Rodgers and Charnley (1998). These results are to be compared with the fluxes obtained with the model of this work, shown in Fig. 16. It can be seen that the resulting fluxes for HNC differ significantly. This is caused by the negligence of the superthermal species in the model of this work. Rodgers and Charnley (1998) point out that for this species the superthermal species are of importance. For all other species, at nucleocentric distances beyond about 10^2 km the results are in an acceptable agreement. Remaining slight differences may be caused by differences in the reaction network applied by Rodgers and Charnley (1998) and in this work. At nucleocentric distances less than about 10^2 km, the fluxes for daughter species differ between the computations by Rodgers and Charnley (1998) and this work. The results by Rodgers and Charnley (1998) show a very steep increase immediately above the nucleus surface and then a less steep increase compared to the results of this work. The reason for this difference is not known, but it may be caused by differences in the initial values applied for the daughter species. The overall agreement of the results of this work with the results by Rodgers and Charnley (1998) is satisfactory.

*Table 16: Input parameters for the coma chemistry model used for comet Hyakutake by Rodgers and Charnley (1998) and for the modelling of the coma of comet Hale-Bopp on December 19, 1997, by Helbert (2002). The input parameters for Hale-Bopp are taken from Helbert (2002) except the values indicated with *, which are computed by the model of this work. Q denotes the production rate, M shows the mixing ratio with respect to water.*

Parameter	Value	
	Hyakutake	Hale-Bopp
Nuclear Radius (r_N)	2.2 km	20 km
r_h	1.1 AU	3.78 AU
$T_{gas}(r = r_N)$	200 K	165.6 K*
v(r = $\mathrm{r_N}$)	500 m s^{-1}	310.6 m s^{-1*}
Q(H_2O)	$1.7 \cdot 10^{29}$ s^{-1}	$4 \cdot 10^{28}$ s^{-1}
M(CO)	0.06	2.0175
M(CH_4)	0.007	0.0284
M(C_2H_2)	0.003	–
M(C_2H_6)	0.004	–
M(N_2)	0.001	–
M(NH_3)	0.003	0.0033
M(HCN)	0.0016	0.0082
M(H_2CO)	0.002	0.008
M(CH_3OH)	0.01	0.0114
M(CS_2)	–	0.0020
M(H_2S)	–	0.0023
M(CH_3CN)	–	0.00097
M(NH_2CH_3)	–	0.0745

6.2 Test Computation for Comet C/1995 O1 Hale-Bopp

The sunward and tailward radial profiles of the C_3 and C_2 emissions of a spectrum of comet C/1995 O1 Hale-Bopp obtained on December 19, 1997, were fitted by using the chemistry model presented in this work. The parent species C_3H_4, C_2H_2, and C_2H_6 were therefore taken into account, and the reaction network as used by Helbert (2002) was applied. The inital composition of the coma was also taken from Helbert (2002) and is summarized in Tab. 16.

The resulting best-fitting radial profiles are shown in Fig. 17 and Fig. 18, together with the observed radial column density profiles. A satisfying fit was possible to both the C_3 and C_2 column density profiles in the sunward and tailward direction. Fig. 19, upper panel, shows the normalized χ^2 values for various fixed mixing ratios of C_2H_2 with respect to C_2H_6. In the lower panel of this Figure, the resulting mixing ratios of C_2H_2

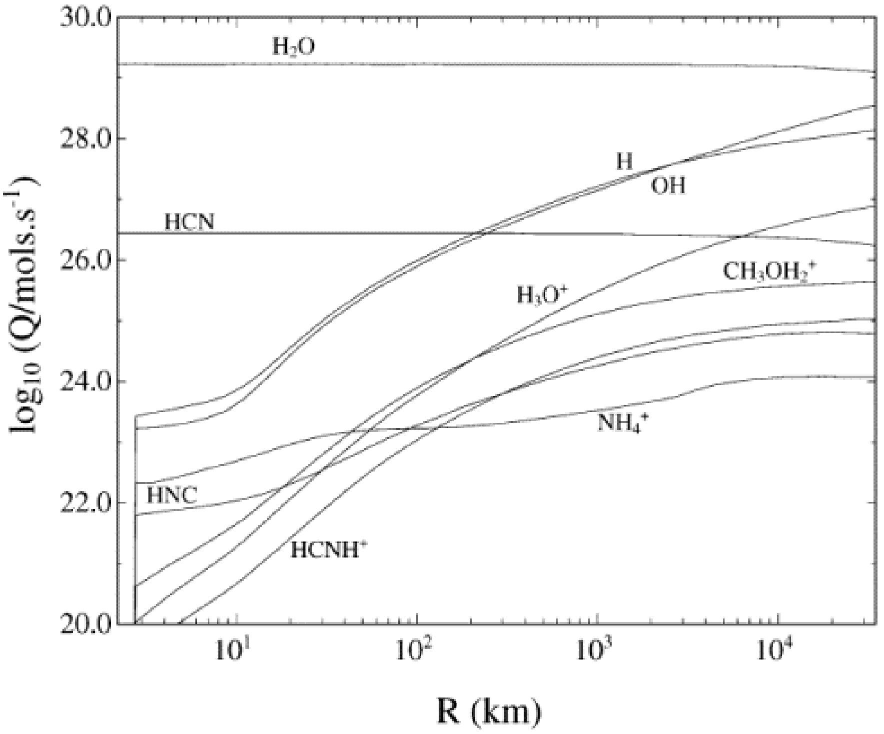

Figure 15: Fluxes (in this Figure denoted with Q) of several species as a function of nucleocentric distance for comet Hyakutake. This Figure is taken from Rodgers and Charnley (1998). The flux for a particular species is given by the number density of the species times $4\pi r^2 v(r)$, where r is the nucleocentric distance and v(r) is the gas velocity.

and C_2H_6 with respect to water are shown for the best-fitting profiles obtained for fixed ratios of $Q(C_2H_2)/Q(C_2H_6)$. It can be seen that the very low ratios of $Q(C_2H_2)/Q(C_2H_6)$ provide a poor fit to the observed column density profiles. Therefore, C_2H_6 as the sole parent of C_2 can be ruled out. On the sunward side, the normalizd χ^2 values show a clear minimum for mixing ratios of $Q(C_2H_2)/Q(C_2H_6)$ around 0.04. On the tailward side, no minimum can be observed. However, the minimum of χ^2 on the sunward side correspond to a C_2H_6 abundance higher than the abundance of water. C_2H_6 would therefore be the second abundant parent species in the coma after CO. This is unlikely and the minimum is therefore most likely to be artificial. The value of χ^2 does not significantly change over a wide range of ratios of $Q(C_2H_2)/Q(C_2H_6)$ for the column density profiles in both directions from the nucleus. The abundance of C_2H_2 with respect to water does not change significantly for the various fixed ratios of $Q(C_2H_2)/Q(C_2H_6)$. In the following, C_2H_2 is assumed to be the sole parent of C_2 (in addition to C_3).

The mean production rates of C_3H_4 and C_2H_2 averaged from the tailward and sunward direction from the nucleus are $10.6 \cdot 10^{26}$ s^{-1} and $16.8 \cdot 10^{26}$ s^{-1}, respectively. These values are about a factor 2 to 2.5 higher than the results by Helbert (2002) for data of the same night. A possible explanation for this result may be the negligence of magnetic fields

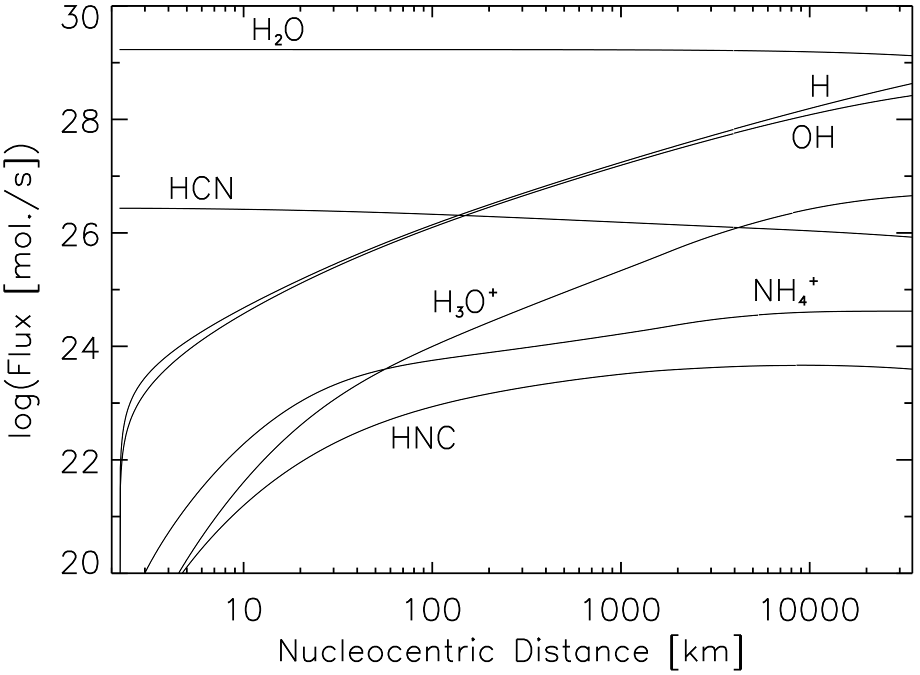

Figure 16: Fluxes of several species as a function of nucleocentric distance computed with the model described in this work by using the same input parameters as presented by Rodgers and Charnley (1998).

in the model used in this work. The consideration of the magnetohydrodynamics in the cometary coma is a main difference between the model by Schmidt *et al.* (1988) employed by Helbert (2002) and the model of this work.

To conclude, the observed radial column density profiles of C_3 and C_2 in comet Hale-Bopp can be reproduced by the model presented in this work and the reaction network derived by Helbert (2002). The qualitative conclusions are the same as by Helbert (2002), while the production rates for C_3H_4 and C_2H_2 derived in this work are about a factor 2 to 2.5 higher than the values obtained by Helbert (2002).

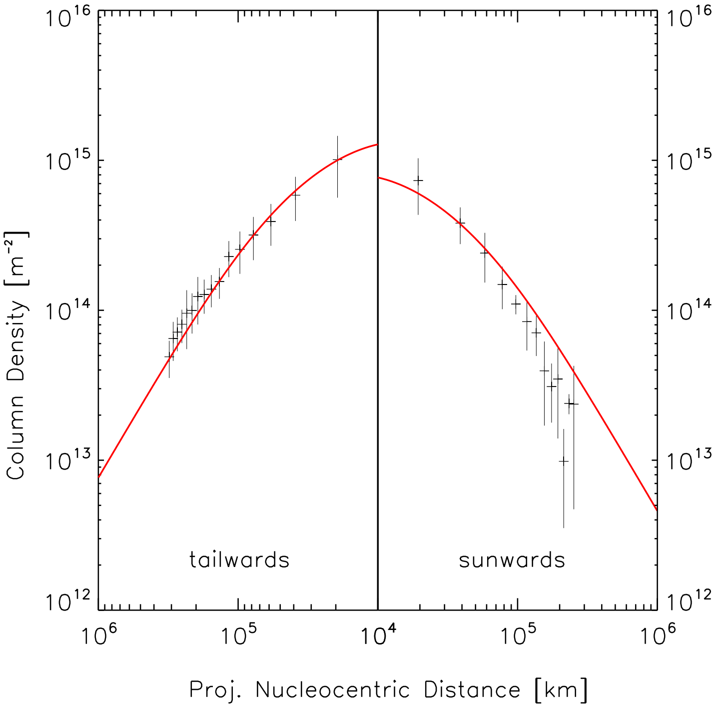

Figure 17: Observed C_3 column density profiles of comet C/1995 O1 Hale-Bopp obtained on December 19, 1997, together with the best-fitting column density profiles obtained with the chemistry model presented in this work (red curves).

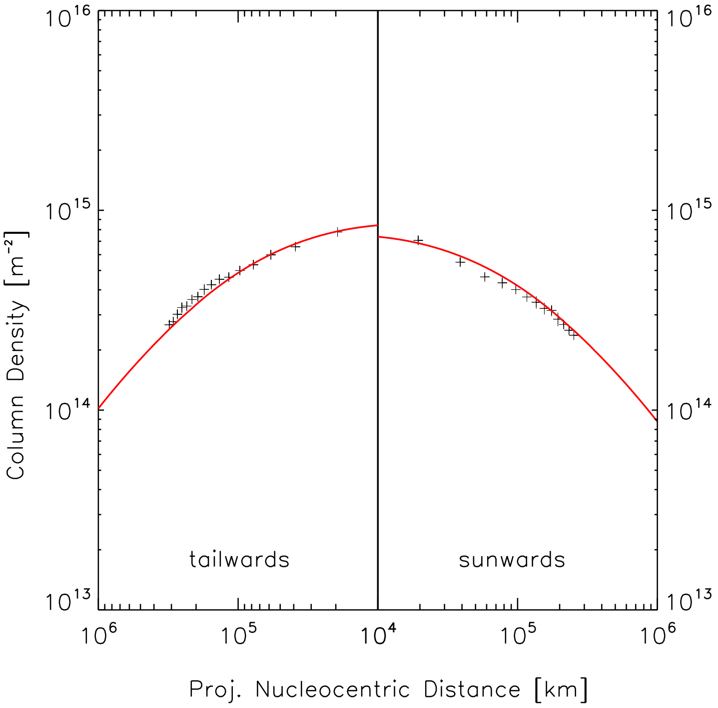

Figure 18: Observed C_2 column density profiles of comet C/1995 O1 Hale-Bopp obtained on December 19, 1997, together with the best-fitting column density profiles obtained with the chemistry model presented in this work (red curves).

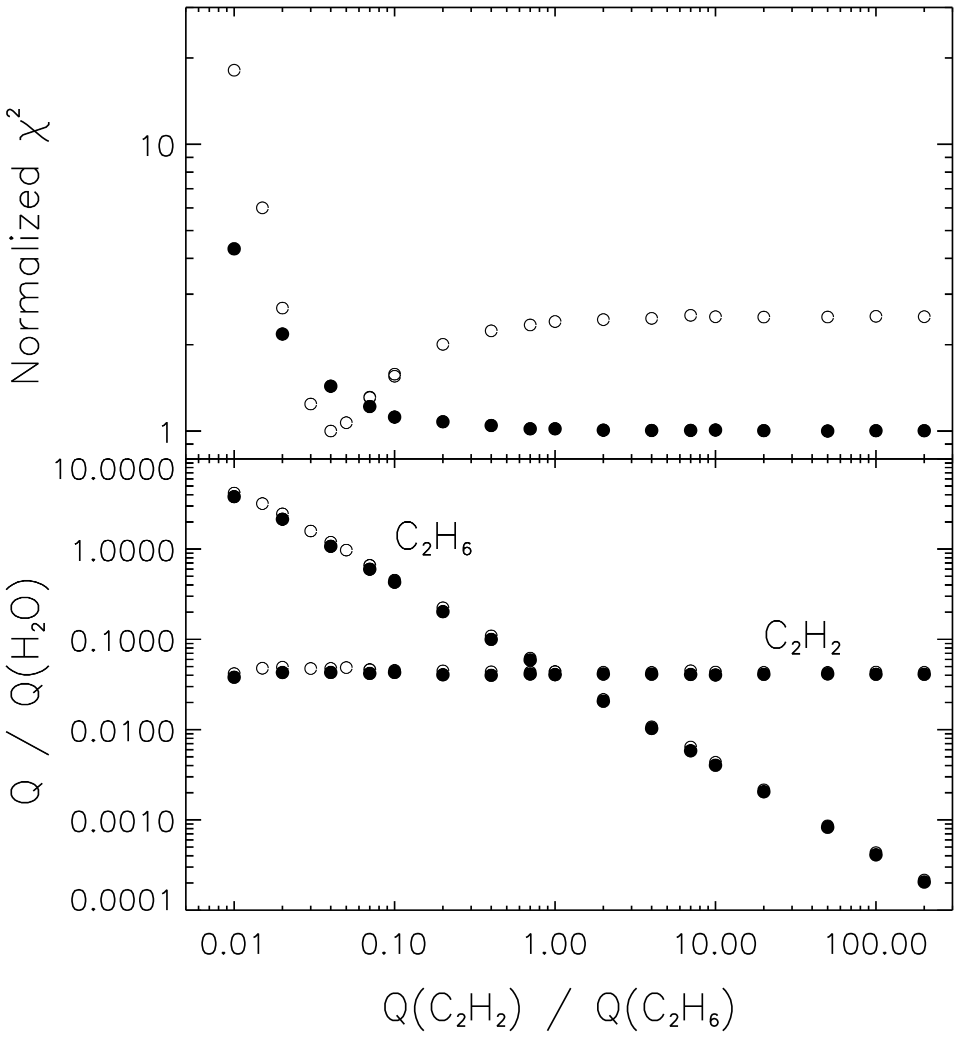

Figure 19: **Upper panel:** *Normalized χ^2 values for the best-fitting C_2 column density profiles obtained for various fixed ratios of $Q(C_2H_2)/Q(C_2H_6)$. Open symbols show values from the sunward side of the nucleus, filled symbols from the tailward side.* **Lower panel:** *Mixing ratios of C_2H_2 and C_2H_6 with respect to water obtained from the best-fitting C_2 column density profiles for various fixed ratios of $Q(C_2H_2)/Q(C_2H_6)$. Again, open symbols show results from the sunward side of the nucleus, filled symbols from the tailward side.*

7 Applications of the Chemistry Model with the Reaction Network by Helbert (2002)

The described model for the chemistry in the cometary coma was applied to reproduce the observed C_3 and C_2 column density profiles of the comets C/2001 Q4 NEAT, C/2002 T7 LINEAR, and 9P/Tempel 1. The results described in this chapter were obtained by using the reaction network derived by Helbert (2002) to explain the formation of C_3 and C_2. The study by Helbert (2002) was done by using the model for the chemistry in cometary comae by Schmidt *et al.* (1988).

7.1 Overview of the Input Parameters

The input parameters for the coma model are summarized for the three comets studied in Tab. 17 to Tab. 19. The production rates of the majority of species are unknown for the three comets analysed in this work. For the production rate ratios relative to water, values derived for comet C/1995 O1 Hale-Bopp at a heliocentric distance of about 1 AU (Bockelee-Morvan and Crovisier, 2003) were used in the absence of data from the corresponding comet. The same ratio of the CO production rate for comet C/2001 Q4 is also applied for comet C/2002 T7. A variation of this value by a factor of five does not have a significant impact on the computed C_3 and C_2 column density profiles. The CO_2 mixing ratio as determined by Bockelee-Morvan and Crovisier (2003) for comet Hale-Bopp was obtained at a larger heliocentric distance of about 2.9 AU and is thus not applicable for the comets studied in this work. A lower mixing ratio of 4% was instead applied. CO_2 production rates have been measured in four comets, and the mixing ratios relative to water range from 2.5% to 12% (Despois, 2005). Therefore, the 4% estimate appears reasonable. However, a variation of the assumed CO_2 mixing ratio by a factor of five does not significantly affect the computed column density profiles of C_3 and C_2.

It has to be noted that the water production rate for comet 9P/Tempel 1 is very uncertain. The value of $3.4 \cdot 10^{27}\,\mathrm{s}^{-1}$ by Küppers *et al.* (2005) represents the lowest value published in the literature, while Feldman *et al.* (2006) presents a water production rate of $10.4 \cdot 10^{27}\,\mathrm{s}^{-1}$. Biver *et al.* (2005) and Schleicher *et al.* (2006) present values that lie in between. These deviations may at least in part be caused by a variation of gas activity with the rotation of 9P/Tempel 1's nucleus. A variation of the activity of CN, C_2, C_3, and NH_2 was detected, as described in chapter 12. Such variation is also likely for the water production.

7.2 Selection of the Column Density Profiles

In this work, the sunward and tailward column density profiles of C_3 and C_3 of the comets C/2001 Q4, C/2002 T7, and 9P/Tempel 1 are analysed. In order to have a comparable

*Table 17: Overview of the input parameters used for comet 9P/Tempel 1. Q means production rate, M means the mixing ratio relative to water. R_N denotes the nucleus radius, T the initial temperature of the three fluids, and v the gas velocity. * marks values that were derived for comet C/1995 O1 Hale-Bopp around a heliocentric distance of one AU. These values are used since measurements for comet 9P/Tempel 1 are not available.*

Parameter	Value	Reference	Remark
$Q(H_2O)$	$3.4 \cdot 10^{27}\,s^{-1}$	Küppers *et al.* (2005)	
M(CO)	0.147	Feldman *et al.* (2006)	
$M(CO_2)$	0.04		estimate (see text)
$M(CH_4)$	0.006^*	Bockelee-Morvan and Crovisier (2003)	
$M(H_2CO)$	0.011^*	Bockelee-Morvan and Crovisier (2003)	
$M(CH_3OH)$	0.048	Mumma *et al.* (2005)	
$M(NH_3)$	0.007^*	Bockelee-Morvan and Crovisier (2003)	
M(HCN)	0.006	Mumma *et al.* (2005)	
M(HNCO)	0.001^*	Bockelee-Morvan and Crovisier (2003)	
$M(CH_3CN)$	0.0002^*	Bockelee-Morvan and Crovisier (2003)	
R_N	3.0 km	A'Hearn *et al.* (2005)	based on resolved images
$T(r = R_N)$	166.2 K	this work	
$v(r = R_N)$	319.9 m s^{-1}	this work	
r_h	1.51 AU		perihelion

dataset, profiles from other slit orientations available for comet 9P/Tempel 1 are not regarded. For comet 9P/Tempel 1, the mean profiles from the night July 3/4, 2005 are analysed. The observations of this night were done before the Deep Impact event, and no change in the radial intensity profiles during that night is observable, making them suitable for averaging. Since short-term variations in the gas activity are not of interest for the study of the C_3 and C_2 formation performed here, the analysis is restricted to the data from one night.

For comets C/2001 Q4 and C/2002 T7 two spectra per night are available. However, the signal-to-noise ratio of a single spectrum is already very high. The error in the C_3 column density profiles is dominated by the separation of the C_3 emission lines from the neighbouring CN emission, since the observations were done with a larger slit width (see section 2.3). Averaging the column density profiles from the two spectra available per night would therefore not increase the signal-to-noise ratio. Only single spectra are therefore analysed in this work.

Table 18: Same as Tab. 17, but for comet C/2002 T7.

Parameter	Value	Reference	Remark
$Q(H_2O)$	$6.9 \cdot 10^{28}\,s^{-1}$	Howell *et al.* (2004)	scaled $\sim r_h^{-2}$ to required r_h
$M(CO)$	0.04		estimate
$M(CO_2)$	0.04		estimate
$M(CH_4)$	0.006^*	Bockelee-Morvan and Crovisier (2003)	
$M(H_2CO)$	0.011^*	Bockelee-Morvan and Crovisier (2003)	
$M(CH_3OH)$	0.038	Remijan *et al.* (2006)	
$M(NH_3)$	0.007^*	Bockelee-Morvan and Crovisier (2003)	
$M(HCN)$	0.0033	Friedel *et al.* (2005)	
$M(HNCO)$	0.001^*	Bockelee-Morvan and Crovisier (2003)	
$M(CH_3CN)$	0.0002^*	Bockelee-Morvan and Crovisier (2003)	
R_N	44.2 km	this work	upper limit
$T(r = R_N)$	169.3 K	this work	
$v(r = R_N)$	$322.9\ m\ s^{-1}$	this work	
r_h	1.20 AU		post-perihelion

7.3 Results of the Fitting of the C_3 Column Density Profiles

The best fits to the observed column density profiles that were obtained by using the reaction network by Helbert (2002) are displayed in Fig. 20 for C_3. It can be seen that for comet 9P/Tempel 1 an acceptable fit was only possible in the intermediate to outer coma. For comets C/2001 Q4 and C/2002 T7, no acceptable fit could be obtained at all. For these comets the decrease in the C_3 column density profiles with increasing projected nucleocentric distance obtained with the chemistry model is not steep enough compared with the observations. The shape of the computed column density profiles is dominated by the onset of the electron impact reactions in the intermediate coma. This onset is caused by the steep increase of the electron temperature in the coma when it decouples from the neutral temperature. A detailed discussion on the electron temperature profiles is presented in section 9.3. The onset causes an increase in the production of C_3 at projected nucleocentric distances of $6 \cdot 10^3$ km to 10^4 km.

7.4 Results of the Fitting of the C_2 Column Density Profiles

Fig. 21 shows the obtained best fits of the observed C_2 column density profiles. It can be seen that for none of the observed radial column density profiles an acceptable fit could be obtained. The decrease of the computed C_2 column densities with increasing projected nucleocentric distance is in general not steep enough compared with the observations.

Table 19: Same as Tab. 17, but for comet C/2001 Q4.

Parameter	Value	Reference	Remark
$Q(H_2O)$	$1.9 \cdot 10^{29}\,s^{-1}$	Weaver *et al.* (2004)	
$M(CO)$	0.042	Feldman *et al.* (2004a)	
$M(CO_2)$	0.04		estimate
$M(CH_4)$	0.006^*	Bockelee-Morvan and Crovisier (2003)	
$M(H_2CO)$	0.011^*	Bockelee-Morvan and Crovisier (2003)	
$M(CH_3OH)$	0.015	Remijan *et al.* (2006)	
$M(NH_3)$	0.007^*	Bockelee-Morvan and Crovisier (2003)	
$M(HCN)$	0.00047	Friedel *et al.* (2005)	
$M(HNCO)$	0.001^*	Bockelee-Morvan and Crovisier (2003)	
$M(CH_3CN)$	0.0002^*	Bockelee-Morvan and Crovisier (2003)	
R_N	3.75 km	Tozzi *et al.* (2003)	estimate
$T(r = R_N)$	171.6 K	this work	
$v(r = R_N)$	$325.1\ m\ s^{-1}$	this work	
r_h	1.00 AU		pre-perihelion

7.5 Discussion

The reaction network for the formation of C_3 and C_2 in the cometary comae that allowed to reproduce the observed radial column density profiles at heliocentric distances larger than about 2.8 AU is not suitable to explain the column density profiles observed at heliocentric distances of about 1.0 AU to 1.5 AU. The computed column density profiles of both, C_3 and C_2 decrease too slowly with increasing projected nucleocentric distance. Furthermore, the shape of the C_3 column density profiles obtained with the model shows the onset of the electron impact reactions when the electron temperature decouples from the neutral temperature due to the low water number densities. The resulting shape of the computed C_3 column density profiles is not observed in the coma of the three comets studied in this work.

In the work by Helbert (2002), the onset of the electron impact reactions was not within the range of projected nucleocentric distances at which the C_3 and C_2 column density profiles of comet C/1995 O1 Hale-Bopp were studied. At the large heliocentric distances at which comet Hale-Bopp was studied by Helbert (2002), the water production rate was so low that the onset of the electron impact reactions occurred at nucleocentric distances of about 10^3 km or less. The column density profiles were analysed only at projected nucleocentric distances larger than 10^4 km. Therefore, this effect may have remained undetected.

For the comets C/2001 Q4 and C/2002 T7, the onset of the electron impact reactions lies within the range of projected nucleocentric distances at which the column density profiles were analysed. For comet 9P/Tempel 1, due to its low water production rate, the onset of the electron impact reactions lies at smaller nucleocentric distances than covered by the observations (see chapter 9.3). For this comet, the obtained fits to the observed C_3 column density profiles are acceptable except for the innermost coma. This result suggests that the electron impact reactions in the cometary comae are overestimated in the reaction network by Helbert (2002), allowing for a good fit of the observed C_3 column density profiles only in case when the projected nucleocentric distances regarded are significantly larger than the onset distance of the electron impact reactions. A revision of the reaction network is therefore required.

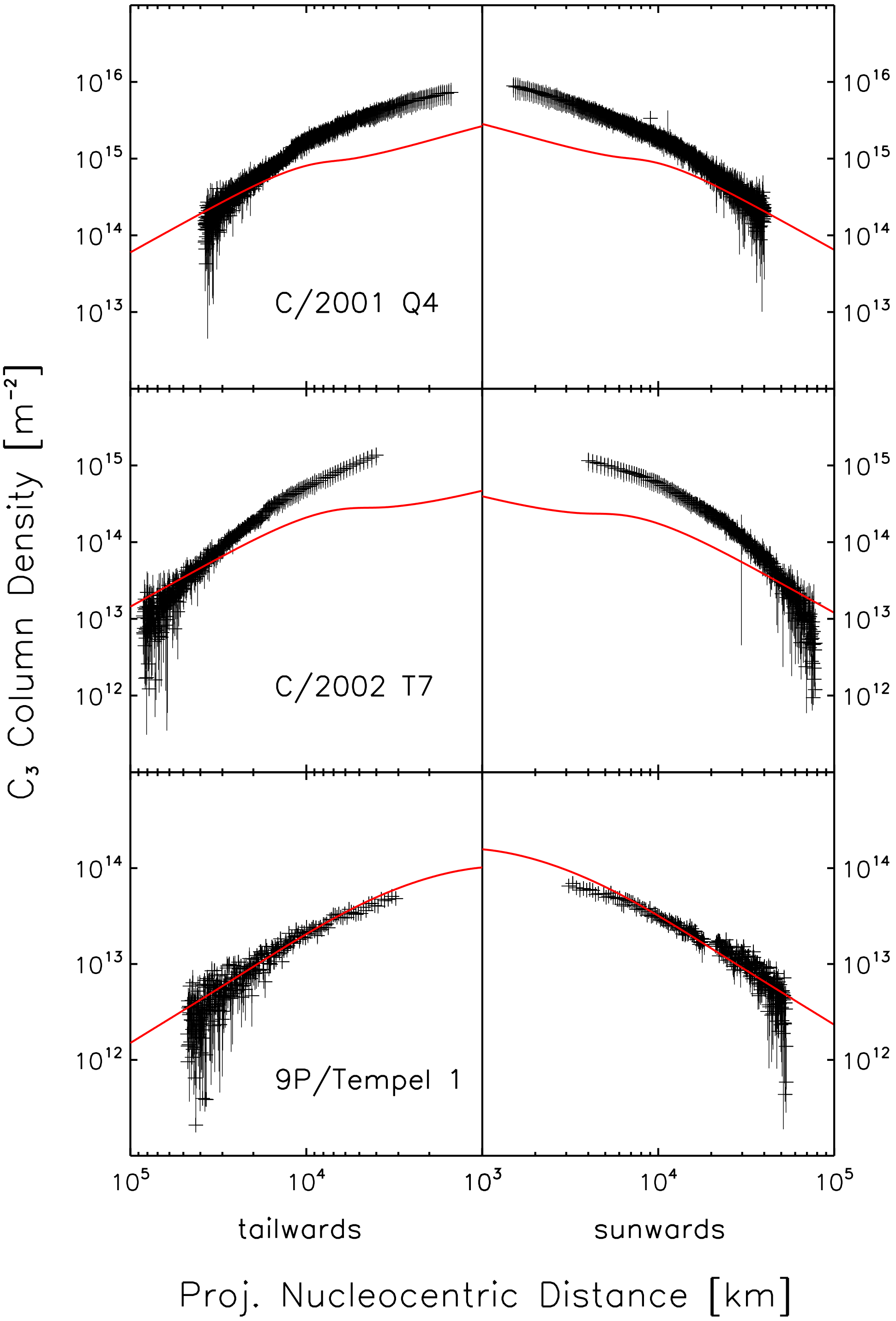

Figure 20: Best fits to the observed C_3 column density profiles of the comets C/2001 Q4, C/2002 T7, and 9P/Tempel 1, obtained by using the reaction network by Helbert (2002).

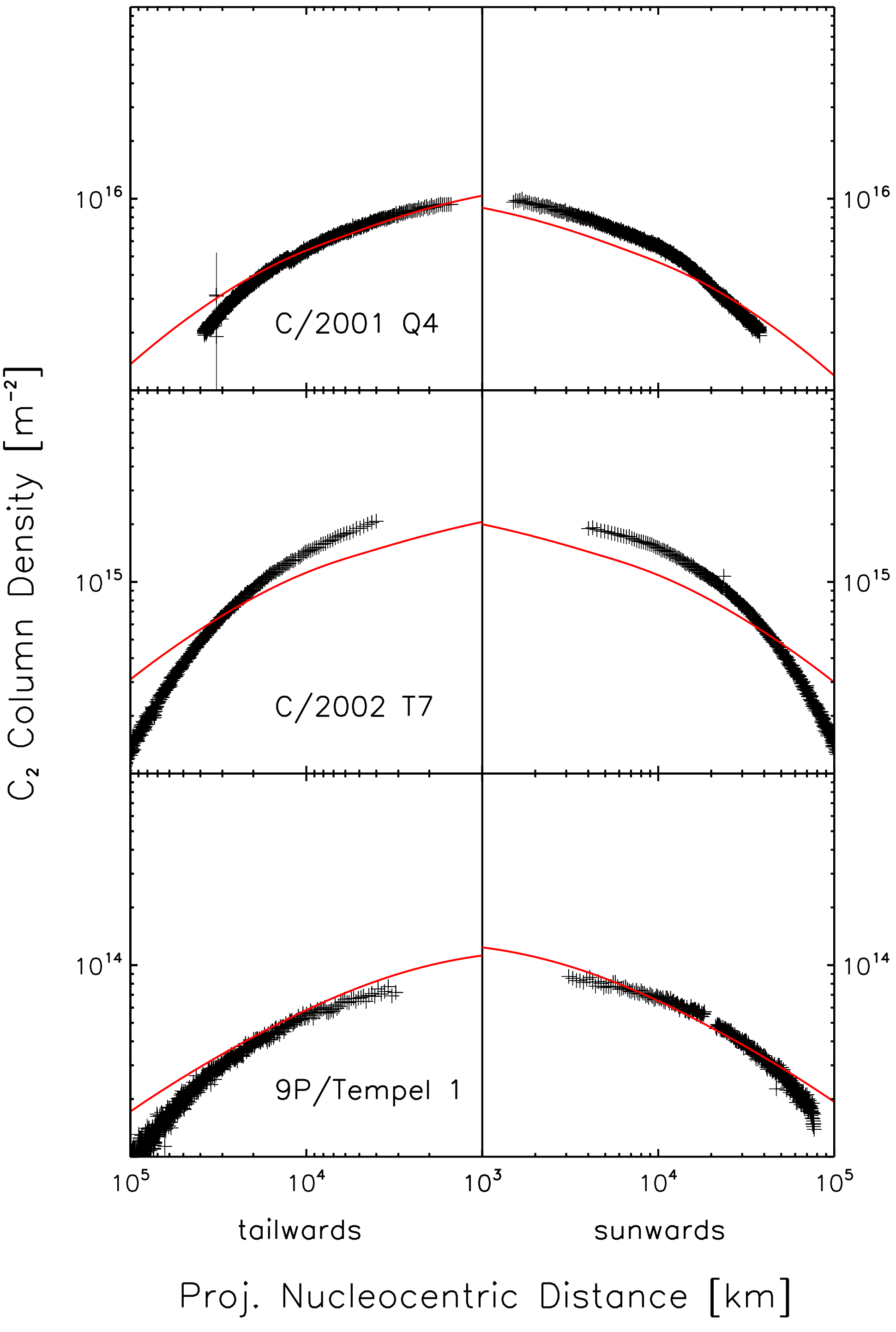

Figure 21: Best fits to the observed C_2 column density profiles of the comets C/2001 Q4, C/2002 T7, and 9P/Tempel 1, obtained by using the reaction network by Helbert (2002).

8 Revised Formation Chemistry of C_3 and C_2

The observed column density profiles of C_3 and C_2 of the comets C/2001 Q4, C/2002 T7, and 9P/Tempel 1 analysed in this work could not be fitted by using the reaction network presented by Helbert (2002). Therefore, in this chapter we review the formation mechanisms for C_3 and C_2. The reaction rate coefficients are updated in the chemical reaction network and some new reactions are included. Furthermore, additional parent species are discussed.

8.1 Potential C_3 and C_2 Parent Species

8.1.1 C_3H_4, C_2H_2, and C_2H_6

The formation of C_3 and C_2 from the three parent species C_3H_4, C_2H_2, and C_2H_6 was described by Helbert (2002) and an overview of the formation scheme is shown in Fig. 2. In this scheme, a number of reaction rates were updated for this work and some new electron impact reactions were introduced, as described in section 8.2.

8.1.2 C_4H_2

C_4H_2 was suggested to be a parent species of C_3 by Krasnopol'Skii (1991). Indeed, C_4H_2 was detected in comet C/2002 C1 Ikeya-Zhang (Despois, 2005) with a preliminary abundance relative to water of 0.05%. It was suggested by Krasnopol'Skii (1991) that C_4H_2 forms C_3 mainly via the reaction:

$$C_4H_2 + \gamma \rightarrow C_3 + CH_2 \ . \tag{115}$$

Furthermore, Glicker and Okabe (1987) studied the three photodissociation reactions of C_4H_2:

$$\begin{aligned} C_4H_2 + \gamma &\rightarrow C_4H + H & (116)\\ C_4H_2 + \gamma &\rightarrow C_2H_2 + C_2 & (117)\\ C_4H_2 + \gamma &\rightarrow C_2H + C_2H \ . & (118) \end{aligned}$$

The quantum yields for the three reactions at a wavelength of 1470 Å, $\Phi(1470)$, are 0.2, 0.1, and 0.07, respectively. These values were used to estimate the rate coefficients of the three reactions, k_j, using the relation:

$$k_j = \int_{\lambda_1}^{\lambda_j,} \Phi_j(\lambda)\sigma_{UV}(\lambda) \cdot f_{\odot}(\lambda)\, \mathrm{d}\lambda \tag{119}$$

In this equation, $\sigma_{UV}(\lambda)$ denotes the absorption cross section of C_4H_2 at wavelength λ in the ultraviolet wavelength range. This quantity is taken from Glicker and Okabe (1987) and Okabe (1981). $f_\odot(\lambda)$ denotes the solar flux at wavelength λ. The solar spectrum tabulated by Huebner *et al.* (1992) was used for the computation of the rate coefficients. The quantum yields of the reactions, Φ_j, were assumed to be independent of the wavelength, since only one value for each reaction measured at a single wavelength is available. The upper integration limit, λ_j, is determined by the energy required to dissociate the C_4H_2 molecule by the different photodissociation processes. The values for λ_j were taken from Glicker and Okabe (1987). The lower integration limit, λ_1, was assumed to be 1200 Å, since no information on the absorption cross section below this wavelength is available. However, since the solar flux decreases strongly below this wavelength, no significant contribution to the photoreaction rate is expected as a result of this omission. With the assumptions made, the reaction rate coefficients are estimated to be $6.62 \cdot 10^{-5}\,\mathrm{s}^{-1}$, $1.39 \cdot 10^{-5}\,\mathrm{s}^{-1}$, and $9.58 \cdot 10^{-6}\,\mathrm{s}^{-1}$ for the reactions (116), (117), and (118), respectively, at a heliocentric distance of 1 AU. The rate coefficient of the reaction (115) was estimated by assuming the quantum yield of this reaction to be 0.63. In the simple picture assumed here, this means that every absorbed photon not leading to the reactions (116), (117), or (118), is leading to reaction (115). For the threshold wavelength λ_j, the value of 1680 Å given by Krasnopol'Skii (1991) was applied. These assumptions lead to a rate coefficient of $6.47 \cdot 10^{-5}\,\mathrm{s}^{-1}$ at 1 AU.

The photodissociation of C_4H produced by reaction (116) is not well defined. Woodall *et al.* (2006) mentions the photodissociation reactions

$$C_4H + \gamma \rightarrow C_2H + C_2 \tag{120}$$

and

$$C_4H + \gamma \rightarrow C_4 + H \ . \tag{121}$$

The produced C_4 can decay according to

$$C_4 + \gamma \ \rightarrow \ C_3 + C \tag{122}$$

$$C_4 + \gamma \ \rightarrow \ C_2 + C_2 \ . \tag{123}$$

Unfortunately, no rate coefficients are available for these four reactions. Therefore, an estimate is used in this work, obtained from comparison with similar reactions for radicals containing two or three carbon atoms. The rate coefficients used in this work are $3 \cdot 10^{-5}\,\mathrm{s}^{-1}$ for reactions (120) and (121) and $1 \cdot 10^{-4}\,\mathrm{s}^{-1}$ for reactions (122) and (123).

8.1.3 C_3H_2O

C_3H_2O was by now not detected in cometary comae. However, formation of C_3 from C_3H_2O was suggested by Krasnopol'Skii (1991) according to the reaction:

$$C_3H_2O + \gamma \rightarrow C_3 + H_2 + O \ . \tag{124}$$

Furthermore, a photodissociation process according to:

$$C_3H_2O + \gamma \rightarrow C_2H_2 + CO \tag{125}$$

was suggested. The formation of CO by the photodissociation of C_3H_2O was indeed observed in laboratory measurements (Kumar and Huber, 1976). However, the photodissociation rates of C_3H_2O are not known. Therefore, this parent molecule was not taken into consideration in this work.

8.1.4 HC_3N

HC_3N has been detected in three comets to date (Despois, 2005), with an abundance relative to water of about 0.02%. HC_3N contributes to the formation of C_2 via the photodissociation reactions:

$$HC_3N + \gamma \rightarrow C_2H + CN \tag{126}$$

$$HC_3N + \gamma \rightarrow C_3N + H \ . \tag{127}$$

The products of these two reactions form C_2:

$$C_2H + \gamma \rightarrow C_2 + H \tag{128}$$

$$C_3N + \gamma \rightarrow C_2 + CN \ . \tag{129}$$

Huebner *et al.* (1992) gives a reaction rate coefficient for reaction (126) of $3.92 \cdot 10^{-5}\,s^{-1}$ at 1 AU. However, later publications point out that this reaction is only a minor destruction pathway of HC_3N (Seki *et al.*, 1996). The main photodissociation path is the reaction (127). Therefore, the rate coefficients of reactions (126) and (127) are estimated in this work. To do this, the ultraviolet absorption spectrum of HC_3N in the wavelength range of 1900 Å to 2500 Å and the quantum yields of the two reactions measured at 1930 Å, 0.02 and 0.3, respectively, are used (Seki *et al.*, 1996). The threshold wavelengths for the two reactions are 2000 Å (Halpern *et al.*, 1988) and 2440 Å (Halpern *et al.*, 1990). With these assumptions, and the solar spectrum of Huebner *et al.* (1992), rate coefficients of $3.39 \cdot 10^{-8}\,s^{-1}$ and $1.03 \cdot 10^{-5}\,s^{-1}$ are obtained.

The rate coefficient for reaction (129) is even more uncertain. Halpern *et al.* (1990) presents a threshold wavelength of 1930 Å for this reaction, and an estimated range of the ultraviolet absorption cross section of $1 \cdot 10^{-18} - 5 \cdot 10^{-17}\,cm^2$ at a wavelength of 1930 Å. The quantum yield for this reaction is not known. If one assumes the quantum yield to be 0.5 and the value of $1 \cdot 10^{-18}\,cm^2$ to be the mean absorption cross section, one obtains a reaction rate coefficient of $7.20 \cdot 10^{-7}\,s^{-1}$. This value is used as an approximate estimate in this work.

Table 20: Overview on electron impact reactions important for the formation of C_3 and C_2, taken from Alman et al. *(2000) (ref = 1) and the UMIST database (ref = 2). Reactions newly introduced into the chemical reaction network of this work are marked by †. A_j, B_j, and C_j list the Arrhenius coefficients, A_j is in units of $[\,10^{-9}\,cm^3\,s^{-1}\,]$.*

Reaction	A_j	B_j	C_j	ref
Electron Impact Dissociation				
$C_3H_4 + e^- \rightarrow C_3 + H_2 + 2\,H + e^-$	10.3	0.369	116800	1
$C_3H_4 + e^- \rightarrow C_3H_3 + H + e^-$	4.80	0.595	115847	$1^\dagger$
$C_3H_3 + e^- \rightarrow C_3H_2 + H + e^-$	4.56	0.595	115800	$1^\dagger$
$C_3H_3 + e^- \rightarrow C_3H + 2\,H + e^-$	9.78	0.369	116800	$1^\dagger$
$C_3H_2 + e^- \rightarrow C_3H + H + e^-$	6.45	0.596	115800	$1^\dagger$
$C_3H + e^- \rightarrow 3\,C + H + e^-$	6.22	0.591	115900	$1^\dagger$
$C_2H_2 + e^- \rightarrow C_2 + H + H + e^-$	4.51	0.595	115843	1
$C_2H + e^- \rightarrow C + C + H + e^-$	3.96	0.598	115818	$1^\dagger$
$C_2H_3 + e^- \rightarrow C_2 + H_2 + H + e^-$	3.24	0.590	115903	$1^\dagger$
$C_2H_3 + e^- \rightarrow C_2 + 3\,H + e^-$	6.89	0.366	116796	$1^\dagger$
$C_2H_4 + e^- \rightarrow C_2 + H_2 + 2\,H + e^-$	7.67	0.362	116831	$1^\dagger$
Electron Impact Ionisation / Dissociative Ionisation				
$C_3H_4 + e^- \rightarrow C_3H_4^+ + 2\,e^-$	0.17	0.770	115105	$1^\dagger$
$C_3H_4 + e^- \rightarrow C_3H_3^+ + H + 2\,e^-$	0.16	0.729	138478	$1^\dagger$
$C_3H_4 + e^- \rightarrow C_3H_2^+ + 2\,H + 2\,e^-$	0.76	0.736	138386	$1^\dagger$
$C_3H_3 + e^- \rightarrow C_3H_3^+ + 2\,e^-$	0.16	0.767	115143	$1^\dagger$
$C_3H_3 + e^- \rightarrow C_3H_2^+ + H + 2\,e^-$	0.15	0.730	138460	$1^\dagger$
$C_3H_3 + e^- \rightarrow C_3H^+ + 2\,H + 2\,e^-$	0.72	0.737	138370	$1^\dagger$
$C_3H_2 + e^- \rightarrow C_3H_2^+ + 2\,e^-$	0.48	0.763	115182	$1^\dagger$
$C_3H_2 + e^- \rightarrow C_3H^+ + H + 2\,e^-$	0.42	0.735	138396	$1^\dagger$
$C_3H + e^- \rightarrow C_3H^+ + 2\,e^-$	0.75	0.769	115114	$1^\dagger$
$C_2H + e^- \rightarrow C_2H^+ + 2\,e^-$	0.35	0.754	115257	$1^\dagger$
$C_2H + e^- \rightarrow C^+ + C + H + 2\,e^-$	0.32	0.734	138369	$1^\dagger$
$C_2H_2 + e^- \rightarrow C_2H_2^+ + 2\,e^-$	0.36	0.754	115267	$1^\dagger$
$C_2H_2 + e^- \rightarrow C_2H^+ + H + 2\,e^-$	0.30	0.738	138330	$1^\dagger$
$C_2H_3 + e^- \rightarrow C_2H_3^+ + 2\,e^-$	0.12	0.771	115064	$1^\dagger$
$C_2H_3 + e^- \rightarrow C_2H_2^+ + H + 2\,e^-$	0.11	0.731	138414	$1^\dagger$
$C_2H_3 + e^- \rightarrow C_2H^+ + H_2 + 2\,e^-$	0.59	0.725	138491	$1^\dagger$
$C_2H_4 + e^- \rightarrow C_2H_4^+ + 2\,e^-$	0.12	0.773	115054	1
$C_2H_4 + e^- \rightarrow C_2H_3^+ + H + 2\,e^-$	0.11	0.733	138403	$1^\dagger$
$C_2H_4 + e^- \rightarrow C_2H_2^+ + H_2 + 2\,e^-$	0.60	0.727	138486	$1^\dagger$
$C_2H_5 + e^- \rightarrow C_2H_5^+ + 2\,e^-$	0.14	0.770	115088	$1^\dagger$
$C_2H_5 + e^- \rightarrow C_2H_4^+ + H + 2\,e^-$	0.13	0.730	138444	$1^\dagger$
$C_2H_5 + e^- \rightarrow C_2H_3^+ + H_2 + 2\,e^-$	0.61	0.738	138346	$1^\dagger$
$C_2H_6 + e^- \rightarrow C_2H_6^+ + 2\,e^-$	0.16	0.765	115138	$1^\dagger$
$C_2H_6 + e^- \rightarrow C_2H_5^+ + H + 2\,e^-$	0.14	0.728	138446	$1^\dagger$
$C_2H_6 + e^- \rightarrow C_2H_4^+ + H_2 + 2\,e^-$	0.69	0.736	138361	$1^\dagger$

Table 20 (continued):

Reaction	A_j	B_j	C_j	ref
Dissociative Recombination				
$C_2H_5^+ + e^- \rightarrow C_2H_3 + H_2$	300	−0.50	0.0	$2^\dagger$
$C_2H_3^+ + e^- \rightarrow C_2H + H_2$	57.5	−1.38	0.0	$2^\dagger$
$C_2H_3^+ + e^- \rightarrow C_2H + 2\,H$	565	−1.38	0.0	$2^\dagger$
$C_2H_3^+ + e^- \rightarrow C_2H + H_2$	300	−1.38	0.0	$1^\dagger$
$C_2H_3^+ + e^- \rightarrow C_2 + H + H_2$	28.7	−1.38	0.0	$1^\dagger$
$C_2H_3^+ + e^- \rightarrow C_2H_2 + H$	278	−1.38	0.0	2
$C_2H_3^+ + e^- \rightarrow CH_3 + C$	5.75	−1.38	0.0	$2^\dagger$
$C_2H_3^+ + e^- \rightarrow CH_2 + CH$	2.87	−1.38	0.0	$2^\dagger$
$C_2H_2^+ + e^- \rightarrow C_2 + H + H$	141	−0.50	0.0	$1^\dagger$
$C_2H_2^+ + e^- \rightarrow CH + CH$	141	−0.50	0.0	$1^\dagger$
$C_2H^+ + e^- \rightarrow C + C + H$	289	−0.50	0.0	$1^\dagger$
$C_2H^+ + e^- \rightarrow CH + C$	289	−0.50	0.0	$1^\dagger$
$C_3H_4^+ + e^- \rightarrow C_3H_3 + H$	342	−0.50	0.0	$1^\dagger$
$C_3H_4^+ + e^- \rightarrow C_3H_2 + H_2$	342	−0.50	0.0	$1^\dagger$
$C_3H_3^+ + e^- \rightarrow C_3H_2 + H$	342	−0.50	0.0	$1^\dagger$
$C_3H_3^+ + e^- \rightarrow C_3H + H_2$	342	−0.50	0.0	$1^\dagger$
$C_3H_2^+ + e^- \rightarrow C_2 + CH_2$	30.0	−0.50	0.0	$2^\dagger$
$C_3H_2^+ + e^- \rightarrow C_3 + H_2$	60.0	−0.50	0.0	$2^\dagger$
$C_3H_2^+ + e^- \rightarrow C_2H_2 + C$	30.0	−0.50	0.0	$2^\dagger$
$C_3H_2^+ + e^- \rightarrow C_3H + H$	342	−0.50	0.0	$1^\dagger$
$C_3H_2^+ + e^- \rightarrow C_2H + CH$	342	−0.50	0.0	$1^\dagger$
$C_3H^+ + e^- \rightarrow C_2H + C$	228	−0.50	0.0	$1^\dagger$
$C_3H^+ + e^- \rightarrow CH + 2\,C$	228	−0.50	0.0	$1^\dagger$
$C_3H^+ + e^- \rightarrow 3\,C + H$	228	−0.50	0.0	$1^\dagger$

8.2 Revised Reaction Rate Coefficients

8.2.1 Electron Impact Reactions

Electron impact dissociation of C_3H_4 is regarded as important for the formation of the C_3 radical (Helbert, 2002). A formation of C_3 from C_3H_2 via multiple steps was expected, but since the electron impact reaction pathways were only poorly known, a formation of C_3 from C_3H_4 in only one step with an estimated Arrhenius coefficient was applied in the chemical reaction network. The work by Alman *et al.* (2000) provides estimates of electron impact reaction cross sections, parameterized as a function of the impact energy, E.

From the parametrisation of the reaction cross sections of electron impact dissociation, electron impact ionisation, and dissociative recombination reactions given by Alman *et al.* (2000), the Arrhenius coefficients of the reactions were determined. From the energy-dependent cross sections $\sigma(E)$, the reaction rate coefficients k were computed according to (Wedler, 2004):

$$k = \int_0^\infty v(E)\, f(E)\, \sigma(E)\, \mathrm{d}E \; . \tag{130}$$

In this equation, $v(E)$ means the relative velocity of the electron and the reactant molecule, $v(E) = \sqrt{2\,E/m}$, and $f(E)$ is the frequency distribution of the electrons with energy, E. For $f(E)$, a Maxwell distribution for a temperature, T was assumed. The rate coefficient, k was computed for 1000 equidistant temperature steps between 40 K and $4 \cdot 10^4$ K, and the resulting rate coefficients $k(T)$ were fitted according to equation (77) to determine the Arrhenius coefficients A, B, and C.

The reactions for which the Arrhenius coefficients were determined from the work by Alman *et al.* (2000) are listed in Tab. 20.

Futhermore, new electron impact reactions taken from the UMIST database (Woodall *et al.*, 2006) were introduced into the reaction network. These reactions are also listed in Tab. 20. Reactions that were newly introduced in the chemical reaction network from Alman *et al.* (2000) and the UMIST database compared to Helbert (2002) are marked. The Arrhenius coefficients of reactions already included in the chemical reaction network of Helbert (2002) were updated with the values listed in this Table. The new Arrhenius coefficients derived here result in lower electron impact reaction rates than the Arrhenius coefficients used before. Therefore, electron impact reactions become less important for the formation of C_3 and C_2.

8.2.2 Photoreactions

Helbert (2002) determined the photodissociation rate coefficients for the reactions:

$$C_3H_2 + \gamma \;\rightarrow\; C_3 + H_2 \tag{131}$$

$$C_3 + \gamma \;\rightarrow\; C_2 + C \tag{132}$$

from the analysis of the radial C_3 column density profiles in the coma of comet C/1995 O1 Hale-Bopp. As shown in this work, it is not possible to obtain a satisfying fit of the C_3 column density profiles of a comet at small heliocentric distances with only C_3H_4 as the parent of C_3, using the reaction network by Helbert (2002). This suggests errors in the reaction network. Therefore, in this work the rate coefficients of $1.9 \cdot 10^{-6}\,\mathrm{s}^{-1}$ and $1.0 \cdot 10^{-4}\,\mathrm{s}^{-1}$ are used for reactions (131) and (132), respectively, instead of the values derived by Helbert (2002) (see Helbert (2002) for more details).

8.3 Summary of the Revised Formation of C_3 and C_2

The revised reaction network leading to the formation of C_3 and C_2 is summarized in Fig. 22. As shown in detail in section 9.2 of this work, the C_2H_6-branch shown in Fig. 2 can be neglected and is thus not included in this Figure. Instead, the additional parent

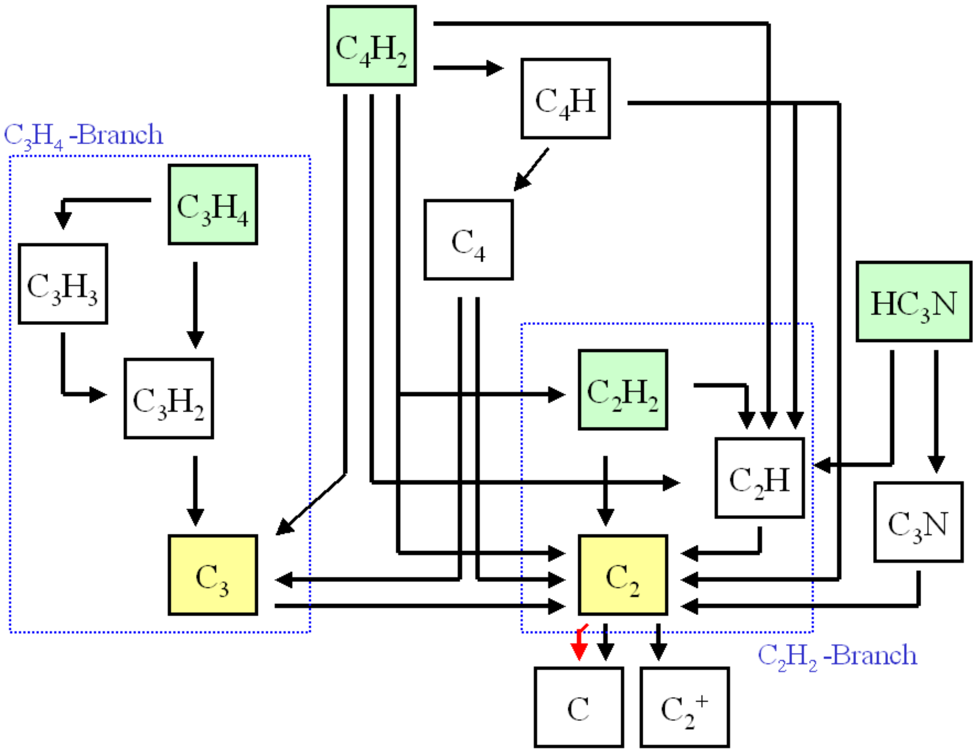

Figure 22: Revised formation scheme of C_3 *and* C_2*. The parent species,* C_3H_4*,* C_4H_2*,* C_2H_2*, and* HC_3N*, are indicated in light green, the observable radicals* C_3 *and* C_2 *are indicated in yellow. Red arrows indicate electron impact reactions, black arrows indicate photoreactions.*

species HC_3N and C_4H_2 are introduced. HC_3N connects to C_2H and via C_3N to C_2. For C_4H_2 the situation is more complicated. It connects directly and via C_4H and C_4 to C_3. Furthermore, it contributes to the formation of C_2. C_4H_2 is connected directly to C_2H_2, C_2H, and C_2. Via C_4H it is connected to C_2H and C_2, and via C_4H and C_4 it is connected to C_2.

Due to poor knowledge on electron impact reactions of the species newly introduced into this formation scheme, only photoreactions are taken into account.

9 Analysis of the C_3 and C_2 Column Density Profiles

In this chapter, the influence of the solar activity cycle upon the photoreaction rates is discussed. The efficiency of the different parent species for producing C_3 and C_2 in the cometary comae is studied. Furthermore, the influence of the electron temperature, the gas velocity, and the assumption on the nucleus size upon the computed C_3 and C_2 column density profiles is studied.

9.1 Influence of the Solar Activity Cycle

As stated before, all photoreaction rates used in this work are valid for solar minimum conditions. As stated by Huebner *et al.* (1992), photoreaction rates of hydrocarbons increase typically by a factor of two to three from solar minimum to solar maximum conditions due to the changing solar ultraviolet flux. Therefore, the position in the solar activity cycle has to be considered when using the presented model of the coma chemistry for the interpretation of comet observations. Fig. 23 presents the monthly averaged values of the number of sunspots and the disc-integrated solar radio flux at 10.7 cm wavelength from the years 1991 to 2006. These two quantities represent indicators for the solar activity. The variation in solar activity can be clearly seen. The times of the comet observations analysed with the chemistry model in this work are indicated in this Figure. All observations were performed at a similar solar activity close to solar minimum. The assumption of reactions rates for solar minimum conditions is therefore justified in this work.

9.2 Influence of the Different Parent Species upon the C_3 and C_2 Column Density Profiles

In this work the parent species C_3H_4, C_4H_2, C_2H_2, C_2H_6, and HC_3N are studied with respect to the formation of C_3 and C_2. In order to estimate the relative importance of these parent species for the resulting radial column density profiles, test computations were performed. In each of these computations, only one of the five parent species were assumed to be present in the coma with an initial production rate ratio with respect to water of 0.01. All other parameters were those for comet C/2002 T7. Fig. 24 shows the resulting abundances of the C_3 parent species C_3H_4 (panel a) and C_4H_2 (panel b), together with the most important daughter species, plotted versus nucleocentric distance. In this Figure, the number densities were multiplied by $4\pi r^2\, v(r)$ to correct for geometrical dilution and the influence of varying expansion velocity. The resulting values were normalized to the initial value of the parent species. Therefore, all deviations of the relative abundances in Fig. 24 from a constant value are caused by chemical reactions only.

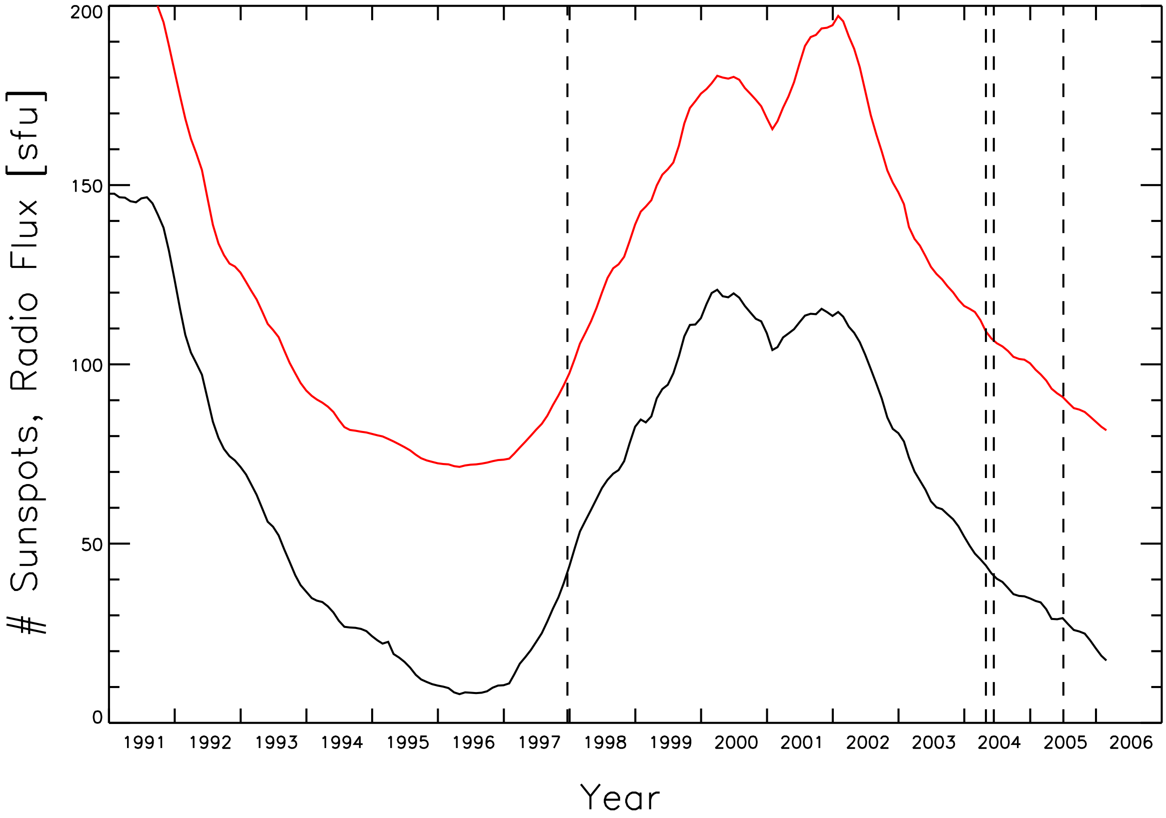

Figure 23: Monthly averaged number of sunspots (Brussels International Sunspot Number, black curve) and monthly averaged disc-integrated 10.7 cm solar radio flux in Solar Flux Units (1 Solar Flux Unit (sfu) corresponds to $10^{-22}\,W\,m^{-2}\,Hz^{-1}$) (Penticton Radio Observatory, B.C., Canada, red curve) verus time. The presented values are smoothed and were provided by the Space Environment Center of the National Oceanic and Atmospheric Administration (`www.sec.noaa.gov`). The times of observations of comets analysed with the chemistry model in this work are indicated by dashed lines.

In Fig. 24 (a), C_3 appears to be produced by two processes, since its abundance increases steeply above the surface of the nucleus, and again increases at nucleocentric distances of about 10^4 km. In the innermost coma, C_3 is mainly produced via the dissociative recombination reaction

$$C_3H_5^+ + e^- \rightarrow C_3 + H_2 + H_2 + H \; , \tag{133}$$

where the ion $C_3H_5^+$ is predominantly formed by the reaction:

$$C_3H_4 + H_3O^+ \rightarrow C_3H_5^+ + H_2O \; . \tag{134}$$

For H_3O^+ a variety of formation reactions are included in the reaction network used in this work. The importance of reaction (133) becomes obvious when comparing the relative abundance of C_3 computed with this reaction (solid blue line in Fig. 24 (a))

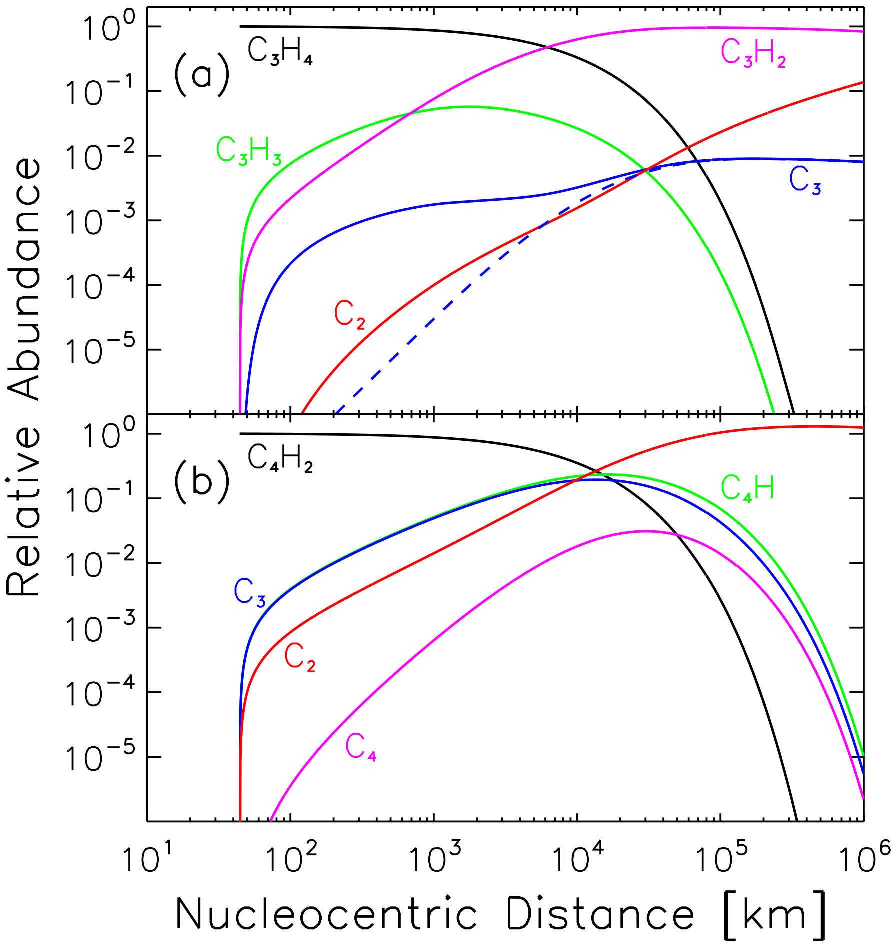

Figure 24: Relative abundances of C_3H_4 and some decay products (panel a), and C_4H_2 and some decay products (panel b). The abundances are corrected for geometric dilution and changes in velocity and normalized to the initial number density of C_3H_4 and C_4H_2 (1% of the water production rate), respectively. The dashed curve in panel a shows the abundance of C_3 without taking dissociative recombination into account. See text for more details.

with its relative abundance computed without taking reaction (133) into account (dashed blue line in Fig. 24 (a)). The second increase of the C_3 abundance at about 10^4 km nucleocentric distance is caused by photodissociation of C_3H_4 and its decay products. When comparing Fig. 24 (a) and (b), it becomes clear that C_4H_2 is more effective in producing C_3 in the coma up to nucleocentric distances of about 10^5 km. Furthermore, it is significantly more effective at all nucleocentric distances in producing C_2. This becomes clear when one considers that breaking a C−C bond in a species containing only three carbon atoms produces only one C_2 compound, while breaking the central C−C bond in C_4 produces two C_2-bearing radicals.

Fig. 25 is similar to Fig. 24, but for the additional C_2 parent species, C_2H_2, C_2H_6, and HC_3N. It can be seen when comparing Fig. 25 (a) with Fig. 25 (b) that C_2 is formed

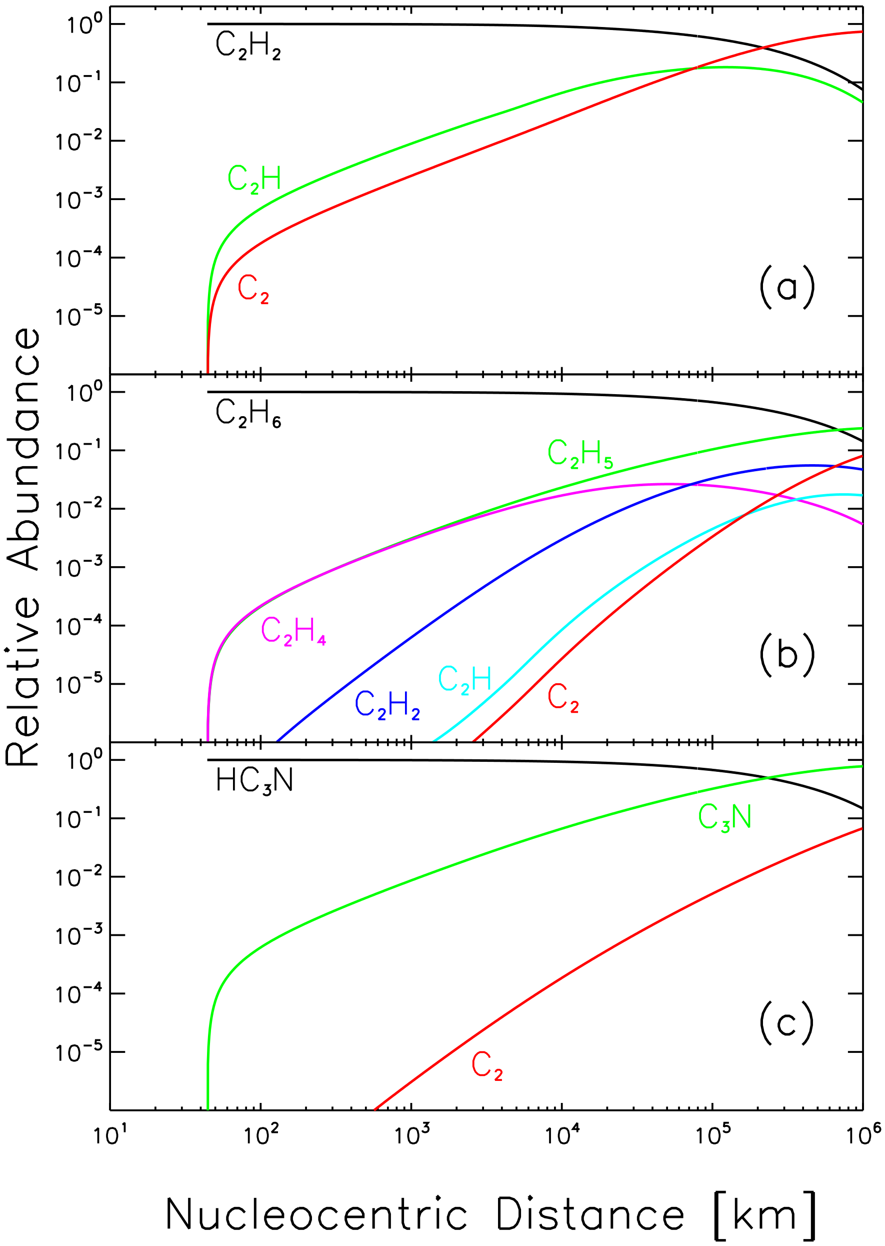

Figure 25: Relative abundance of C_2H_2 *(panel a),* C_2H_6 *(panel b),* HC_3N *(panel c), and some daughter species, respectively. The values were corrected for geometric dilution and variations in the expansion velocity and normalized to the initial value of the parent species (1% of the water production rate). For details see text.*

much faster from C_2H_2 than from C_2H_6. The reactions leading to the destruction of C_2H_2 are only slightly faster than the destruction reactions for C_2H_6, but due to the larger number of intermediate steps before the formation of C_2 from C_2H_6, the increase in C_2 is significantly delayed. Also, the parent species HC_3N is only slightly more effective in producing C_2 than C_2H_6, as can be seen when comparing Fig. 25 (b) and (c).

When comparing Fig. 24 and 25, it can be seen that C_4H_2 is the most effective species for the formation of C_2. C_3H_4 is less effective than C_4H_2 and C_2H_2, but more effective than C_2H_6 and HC_3N.

In order to estimate the influence of the different relative abundances upon the radial column density profiles, which are the quantities to be compared with observations, the ratios of the column densities are shown in Fig. 26. The method of conversion from number densities to column densities is described in section 5.1. The resulting column densities obtained with pure C_2H_6, HC_3N, C_3H_4, and C_4H_2 as parents were divided by the column densities obtained with a pure C_2H_2 as the parent species and plotted versus projected nucleocentric distance. In the range of projected nucleocentric distances important for the comparison with observations (between about 10^3 km and 10^5 km), C_3H_4 contributes more than 10% of the C_2, while C_2H_6 only provides up to a few percent at large projected nucleocentric distances. C_4H_2 contributes by far most to the C_2 column densities, whereas HC_3N never contributes more than a few percent.

All the comparisons were made by using the same ratio of the parent production rates with respect to water. Direct observations of C_2H_2 and C_2H_6 in a number of comets (e.g. in comet Hale-Bopp (Bockelee-Morvan and Crovisier, 2003) and 9P/Tempel 1 (Mumma *et al.*, 2005)) indicate that the production rate of C_2H_6 is typically about two to three times higher than the production rate of C_2H_2. Estimates of the C_3H_4 production rates in comet Hale-Bopp at heliocentric distances between 2.8 AU and 4.7 AU by Helbert (2002) showed that C_3H_4 might be only slightly less abundant than C_2H_2 ($Q(C_3H_4)/Q(C_2H_2) = 0.65 \pm 0.37$). Taking 20% of the observed column density as a limit for a significant contribution of a parent molecule at about 10^4 km projected nucleocentric distance, then about 30% of C_3H_4 with respect to C_2H_2 would be detectable, whereas between 35 to 40 times more C_2H_6 than C_2H_2 would be required to reach that limit. Therefore, C_2H_6 is neglected in the following discussion of C_2 formation in the coma.

The relative abundances of C_4H_2 and HC_3N in comets are presently only poorly known. Direct observations of these two species suggest that they are about a factor of ten less abundant than C_2H_2 (Despois, 2005). This would mean that they represent no important parent species is of C_3 and C_2. But since these measurements are based only on detections in one and three comets, respectively, the two species are included in the further analysis.

9.3 Influence of Electron Impact Reactions upon the C_3 and C_2 Column Density Profiles

The reaction rates for electron impact reactions strongly depend on the electron temperature T_e. The steep increase of the electron temperature in the coma therefore determines the onset of the electron impact reactions. In order to estimate the influence of the radial position of the increase in T_e upon the resulting C_3 and C_2 column density profiles, test

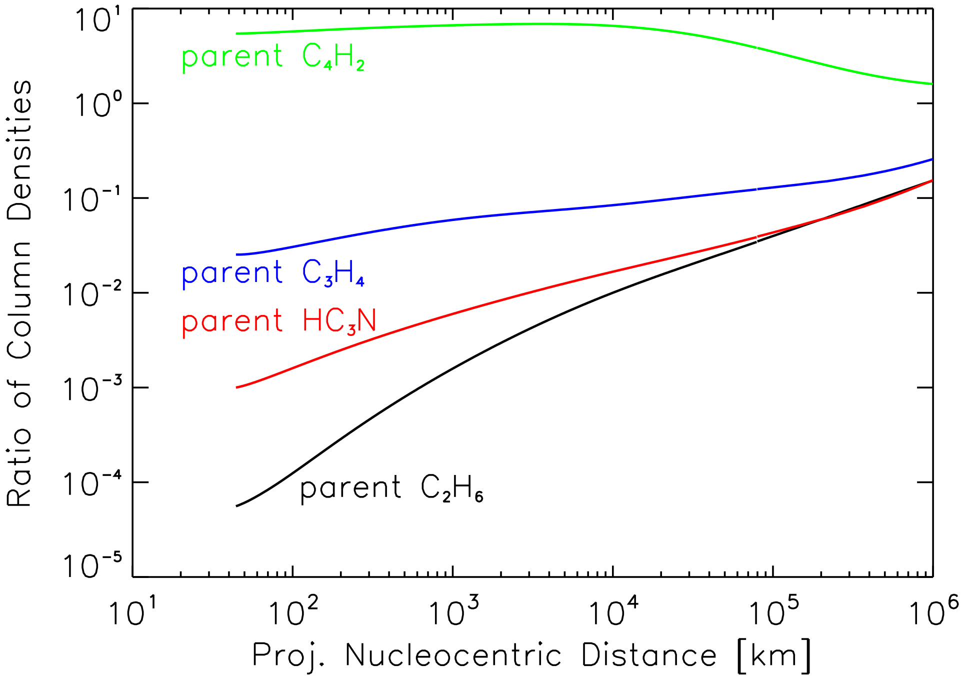

Figure 26: Ratios of the column densities of C_2 originating only from C_2H_6, C_4H_2, HC_3N, and C_3H_4 as the parent species, relative to the column densities with C_2H_2 as the only parent species. For details see text.

computations with artificial radial electron temperature profiles were performed for the comets 9P/Tempel 1 (having the lowest water production rate) and C/2004 Q4 (having the highest water production rate). In the computations, all C_3 and C_2 parent species are included with a production rate of 0.01 relative to water. The most simple approach, using a step function for $T_e(r)$, cannot, however be handled by the integrators used. To obtain a more smooth increase of T_e, an increase according to a Gaussian function was used. T_e starts from a minimum temperature in the innermost coma and increases with a Gaussian profile to a maximum value. From the maximum of the Gaussian on, T_e is assumed to be constant. The artifical value of the electron temperature is therefore given by:

$$T_e = (T_{max} - T_{min})\, e^{-z^2/2} + T_{min} \quad [\, \mathrm{r} < \mathrm{r}_0 \,] \tag{135}$$

$$T_e = T_{max} \quad [\, \mathrm{else} \,]\ , \tag{136}$$

with $z = (r - r_0)/\sigma$ and $\sigma = r_0/5$. The parameter r_0, determining the nucleocentric distance at which the maximum electron temperature is reached, was then varied. T_{min} and T_{max} were chosen in such a way that the electron temperatures from the full model without artificial manipulation of T_e were matched in the inner and the outer coma by the artificial radial electron temperature profiles.

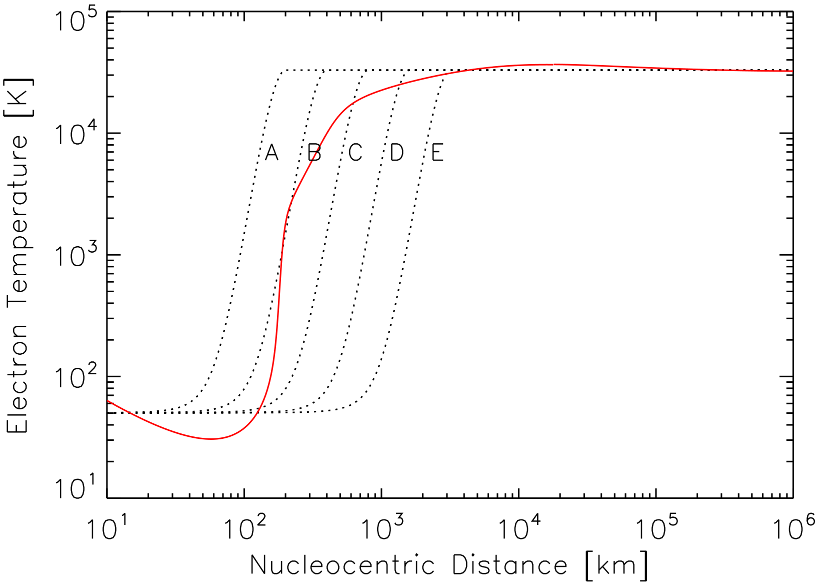

Figure 27: The electron temperature as a function of nucleocentric distance for comet 9P/Tempel 1 (red curve) as obtained with the described full model. The dotted curves give five different artificial electron temperature profiles used for testing reasons, labeled A to E. See text for more details.

Fig. 27 shows the electron temperature obtained with the full model computation for comet 9P/Tempel 1, together with five artificial electron temperature profiles used for the computation of the C_3 and C_2 column densities. Between two artificial electron temperature profiles, r_0 changes by a factor of two. The corresponding column densities are shown in Fig. 28. It can be seen that the C_2 column density profiles react slightly more sensitive to a change in the electron temperature profiles, but for comet 9P/Tempel 1, a change in the onset distance of the electron impact reactions by in total a factor of 16 has a negligible effect.

The corresponding plots of the electron temperature profiles and the C_3 and C_2 column density profiles for comet C/2001 Q4 are shown in Fig. 29 and 30. As can be seen in Fig. 29, the higher water production rate of this comet results in an increase of the electron temperatures at larger nucleocentric distances compared to comet 9P/Tempel 1. For comet C/2001 Q4 the effect of varying the electron temperature is larger compared to comet 9P/Tempel 1. Changes at small nucleocentric distances (profile A in Fig. 29) results in a significant change in the C_2 column density profiles, as can be seen in Fig. 30. However, a change in the onset distance of the electron impact reactions by up to a factor of 8 has a negligible effect.

Instead of the parametrisation of the inelastic electron-water scattering according to Cravens and Korosmezey (1986), the model of Schmidt *et al.* (1988) uses a parametrisation

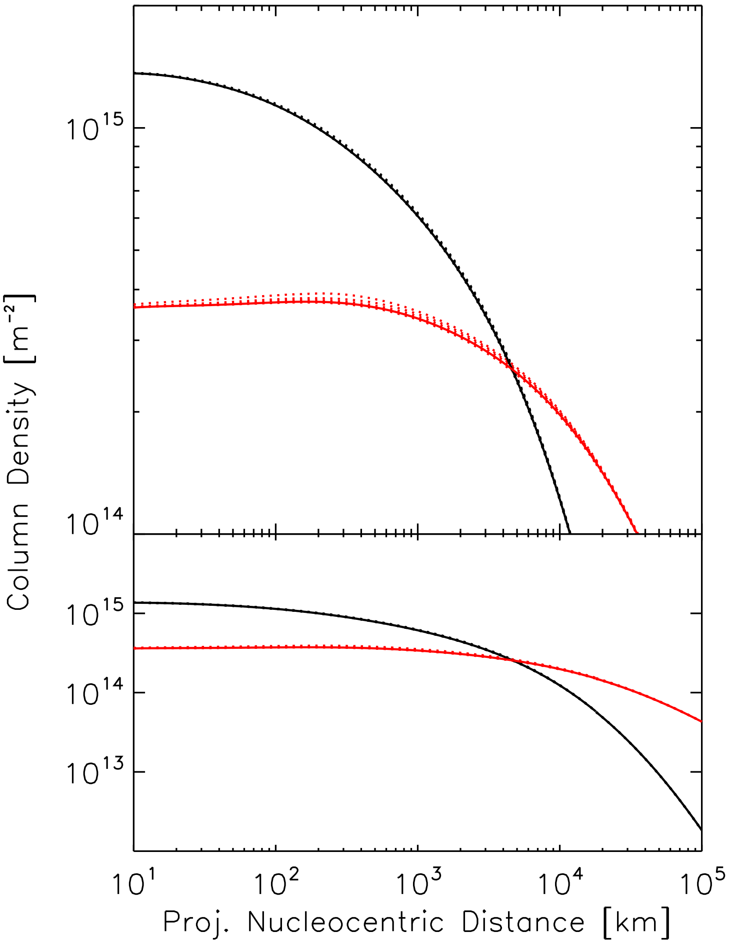

Figure 28: Radial column density profiles for C_3 (black curves) and C_2 (red curves) for comet 9P/Tempel 1. The upper panel presents a detail of the lower panel. The dotted curves show the column densities computed by using the five artificial electron temperature profiles from Fig. 27. The solid lines show the results from the full model calculation.

according to Ashihara (1975) and Marconi and Mendis (1983). In the latter case the energy loss by rotational excitation of water is given by:

$$G_{rot} \approx 1.9 \cdot 10^{-20} \left(\frac{T_e - T_n}{T_e^{3/2}} \right) \left[\ln \left(0.58 \frac{T_e^2}{T_n} \right) + 0.79 \right] n_e \, n_{\mathrm{H_2O}} \quad \left[\mathrm{erg\ cm^{-3}\ s^{-1}} \right] , \qquad (137)$$

and the vibrational/electronic term is given by

$$G_{vib} \approx 1.1 \cdot 10^{-20} \, (k_B T_e)^{1/2} \, n_e \, n_{\mathrm{H_2O}} \, e^{P(\chi)} \quad \left[\mathrm{erg\ cm^{-3}\ s^{-1}} \right] . \qquad (138)$$

In this equation, $P(\chi)$ is

$$P = -3.597 + 1.305\chi + 0.5917\chi^2 + 0.1213\chi^3 - 0.0359\chi^4 , \qquad (139)$$

and $\chi = \ln(k_B T_e)$, where $k_B T_e$ has to be inserted in eV. The expressions (137) and (138) lead to similar electron temperatures as for the approach by Cravens and Korosmezey

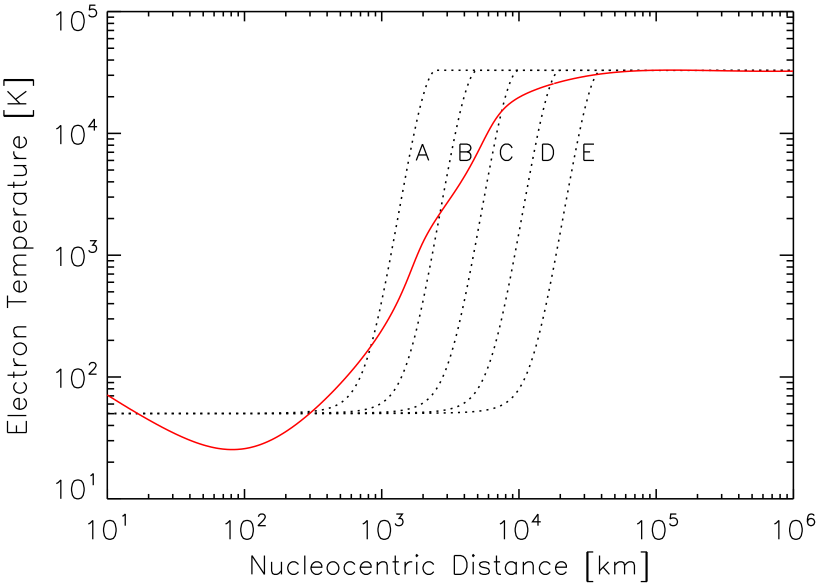

Figure 29: The electron temperature as a function of nucleocentric distance for comet C/2001 Q4 (red curve). The dotted curves give five different artificial electron temperature profiles used for testing reasons, labeled with A to E. See text for more details.

(1986) at small and large nucleocentric distances, and also the position of the increase of electron temperatures remains the same. Nevertheless, equations (137) and (138) result in a steeper increase of T_e. This is shown in Fig. 31 for the case of comet 9P/Tempel 1. The change in the increase of the electron temperatures results in virtually no change in the column densities obtained with the two assumptions.

9.4 Influence of the Gas Expansion Velocity upon the Column Density Profiles

Due to the negligence of the superthermal species, the gas expansion velocities are overestimated at large nucleocentric distances. In order to estimate the influence of the gas expansion velocities upon the computed C_3 and C_2 column density profiles, artificial variations of the gas velocity were applied. As test cases, a constant gas expansion velocity of 1 km s^{-1} and an artificial upper limit of 1.5 km s^{-1} were used. The former is usually used in the Haser model, and computations with models including energy loss due to superthermal species (Schmidt *et al.*, 1988; Rodgers and Charnley, 2002) imply a stabilisation of the gas velocity at about 1.5 km s^{-1}. The column densities obtained with these constraints are displayed in Fig. 32. The computations were performed for comet 9P/Tempel 1 at a heliocentric distance of 1.51 AU. It can be seen that a constant gas velocity significantly changes the shape of the radial column density profiles at all projected nucleocentric distances, compared to the output from the full model. Limiting the gas

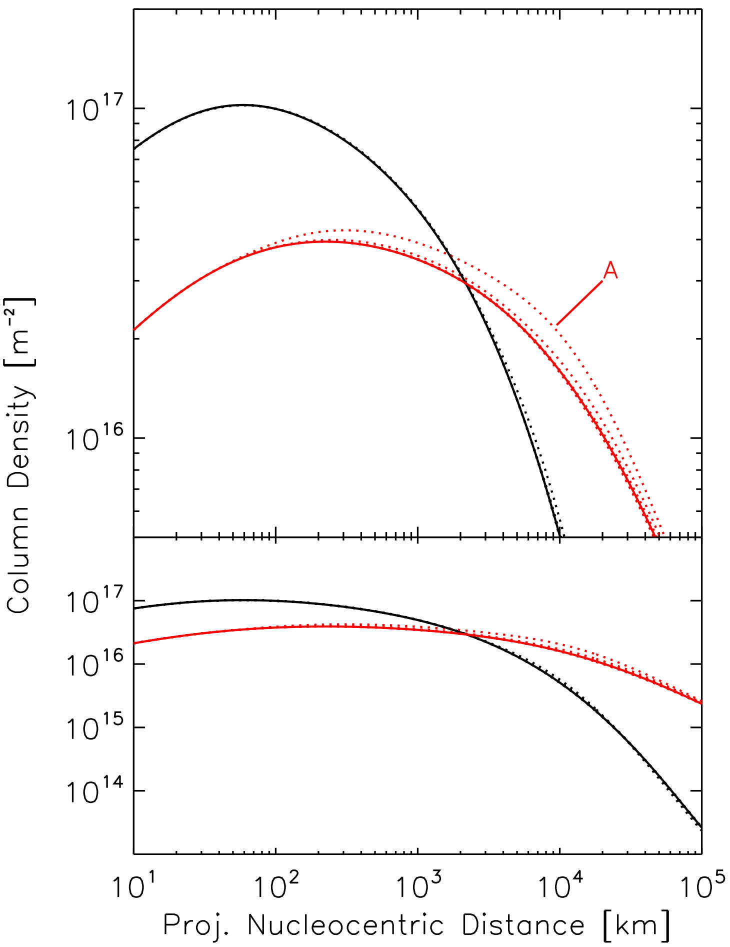

Figure 30: Radial column density profiles for C_3 (black curves) and C_2 (red curves) for comet C/2001 Q4. The upper panel presents a detail of the lower panel. The dotted curves show the column densities computed by using the corresponding artificial electron temperature profiles from Fig. 29. The solid lines show the results from the full model calculation, the dotted line marked with A was computed with the electron temperature profile A in Fig. 29.

expansion velocity to 1.5 km s^{-1} leads to smaller deviations from the full model output. In general, the C_3 column densities are less affected by changes in the gas velocity. While the influence upon the C_3 column densities is negligible, an uncertainty of about a factor of two in the C_2 column densities at large nucleocentric distances remains.

Because of the negligence of superthermal species taking away energy from the neutral fluid in the coma, the gas velocity is overestimated in this work. As a consequnce, the computed column densities can be expected to decrease steeper compared to a model taking the superthermal species into account. The observed flater decrease of the C_3 and C_2 column density profiles compared to the observations reported in chapter 7 are therefore unlikely to be caused by an improper treatment of the gas expansion velocity in the model.

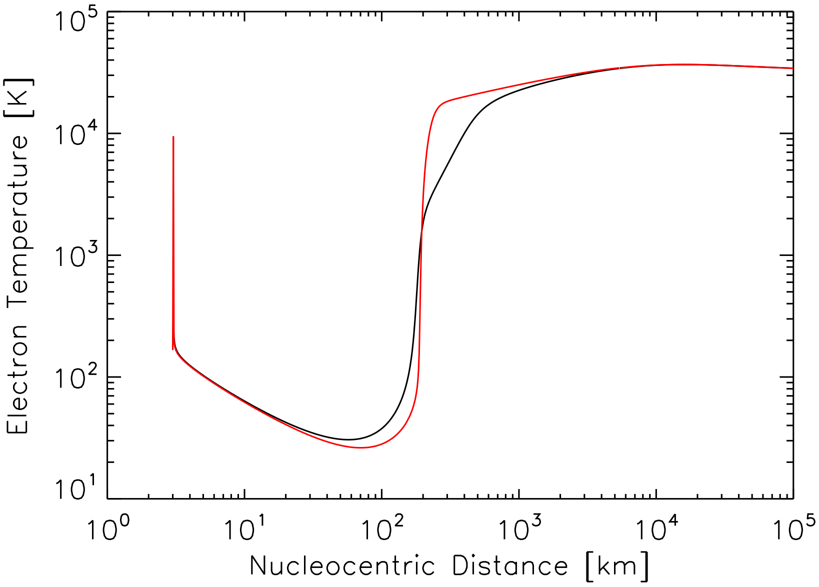

Figure 31: Electron temperatures for comet 9P/Tempel 1, computed with the approaches of Cravens and Korosmezey (1986) (black line) and of Ashihara (1975) and Marconi and Mendis (1983) (red line).

9.5 Influence of the Nucleus Size

The nucleus size is an input parameter of the model that is only poorly constrained for the majority of long-period comets. The assumed nucleus radius, R_N, of comet C/2001 Q4 NEAT of 2.5 km to 5 km is an estimate based on the observed activity, while the nucleus size of comet C/2002 T7 LINEAR of 44.2 km is strictly speaking only an upper limit, and the true radius might be significantly smaller. In order to estimate the influence of the nucleus radius upon the computed C_3 and C_2 column density profiles, a comparison between the results obtained for comet C/2002 T7 with $R_N = 44.2$ km and $R_N = 4.42$ km is displayed in Fig. 33. The water production rate was kept fixed for the two computations. The column densities are only affected at small projected nucleocentric distances, while at distances above approximately 10^3 km, where the comparison with observations is done, the differences become negligible. Therefore, the determination of the production rates of the C_3 and C_2 parent species by using the model presented in this work is not sensitive to the assumed comet nucleus size.

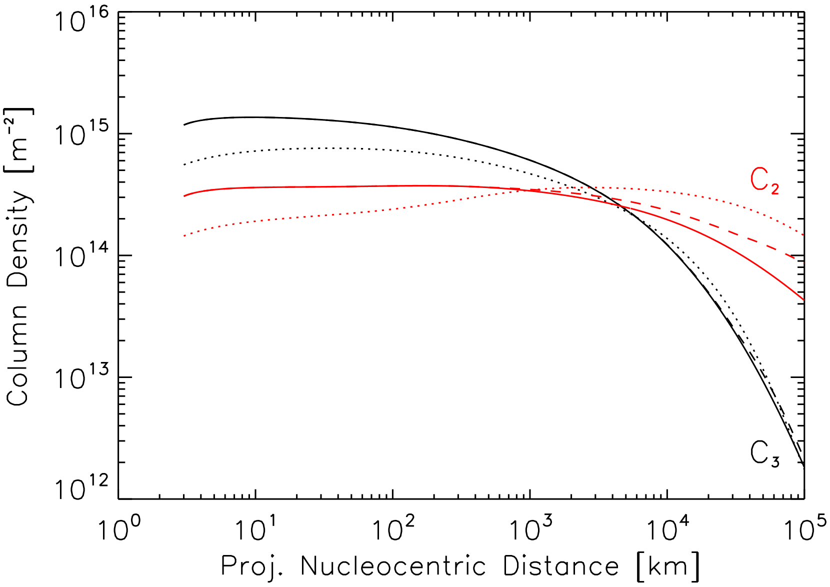

Figure 32: Column densities of C_3 and C_2 computed for comet 9P/Tempel 1 with different assumptions for the gas expansion velocity. Solid lines: output from the full model, dashed lines: gas velocity artificially restricted to 1.5 km s^{-1}, dotted lines: constant gas velocity of 1 km s^{-1}.

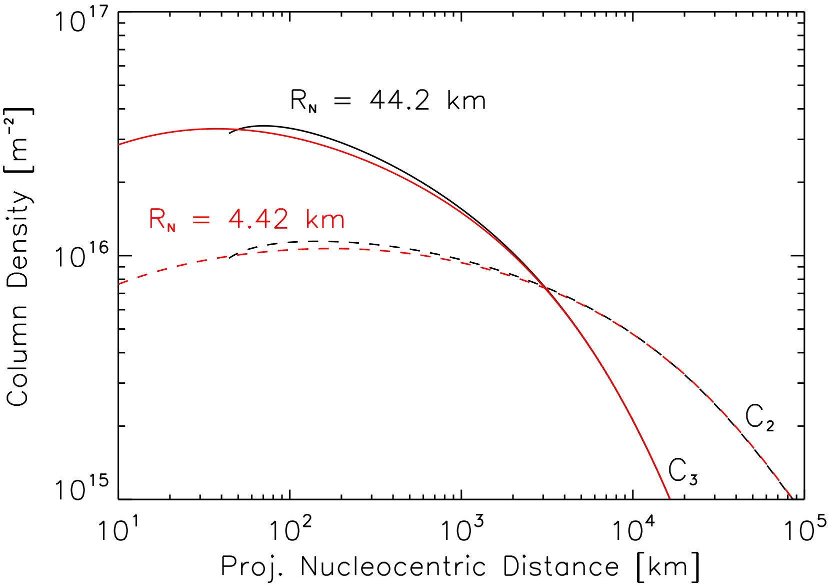

Figure 33: Comparison of the C_3 (solid lines) and C_2 (dashed lines) column density profiles of comet C/2002 T7 LINEAR, computed with different nuclear radii, R_N.

10 Applications of the Chemistry Model with Revised Reaction Network

In this chapter the chemistry model for cometary comae using the revised reaction network for the formation of the C_3 and C_2 radicals is applied to the observations of the comets C/2001 Q4, C/2002 T7, and 9P/Tempel 1.

10.1 Fitting of the C_3 Column Density Profiles

Fig. 34 shows the χ^2 values obtained for the best fitting C_3 column density profiles for various fixed ratios of the production rates of C_3H_4 and C_4H_2. The results are shown for fits to the column density profiles measured in the projected sunward and tailward directions independently.

For all three comets and for both the sunward and tailward sides from the nucleus it can be seen that the χ^2 is increased for high C_3H_4/C_4H_2 production rate ratios. C_3H_4 as the dominating parent species therefore provides no good fitting of the C_3 column density profiles. This suggests that C_3H_4 is not the sole parent of C_3 in the comae of the studied comets. For all three comets a clear minimum in χ^2 versus the C_3H_4/C_4H_2 production rate ratio can be seen, thus making it also unlikely that C_4H_2 is the sole parent species for C_3.

For the comets C/2001 Q4 and C/2002 T7, the positions of the minima of χ^2 for the sunward and tailward side are in good agreement, respectively. For comet 9P/Tempel 1, the position of the minima are not in agreement. This is likely caused by an uncertainty in the data calibration. The instrument FORS 2 used for the observation of comet 9P/Tempel 1 has two CCD chips (see chapter 3). The sunward profile is spread over both CCD chips, while the tailward profile is observed on only one chip. If a small bias between the two CCD chips was present, the position of the minimum would change. Fig. 35 shows the computed C_3 column density profiles best fitting the observations. As can be seen in this Figure, one chip seems indeed to provide slightly higher values than the other. The result obtained on the tailward side in the coma of comet 9P/Tempel 1 may provide a more reliable result.

The minimum in χ^2 obtained from fits to the tailward column density profile of comet 9P/Tempel 1 and for comet C/2001 Q4 occur at similar C_3H_4/C_4H_2 production rate ratios. The position of the minima in χ^2 for comet C/2002 T7 are at production rate ratios about one order of magnitude lower than for comet 9P/Tempel 1 and C/2001 Q4.

Fairly good fits could be obtained to the C_3 column density profiles measured in comet 9P/Tempel 1 and on the tailward side of the coma of comet C/2002 T7. Although still within the observational uncertainty, the fits to the remaining column density profiles are less good.

10.2 Fitting of the C_2 Column Density Profiles

Fig. 36 shows the χ^2 for the best fits to the measured C_2 column density profiles obtained with various fixed production rate ratios of C_2H_2 and HC_3N. With the only exception of the tailward column density profile of comet C/2001 Q4, all χ^2 values show the same tendency. They remain about constant for high production rate ratios, and then increase as the relative content of HC_3N increases. HC_3N is therefore unlikely to be the sole parent (beside the contribution of C_2 that is formed by the C_3 parent species) of C_2. The best fit to the measured C_2 column density profiles is obtained with only C_2H_2 as the C_2 parent. The only exception is the tailward column density profile of comet C/2001 Q4, where a mixure of C_2H_2 and HC_3N provides the best fit.

However, even the best fits to the observed C_2 column density profiles are not satisfying. Fig. 37 compares the computed best fits with the observations. While for comet C/2001 Q4 the fits are still within the observational uncertainties, for C/2002 T7 and 9P/Tempel 1 the observed column densities could not be reproduced.

10.3 Production Rates of the C_2 and C_3 Parent Species

The ratios of the production rates of C_3H_4 and C_4H_2 and C_2H_2 and HC_3N that produce the best fits to the observed column density profiles are summarized in Tab. 21. Since the simultaneous fit of the observed C_3 and C_2 column density profiles failed, these values are displayed only to demonstrate the deviation of production rates from the model output and to estimate their order of magnitude. The ratios of the production rates were derived from the results shown in Fig. 34 and 36. The χ^2 values obtained from the fits to the C_3 and C_2 profile were interpolated to a grid with a step size of 0.001. This interpolation was done by using a quadratic fit to a three-point neighborhood, $[\chi^2_{i-1}, \chi^2_i, \chi^2_{i+1}]$ surrounding each value χ^2_i determined from the fits. The minimum of the new array containing the interpolated χ^2 values was regarded as the best fit to the corresponding profile. The error was determined assuming that all changes in χ^2 larger than 10% of the minimum value are significant.

The production rate ratios with respect to water were determined in a similar way. The production rate ratios of the C_3 and C_2 parent species with respect to water obtained for the best fit with a fixed hydrocarbon production rate were interpolated to a grid with a small step size. A quadratic fit to a four-point neighbourhood of χ^2_i, $[\chi^2_{i-1}, \chi^2_i, \chi^2_{i+1}, \chi^2_{i+2}]$ was used in this case since a smoother interpolation could be obtained with this choice. Then, the production rate ratios with respect to water were determined for the overall best fit as well as for the uncertainties. This procedure is illustrated using C_3H_4 and C_4H_2 for the tailward C_3 column density profile of comet 9P/Tempel 1 as examples. Fig. 38 shows in the upper panel the interpolated χ^2 values as a function of the production rate ratio of C_3H_4 to C_4H_2 and in the lower panel the conversion into production rate ratios

Table 21: Summary of the derived production rate ratios of the C_3 and C_2 parent species.

Ratio		C/2001 Q4	C/2002 T7	9P/Tempel 1
$Q(C_3H_4)/Q(C_4H_2)$	sunwards	$18.6^{+10.7}_{-7.5}$	$2.3^{+1.9}_{-1.6}$	$56.1^{+10.8}_{-11.5}$
	tailwards	$21.8^{+4.6}_{-4.0}$	$1.9^{+1.1}_{-0.9}$	$25.5^{+11.8}_{-8.8}$
$Q(C_2H_2)/Q(HC_3N)$	sunwards	> 0.26	> 0.09	> 0.36
	tailwards	$0.085^{+0.085}_{-0.033}$	> 0.09	> 0.42

with respect to water.

Using the water production rates listed in Tab. 17 to 19, the ratios with respect to water were converted into production rates. Tab. 22 summarizes the derived mixing ratios with respect to water and the corresponding production rates of C_3H_4, C_4H_2, C_2H_2, and HC_3N.

10.4 Summary and Discussion

Using the described model of the chemistry in the cometary coma and the revised chemical reaction network, the radial emission profiles of C_3 could be reproduced. Especially the signature of the onset of electron impact reactions in the C_3 column density profiles reported in chapter 7 are avoided due to the lower electron impact reaction rates in the revised reaction network. The fitting of the C_3 column density profiles is possible by assuming two parent species of C_3. With C_3H_4 as the only parent species, no satisfying fit of the observed emission profiles of C_3 is possible. The abundances of C_4H_2 determined from the fitting are between about 0.14% and 0.25% of the water production rates. These values are somewhat higher than the preliminary abundance of C_4H_2 in the coma of comet Ikeya-Zhang of 0.05% with respect to water (Despois, 2005), but appear still reasonable.

For C_2, no satisfying simultaneous fit to the observed emission profiles was possible with the revised reaction network. In general, the computed C_2 column densities decrease slower with increasing projected nucleocentric distance than the observed ones. This could either be caused by an underestimated destruction rate of C_2, or by an underestimated formation rate.

The two main photochemical destruction reactions for C_2 included in the reaction network are

$$\mathrm{C_2} + \gamma \rightarrow \mathrm{C} + \mathrm{C} \tag{140}$$

$$\mathrm{C_2} + \gamma \rightarrow C_2^+ + e^- \; . \tag{141}$$

Furthermore, C_2 is destroyed by the electron impact reactions

$$\mathrm{C_2} + \mathrm{e^-} \rightarrow \mathrm{C} + \mathrm{C} + \mathrm{e^-} \tag{142}$$

$$\mathrm{C_2} + \mathrm{e^-} \rightarrow \mathrm{C_2^+} + \mathrm{e^-} + \mathrm{e^-} \; . \tag{143}$$

Table 22: Overview of the production rates derived from the fitting of the C_3 and C_2 emission profiles. The column labeled with M lists the production rate ratios with respect to water, the column labeled with Q shows the corresponding production rates.

Species		M [%]	Q [s^{-1}]
C/2001 Q4			
C_3H_4	sunwards	$3.56^{+0.74}_{-0.81}$	$(6.76^{+1.41}_{-1.54}) \cdot 10^{27}$
	tailwards	$3.51^{+0.18}_{-0.23}$	$(6.67^{+0.34}_{-0.44}) \cdot 10^{27}$
C_4H_2	sunwards	$0.192^{+0.056}_{-0.045}$	$(3.65^{+1.06}_{-0.86}) \cdot 10^{26}$
	tailwards	$0.161^{+0.024}_{-0.020}$	$(3.06^{+0.46}_{-0.38}) \cdot 10^{26}$
C_2H_2	sunwards	0.85	$1.62 \cdot 10^{27}$
	tailwards	$0.66^{+0.15}_{-0.11}$	$(1.25^{+0.29}_{-0.21}) \cdot 10^{27}$
HC_3N	sunwards	< 2.6	$< 4.9 \cdot 10^{27}$
	tailwards	$7.7^{+2.9}_{-3.0}$	$(1.46^{+0.55}_{-0.57}) \cdot 10^{28}$
C/2002 T7			
C_3H_4	sunwards	$0.56^{+0.40}_{-0.37}$	$(3.86^{+2.76}_{-2.55}) \cdot 10^{26}$
	tailwards	$0.45^{+0.22}_{-0.20}$	$(3.11^{+1.52}_{-1.38}) \cdot 10^{26}$
C_4H_2	sunwards	$0.248^{+0.018}_{-0.018}$	$(1.71^{+0.12}_{-0.12}) \cdot 10^{26}$
	tailwards	$0.242^{+0.008}_{-0.013}$	$(1.67^{+0.06}_{-0.09}) \cdot 10^{26}$
C_2H_2	sunwards	0.64	$4.42 \cdot 10^{27}$
	tailwards	0.56	$3.86 \cdot 10^{27}$
HC_3N	sunwards	< 4.0	$< 2.8 \cdot 10^{27}$
	tailwards	< 4.4	$< 3.0 \cdot 10^{27}$
9P/Tempel 1			
C_3H_4	sunwards	$8.19^{+0.98}_{-1.23}$	$(2.78^{+0.33}_{-0.42}) \cdot 10^{26}$
	tailwards	$3.52^{+1.07}_{-1.09}$	$(1.20^{+0.36}_{-0.37}) \cdot 10^{26}$
C_4H_2	sunwards	$0.146^{+0.010}_{-0.009}$	$(4.96^{+0.34}_{-0.31}) \cdot 10^{24}$
	tailwards	$0.138^{+0.008}_{-0.015}$	$(4.69^{+0.27}_{-0.51}) \cdot 10^{24}$
C_2H_2	sunwards	1.13	$3.84 \cdot 10^{25}$
	tailwards	1.07	$3.64 \cdot 10^{25}$
HC_3N	sunwards	< 2.8	$< 9.5 \cdot 10^{25}$
	tailwards	< 2.4	$< 8.2 \cdot 10^{25}$

For both photoreactions, Woodall *et al.* (2006) gives uncertainties in the reaction rate coefficients of a factor two (for the interstellar radiation field). However, even an increase of the reaction rate coefficients by a factor of 100 is not sufficient to destroy C_2 fast enough to obtain a satisfying fit to the observed C_2 column density profiles, which is far beyond the uncertainty of the photoreaction rates. Since electron impact reactions are unlikely to be effective at large nucleocentric distances due to the low number densities, a faster formation of C_2 than assumed in the reaction network is the more likely explanation for the disagreement. Since the photodissociation rates for C_4H_2 and the corresponding decay products are very uncertain and in parts only estimated in this work, this possibility cannot not be ruled out. As discussed in chapter 8, C_4H_2 is very effective in producing C_2. If this species is indeed an important parent species of C_2, the photodissociation towards C_3 has to be much more effective than towards the formation of C_2 by breaking of the central C−C bound. C_3H_2O would be a more promising parent species for C_3 since it is expected to be less efficient in producing C_2 than C_4H_2. Unfortunately, for C_3H_2O no photodissociation rate coefficients are available. For a more detailed study of the formation of C_2 and C_3 in the cometary coma, more information on the photochemical reactions involved would be required. Due to the large number of poorly constrained parameters, from observations of the column density profiles alone it is not possible to constrain both, the reaction rates leading to the formation of C_3 and C_2 and the roles of the different potential parent species.

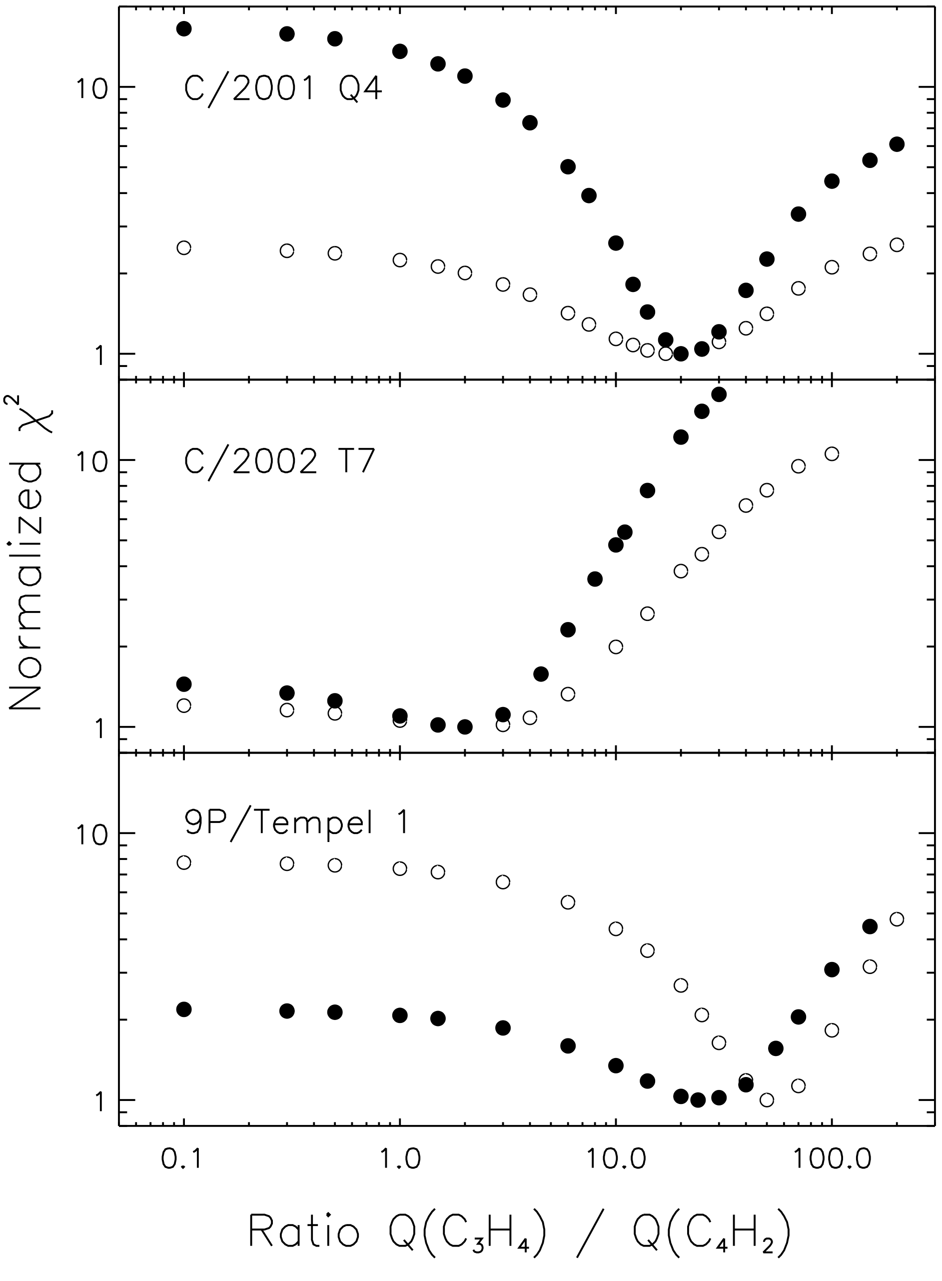

Figure 34: χ^2 of the best fits to the observed C_3 column density profiles for different ratios of the production rates, Q of C_3H_4 and C_4H_2. The shown values of χ^2 are normalized to the minimum value. Open symbols correspond to results from the fitting of the column density profiles in the projected sunward direction, filled symbols to those from the projected tailward direction.

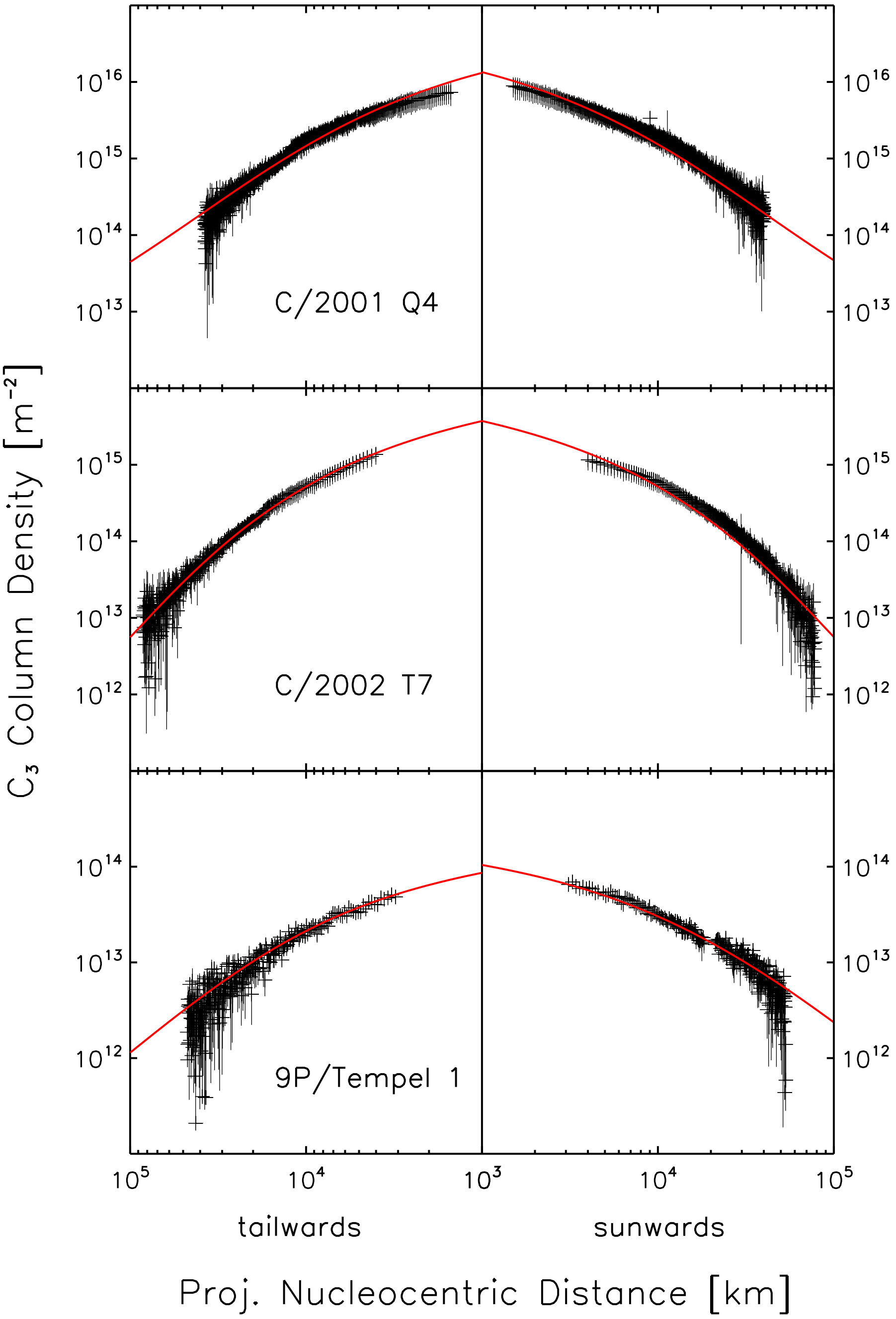

Figure 35: Best fits to the measured C_3 column density profiles in the tailward and sunward direction for comet C/2001 Q4, C/2002 T7, and 9P/Tempel 1. The gap within the measured sunward column density profile of comet 9P/Tempel 1 results from a gap between two individual CCD chips in the instrument used for observations. The part of the column density profile to the right of the gap seems to be slightly enhanced compared to that to the left with the other CCD chip.

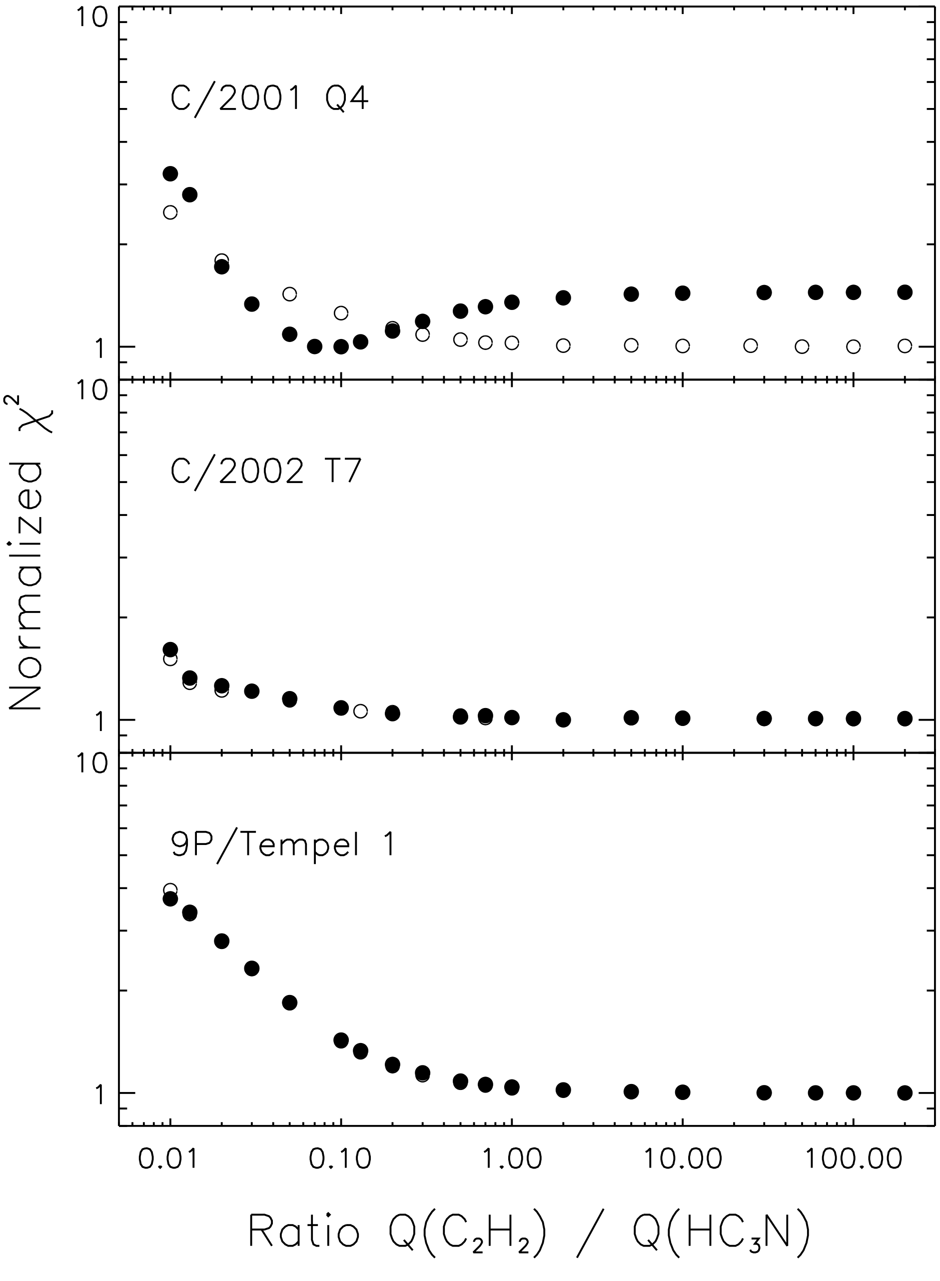

Figure 36: χ^2 of the best fits to the observed C_2 column density profiles for different ratios of the production rates, Q of C_2H_2 and HC_3N. The shown values of χ^2 are normalized to the minimum value. Open symbols correspond to results from the fitting of the column density profiles in the projected sunward direction, filled symbols to those from the projected tailward direction.

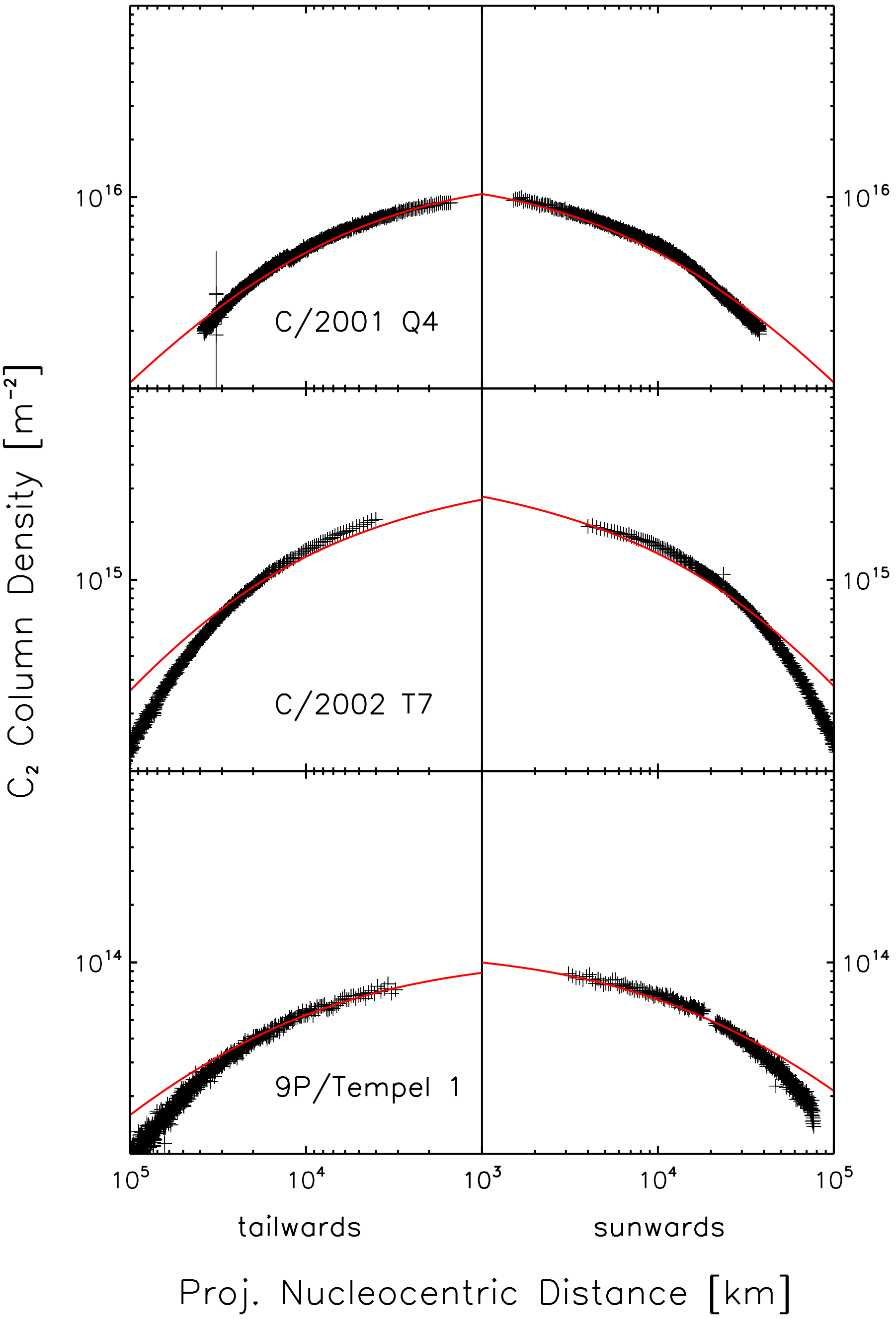

Figure 37: Best fits to the measured C_2 column density profiles in the tailward and sunward direction for comet C/2001 Q4, C/2002 T7, and 9P/Tempel 1.

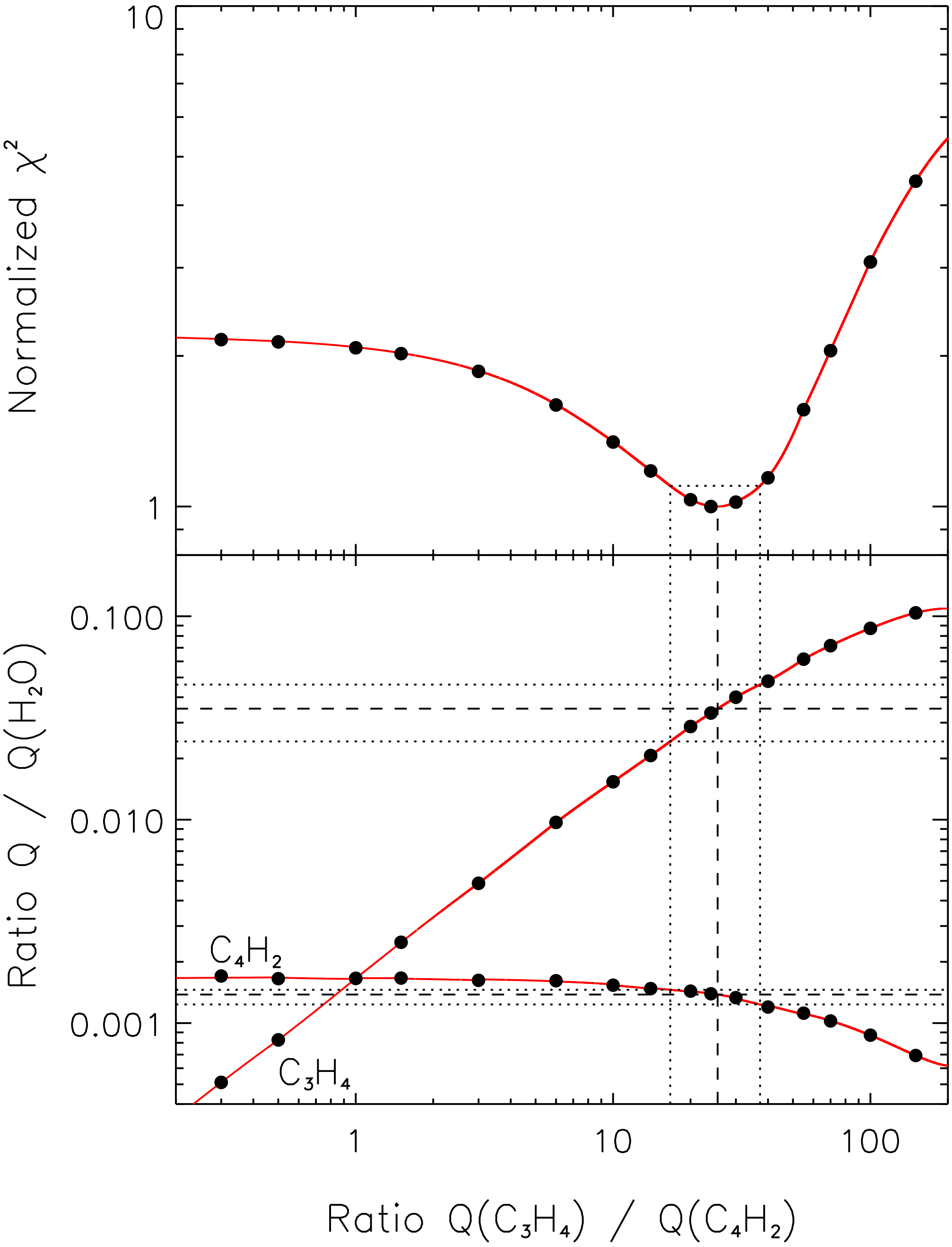

Figure 38: **Upper panel:** *Normalized* χ^2 *as a function of the production rate ratio of* C_3H_4 *to* C_4H_2*. The minimum* χ^2 *value is indicated by a dashed line, while the uncertainties are indicated by dotted lines.* **Lower panel:** *The ratio of the production rates of* C_3H_4 *and* C_4H_2 *with respect to the production rate of water, plotted versus the production rate ratio* $Q(C_3H_4)$ *to* $Q(C_4H_2)$*. The abundances of the hydrocarbons with respect to water for the best fit are indicated by dashed lines, the corresponding uncertainties are indicated by dotted lines.*

11 Comet of Special Interest: 67P/Churyumov-Gerasimenko

The results presented in this chapter were published in:
Weiler, M., Rauer, H., Helbert, J., 2004, *Optical observations of Comet 67P/Churyumov-Gerasimenko*, Astronomy and Astrophysics, 414, 749–755,
and
Weiler, M., Knollenberg, J., Rauer, H., 2004, *The dust activity of Comet 67P/Churyumov-Gerasimenko*, Astrophysis and Space Science Library, 311, 37–46. The contribution from the Astrophysics and Space Science Library is reproduced here with kind permission of Springer Science and Business Media.

11.1 Introduction

The mission Rosetta by the European Space Agency was originally intended to visit the Jupiter family comet 46P/Wirtanen. However, after a launch delay due to problems with the launch vehicle, the Ariane 5G rocket, the start window to comet Wirtanen was missed. The Jupiter family comet 67P/Churyumov-Gerasimenko (hereafter 67P/C-G) is the new target for the Rosetta space mission, that was finally launched on March 2, 2004. The Rosetta spacecraft will reach its new target in 2014. Since the knowledge about the properties and the long-term behavior of this new target comet is poor, detailed studies of comet 67P/C-G are required as mission support.

Comet 67P/C-G has an orbital period of approximately 6.6 years. Due to the geometrical orientation of the Earth, the Sun, and 67P/C-G, the observing conditions are good only every second perihelion passage, otherwise the solar elongation of the comet during perihelion passage is too small. Production rates available in the literature (e.g. Lowell Observatory Cometary Database (LOCD), described by A'Hearn *et al.* (1995); Cochran *et al.* (1992)) for OH, CN, C_3, C_2 and NH were derived from observations during the 1982 apparition. Based on observations made in 1982, comet 67P/C-G was found by Osip *et al.* (1992) and A'Hearn *et al.* (1995) to be depleted in C_2.

In this work, long-slit spectra taken during the 1996 perihelion passage of 67P/C-G are used to determine both the CN production rate and an upper limit for the C_3 production rate. The continuum of scattered sunlight in the long-slit spectra is used to study the dust production and the dust colour. Furthermore, broadband filter images obtained in March 2003 with the 2-m telescope of the Thüringer Landessternwarte (TLS) in Tautenburg (Germany) reveal a dust anti-tail and were used to study the presence of coma structures.

The question addressed by this study is whether the development of activity of comet 67P/C-G is similar between different perihelion passages, or if changes occur. The study of coma structures gives hints on the structure of the nucleus surface, such as the presence of active surface areas and their location with respect to the orientation of the nucleus rotation axis. Such information is required to characterize the environment the Rosetta spacecraft will be exposed to.

11.2 Study of the Gas Coma

The long-slit spectra obtained on February 10/11, 1996, (see Tab. 4) were used to determine the production rate of CN from the observed emission of the violet band at 3880 Å using a Haser model (see chaper 4.7). Fig. 39 shows a spectrum of comet 67P/C-G after continuum subtraction. To increase the signal to noise ratio the spectrum shown is averaged from 3766 km to 7531 km projected nucleocentric distance on the tailward side of the nucleus. The C_3 emission at 4050 Å could not be clearly detected. Therefore, only an upper limit for the C_3 production rate is derived.

The Haser scale lengths for CN from Fink *et al.* (1991) are used and a gas velocity of 1 km s^{-1} is assumed. The g-factor to be applied for the comet at the time of observations, having a radial component of the heliocentric velocity of 4.5 km s^{-1}, is derived based on the values given by Schleicher (1983). For C_3, the scale lengths and the g-factor from A'Hearn *et al.* (1995) are applied.

For the determination of the production rates, all three spectra obtained on February 10/11, 1996 were added, leading to an effective exposure time of 50 minutes.

A CN production rate of $(1.35 \pm 0.35) \cdot 10^{25}$ s^{-1} was computed from the spectra, averaged over the sunward and the tailward side of the nucleus. The use of scale lengths from other authors (A'Hearn *et al.*, 1995; Cochran, 1985; Rauer *et al.*, 2003) leads to less good fits to the radial intensity profiles, but the effect on the production rates is less than 20%.

An upper limit for the C_3 production rate of 10^{25} s^{-1} was determined. The determination of the gas production rates of comet 67P/C-G was done in collaboration with Dr. Jörn Helbert.

The CN production rates from the 1982 perihelion passage of comet 67P/C-G are shown in Fig. 40 (taken from LOCD and Cochran *et al.* (1992)), together with the value presented in this work. A perihelion asymmetry in the CN activity can be seen in the data from the 1982 perihelion passage. Comparing the CN production rates from 1982 with the value from 1996 derived in this work, no significant change in activity occurred.

11.3 Study of the Dust Coma

11.3.1 Dust Colour

The colour of a cometary coma is defined by Jewitt and Meech (1986). It is given by the derivation of the reflectivity with respect to wavelength, while the reflectivity is the

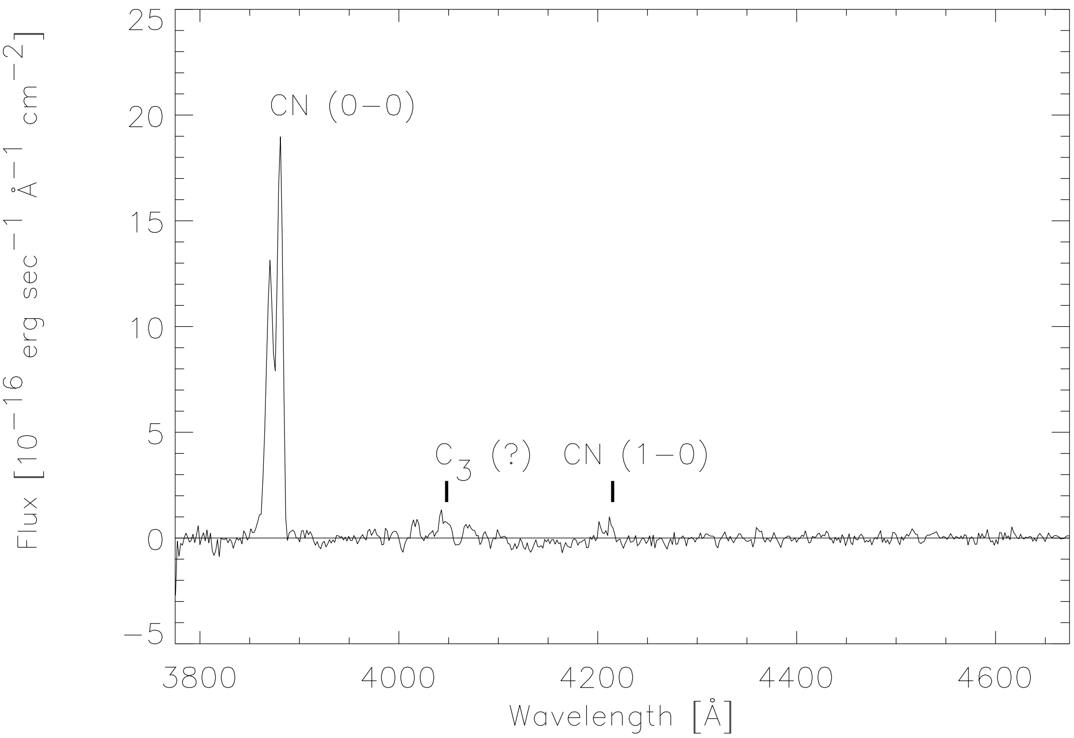

Figure 39: Spectrum of comet 67P/C-G, obtained on February 10, 1996 and averaged between 3766 km and 7531 km projected nucleocentric distance on the tailward side of the nucleus for better display. The continuum is subtracted.

ratio of the cometary flux and the solar flux as functions of wavelength. The dust colour was determined by a linear fit over the wavelength interval [4070 Å, 4600 Å] from the long-slit spectra taken in February 1996. Since a solar analogue star may show slight deviations from the solar spectrum, a comparison of the comet spectrum with a solar catalogue spectrum was done. The catalogue spectrum (Kurucz *et al.*, 1984) was reduced to the same resolution as the comet spectra. The flux calibrated cometary spectra were then divided by the solar spectrum to obtain the reflectivity. This was done for a mean spectrum of the cometary coma, obtained by adding the innermost 12 columns on both sides of the nucleus, corresponding to $\pm 1.1 \cdot 10^4$ km projected nucleocentric distance. By using the flux calibrated spectra before separation of the continuum and the gas emissions, additional errors due to continuum fitting were avoided. Within the wavelength interval employed, a weak CN emission and remnant of a night sky line were present. Nevertheless, a good linear fit to the reflectivity was possible on this wavelength range.

A mean colour of (-0.7 ± 5.1) %/10^3Å was determined over the interval [4070 Å,4600 Å].

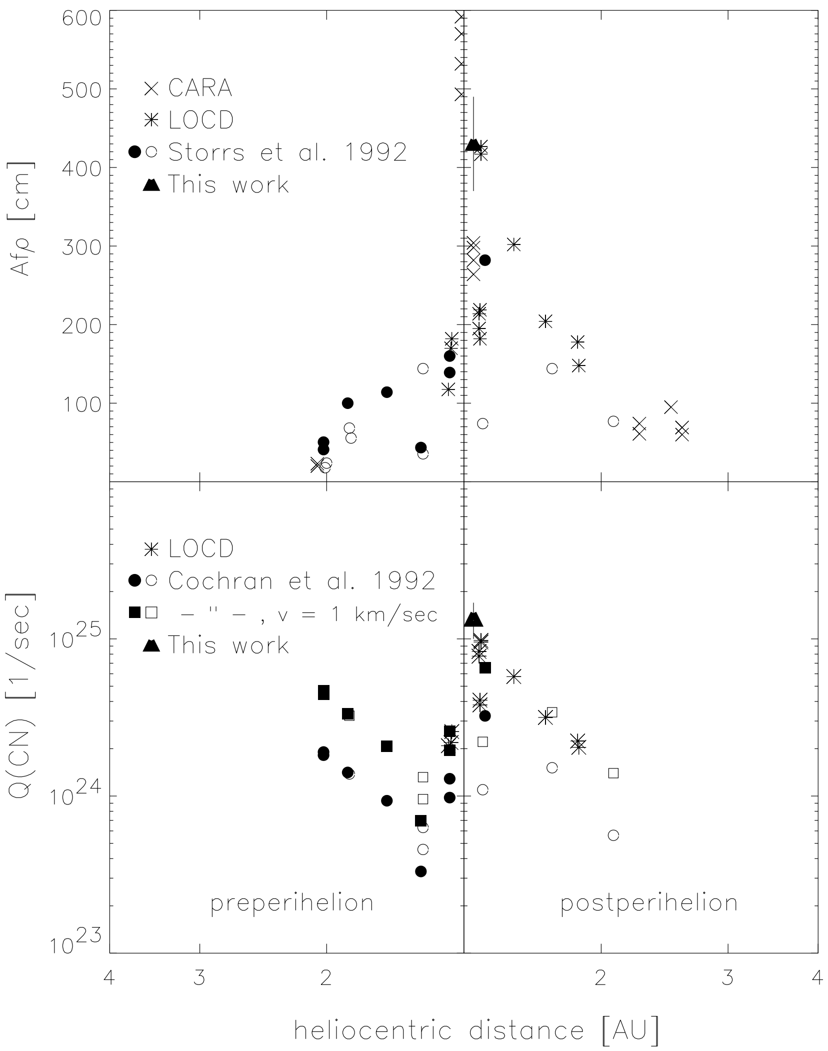

Figure 40: **Upper panel:** *Afρ values for comet 67P/C-G. The data from LOCD and Storrs* et al. *(1992) are from the 1982 perihelion passage. CARA marks values published in the Cometary Archive for Amateur Astronomer of the Italian Comet Section (Sezione Comete UIA). Note that all pre-perihelion values from CARA are from the 1996 apparition and all post-perihelion values from this reference are from the 2002 apparition. The triangle shows the Afρ-value from this work for the 1996 perihelion passage. The Afρ parameters are determined at a wavelength of 5240 Å by Storrs* et al. *(1992) from the flux through a continuum filter with transmission between 4770 Å and 4830 Å in the LOCD and at a wavelength of 4160 Å in this work. CARA values were obtained at various wavelengths, all lying within the red wavelength range.* **Lower panel:** *CN production rates,* Q(CN), *from the 1982 perihelion passage (LOCD, Cochran* et al. *(1992)) and for the 1996 perihelion passage (triangle). Open symbols in the data from Storrs* et al. *(1992) and Cochran* et al. *(1992) mark data from nights without photometric conditions. Squares give the CN production rates from Cochran* et al. *(1992), corrected to a constant gas velocity of 1 km s^{-1}, as used for the LOCD data.*

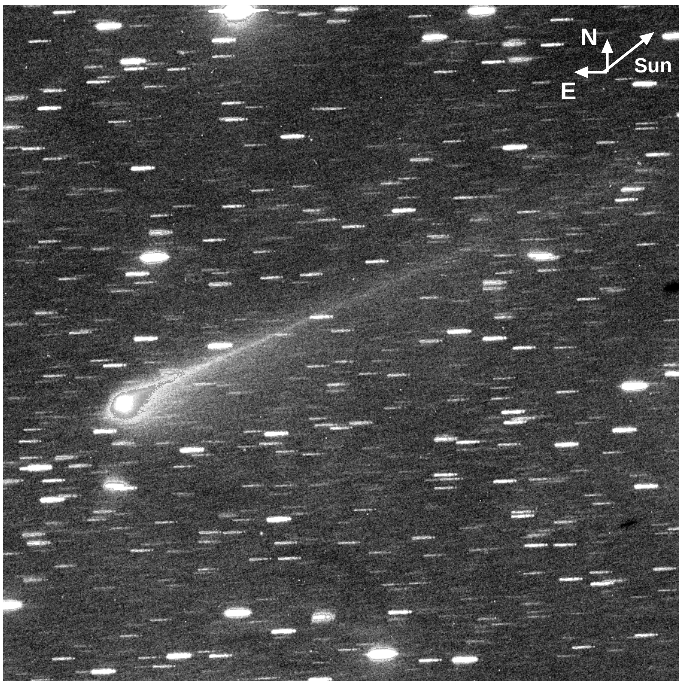

Figure 41: R-filter image of comet 67P/C-G, obtained on March 27, 2003 (see Tab. 5). The field of view is 16.8′ × 16.8′. The exposure time was 36 minutes and a non-linear brightness scale was applied to enhance the structure of the coma.

11.3.2 Dust Coma Morphology

Fig. 41 shows comet 67P/C-G on March 27, 2003. An asymmetric coma and an extended neck-line structure can be seen (Fulle *et al.*, 2004), since the Earth is very close to the comet's orbital plane (2.9° south of the orbital plane at the time). The neck-line can be detected over a length of approx. 10′, corresponding to $7.4 \cdot 10^5$ km projected nucleocentric distance. The spatial brightness distribution in the coma, originating from the scattering of sunlight, can be used to derive information on the dust ejection velocity and the size distribution of the dust particles. This is also true for the brightness distribution in the neck-line. Such an analysis was performed by Fulle *et al.* (2004) and can be used for the determination of the dust production rates.

In order to reveal structures in the dust coma of comet 67P/C-G, a mean radial intensity profile was subtracted from the comet images. To obtain the mean coma intensity profile, the comet image was transformed into polar coordinates with the optocenter as the center of the polar coordinate system. The mean profile obtained from averaging over all position angles was fitted and subtracted. Fig. 42 shows the mean intensity profile of the coma for the observation on March 27, 2003, together with a fit to the profile. The mean profile varies not according to i^{-1} as indicated by the dashed line, where i is distance from the optocenter in pixels. A i^{-1}−dependency would be expected in the case of an isotropic emission of dust with a constant velocity from the nucleus of a comet.

Fig. 43 shows the azimuthal deviation of the cometary coma intensity from the fitted mean intensity distribution for the observations on March 7, 27, 28 and 30. The profiles shown are averaged in radial direction from 4 to 8 pixels from the optocenter on March 7 and from 5 to 9 pixels for all other dates to cover a similar range of projected nucleocentric distances. These ranges of pixels correspond to projected nucleocentric distances of 6655 km to 13314 km, slightly varying on the different dates because of the changing geocentric distance between the times of observation. The position angle is measured from the North towards the East.

Fig. 43 clearly shows coma asymmetry which leads to lower intensities compared to the mean at small and high position angles and higher intensities at intermediate angles.

Two weak increased intensity features are marked as structure A and structure B in Fig. 43. These two structures appear in all of the analysed observations at approximately the same position angles. For this reason faint background stars can be ruled out as an explanation for these structures. An increased intensity in the coma at the position of structures A and B can also be detected in single 2-minute exposures. Thus, it is unlikely that the structures are artefacts from image processing, e.g. resulting from the shifting and the co-addition of the images.

As an example Fig. 44 shows the resulting images after subtraction of the mean coma intensity for the observations made on March 7 and in the evening of March 28. Structures A and B are marked by arrows.

The presence of coma structures could indicate the presence of surface areas with enhanced activity. A low active surface fraction has been regarded as an indication for localized active areas on the nucleus surface of 67P/C-G (Lamy *et al.*, 2003). However, since structure B is oriented 180° with respect to the extended neck-line, this structure could also be a part of the tail structure of comet 67P/C-G.

11.3.3 The Afρ Parameter

The Afρ parameter, as defined by A'Hearn *et al.* (1984), provides a measure for the dust within a certain aperture. If the aperture has the radius ρ in the plane of the comets nucleus (in units of length), and if $F_{comet}(\lambda)$ is the cometary flux within that aperture at a wavelength λ, and $F_{\odot}(\lambda)$ is the solar flux at the same wavelength, $Af\rho$ is given by

$$Af\rho = \frac{(2r_h\Delta)^2}{\rho}\frac{F_{comet}(\lambda)}{F_{\odot}(\lambda)} \; . \tag{144}$$

Here, r_h as to be inserted in AU, while Δ has to be specified in the same units as ρ. The $Af\rho$ parameter was determined from the long-slit spectra at the wavelength of 4160 Å. Near this wavelength no strong gaseous emissions are present in cometary spectra. To derive Afρ, it was assumed that the cometary coma was rotationally symmetric. The spatial intensity profile was extracted from the long-slit spectra. Then, the hypothetical

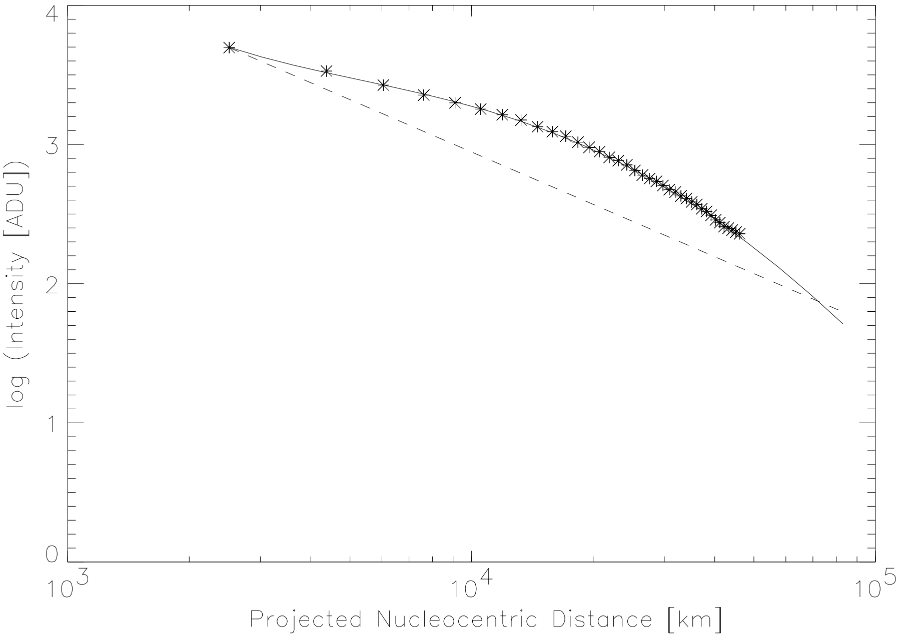

Figure 42: The mean radial intensity profile for the innermost pixels of the coma of comet 67P/C-G on March 27, 2003. The solid line is a fit to the profile used for coma subtraction. The dashed line indicates a dependency according to i^{-1}*, where i is the pixel number counted from the optocenter (for optocenter, i=0).*

flux through a diaphragm with a projected radius, ρ of $5 \cdot 10^4$ km was computed and used for the determination of Afρ. This was done for the sunward and the tailward side of the long-slit spectra independently to estimate the influence of the coma asymmetry.

A mean Afρ value of 428.2 cm was determined with a deviation of ±59.8 cm on the sunward and the tailward side of the slit due to coma asymmetries.

The Afρ parameter derived from long-slit spectra is rather high but of the same order of magnitude as Afρ determined at the 1982 perihelion passage by LOCD and Storrs *et al.* (1992) at similar heliocentric distances (see Fig. 40). Unfortunately, due to the lack of images in Feburary 1996 it cannot be ruled out that Afρ from the longslit spectra is influenced by a strongly asymmetric coma.

11.3.4 Dust Production Rates with a Test Particle Approach

When making the assumption of an isotropic emission of dust from a spherical nucleus, the observational parameter Afρ is related to the dust number production rate $\mathrm{Q_N}$ by (Jorda, 1995):

$$Q_N = \frac{\mathrm{Af}\rho}{2\pi^2 A_B(\lambda) D(\beta)} \left[\int_{a_1}^{a_2} \frac{f(a)a^2}{v(a)} \, \mathrm{d}a \right]^{-1} , \qquad (145)$$

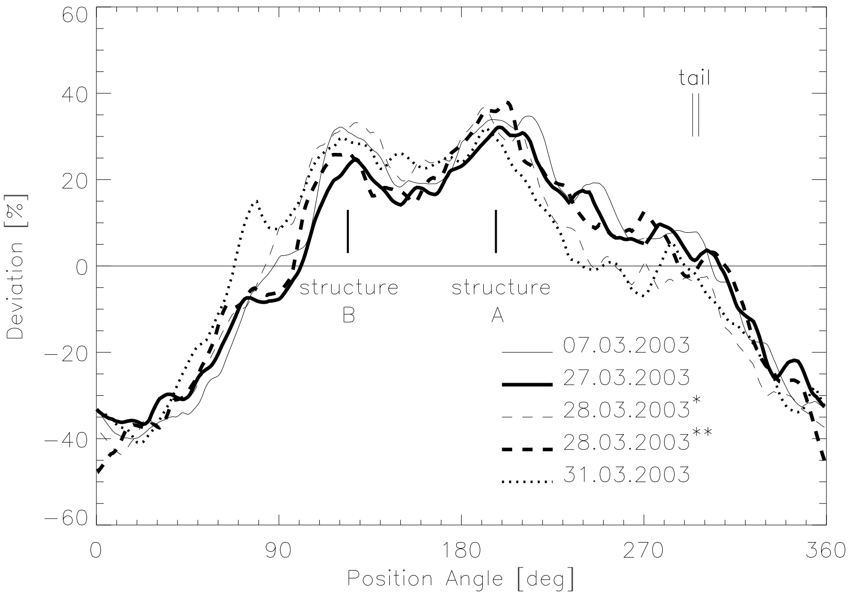

Figure 43: Deviation from the mean coma intensity profile for observations in March, 2003. The azimuthal profiles shown are averaged between about 6657 km and 13314 km projected nucleocentric distance. The feature at 75° *on March 31 is a star trace. The position angle is measured from the North towards the East, the tail position varies between the two lines during the observation period.* * *is the observation made in the morning,* ** *is the observation made in the evening of March 28, 2003.*

and the mass production rate Q_M is given by:

$$Q_M = Q_N \frac{4\pi}{3} \int_{a_1}^{a_2} \rho(a)\, a^3 f(a)\, \mathrm{d}a. \qquad (146)$$

Here a denotes the radius of the dust particles and A_B is their Bond-albedo, $\rho(a)$ denotes the density of a dust particle with radius a, $f(a)$ is the normalized size frequency distribution of the dust particles, $v(a)$ is the size-dependent dust velocity with respect to the cometary nucleus, and $D(\beta)$ denotes the phase function. The parameters a_1 and a_2 are the minimum and the maximum dust grain radii regarded.

The model described by Weiler *et al.* (2003) was used to determine the dust mass production rate. This model makes use of equation (146) and determines the maximum grain size that can be lifted off the nucleus surface, a_2, and the dust velocity $v(a)$ by solving the equation of motion of a test particle with radius a in a gas flow resulting from free sublimation of ice. This model has turned out to be able to provide a good explanation for the observed variation of Afρ with heliocentric distance compared to other models with a more simplified treatment of the maximum dust grain sizes and dust velocities (Weiler *et al.*, 2003).

In order to estimate the area of ice on the nucleus surface, as an approximation of the

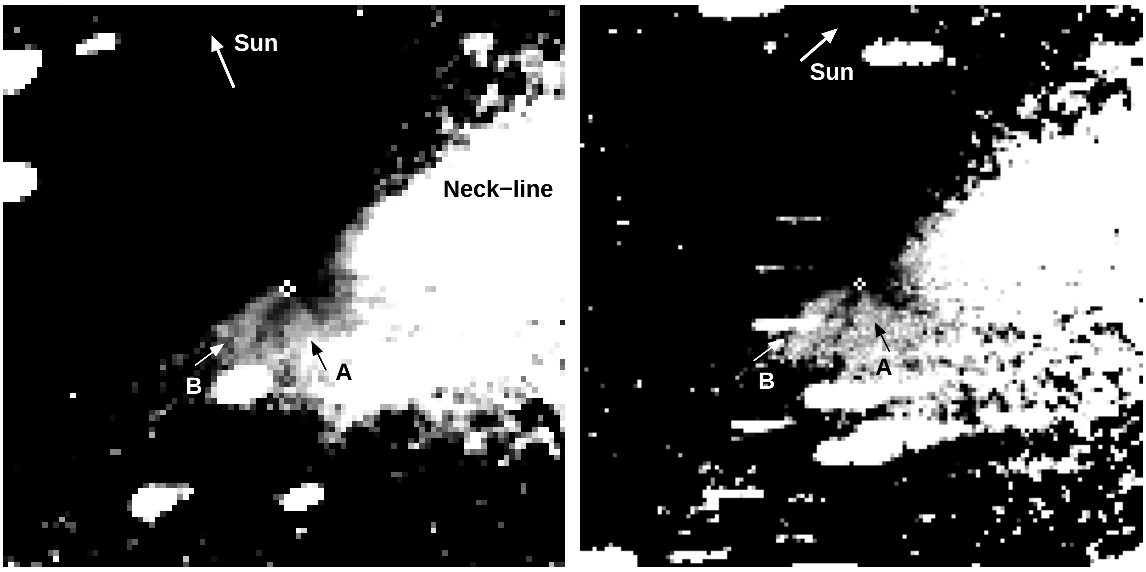

Figure 44: Coma of comet 67P/C-G on March 7, 2003 (left image) and on March 28, 2003, evening (right image) after subtraction of the mean coma intensity. The structures A and B (see Fig. 43) are marked. A non-linear grayscale between 10% and 60% deviation from the mean intensity profile has been applied. North is upwards, East is to the left. The projected direction of the Sun is marked. The images cover 2.6 ' × 2.6 ' corresponding to $1.66 \cdot 10^5$ km (left image) and $1.91 \cdot 10^5$ km (right image) projected width, respectively. The optocenter of the coma is located in the center of the images.

water production rate, the OH production rates published in the LOCD are used. With a nucleus radius of 2 km (Lamy *et al.*, 2003), an active surface fraction of 10% as the lower limit results. This value is assumed not to vary along the orbit. For the computation of a_2, a density of 1 g cm^{-3} for the nucleus was used for the computation. The dust density function according to Newburn and Spinrad (1985),

$$\rho(a) = \rho_0 - \rho_1 \cdot \frac{a}{a + \tilde{a}} , \tag{147}$$

with $\rho_0 = 3000$ kg m^{-3}, $\rho_1 = 2200$ kg m^{-3} and $\tilde{a} = 2$ μm, was applied. With these parameters one obtains a maximum radius of 9.5 cm for particles that can be lifted from the surface by the gas flow against the gravity at the maximum of activity on December 14, 1982, at 1.36 AU postperihelion. This maximum radius decreases to 0.8 cm at 1.5 AU postperihelion in March, 1983.

In order to determine the dust production rate, the "standard" values were used for the parameters needed. A dust size distribution according to Newburn and Spinrad (1985) was applied, having the form:

$$f(a) = \tilde{N} \left(1 - \frac{a_1}{a}\right)^M \left(\frac{a_1}{a}\right)^N . \tag{148}$$

This function has two exponents as free parameters, the first exponent M determines the position of the peak of the frequency distribution, whereas the second exponent, N,

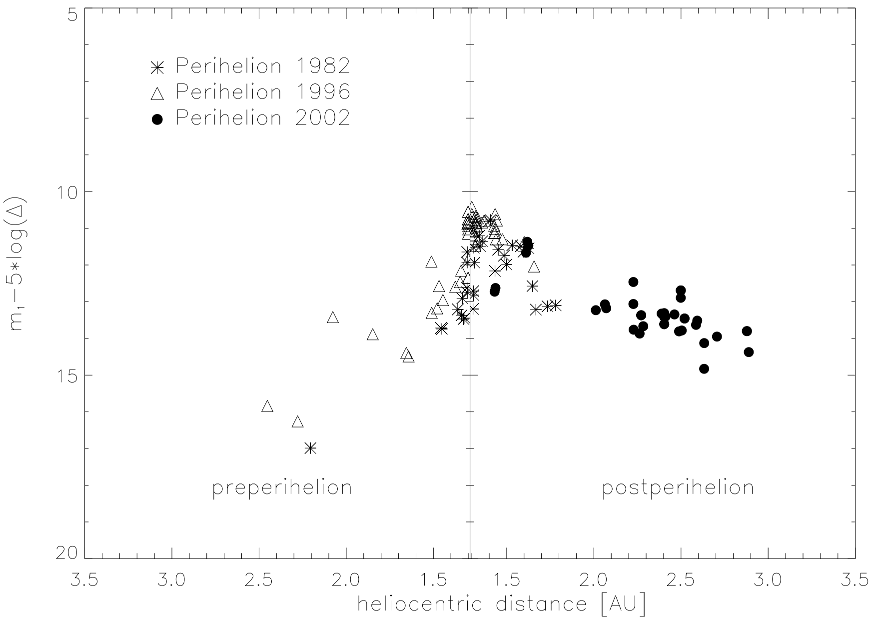

Figure 45: Estimated magnitudes, m_1*, of comet 67P/C-G for three perihelion passages. The magnitudes were taken from the ICQ/IAUC, the German and Italian Comet Section archive and are corrected for the changing geocentric distances,* Δ*.*

determines the decrease of frequency with increasing particle radius. $\tilde{N}$ is a normalization factor, chosen in such a way that the integral over $f(a)$ is unity. A peak in the size distribution at 0.4 μm and a decrease with an exponent of -3.5 is used for a first computation of the dust production rates, since these represent the "canonical" values for a comet. A value for N of 3.5 is also the maximum value determined for comet 67P/C-G from inverse coma modelling by Fulle *et al.* (2004). A Bond albedo of 0.2 and a phase function according to Divine (1981) are used. The Afρ values from the LOCD for which OH production rates are measured at the same time are used for computation of the dust production rates. Other species, like CO, are neglected here. A peak dust production rate of $2.08 \cdot 10^3$ kg s^{-1} in mid December 1982 is determined with those standard parameters at 1.36 AU postperihelion. The dust production decreases to 95 kg s^{-1} at 1.85 AU postperihelion in 1983. These values are higher than the dust production rates published previously. The maximum dust production rates are 220 kg s^{-1} in Hanner *et al.* (1985) or 170 kg s^{-1} in Krishna Swamy (1991) near the maximum of activity. The higher dust production rates in this work may be partly caused by the large value for the maximum grain size compared to other publications. Krishna Swamy (1991) assumes the maximum grain size to be only 100 μm.

The mean dust-to-water mass ratio derived from all data given by LOCD is 4.8. With the parameters used here, 67P/C-G is a very dusty comet.

11.3.5 Dust Velocities with Full Gas-Dust Interaction

In the case of a very high dust mass loading of the gas flow, it could also be important to take into account the influence of the dust upon the gas flow (e.g. by heat transfer), which was not done in the test particle approach. Therefore, an evaluation on the influence of the high dust mass loading on the dust velocities hence on the dust production rates is required before drawing conclusions from the determined dust productions rates. This evaluation is performed here.

In order to estimate the error caused by the treatment of dust grains as test particles when computing the dust velocities, the maximum value for the dust-to-gas mass ratio is assumed, and the dust velocity is computed again in a continuum approach, taking into account the reaction of the dust onto the gas flow. The set of equations to be solved is then (Knollenberg, 1993):

$$\frac{\partial}{\partial t}\mathbf{w} + \frac{1}{r^2}\frac{\partial\, r^2\mathbf{G}}{\partial r} = \mathbf{S}\ , \tag{149}$$

where

$$\mathbf{w} = \begin{pmatrix} \rho_{gas} \\ \rho_{gas}u_{gas} \\ \rho_{gas}\ e \\ \rho_1 \\ \rho_1 v_1 \\ \dots \\ \rho_n \\ \rho_n v_n \end{pmatrix}, \tag{150}$$

$$\mathbf{G} = \begin{pmatrix} \rho_{gas}u_{gas} \\ \rho_{gas}u_{gas}^2 + p_{gas} \\ u_{gas}(\rho_{gas}\ e + p_{gas}) \\ \rho_1 v_1 \\ \rho_1 v_1^2 \\ \dots \\ \rho_n v_n \\ \rho_n v_n^2 \end{pmatrix}, \tag{151}$$

$$\mathbf{S} = \begin{pmatrix} 0 \\ \frac{2}{r}p_{gas} - F_{gd} \\ -Q_{gd} \\ 0 \\ f_{gd,1} \\ \dots \\ 0 \\ f_{gd,n} \end{pmatrix}. \tag{152}$$

In these equations, u_{gas}, ρ_{gas}, and p_{gas} denote the gas velocity, density and pressure, respectively, and e is the total specific energy of the gas. The source terms F_{gd} and Q_{gd} are given by:

$$\begin{aligned} F_{gd} &= \sum_{i=1}^{n} \frac{1}{2} C_D \frac{\pi a^2}{m_{dust}} (u_{dust} - u_{gas})^2 \rho_{dust} \rho_{gas} = \sum_{i=1}^{n} f_{gd,i} && (153) \\ Q_{gd} &= 4 \frac{\pi a^2}{m_{dust}} |u_{dust} - u_{gas}| \rho_{dust} S_t \frac{\gamma}{\gamma - 1} \frac{k_B}{m_{gas}} \rho_{gas} (T_r - T_{dust}). && (154) \end{aligned}$$

C_D is the drag coefficient, S_t is the Stanton number, and T_r is the recovery temperature. These quantities are taken from Probstein (1969) and Kitamura (1986). In the set of equations (149), the first three rows are the continuity equation and the conservation of momentum and energy for the gas component. These equations become the equations (14), (15), and (16) (chapter 4) in the stationary case. The indices *1* to n mark the continuity equations for the mass and the momentum of dust particles in the size range i, where i runs from *1* to n, and n is the number of discrete intervals of the dust size range $[a_1, a_2]$. The equations of energy conservation for the dust particles are not considered here, since the temperature of the dust grains is assumed to be constant. The dust grain temperature values are determined using the scaling with heliocentric distance given by Divine (1981):

$$T_{dust} = 310\ K \cdot \left(\frac{r_h}{1\ AU} \right)^{-0.58}. \qquad (155)$$

The system of differential equations (149) was solved using a Godunov-type scheme of second order for the gas equations and an upwind scheme of second order for the dust equations. These routines were kindly provided by Dr. Jörg Knollenberg. The boundary conditions on the nucleus surface for the gas equations were determined as described by Weiler *et al.* (2003). Again, an active fraction of 10% for the nucleus of comet 67P/C-G is assumed. The dust velocity at the nucleus surface is zero and the dust density in the size interval, i, is computed by using the dust size-distribution and the dust-to-gas mass ratio. For the dust size-distribution, the function (148) is applied again.

In Fig. 46, the dust velocities computed with the test particle approach and the dust-gas interaction are shown for the maximum of activity in the LOCD data on December 14, 1982 at 1.36 AU heliocentric distance. The solid line shows the dust velocity computed with the dust density function (147) in the test particle approach. For comparison, the dashed line shows the dust velocities for a constant density of 1000 kg m^{-3}. The differences are caused by a density larger than 1000 kg m^{-3} for small particles and a lower density for larger particles. The dotted lines show the dust velocities determined by Fulle *et al.* (2004) at perihelion (upper line) and 50 days after perihelion (lower line) in 2002. The dates correspond to 1.29 AU and 1.47 AU heliocentric distance. These velocities follow a dependency of $v(a) \sim 1/\sqrt{a}$, where the proportionality factor was determined from inverse dust tail modelling. The dust velocities from this work are slightly higher than the velocities of Fulle *et al.* (2004), but they are computed for the maximum of activity. Keeping also in mind that the results of this work and Fulle *et al.* (2004) correspond to different perihelion passages, then the results from these two independent models are in fairly good agreement.

The crosses show velocities computed with the dust-gas interaction method, assuming not the mean dust to gass mass ratio of 4.8 but its maximum value of 8.5, and $N = 3.5$ and $M = 15.4$, corresponding to a peak in the dust size distribution at $a = 0.54$ μm (Hanner *et al.*, 1985). A dust temperature of 259 K was used. The deviation in velocity between the two methods is about 2.8%.

Assuming the dust size parameters to be $N = 4.0$ and $M = 17.6$, which leads to the same position of the peak in the size distribution, results in a dust-to-gas mass ratio of 0.89 in the test particle approach. The use of these parameters to compute the velocities in the continuum approach again results in dust velocities differing by less than 3% from the results of the test particle approach. This would suggest that the dust mass loading can be neglected for computation of the dust production rates of comet 67P/C-G. The parameters $N = 4.5$ and $M = 19.8$ lead to an even lower dust-to-gas mass ratio and also to a difference of less than 3%.

Therefore, even at dust mass loadings of the gas flow as high as 8.5, the influence of the dust upon the gas flow can be neglected. In the following, all computations of dust velocities needed for the determination of the dust production rates employ the test particle approach.

11.3.6 Dust Production Rates of Comet 67P/Churyumov-Gerasimenko

After determining the dust velocities, the dust production rates can be determined by using equations (145) and (146). Fulle *et al.* (2004) found that the dust size parameter N was close to 3.5 and constant from 150 days before perihelion in August 2002 to approximately 50 days after perihelion passage. Between 50 days and 150 days after the perihelion passage, N increases to approximately 4.5. Since the development of the activity of comet 67P/C-G with heliocentric distance seems to be very similar from one perihelion passage to another, we can estimate what effect different values of N would have, based on the data from LOCD, corresponding to the 1982 perihelion passage. Fig. 47 shows in the upper left panel, the dust mass production rates computed with $N = 3.5$, 4.0 and 4.5 and a peak of the size distribution function at 0.54 μm. The constant position of the peak causes the parameter M to be 15.4, 17.6 and 19.8. The corresponding number production rates, Q_N, are shown in the upper right panel. A higher value of N, meaning a steeper decrease of the frequency of large particles, causes higher number production rates. Because of the smaller frequency of large particles a higher number of particles in total is in this case required to obtain the observed scattering area of the cometary dust.

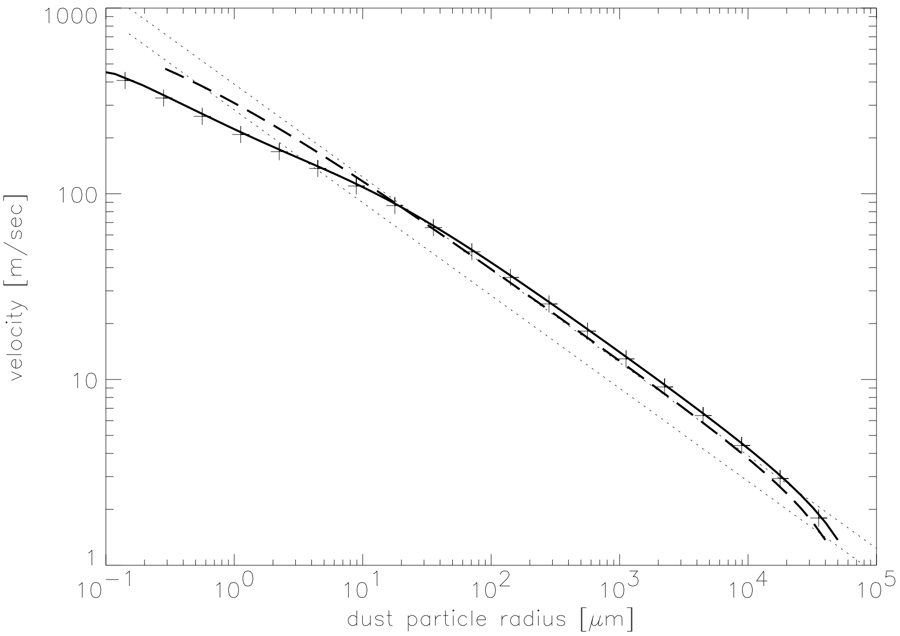

Figure 46: Cometocentric dust velocities as a function of the dust size. The solid line shows the velocities computed with the test particle approach and the dust particle density function according to Newburn & Spinrad (1985). The dashed line is valid for a constant density of 1000 kg m^{-3}*. For comparison, the dotted lines show the dust velocities at the 2002 perihelion (upper dotted line) and 50 days after perihelion (lower dotted line) according to Fulle et al. (2004). The crosses mark dust velocities computed in the continuum approach assuming the dust-to-gas mass ratio to be 8.5 and the dust size parameters to be* $N = 3.5$ *and* $M = 17.6$*, and the density according to equation (147).*

If a strong increase of the parameter N as derived by Fulle *et al.* (2004) from observations in 2003 had also occured in the 1982 apparition of comet 67P/C-G, the dust production rates would have dropped by about one order of magnitude compared to the case of a constant N close to 3.5.

Fig. 47 shows in the lower left panel, the dust-to-gas mass ratios determined by using the different parameters. With $N = 3.5$, the dust-to-gas mass ratio increased during the maximum activity of the comet after perihelion and is close to 4 during the other observations. This increase is associated with a strong increase in the maximum radius of grains which can be lifted from the nucleus surface. The values of this maximum radius, a_2, are shown in the lower right panel in Fig. 47. In the case of a higher value of N, this increase disappears because large grains, although they can be lifted from the surface, are very rare and the main contribution to the dust-to-gas mass ratio comes from the small dust grains. Higher values of N lead to a slight increase in the dust-to-gas mass ratio with heliocentric distance and to dust mass production rates about one order of magnitude lower than for $N = 3.5$. A decrease of N with time after perihelion would therefore imply a strong decrease of the dust-to-gas mass ratio. Furthermore, a considerable uncertainty

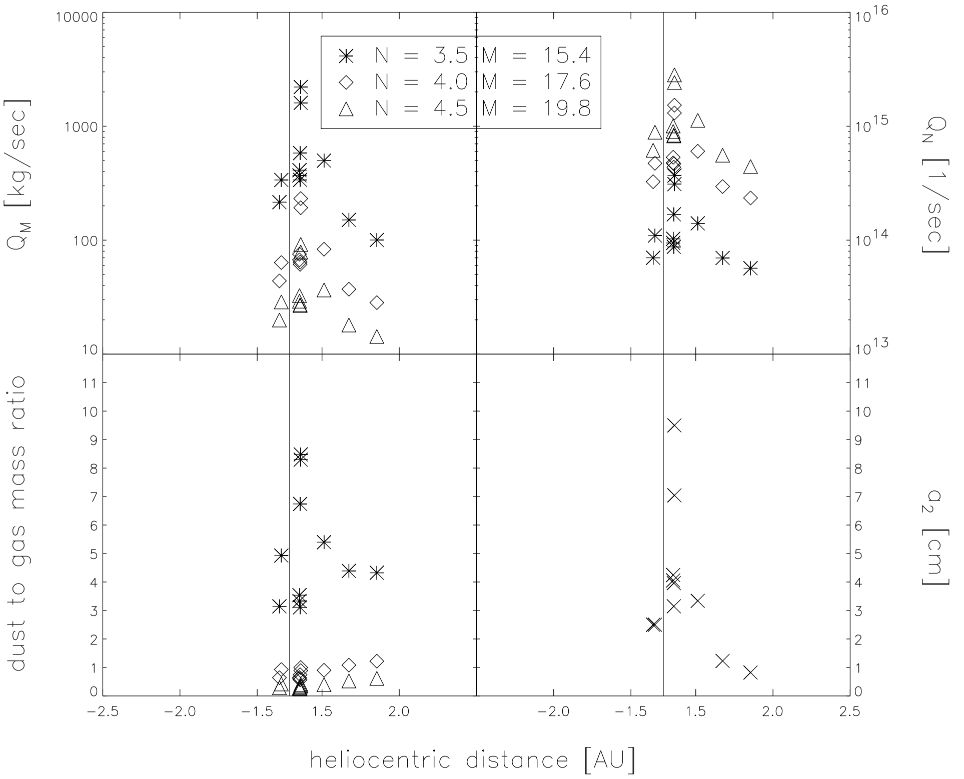

Figure 47: **Upper left panel:** *Dust mass production rates Q_M as a function of heliocentric distance. The different symbols correspond to the different dust size distribution parameters N and M. The peak of the size distribution function is at 0.54 μm in all cases. The dust production rates are computed from all LOCD data with simultaneous measurements of Afρ and OH production rates.* **Upper right panel:** *Dust number production rates Q_N for the different parameters used.* **Lower left panel:** *Dust-to-gas mass ratios as a function of heliocentric distance for the dust production rates shown in the upper panel.* **Lower right panel:** *Maximum dust particle radius a_2 as a function of heliocentric distance. A dust particle density according to equation (147) was used.*

arises from the assumption made on the active surface fraction. If this fraction is larger than assumed, the maximum particle size that can be lifted from the nucleus decreases significantly and, therefore, the dust mass production rate, too. The variation of the active fraction by 50% changes the dust mass production rates by nearly a factor of two. Thus this parameter, which is poorly constrained, represents a large source of uncertainty.

11.3.7 Implications for the Dust Flux

From the solution of equation (149) one obtains the density of dust particles and their nucleocentric velocities. It is therefore possible to determine the fluxes of dust particles as a function of dust size and nucleocentric distance. This quantity is of interest, since the Rosetta spacecraft is going to be exposed to the dust environment, and the risk for

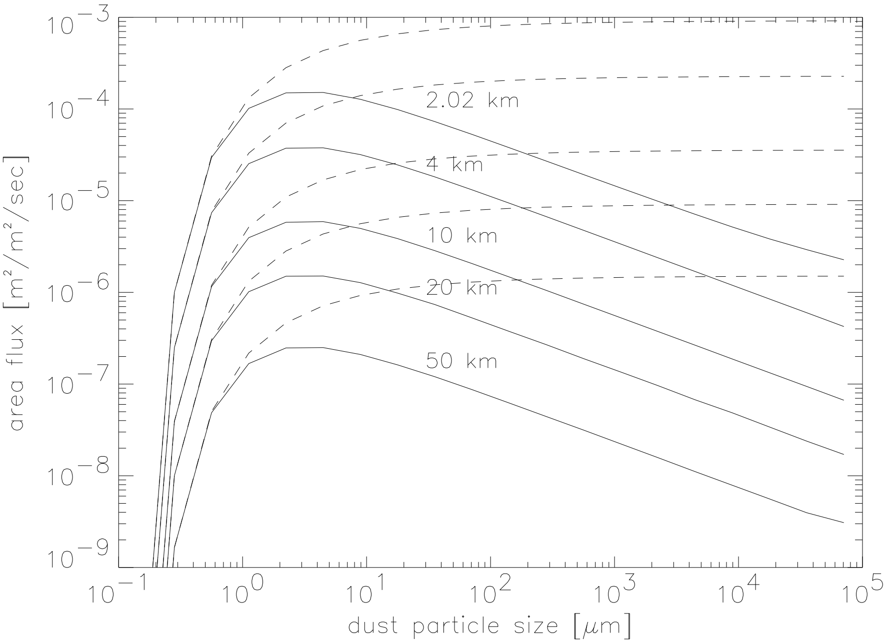

Figure 48: Fluxes of projected dust area as a function of dust size for four different nucleocentric distances. The radius of the nucleus is assumed to be 2 km. The dashed lines show the cumulative area flux. The values are computed at the maximum of cometary activity in the LOCD data.

the spacecraft needs to be estimated. Fig. 48 shows the area flux, which is the projected area of dust passing through an area unit per time interval for four different nucleocentric distances. The data presented were computed for $N = 3.5$ and $M = 15.4$. The area fluxes are highest for dust particles of a few μm in size. For large particles with radii of a few cm, the area fluxes correspond to number fluxes of the order 10^{-6} s^{-1} m^{-2} at a distance of 20 km from the center of the nucleus. The dashed lines show the cumulative area fluxes. The total area flux integrated over all dust particle radii is $9.1 \cdot 10^{-4}$ m^2 (m^2 s)$^{-1}$ at 20 m above the nucleus surface, and this value decreases to $9.1 \cdot 10^{-6}$ m^2 (m^2 s)$^{-1}$ at a distance of 20 km. These results are computed at the maximum activity of comet 67P/C-G and with an active fraction of 10%. Therefore the results represent the "worst case scenario", which has to be kept in mind when estimating the dust flux that Rosetta will be exposed to. Since the activity is significantly lower at the larger heliocentric distances where Rosetta will approach the comet, the dust fluxes will also be much smaller.

11.4 Discussion of the Coma Analysis

Comet 67P/C-C showed a strong perihelion asymmetry. The enhanced activity after the perihelion passage can be seen in the CN production rates and Afρ values (see Fig. 40). The range of heliocentric distances covered by production rates for other species is small, but the asymmetry in activity seems to be present also for OH, C_2, C_3 and NH in the

data by LOCD and Cochran *et al.* (1992).
The lightcurve derived from optical observations shows the same development of activity with heliocentric distance for the 1982 and the 1996 apparition. In Fig. 45, estimated magnitudes of the 1982, 1996 and 2002 perihelion passages are shown. A similar dependence of the activity from the geocentric distance can be seen for the 1982 and 1996 apparition with the maximum of activity post-perihelion.

It has been suggested that the storage of heat in cometary nuclei can cause perihelion asymmetries in their activity. Nevertheless, a steep increase of activity as seen for 67P/C-G is unlikely to result from this effect. Since the increase of activity occured at the same point of the orbit in the 1982 and 1996 apparition (see Fig. 45), it is unlikely that outbursts caused the higher activity observed. The strong perihelion asymmetry may result from an inclination of the rotation axis with respect to the orbital plane. If the rotation axis in inclined, the illumination of parts of the surface can vary strongly along the comet's orbit. The sudden steep increase of activity at nearly the same point along the orbit in the 1982 and 1996 perihelion passage could be caused by an active surface area. If an active area on the nucleus surface is exposed to sunlight from one point of the comet's orbit onwards, the total activity of the comet can increase within a short time period. This is also the case if another hemisphere of the nucleus, having a less eroded surface, is exposed to the Sun on one part of the orbit. This would imply that the rotation axis of the nucleus would not be perpendicular to the orbital plane. If the asymmetry was caused by active surface areas, jet-like structures in the dust coma would likely occur.

In R-filter images of comet 67P/C-G, obtained in March and May 2003, two weak jet-like features could be clearly detected. No variation of these features was observed during the time covered by observations at the TLS.

For the nucleus of comet 67P/C-G a rotation period of 12.3 h was determined by Lamy *et al.* (2003). Since the dates and times of the observations correspond to different rotational phases, the same visual appearance is not caused by unfavourable sampling of the observations.

One of these structures (structure B) could be part of the neck-line structure. In this case it is not expected to vary significantly within this time period. But since both observed structures show no variation, it is also possible that both result from one active area on the surface. In this case, they would represent the edges of a cone resulting from an active spot on the rotating nucleus. A scenario like this was proposed to explain similar structures in the coma of comet Hale-Bopp (Sekanina, 1999). This explanation allows one to put constraints on the orientation of the rotation axis of the nucleus. Since the axis is expected to be centered in the cone, the observed jet structures suggest an inclination of the projected rotational axis of approximately 40° with respect to the orbital plane. This result is in agreement with a proposed inclination of the rotational axis to explain the observed asymmetry in the lightcurve of comet 67P/C-G with respect to its perihelion.

However, at this point the orientation of the rotation axis is speculative, and further observations and a proper modelling of the coma hydrodynamics are required to obtain better constraints.

The dust velocities as a function of particle size were computed with a test particle approach and a continuum approach. The difference between the velocity values were found to be only about 3%, even for a mass loading of the gas flow of 8.5, computed using a standard size distribution for the dust particles, and thus are in a very good agreement. The mass loading of the gas flow can therefore be neglected when computing the dust production rates of comet 67P/C-G.

The exact size distribution of the dust particles in comet 67P/C-G is not known. A value of N close to 3.5 is usually supposed for comets, but changes of N along the comet's orbit have also been suggested for comet 67P/C-G (Fulle *et al.*, 2004). To estimate the effect of variations of the dust size distribution upon the dust-to-gas mass ratio, the values for N were varied from 3.5 to 4.5. Using a high value for N leads to a decrease of the dust-to-gas mass ratio from about 4.8 to values close to 0.6. Thus, if N varies along the orbit as suggested, the change in the dust-to-gas mass ratio would be very high.

Finally, from the results of the gasdynamical model one also obtains the dust particle fluxes in the coma of comet 67P/C-G. As an estimate made for the maximum of the cometary activity, a total area flux of $9.1 \cdot 10^{-6}$ m^2 $(\mathrm{m}^2\ \mathrm{s})^{-1}$ at a nucleocentric distance of 20 km was computed.

12 Comet of Special Interest: 9P/Tempel 1

The results presented in this chapter were published in:
Rauer, H., Weiler, M., Sterken, C., Jehin, E., Knollenberg, J., Hainaut, O., 2006, *Observations of CN and dust activity of Comet 9P/Tempel 1 around Deep Impact*, Astronomy and Astrophysics, 459, 257−263
and
Weiler, M., Rauer, H., Knollenberg, J., Sterken, J., 2006, *The gas production of Comet 9P/Tempel 1 around the Deep Impact date*, Icarus, in press.

12.1 Introduction

Comet 9P/Tempel 1 was the target of the NASA Deep Impact space mission. Within that mission, on July 4, 2005 a projectile spacecraft of 370 kg mass impacted on comet 9P/Tempel 1 with a relative velocity of 10.3 km s^{-1}. A crater was produced on the surface and a cloud of ejecta material expanded from the nucleus (A'Hearn et al. 2005). Additionally, a fly-by spacecraft observed the impact event. The Deep Impact mission had two primary science goals: to determine the strength and structure of the nucleus surface from the observation of the impact crater, and to investigate the differences between the nucleus surface layers, from which the regular cometary activity is believed to originate from, and the deeper sub-surface layers. The first goal can only be addressed by observations from the fly-by spacecraft. The second science goal requires the observations of the ejecta cloud after impact, and the subsequent cometary activity. This goal can also be addressed by ground-based observations.

While the nucleus layers close to the surface may be affected by alteration processes, such as the formation of an inactive crust or the depleation of hypervolatile species (see section 1.2.1), the material in the nucleus interior is believed to have remained in a primordial state. The Deep Impact experiment presented the opportunity to study material released not from near the surface of a cometary nucleus but from the interior. A comparison of the composition of the impact ejecta material with the composition of the pre-impact coma therefore allows to put constrain on the degree to which the nucleus surface is actually altered.

The Deep Impact event was observed not only from the impactor and the fly-by spacecraft, but also in a world-wide ground-based observing campaign (Meech *et al.*, 2005). At the European Southern Observatory (ESO) two observing campaigns were performed around the impact time to investigate the gas and dust components of the comet. All ESO telescopes were involved in these campaigns to provide information on the target comet over all available wavelength bandpasses from the optical to the thermal infrared. One of the ESO scientific programs was the observation of the cometary coma by means of low-resolution optical long-slit spectroscopy. These observations were done

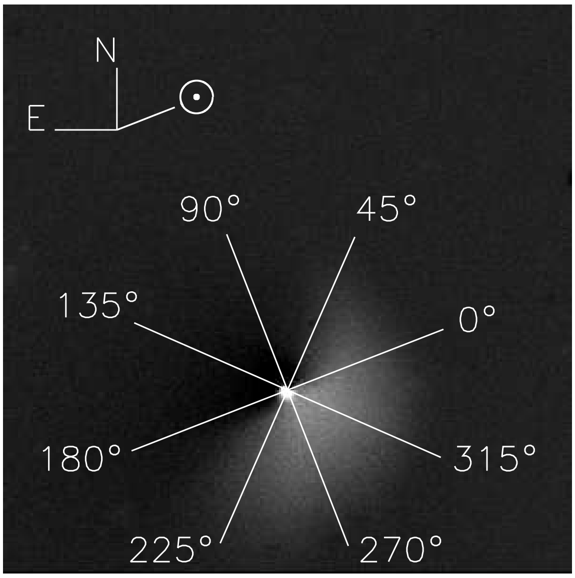

Figure 49: Difference of R-filter images before and after impact. The impact dust cloud can be seen to the Southwest. The field of view is 1.3 '×1.3 ', corresponding to 4.94 · 10^4 km for the edge of the image. The slit orientations discussed in the text are indicated by lines. Stars in the field of view were removed by interpolation from the neighbouring pixels. The projected solar direction is indicated.

to investigate the radicals in the coma before and after the impact event. The scientific goals of these observations were to investigate whether new emission lines would appear in the spectrum after the impact, to quantify the gas sublimated before, during and after the impact, to search for new active surface areas on the comet and to investigate for how long the additional activity is sustained. A comparison with pre-impact conditions is made to investigate possible differences in abundance ratios of the ices in the nucleus.

Observations of comet 9P/Tempel 1 were done from July 02/03, 2005, two days before the impact, until July 12 (see Tab. 6). Fig. 49 shows comet 9P/Tempel 1 taken in R-band 17^{h} 32^{m} after the impact, after subtraction of the pre-impact coma. The different orientation angles of the long-slit at which spectra were obtained are indicated. A dust cloud produced by the impact can be seen towards the southwest.

An example of calibrated and continuum subtracted spectra taken before and after the impact is shown in Fig. 50.

12.2 Comparison of the Pre- and Post-Impact Spectra

Fig. 50 shows spectra from the sunward side of the coma as seen from the nucleus after continuum subtraction. The emission lines usually present in optical comet spectra are detected, caused by CN ($0-0$ and $1-0$ transitions), C_3, C_2 (Δv $= 1, 0, -1, -2$), and

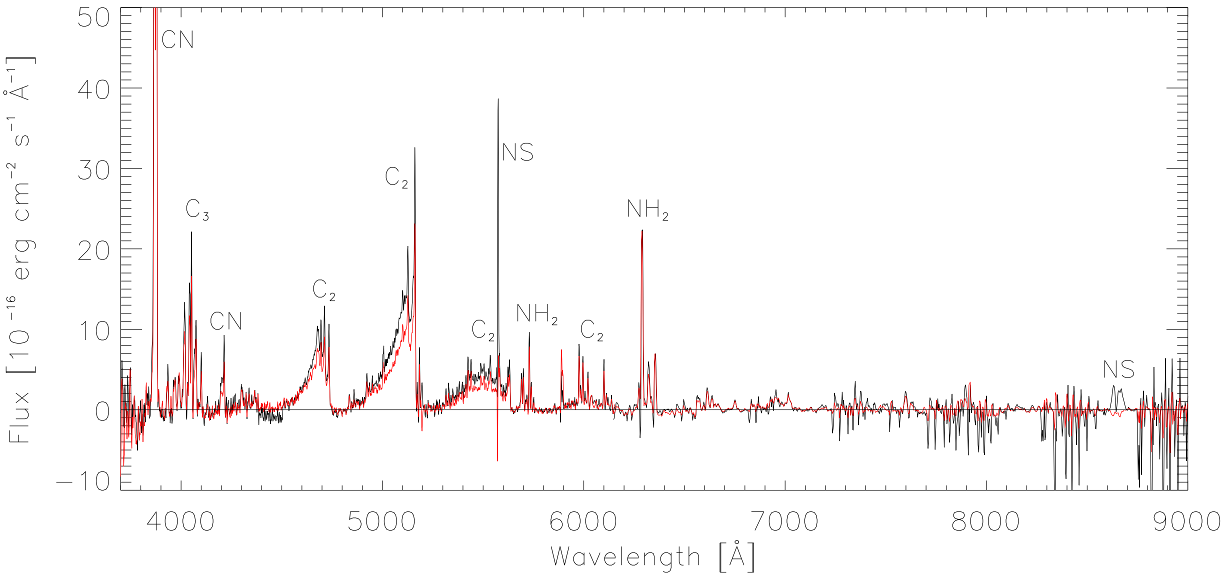

Figure 50: Continuum subtracted spectra taken 1^{h} 49^{m} before the impact (red) and 17^{h} 59^{m} after the impact (black). The spectra are integrated from $0 - 6.5 \times 10^{4}$ km along the projected Sun direction to enhance the signal-to-noise ratio. Remnants of night sky lines are marked with NS.

NH_2 ((0, 10, 0) and (0, 8, 0) transitions). No emissions of H_2O^+ or CO^+ were seen.

To investigate whether new emission bands appeared after the impact of the projectile spacecraft into the comet, spectra taken before and after the event were compared. To enhance the signal-to-noise ratio in the reference before the impact, all spectra taken on July 3/4 were co-added. After the impact, the ejecta cloud moved through the field-of-view, so only individual spectra were used for comparison. All gas emission lines increased in intensity (Fig. 50) after the impact. However, no new emissions were present, and thus, no new molecules have been detected.

12.3 Spatial Gas and Dust Profiles

Fig. 51 (left panel) shows the intensity distribution of the continuum, caused by solar light scattered by dust particles, along the slit parallel to the Sun-comet line. Two profiles are shown for the night of July 04/05 and one for all other nights. The ejected dust cloud can be seen in the slit after the impact on the sunward side. The cloud moves and expands along the sunward direction. After five days the cloud vanished and the coma was back to an intensity profile similar to the pre-impact one. No change in the intensity profile is seen in the anti-solar direction.

The corresponding spatial profiles of the CN emission (violet system) are shown in

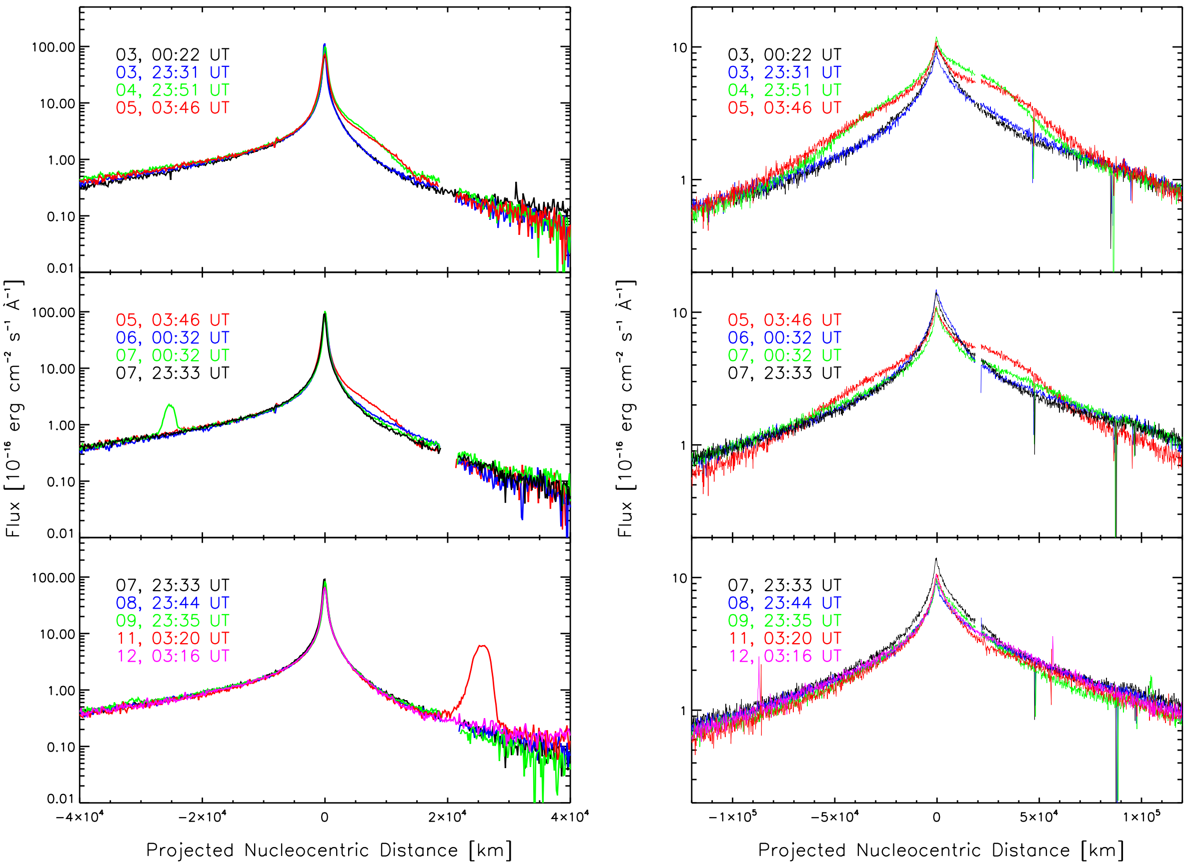

Figure 51: Continuum flux, measured at 5540 Å to 5575 Å(left image) and CN emission flux (right image) along the Sun-comet line for different nights. The different colours show the profiles in different nights. Isolated peaks in the profiles are caused by background objects (e.g. stars) within the slit. Positive distance is counted towards the projected solar direction, negative distance in the anti-solar direction.

Fig. 51 (right panel). Like in the continuum profiles, a cloud of ejected material moves in the sunward direction after the impact. However, the CN cloud is also visible in the anti-solar direction already 18 hours after the impact, again expanding and diluting in the subsequent nights. The fast lateral expansion of gas molecules in the coma causes the gas cloud to spread around the nucleus quickly. The long-slit spectra indicate that this cloud then expands outwards from the nucleus. Four days after the impact, the cloud has diluted and is only visible by a higher intensity profile in comparison to pre-impact conditions. Again, at the end of our observing period the CN profile returns to pre-impact conditions. Fig. 52 shows the same plot as Fig. 51, but for the 90°−270° slit orientation. Again, the CN impact cloud can be seen on both sides of the nucleus, while the dust cloud expands only in the 270° direction.

The impact cloud is especially prominent in the CN and C_2 emissions (C_2 not shown), providing a good signal-to-noise ratio, and can also be identified in the emissions of C_3 and

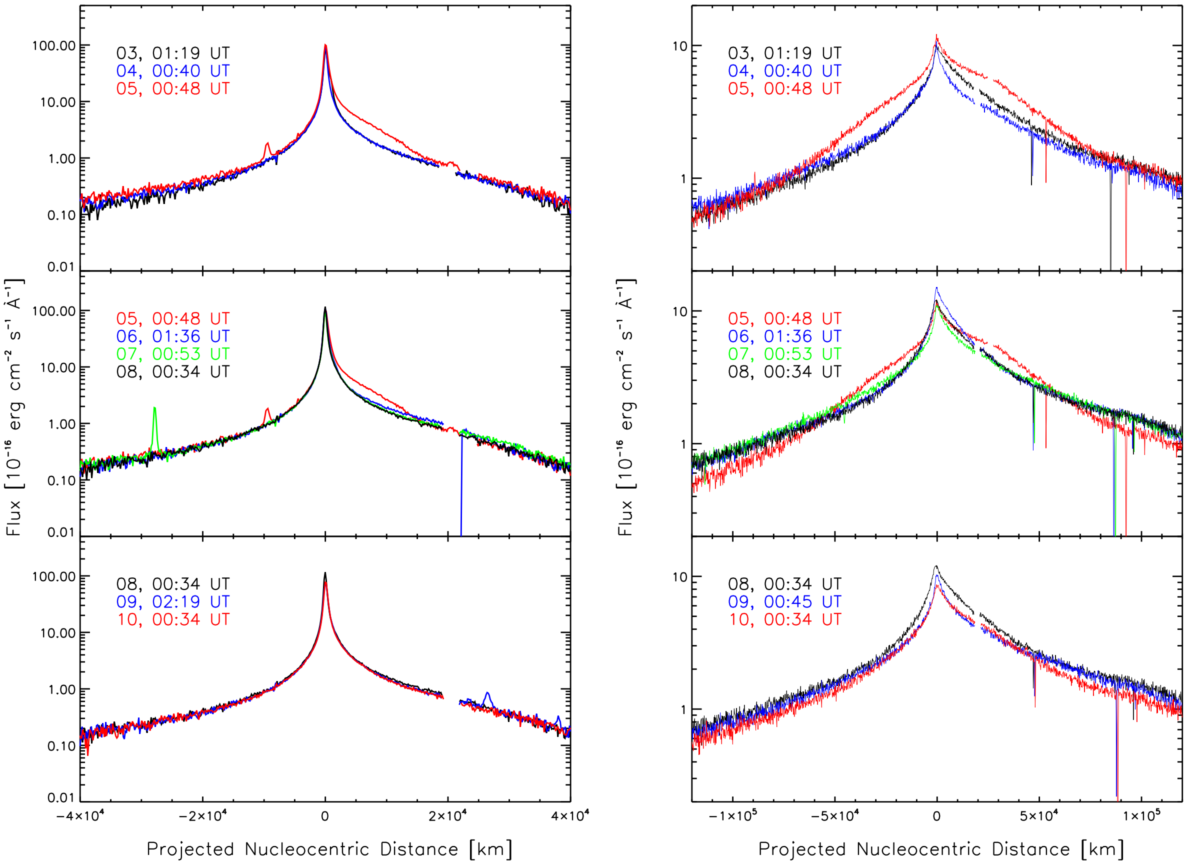

Figure 52: Same as Fig. 51, but for the 90°−270° position angles. Positive distance is counted towards the 270° direction, negative distance in the 90° direction.

NH_2 (not shown), although with a low signal-to-noise ratio. The cloud could be observed at all position angles used, thus had moved all around the nucleus. Fig. 53 shows the radial emission profiles of the CN violet system along the 0°−180° direction on the night of July 04/05, after subtraction of the mean profile of the night before. The impact cloud on both sides of the nucleus and its movement within the night can be seen. The gas cloud can be observed for four nights after the impact. Then, all gas emissions are back to the pre-impact level.

In the night of July 04/05, the entire cloud lies within the field of view of the slit and thus, the radial expansion velocity of the outermost part of the cloud can be determined from its position in spectra taken at different times within that night. This was done by comparing a post-impact radial emission profile with the pre-impact emission profile and determining the radial position inside which the profiles differ. The errors were estimated from determining the positions at which the radial emission profiles are clearly in agreement and disagreement, respectively. Fig. 54 shows the first post-impact radial emission profile for CN taken in the 180°−direction, together with the mean CN profile along this direction from the night of July 03/04. The estimated position of the outermost detectable part of the CN cloud is indicated, together with the estimated uncertainties. Since this method cannot take into account slight offsets between the two emission profiles due to uncertainties in the photometric calibration or the continuum subtraction, the true errors may be somewhat larger than the estimated ones.

Table 23 summarizes the positions of the outermost detectable part of the CN and C_2 cloud at different times, together with the projected mean gas expansion velocities derived. The velocities were computed by dividing the position of the outermost detectable part of the gas cloud by the time since impact. No significant difference in projected mean velocities between the two species were found. Since the position of the C_3 and NH_2 clouds cannot be measured with sufficient accuracy for this purpose, these species were not used for the determination of velocities.

For comparison, Table 24 shows the velocities determined for the outermost detectable part of the dust cloud in the projected solar direction. The dust cloud expands more slowly compared the the gas, and a reduction of the projected velocity component in the $0°-$direction with time can be seen. This reduction is caused by the radiation pressure, accelerating the dust particles in the anti-sunward direction.

Furthermore, the velocity of the center of the CN and C_2 clouds were determined. Therefore, the geometric dilution of the cloud when expanding outwards from the nucleus has to be considered. In the case of a steady-state outflow from the nucleus with constant velocity, the observed column density decreases with the projected nucleocentric distance r as r^{-1}. However, in the case of the Deep Impact event, a transient expansion of an isolated cloud in the coma has to be regarded. The detailed expansion of such a cloud cannot be modelled in within this work, instead simplified assumptions are used. The volume of the impact cloud is assumed to increase with the inverse nucleocentric distance to the power of three. In the extreme case of weak lateral expansion, such a cloud may be represented by a sphere with homogenious density whose diameter increases linearly with the nucleocentric distance as the center of the cloud moves outwards. In the other extreme case of strong lateral expansion, the cloud may represent a shell around the nucleus whose thickness increases linearly with increasing nucleocentric distance as the shell moves outwards. In such cases, the maximum value of the column density decreases with r^{-2}. Although this model is strongly simplified, we assume a dilution with r^{-2} to be a more appropriate choice than to assume a dependency as r^{-1}. Therefore, the flux value measured at a certain distance to the nucleus position was multiplied with the square of its distance to the nucleus in order to correct for the geometric dilution.

A Gaussian profile was then fitted to the inner part of the distance-corrected cloud and the resulting position of the center of the Gaussian was assumed to be the position of the center of the gas cloud. This method was applied to the CN and C_2 profiles. For C_3 and NH_2 the signal-to-noise ratio was not sufficient to obtain a reliable Gaussian fit. The resulting velocities of the center of the CN and C_2 clouds are presented in Table 25.

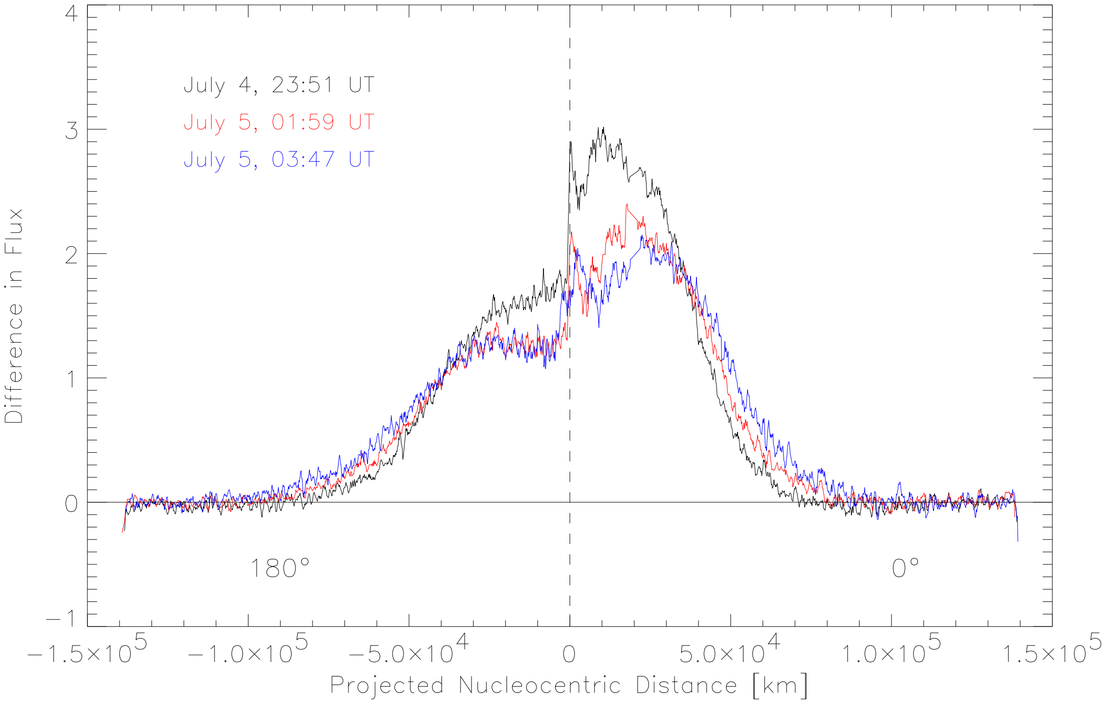

Figure 53: The CN impact cloud, observed at different times. The radial CN emission profiles obtained in the 0° − 180° direction during the night of July 04/05 are shown. The mean radial intensity profile from the night of July 03/04 is subtracted, and the resulting profiles are smoothed over a range of 5 pixels. At projected nucleocentric distances from 0 km to about 10^4 km, an increase in the CN flux profile can be seen, moving away from the nucleus position with time. The difference in flux is given in 10^{-16} erg cm^{-2} s^{-1} Å^{-1}.

12.4 Gas Production Rates

In order to study the effects of the impact event on an intermediate time scale, the production rates for the parent species CN, C_2, C_3 and NH_2 were determined in the two nights before the impact and in the fifth and the sixth night (July 08/09 and 09/10) after the impact, when the coma was back to its pre-impact state. The production rates were derived using the Haser model (see section 4.7 for a description of this model). In order to estimate the influence of coma asymmetry on the production rates, the radial intensity profiles at four different position angles available for all pre-impact observing nights (0°, 90°, 180° and 270°) were used independently. The parent and daughter scale lengths and the production rates were fitted simultaneously to the radial column density profiles. The resulting scale lengths are summarized in Table 26. Since the CN daughter scale length is quite large, it could only be determined in the night of July 02/03, where the comet was placed close to the edge of the long-slit in some exposures. The CN daughter scale length derived from this night was then used for the computation of the CN production rates in all other nights. The C_3 scale lengths could only be determined if at least four spectra (of the same slit orientation) were co-added to increase the signal-to-noise ratio. This was

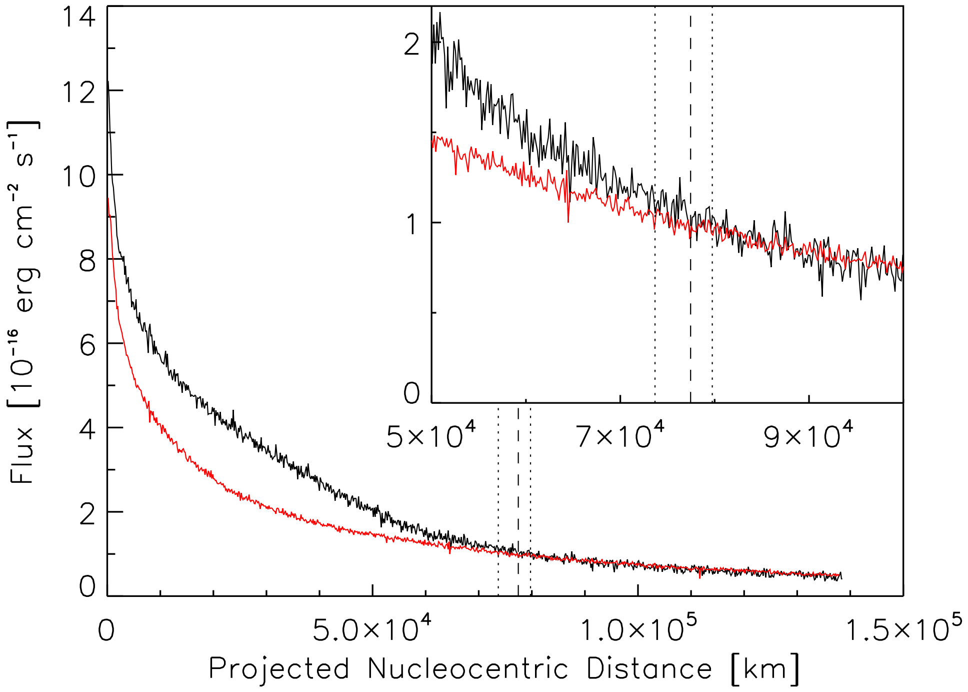

Figure 54: Mean radial CN emission profile of the night July 03/04 in the 180°−direction (red), compared with the first CN emission profile in the same direction obtained after impact (black). The estimated position of the outermost detectable part of the CN cloud is indicated by a dashed line, while the estimated uncertainties are indicated by dotted lines. The insert in the upper right corner shows a detail of the larger diagram.

only possible in the nights of July 02/03 and of July 03/04. The derived scale lengths also lead to a good fit of the radial intensity profiles in all other nights. The *g*-factors applied for the conversions from observed emission line fluxes to column densities are listed in Table 15. A mean nucleus radius of 3.0 km for comet Tempel 1 (A'Hearn *et al.*, 2005) was used. In order to be comparable with other publications, the commonly used gas expansion velocity of 1 km s^{-1} was used for the determination of the gas production rates. The production rates are shown in Table 27.

No significant change in production rates can be seen five days after the impact compared to the pre-impact activity.

12.5 Quantitative Study of the Impact Cloud

Since the detailed dynamics of the impact cloud is not known, the abundances of the parent species can only be determined by treating the cloud as a whole. This is possible if the total number of daughter radicals in the impact cloud can be determined, i.e. as long as the whole cloud lies within the field of view of the long-slit. It is assumed that all the material that lead to the formation of the cloud was released at the same time, and a simple chemical model with a two-step formation and destruction of the observed

Table 23: Determination of the projected velocities of the outermost detectable part of the impact gas cloud. T is the time since impact and x shows the radial position of the outermost detectable part of the impact ejecta cloud.

p.a.	T [s]	CN		C_2	
		x [10^3 km]	v [km s^{-1}]	x [10^3 km]	v [km s^{-1}]
0°	65182	$75.0^{+2.5}_{-2.5}$	$1.15^{+0.04}_{-0.04}$	$76.3^{+1.1}_{-1.6}$	$1.17^{+0.02}_{-0.03}$
	72861	$84.5^{+2.5}_{-5.7}$	$1.16^{+0.03}_{-0.08}$	$75.2^{+1.6}_{-1.6}$	$1.03^{+0.02}_{-0.02}$
	79334	$88.3^{+6.2}_{-2.1}$	$1.11^{+0.08}_{-0.03}$	$80.6^{+3.3}_{-2.6}$	$1.02^{+0.04}_{-0.02}$
45°	71514	$105.8^{+5.7}_{-3.3}$	$1.48^{+0.08}_{-0.05}$	$72.7^{+11.2}_{-\ 5.7}$	$1.02^{+0.16}_{-0.08}$
90°	68628	$77.8^{+3.3}_{-1.5}$	$1.15^{+0.05}_{-0.02}$	$102.1^{+\ 3.8}_{-14.3}$	$1.49^{+0.06}_{-0.21}$
135°	70143	$80.1^{+15.3}_{-\ 6.6}$	$1.14^{+0.22}_{-0.09}$	$83.7^{+3.3}_{-4.9}$	$1.19^{+0.05}_{-0.07}$
	74302	$87.4^{+7.5}_{-8.2}$	$1.18^{+0.10}_{-0.11}$	$81.2^{+8.2}_{-4.1}$	$1.09^{+0.11}_{-0.06}$
	77882	$93.4^{+7.7}_{-4.9}$	$1.20^{+0.10}_{-0.06}$	$80.9^{+8.5}_{-4.6}$	$1.04^{+0.11}_{-0.06}$
180°	65182	$77.5^{+2.3}_{-3.8}$	$1.19^{+0.04}_{-0.06}$	$83.7^{+1.6}_{-1.6}$	$1.28^{+0.03}_{-0.03}$
	72861	$88.6^{+5.1}_{-3.8}$	$1.22^{+0.07}_{-0.05}$	$83.0^{+4.4}_{-1.5}$	$1.14^{+0.06}_{-0.02}$
	79334	$99.0^{+1.8}_{-3.9}$	$1.25^{+0.02}_{-0.05}$	$89.6^{+8.0}_{-3.6}$	$1.13^{+0.10}_{-0.05}$
225°	71514	$89.9^{+1.0}_{-4.8}$	$1.16^{+0.01}_{-0.07}$	$86.2^{+1.1}_{-4.1}$	$1.20^{+0.02}_{-0.06}$
270°	68628	*bad column*		$82.9^{+3.6}_{-2.5}$	$1.21^{+0.05}_{-0.04}$
315°	70143	$80.7^{+3.4}_{-2.8}$	$1.15^{+0.05}_{-0.04}$	$82.1^{+1.6}_{-1.6}$	$1.17^{+0.02}_{-0.02}$
	74302	$88.1^{+6.2}_{-4.4}$	$1.19^{+0.08}_{-0.06}$	$79.6^{+3.3}_{-3.3}$	$1.07^{+0.04}_{-0.04}$
	77882	$89.4^{+18.9}_{-\ 4.4}$	$1.15^{+0.24}_{-0.06}$	$82.5^{+3.9}_{-4.3}$	$1.06^{+0.05}_{-0.06}$
mean		1.23±0.12		1.17±0.14	

daughter species is applied. Information on the radial distribution of the daughter radicals is not required in this case. If a simple two-step chemical reaction network is used, the total number of parent molecules in the impact cloud as a function of time is obtained from the solution of the differential equations

$$\frac{\mathrm{d}N_p}{\mathrm{d}t} = -k_p N_p \tag{156}$$

$$\frac{\mathrm{d}N_d}{\mathrm{d}t} = k_p N_p - k_d N_d \tag{157}$$

with the initial conditions $N_p(t = t_0) = N_p^{impact}$ and $N_d(t = t_0) = 0$. Here t_0 denotes the impact time, N_p and ${}_d$ are the total numbers of the parent and the daughter species, and N_p^{impact} denotes the number of parent molecules set free by the impact event. The solution of the differential equations yields:

$$N_p = N_d(T) \cdot \left(\frac{k_p}{k_d - k_p} \cdot \left[e^{-k_p T} - e^{-k_d T} \right] \right)^{-1} \tag{158}$$

Table 24: Projected mean expansion velocities, of the outermost part of the dust cloud in the projected sunward direction. Δt is the time since impact and x is the projected distance from the nucleus of the outermost detectable part of the impact cloud.

date, time	Δt [s]	x [10^4 km]	v [km s^{-1}]
July 5, 01:58	72861	$1.51^{+0.13}_{-0.15}$	$0.208^{+0.02}_{-0.02}$
July 5, 03:46	79334	$1.56^{+0.16}_{-0.13}$	$0.198^{+0.02}_{-0.02}$
July 7, 00:32	240477	$2.53^{+0.13}_{-0.15}$	$0.104^{+0.006}_{-0.006}$
July 7, 02:20	246965	$2.51^{+0.18}_{-0.23}$	$0.102^{+0.007}_{-0.009}$

The rate coefficients k_p and k_d are derived from the scale lengths determined in the nights before impact using the Haser model, by:

$$k_p = \frac{v}{l_p}, \qquad k_d = \frac{v}{l_d} . \tag{159}$$

v is set equal to the projected expansion velocity of the gas ejecta cloud determined from the spatial CN profiles. The mean value derived from Tab. 23 is (1.19 ±0.07) km s^{-1}. Equations (158) and (159) were used to derive the number of parent molecules released during the impact, N_p^{impact}, assuming isotropic expansion. The mean velocity from the values shown in Table 23 was used for the determination of the number of CN, C_2, and C_3 parent molecules. The scale lengths determined on July 03/04 were used. This approach makes use of the assumption that the radicals in the impact cloud are formed and destroyed by the same mechanism than in the pre-impact coma. The total numbers of daughter radicals within the gas cloud were determined by integrating over the difference between the emission profiles obtained in the night of July 04/05 and the mean emission profile from the previous night. This approach makes the assumption that all differences between the night of July 03/04 and July 04/05 are a result of the impact event. The number of radicals and the derived number of parent molecules are shown in Table 28 for CN, C_2, and C_3. No useful results for NH_2 could be obtained due to the low signal-to-noise ratio of the NH_2 emission.

12.6 Comparison of the Coma and the Impact Cloud Composition

In order to compare the chemical composition of the coma before the impact, after the impact, and the composition of the impact gas cloud, the ratios of the Haser production rates for C_2/CN and C_3/CN were computed. Furthermore, the number of parent molecules for C_2, C_3 and CN as computed for the impact cloud was used to determine the ratio of the number of parent molecules in the cloud. Since the simple chemical model is the

Table 25: Determination of the projected gas bulk velocities, T is the time since impact and x is the radial position of the center of the impact ejecta cloud.

p.a.	T [s]	CN		C_2	
		x [10^3 km]	v [km s^{-1}]	x [10^3 km]	v [km s^{-1}]
0°	65182	37.5±3.0	0.58±0.05	44.7±5.3	0.69±0.08
	72861	43.5±3.2	0.60±0.04	47.6±4.8	0.65±0.07
	79334	47.8±3.2	0.60±0.04	54.9±4.7	0.69±0.06
45°	71514	46.3±3.0	0.65±0.04	54.4±4.6	0.76±0.07
90°	68628	39.5±3.7	0.58±0.05	55.2±6.0	0.80±0.09
135°	70143	42.6±3.2	0.61±0.05	54.6±4.9	0.78±0.07
	74302	43.9±3.1	0.59±0.04	55.6±4.7	0.75±0.06
	77882	47.1±3.1	0.60±0.04	55.3±4.1	0.71±0.05
180°	65182	41.3±3.0	0.63±0.05	50.9±5.1	0.78±0.08
	72861	46.2±3.0	0.63±0.04	51.8±4.3	0.71±0.06
	79334	50.4±3.0	0.64±0.04	58.3±4.3	0.73±0.05
225°	71514	46.9±3.0	0.66±0.04	54.6±4.4	0.76±0.06
270°	68628	49.1±3.1	0.72±0.05	54.0±5.6	0.79±0.08
315°	70143	46.3±3.4	0.66±0.05	51.4±4.0	0.73±0.06
	74302	48.9±3.2	0.66±0.04	54.8±7.1	0.74±0.10
	77882	49.6±3.1	0.64±0.04	55.6±5.8	0.71±0.07
mean			0.63±0.04		0.75±0.04

same for the Haser model and the computation of the number of parent molecules in the impact cloud, the results are comparable. The ratios of the two nights before the impact and the two nights after the impact were averaged. The abundance ratios are given in Table 29 for the different slit orientations and for the corresponding average.

The ratio of C_2/CN makes comet 9P/Tempel 1 typical according to A'Hearn et al. (1995), in agreement with previous observations (e.g. Cochran *et al.* (1992)). The large uncertainty in the ratio of C_3/CN is caused by the low signal-to-noise ratio of the C_3 emission.

It can be seen that the composition of the impact cloud as obtained with the Haser model is identical to the pre-impact coma, as far as C_2, C_3 and CN are concerned. A slightly lower value for C_2/CN after the impact is determined. This is mainly caused by a low C_2 production rate determined along the 270°-direction.

Table 26: Summary of the Haser parent (l_p) and daughter (l_d) scale lengths determined from the observations of comet 9P/Tempel 1. The scale lengths were extrapolated to a heliocentric distance of 1.0 AU by assuming a scaling with r_h^2. All values are in units of [10^4 km].

species	July 02/03	July 03/04	July 08/09	July 09/10
CN	$\mathrm{l_p} = 1.73 \pm 0.69$ $\mathrm{l_d} = 54.67 \pm 41.00$	$\mathrm{l_p} = 2.00 \pm 0.45$ –	$\mathrm{l_p} = 2.43 \pm 0.44$ –	$\mathrm{l_p} = 2.04 \pm 0.52$ –
C_2	$\mathrm{l_p} = 4.58 \pm 1.34$ $\mathrm{l_d} = 4.58 \pm 1.34$	$\mathrm{l_p} = 4.13 \pm 0.83$ $\mathrm{l_d} = 5.80 \pm 2.34$	$\mathrm{l_p} = 4.87 \pm 0.59$ $\mathrm{l_d} = 5.49 \pm 0.85$	$\mathrm{l_p} = 3.93 \pm 0.30$ $\mathrm{l_d} = 4.48 \pm 0.82$
C_3	$\mathrm{l_p} = 0.33 \pm 0.04$ $\mathrm{l_d} = 9.79 \pm 6.26$	$\mathrm{l_p} = 0.31 \pm 0.06$ $\mathrm{l_d} = 17.06 \pm 5.95$	–	–
NH_2	$\mathrm{l_p} = 1.34 \pm 0.28$ $\mathrm{l_d} = 1.51 \pm 0.52$	$\mathrm{l_p} = 1.20 \pm 0.51$ $\mathrm{l_d} = 1.37 \pm 0.49$	$\mathrm{l_p} = 1.28 \pm 0.22$ $\mathrm{l_d} = 1.36 \pm 0.31$	$\mathrm{l_p} = 1.93 \pm 0.56$ $\mathrm{l_d} = 1.93 \pm 0.56$

12.7 Rotational Coma Variations

Short-term variations in the radial emission profiles suggest a possible link with the rotational period of the comet nucleus. Such a short-term variation can be seen in Fig. 53, where an apparently new peak occured in the radial intensity profile within about 6000 km on the sunward side of the nucleus, moving outwards with time. To study the short-term variability, the flux in the inner part of the coma is integrated in single spectra and plotted versus the rotational phase of the nucleus. The inner seven pixels in the coma, corresponding to 1.8", were excluded from the integration since the pixels next to the nucleus are affected by a large uncertainty in the continuum subtraction. Then, the flux within the following 20 pixels, corresponding to 5", was integrated on both sides from the nucleus. This small apperture was chosen to minimize the contribution of the impact cloud to the lightcurve. A rotational period of (40.832±0.33)h (A'Hearn *et al.*, 2005) was applied, while zero rotational phase was set to the time of the impact. Fig. 55 shows the CN flux within the integration area, normalized to the mean value of all data points. The different colours indicate data points from different slit orientations. The error bars in rotational period arise from the uncertainty in the nucleus rotation period. Data points with the same slit orientation show a smooth variation with rotational phase. Differences between the data points from different slit orientations are caused by a coma asymmetry which becomes larger at large rotational phases. A correlation of the inner coma brightness with rotational phase can be seen, with an increased brightness between rotational phases of 0.1 and 0.25, and a second maximum around phase values of 0.65. The data obtained in the night of July 05/06 did not properly fit onto the rotational light curve. This could be caused either by an underestimated photometric error, or by a significant contribution

Table 27: Summary of the Haser production rates determined from the observations of comet 9P/Tempel 1. The row with 'mean' as the position angle (p.a.) presents the production rate averaged over the four p.a. All numbers are expressed in $[10^{24}\ s^{-1}]$.

species	p.a.	July 02/03	July 03/04	July 08/09	July 09/10
CN	0°	10.8±0.4	13.7±0.4.	15.8±2.9	12.8±1.3
	90°	7.3±0.3	8.2±0.2	9.7±0.5	8.1±0.1
	180°	8.4±0.9	8.1±0.3	10.2±0.3	9.1±0.3
	270°	16.6±0.8	13.2±0.3	15.8±0.6	15.4±0.5
CN	mean	10.2±2.6	10.8±3.1	12.9±3.4	11.4±3.4
C_2	0°	19.6±1.6	19.7±1.1	18.5±0.9	14.7±4.0
	90°	14.7±0.1	12.0±4.8	17.2±2.8	13.4±0.3
	180°	14.7±0.7	10.9±3.1	15.0±1.0	12.7±1.2
	270°	24.4±0.6	15.5±4.5	14.8±4.5	15.7±0.6
C_2	mean	18.4±4.6	14.5±4.0	16.4±1.8	14.1±1.3
C_3	0°	2.2±0.1	1.8±0.1	1.8±0.2	1.8±0.1
	90°	1.8±0.1	1.3±0.1	1.8±0.1	1.5±0.1
	180°	1.2±0.2	1.1±0.1	1.1±0.3	1.1±0.2
	270°	1.8±0.1	1.6±0.2	1.8±0.2	1.4±0.2
C_3	mean	1.7±0.4	1.4±0.3	1.6±0.4	1.4±0.3
NH_2	0°	10.3±1.7	11.2±2.5	10.4±1.1	10.9±1.1
	90°	8.6±0.3	6.9±0.8	7.3±0.4	10.7±20.7
	180°	7.2±4.8	5.1±0.8	5.9±0.5	10.1±6.9
	270°	7.5±0.7	5.6±1.9	7.6±0.8	6.5±0.1
NH_2	mean	8.4±1.4	7.2±2.8	7.8±1.9	9.6±2.0

of the impact cloud. The night of July 05/06 is the only one with non-photometric conditions in the observing campaign. The photometric uncertainty was estimated from the deviation of observed standard stars from their catalogue spectra. However, it could not be ruled out that the sky conditions were different at the time of the comet observations, causing the error to be underestimated. Furthermore, the small field of view used for the determination of the light curve should exclude the major part of the impact cloud, nevertheless, one cannot exclude a small remaining contribution of the order of a few percent.

The CN rotational lightcurve determined in this work is in agreement with a CN lightcurve determined before from high-resolution spectra by Jehin *et al.* (2006).

Fig. 56 shows the normalized fluxes originating from the radicals CN, C_2, C_3 and NH_2, including observations from all position angles. Different colours correspond to the fluxes

Table 28: The number of radicals in the impact cloud as determined at different times, and the derived number of parent molecules released by the impact event. All numbers are in units of 10^{29} molecules. T is the time since impact, and p.a. is the position angle with respect to the projected solar direction.

T [s]	p.a.	CN	CN parent	C_2	C_2 parent	C_3	C_3 parent
65182	0°	3.27±0.47	4.63±0.73	1.92±0.30	5.27±1.26	0.82±0.09	1.04±0.26
	180°	2.33±0.35	2.75±0.43	1.62±0.23	3.28±0.90	0.28±0.07	0.33±0.13
68628	90°	2.70±0.50	3.27±0.62	2.51±0.31	6.71±2.06	0.21±0.04	0.28±0.05
	270°	2.40±0.35	2.90±0.44	2.01±0.26	5.61±1.55	0.43±0.04	0.51±0.07
72861	0°	3.38±0.66	4.57±0.94	1.71±0.41	4.48±1.38	1.37±0.12	1.79±0.49
	180°	2.50±0.48	2.88±0.57	1.39±0.30	2.72±0.87	0.53±0.09	0.63±0.24
79334	0°	3.88±0.68	5.09±0.94	2.44±0.44	6.21±1.68	0.93±0.13	1.25±0.40
	180°	2.95±0.49	3.36±0.58	1.84±0.33	3.52±1.05	< 0.12	< 0.15

of the emissions for the four different species. The correlation of the inner coma brightness with rotational phase can be seen for all four species.

The different species included in Fig. 56 show the same behavior with rotation, with the occasional exception of CN. At rotational phases around 0.65, the brightness of the CN line emission in the night of July 06/07 (the black dots with the smaller error bars clustered around rotational phase ~ 0.65 in Fig. 56) is clearly below the normalized brightness of all other species. In the night of July 11/12, at a similar rotational phase, the CN data point and the data point for C_3 are in good agreement with the data from July 06/07. The C_2 and NH_2 data points of that night show no significant difference from the CN value. It remains unclear whether the observations of July 11/12 reflect a change in the physical properties of the cometary coma, or if they are caused by uncertainties in data calibration. Since no correction for possible straylight in the frames taken with FORS 1 was possible, this additional source of uncertainty remains in the FORS 1 observations, compared to the other observations done with FORS 2. At the edges of the slit of FORS 1, where the comet signal is lowest, remnant features in the comet frames after sky subtraction were found, showing differences between both edges of the slit. This improper sky subtraction is more significant at larger wavelengths, while a relatively good sky subtraction was achieved at wavelengths less than about 4300 Å. Therefore, it cannot be ruled out that the observations of C_2 and NH_2 with FORS 1 are affected by calibration uncertainties that cannot be quantified.

Table 29: The ratios between the production rates before and after the impact and the number of molecules in the impact cloud, listed for the different position angles (p.a.). The row marked with "mean" shows the value averaged from the four position angles.

ratio	p.a.	before impact	impact cloud	after impact
C_2/CN	0°	1.60±0.27	1.12±0.21	1.16±0.25
	90°	1.73±0.28	2.05±0.74	1.72±0.37
	180°	1.55±0.33	1.06±0.21	1.44±0.20
	270°	1.34±0.47	1.93±0.61	0.98±0.04
	mean	1.56±0.16	1.54±0.52	1.33±0.32
C_3/CN	0°	0.17±0.05	0.29±0.06	0.17±0.01
	90°	0.19±0.06	0.08±0.02	0.18±0.01
	180°	0.13±0.01	0.16±0.07	0.08±0.03
	270°	0.12±0.01	0.17±0.03	0.12±0.01
	mean	0.15±0.03	0.18±0.09	0.14±0.05

12.8 Summary and Discussion

The analysis of the long-slit spectra and radial emission profiles originating from CN, C_2, C_3 and NH_2 in the nights around the Deep Impact event lead to the following results:

- No new gas emission bands were observed at about 18 hours after the impact, compared to the pre-impact coma.
- After the Deep Impact event at comet 9P/Tempel 1, a gas cloud expanding in the coma was observed. A mean expansion velocity of (1.23±0.12) km s^{-1} for CN and (1.17±0.14) km s^{-1} for C_2 was measured for the outermost part of the cloud. Velocities of (0.63±0.04) km s^{-1} and (0.75±0.04) km s^{-1} were measured for the center of the CN and C_2 clouds, respectively.
- Based on the Haser-like chemistry model, a total number of parent molecules produced by the impact event of $(3.48\pm0.87)\cdot10^{29}$ for the CN parent, $(5.20\pm1.48)\cdot10^{29}$ molecules for the C_2 parent, and $(0.66\pm0.48)\cdot10^{29}$ molecules for the C_3 parent were determined.
- The abundance of C_2 and C_3 relative to CN in the impact cloud is in agreement with the pre-impact coma composition. No signs of compositional differences between the material sublimating from the surface or near-surface of the nucleus and the impact material which was possibly ejected from deeper surface layers were found based on the study of the CN, C_2 and C_3 parent species.
- The production rates of CN, C_2, C_3, and NH_2, as measured on the fifth and sixth night after the impact, are in agreement with the pre-impact production rates.
- A variation of the gas production of all four species studied with the rotation of the nucleus was detected. A primary maximum at a rotational phase of about 0.2 and a

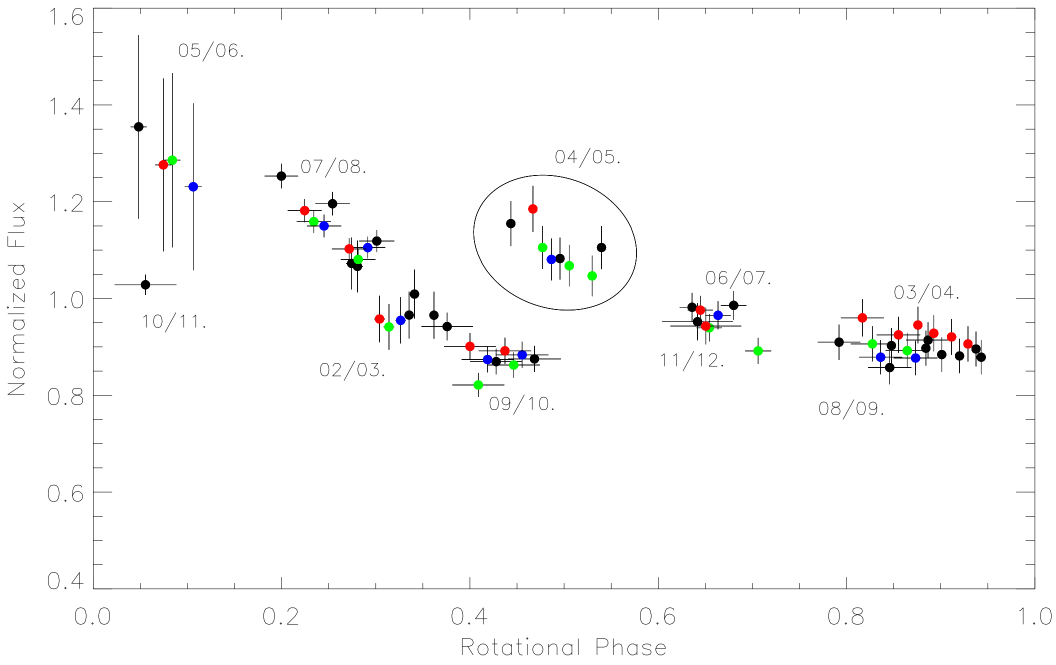

Figure 55: The normalized rotational CN lightcurve. Different position angles are indicated by colours, black: 0°−180°, red: 90°−270°, blue: 45°−225°, green: 135°−315°.

secondary maximum at a rotational phase of 0.65 can be identified. These maxima can be explained by the presence of two active surface areas on the comet nucleus, moving in and out of sunlight as the nucleus rotates.

- The rotational variation of all species are in agreement except at a rotational phase of 0.6 to 0.7. In this phase range, the brightness of the CN emission is significantly lower than the emissions from C_2, C_3, and NH_2 in the night of July 06/07. Additional observations at a similar rotational phase on July 11/12 are not conclusive since the data points for CN and C_3 are in good agreement with earlier observations, while the data points for C_2 and NH_2 are not.

If the observed variation in cometary activity with rotational phase of the nucleus is caused by located active areas on the nucleus surface, the disagreement of the CN lightcurve with the those for the other species at rotational phases around 0.65 could indicate a compositional difference between the different parts of the nucleus surface. The active area causing the secondary maximum in the lightcurve then would have a lower content of the CN parent, most likely HCN, compared to the rest of the comet's nucleus. Indeed, some indication of compositional differences between different parts of the surface of comet 9P/Tempel 1 has already been discussed in the literature. Feaga *et al.* (2006) report of an asymmetry of the CO_2 and H_2O distribution in the inner coma of comet Tempel 1, derived from infrared spectra measured by the Deep Impact fly-by spacecraft. Therefore, even if no compositional difference could be found between the

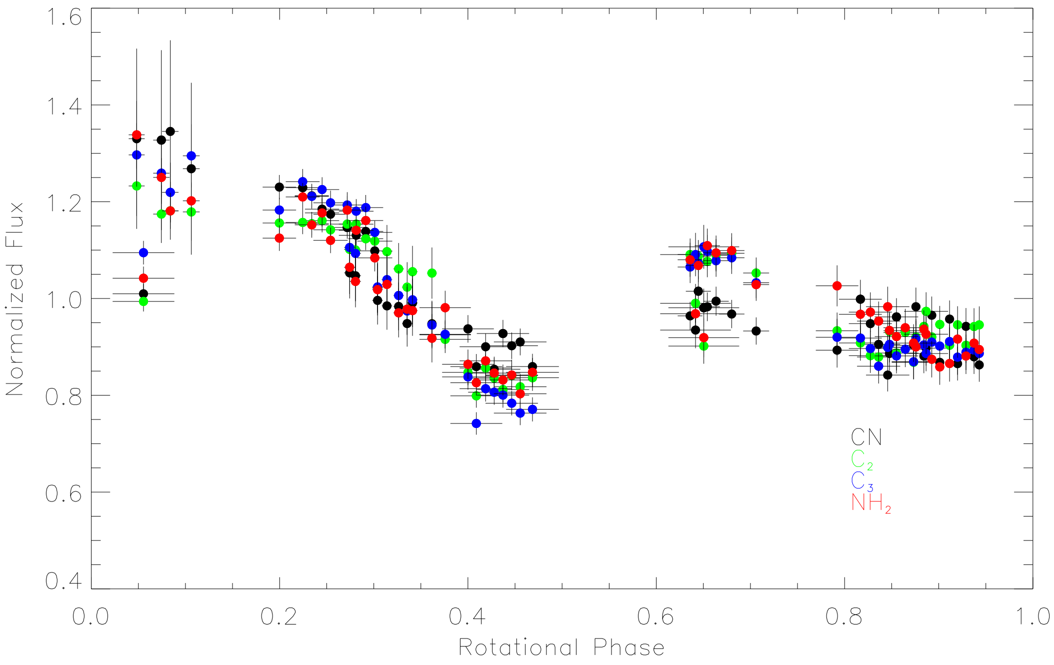

Figure 56: The normalized rotational lightcurve for the species CN, C_2, C_3 and NH_2, given in different colours. All slit orientations are shown. The night of July 04/05, following the impact, is excluded in this Figure.

usual activity of comet Tempel 1 and the material from deeper layers ejected by the impact, there were some suggestions of compositional variations between different parts of the cometary surface.

Assuming HCN to be the main CN parent species, the number of CN parent molecules released by the impact event would correspond to a mass of (17.5±5.4) metric tonnes of HCN. The impact event provided a total kinetic energy of 1.93×10^{10} J. With a sublimation enthalpy of 35.6 kJ/mol for HCN (Stephenson & Malanowski 1987), a total of $3.26\cdot10^{29}$ molecules of HCN could be sublimated due to the impact event if all energy would be used for the sublimation of HCN only. This value is of the same order of magnitude as the number of CN parents produced by the impact. Since HCN is only a minor component of cometary nuclei (for 9P/Tempel 1, an abundance ratio HCN/H_2O of (0.18 ± 0.06)% was determined (Mumma et al. 2005)), the kinetic energy provided by the impact spacecraft is not sufficient to explain the observed total amount of volatiles released due to the impact. Sublimating icy grains ejected into the coma by the impact event are a likely explanation for the observed amount of volatiles in the impact cloud. The assumption of an instantaneous release of all parent species may nevertheless be justified since studies of the dust cloud (Schleicher et al. 2006) indicate typical grain sizes below about 2.5 μm. If icy particles also have such low sizes and contain dark material, the complete sublimation of the grains takes less than 30 minutes (Beer et al. 2006) at heliocentric distances between

1−2 AU. Therefore, the approach chosen may provide a good approximation of the total amount of sublimated HCN.

The interpretation of the derived values for the velocities of the outermost detectable parts of the gas clouds and for their centers is difficult. The observed emission profiles are influenced not only by the movement of material but also by the formation mechanisms of the observed radicals. They are not producted by the impact event but as a function of time by the decay of parent species released by the impact event. During formation, the radicals may receive an excess energy that results in a higher velocity of the radicals compared to their parent species. Since the additional velocity accociated with the excess energy is random distributed in their direction, the observed cloud of radicals can be expected to be more broad than the corresponding cloud of the parent species.

The CN parent Haser scale length is shorter and the daughter scalelength is longer than the corresponding values for C_2, as shown in section 12.4. Therefore, the observed CN radicals in the cloud may be produced earlier than the observed C_2 radicals. Due to the excess velocity, the outermost detectable CN radicals could have reached larger distances than the C_2 radicals within the same time. The position of the center of the CN cloud and the C_2 cloud however is likely to be unaffected by this effect due to the random distribution of the excess velocity vectors. Therefore, one would expect the velocity of the outermost detectable part of the CN cloud to be higher than for the C_2 cloud, while the velocities of the center of the CN and C_2 clouds are similar. However, the opposite effect is observed, and the velocities of the outermost parts of the clouds are similar while the center of the C_2 cloud moved faster than the center of the CN cloud. This remains unexplained by the strongly simplified model used in this work and may has its reason in the detailed dynamics and chemistry in the impact cloud.

13 A Method for Determining Comet Nuclear Sizes

13.1 Overview

The nuclear size is a fundamental comet parameter and is required as an input parameter of models of the chemistry and physics in the cometary coma. Furthermore, the size distribution of the different populations of small bodies in our solar system provides information on the evolution of the solar system. The currently observed sizes of the minor bodies reflect their primordial size distribution overlayed by their collisional processing since the formation of the solar system. The determination of nuclear sizes for a large number of comets is therefore very desirable but this is complicated by the development of cometary activity as they approach the Sun. The increasing solar irradiation causes sublimation of volatile material. Dust particles present in the nucleus are carried away by the sublimating gas. Solar light scattered by the dust particles in the coma of the comet then dominates the signal when the comet is close to the Sun and does not allow measurement of the nucleus magnitude directly. Excluding spacecraft missions to comets, which provide accurate size determinations but are very demanding in terms of resources, three different methods are applied to derive the nuclear size:

a) The cometary nucleus can be observed directly at large heliocentric distances, where no or only negligible gas activity is present. This method implies photometry of distant and thus very faint objects. Furthermore, long period comets tend to show activity up to very large heliocentric distances (e.g., comet Hale-Bopp is still active at 21 AU from the Sun (Rivkin *et al.* (2005), Nakano and Tsumura (2005)). Many short-period comets on the other hand appear inactive at heliocentric distances beyond approximately 5 AU, outside the sublimation regime of water ice. Therefore, most cometary radii have been determined for short-period comets by this method.

b) The nuclear sizes of active comets can be determined if the nucleus magnitude can be separated from the contribution of the coma. The brightness distribution in the coma has to be modelled and subtracted from the images. This method requires a high spatial resolution of the observations and a relatively symmetric coma. Therefore, this method has been applied so far only to a number of observations of short period-comets.

c) If a comet has a close encounter with Earth, its nucleus can be detected directly by radar observations. Since the intensity of the received radar signal from the nucleus decreases with the geocentric distance to the power of four, this method is restricted to a small number of comets reaching sufficiently small geocentric distances.

A number of publications on the size distributions of short-period comets exist; they are based on the three methods described above (see e.g. Meech *et al.* (2004), Lamy *et al.* (2000), Lamy *et al.* (2002), Harmon *et al.* (1997)). But unfortunately, there exist nuclear size determinations only for five long-period comets, which is not sufficient to derive their size distribution. In this chapter, a method for estimating comet nuclear sizes using nucleus magnitudes from survey observations of both, short- and long-period comets, is presented.

A significant number of newly-discovered comets are classified as asteroidal at their first observation. These discoveries are mainly made by large survey programs searching for near-Earth objects, e.g. LINEAR (Lincoln Near Earth Asteroid Research), LONEOS (Lowell Observatory Near Earth Object Search), or NEAT (Near Earth Asteroid Tracking). The number of objects first identified as asteroids is relatively large. For example, from 54 comet discoveries during the year 2004, not counting SOHO[9] discoveries, 28 were regarded as asteroids at the time of their discovery. Assuming that these comets were indeed inactive at that time, their magnitude estimates provide a possibility for the determination of their nucleus size. Of course, a stringent evaluation has to be made as to what extent the first observation of an object has already been affected by cometary activity. Fortunately, a sample of objects remains after such an evaluation that includes both short- and long-period comets.

13.2 The Selected Dataset

All comets originally classified as asteroidal at the time of their discovery from 1998 to 2004 were considered for this work. The analysed observations were published in the Minor Planet Center Extended Computer Service or in Circulars of the International Astronomical Union (IAUC). All reports of discovery of comets and their activity used in this work are listed in Appendix B. The time between the discovery of the object and the discovery of its cometary activity varied over a wide range, from the following night to more than one year. Also the degree of activity observed varied, from a ”slightly softer point spread function than stars” to the observation of a coma and a tail with more than one arcminute of extension. Therefore, it is obvious that in some cases cometary activity was already present at the time of discovery of the object but was not recognized. For this reason, the following selection criteria were defined to separate probably inactive objects from wrong classifications:

1) More than ten days passed between the discovery of the object and the discovery of cometary activity.

2) At least one additional observation within the ten days must be available and not reveal cometary activity. This criterion ensures that obviously wrong classifications of the objects as asteroidal are rejected.

3) Comets with less than ten days between the discovery of the object and its activity were taken into account if pre-discovery observations were available in which the comet was marked as a point source. Again, the combined data then had to fulfil the two

---

[9] SOHO is the SOlar and Heliospheric Observatory, a spaceborne solar observatory that discovered a large number of sun-grazing comets (Marsden, 2005).

conditions above.

4) Further demands on the comets in the dataset were derived from the study of the photometric accuracy and are discussed in detail in the following subsection.

A time period of 10 days was chosen because this time interval would in principle be sufficient to build up a visible coma from an inactive state for all comets included in the analysis. Assuming a dust expansion velocity of 0.1 km/s and the largest geocentric distance in the sample of comets studied, 10 AU, a coma of 24" in diameter can in principle been formed within the 10 days. For such a coma diameter it is very likely that it would have been detected. For the majority of objects in the database selected, estimates of the coma diameter at the time of discovery of cometary activity are given. None of the diameter estimates is larger than 25", typically being around 10".

Furthermore, some of the comets in the dataset used here were on orbits unusual for asteroids (e.g. C/2001 OG_{180} (French, 2002)). Theses were studied in more detail by other observers, who did not find any indication of activity within a longer time period.

In this work, observations of 14 different observers are taken into account. The data used here were obtained from semi-professional or professional observatories, using reflector telescopes between 0.36 m and 1.8 m in aperture and equipped with a CCD camera. The observations are done in broadband V or R filters or in white light. Unfortunately, further specifications on the instruments and methods used for the observations considered here are often not available. In cases where the observers give that information, the pixel scale is around 1" per pixel and the limiting magnitude around 21^{mag}. In order to compare the observations of the different observers, the photometric accuracy is discussed in the following section. Photometric data of other observers are not included in this work to determine nuclear radii, since their data is not sufficient to perform the photometric analysis. Nevertheless, the data of additional observers were considered in classifying a comet as active or inactive.

13.3 Photometric Analysis

The main purpose of the large asteroid search programs is the detection of objects and the determination of their orbits. Thus, the magnitudes published by some observers are likely to be affected by large uncertainties. In order to determine the uncertainty of the given magnitudes, three effects are considered:

1) The typical variation of the magnitude estimates for one object observed by one observer within one night.

2) The systematic deviation in magnitudes between different observers observing the same object at approximately the same time.

3) For objects with well-known size, albedo, and phase function, a theoretical magnitude is calculated and compared to the observed magnitudes. This step provides an

estimate of uncertainty in terms of absolute brightness.

In order to study these three points, observations of asteroids published in Minor Planet Electronic Circulars[10] or the Minor Planet Center Extended Computer Service in the years 2003 and 2004 are considered. In total, 1126 single observations of 126 different asteroids were analysed. The asteroids were selected only with respect to suitable observations to perform this study, thus containing near-Earth objects, main-belt asteroids and transneptunian objects. This choice ensures the presence of objects with different colours within the ensemble. By doing so, the influence of different colours upon the photometric accuracy obtained by using a single filter bandbass is taken into account. Furthermore, near-Earth asteroids tend to have higher amplitudes in their lightcurves than main-belt asteroids. The shape of cometary nuclei is poorly known, but amplitudes up to 0.5^{mag} in lightcurves of cometary nuclei are observed (28P/Neujmin 1, Delahodde *et al.* (2001)) and axis ratios up to 1:2.5 are confirmed by spacecraft flybys (19P/Borrelly, Buratti *et al.* (2002)). Thus, this sample appears to be appropriate for including the influence of lightcurve variations on the photometric accuracy.

All asteroids considered were observed by the different observers nearly simultaneously. It is therefore possible to compare magnitude estimates made by different observers. "Nearly simultaneously" means that no significant change in the observing geometry (heliocentric distance, geocentric distance and phase angle) occured during the observations. The corresponding time interval covered ranges from one hour (for near-earth objects) up to 26 hours (for distant objects).

Observations of one observer obtained nearly simultaneously were averaged to a mean magnitude value, which we will refer to as a "set of observations". In this way, a total of 1126 individual observations could be reduced to 318 sets of observations. In cases when more than five single observations were used to derive the mean magnitude, the standard deviation was calculated as an estimate for the scatter of magnitudes of a particular set of observations. 61 such sets of observations were treated in total. The average uncertainty within one set of observations is $0^{\mathrm{m}}.26$, while approximately 66% of all sets of observations have a deviation below $0^{\mathrm{m}}.30$. Thus, $0^{\mathrm{m}}.30$ is a good estimate of the 1σ uncertainty of a single observation. This value includes the influence of the weather conditions as well as effects due to the rotation of the observed object.

In order to study possible offsets between different observers, the difference between the magnitude values from comparable sets of observations was determined. The mean magnitudes for each set of observations were computed and offsets of mean magnitudes between observers were calculated. These offsets are caused by different filter systems used as well as measurement uncertainties. All observations were subsequently normalized to a reference observer (observatory code[11] 854) with the widest data coverage. Thus all

---

[10] `http://cfa-www.harvard.edu/iau/services/MPCServices.html`

[11] The International Astronomical Union gives to observatories a code consisting of one to three ASCII

data are also normalized with respect to the filter system used by observer 854 (R-filter). The effects of colour of the individual comets as well as rotational modifications of their lightcurves are neglected, since no information on this is available. These effects are however reflected in the resulting large error bar of the mean magnitude of each set of observations after normalization. This error is derived from the analysis of a large number of asteroids observed by the same observer.

In Tab. 30, the mean offsets in magnitude relative to observer 854 are presented. The results for all but four different observers are in agreement within the error bars. Nevertheless, to be consistent, the offset between the observers presented in Tab. 30 were applied to all observations used in this work. The mean uncertainty of the offset between different observers is $0^{\rm m}.46$. Thus, we assume $0^{\rm m}.50$ as the uncertainty of the offsets between different observers. This uncertainty includes e.g. different methods of photometry or different bandpasses (different V and R filters or white light), as discussed above. In the following, the total uncertainty in relative calibration is assumed to be the quadratic sum of the uncertainty of the single set of observations and of the uncertainty of the offsets between the different observers, leading to a total magnitude error of $0^{\rm m}.58$.

Although the data are now calibrated relative to each other, errors can still affect the absolute calibration of the data since the magnitudes are not calibrated in terms of a standard photometric system. In order to test the error in the absolute brightness of the observations, the corrected magnitudes of well-known objects available from the relevant observers can be compared with the theoretical magnitude computed from the known observing geometry and the properties of the observed body. This test was performed for the two asteroids Mathilde and Eros, since their sizes, albedos, and phase functions, are well-known from spacecraft flybys. Also, a larger number of ground-based observations from the observers relevant for this study are available for these two asteroids. Observations during the relevant years 1998 to 2004 were obtained at phase angles between about 10° and 30° for Mathilde and between 10° and 53° for Eros. Phase corrections of 0.04 magnitudes per degree and 0.035 magnitudes per degree, respectively, have been applied. The magnitudes for the time of observations were computed based on the known asteroid properies (i.e. size, albedo, and phase function) and observing geometry. The differences between observed magnitudes and theoretical magnitudes are plotted for the various observers in Fig. 57. The dashed line indicates the mean value, the dotted lines show the estimated 1σ photometric uncertainty of $0^{\rm m}.58$. All results from different observers included are within or only slightly outside the 1σ error.

After excluding all comets not satisfying the criteria mentioned before, there are 29 short-period comets and 19 long-period comets in the database considered here. The comets are listed in Tab. 31, together with the observing cirumstances (heliocentric and geocentric distance, phase angle), the time between the discovery of the object and the

---

signs. This code is used in this work to refer to observations from different observatories.

discovery of its activity, the time of observation relative to the date of the discovery (negative values mean pre-discovery observations), and the magnitude observed. It can be seen, that if the applied limit of more than 10 days between the discovery of the object and the discovery of its activity is modified towards a larger value, the number of objects in the database decreases. Nevertheless, no systematic trend of the nucleus size with the time limit used can be found. Thus, the results of this work do not depend on the applied value of 10 days.

In cases where several sets of observations are suitable for further analysis, they are all used for the size determination. The final column of Tab. 31 refers to the dynamic classes. The long period comets are divided into dynamically old and new comets. Comets on parabolic and hyperbolic orbits are identified as dynamically new in this work, while the dynamically old comets regarded in this study all have semi-major axes smaller than 1300 AU. The classification of comets as dynamically new in this work is somewhat uncertain, since the orbits of these objects may be subject to large uncertainties and possible recent perturbations of the orbits by the giant planets are not ruled out.

Table 30: Mean difference between magnitude estimates of different observers (indicated by their observatory code) relevant for comet observations in this work. The first column shows the observers between which the difference was computed, the second column presents the difference in magnitude and its uncertainty, Δm, and the third one shows the number of sets of observations, n, used to compute the mean difference.

difference for observers	Δm	n
926 − 854	−0.14 ± 0.42	14
649 − 854	−0.18 ± 0.31	14
673 − 854	−0.13 ± 0.58	22
704 − 854	0.26 ± 0.34	12
644 − 854	0.09 ± 0.38	10
A50 − 854	−0.17 ± 0.54	8
699 − 854	−0.32 ± 0.25	12
I05 − 854	−0.09 ± 0.82	6
703 − 854	−0.02 ± 0.59	7
711 − 854	−0.23 ± 0.83	10
291 − 854	0.35 ± 0.35	22
691 − 854	0.31 ± 0.29	11
608 − 854	1.19 ± 0.41	10

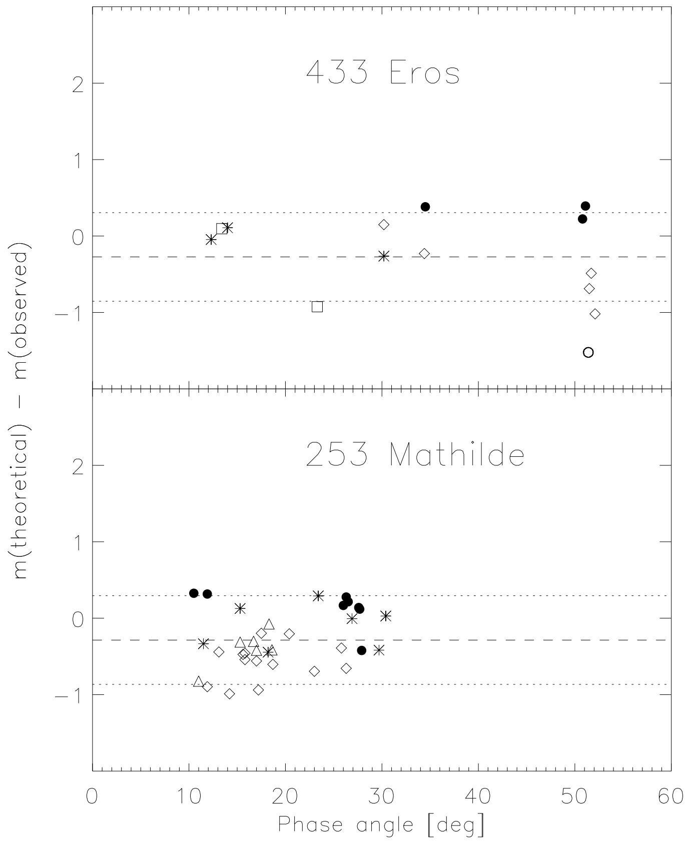

Figure 57: The difference between theoretical and observed magnitudes for asteroids Eros and Mathilde versus the phase angle. The different symbols mark observations by the following observers: squares - 649, open circles - 673, stars - 644, diamonds - 699, triangles - 703, filled circles - 608. The dashed line marks the mean value, the dotted lines mark the estimated error of $0^m.58$. *For further details see text.*

13.4 Nucleus Size Determination

A relation between the observed magnitude m and the nucleus radius R_N is given by the equation (Russell, 1916)

$$R_N = \sqrt{2.24 \cdot 10^{22} \frac{r_h^2 \Delta^2}{p_v} 10^{\,0.4(m_\odot - m + \phi(\beta))}} \, . \tag{160}$$

Here, r_h and Δ denote the heliocentric and the geocentric distance, $m_\odot$ the solar magnitude and p_v the geometric albedo of the cometary nucleus. The function $\phi(\beta)$ represents a correction for the phase angle β at the time of observation.

For p_v, the commonly used value of 0.04 is applied, as determined for comet Halley. The albedo of cometary nuclei is poorly known, but results from other space missions to comets indicated a value similar to p_v for the nuclei of the comets Borrelly and Wild 2, as well as the results from combined groundbased optical and infrared observations (Abell *et al.*, 2005).

Unfortunately, very little is known about the phase function of cometary nuclei. A detailed phase curve between approximately 0.7° and 14.7° is available for comet 28P/Neujmin 1 (Delahodde *et al.*, 2001). This phase curve could be well-fitted by a Shevchenko law, having the form

$$m(\beta) = m(0) - \frac{a}{1+\beta} + b \cdot \beta \, . \tag{161}$$

This law consists of a linear correction in magnitude, m, with phase angle plus an additional term for fitting an opposition spike and has no deeper theoretical background. For the parameters a and b, the values determined for comet Neujmin 1 by Delahodde *et al.* (2001) are used in this work, namely $a = 0.42 \pm 0.05$ and $b = 0.020 \pm 0.008$ mag per degree. This phase function is confirmed for comet Neujmin 1 up to nearly 15° only. Information on the phase function at phase angles larger than approximately 25° is not available for cometary nuclei and is rare even for asteroids. Nevertheless, objects for which a complete phase function could be determined, e.g. the asteroids Mathilde (Clark *et al.*, 1999) and Eros (Clark *et al.*, 2002) and Mercury (Mallama *et al.*, 2002), showed a linear trend up to phase angles of more than 60°, so the Shevchenko law is applied to all observations in the dataset given in Tab. 31, ranging up to nearly 60°.

Commonly, a linear correction is applied for studies of comet nucleus sizes. With 0.04 magnitudes per degree, this correction is steeper than the one used here. Therefore, the obtained nucleus sizes tend to be smaller than the values derived with the linear correction for the phase angle. Nevertheless, since both the short-period as well as the long-period comet size distribution would be slightly shifted to larger nucleus radii, the principle results of the presented work are hardly affected by the choice of the phase function. And since the dataset used here covers an extremely wide range of phase angles, the Shevchenko law appears as a more realistic choice.

From equation (160), the uncertainty in the nuclear radius is related to the uncertainty in magnitude by the relation

$$\sigma(R_N) = 0.46 \cdot R_N \cdot \sigma(m) \, . \tag{162}$$

An uncertainty in magnitude of $0^{\mathrm{m}}.58$ therefore corresponds to an uncertainty of 27% in the nuclear radius.

The resulting nuclear radii for the comets in the analysed data set are also presented in Tab. 31.

13.5 Check for Undetected Activity

The observations used in this work were obtained using quite small telescopes with apertures of around one meter. Thus, for faint objects, cometary activity may remain undetected when the signal-to-noise ratio is low. In addition, no data suitable for a detailed study of the point spread functions of the images obtained are availabe. Undetected activity would, however, lead to an increase of the derived nuclear radii with decreas-

Table 31: Overview on the dataset analysed in this work. The comet's systematic number and name are shown. ΔT_{dis} *denotes the time between the discovery of the object and its activity, given in days,* ΔT_{obs} *is the time between the given observation and the day of discovery, given in days. Negative values imply pre-discovery observations. The selection criterion of at least 10 days between discovery of the object and discovery of its activity corresponds to* $\Delta T_{dis} - \Delta T_{obs} > 9$ *days. m is the observed magnitude, obs states the observatory code.* r_h, Δ *and* β *denote the heliocentric and the geocentric distance and the phase angle at the time of observation.* r_h^* *is the heliocentric distance at the time of the discovery of the cometary activity. The resulting nuclear radius,* R_N *is shown, the uncertainty of the nuclear radius is ± 27%. The column DC displays the dynamical class of the comet (DN - dynamically new long period comets, DO - dynamically old long period comets, JF - Jupiter family, HT - Halley type).*

Comet		ΔT_{dis}	ΔT_{obs}	m	obs	r_h [AU]	Δ [AU]	β [°]	r_h^* [AU]	R_N [km]	DC
C/2004 X2	LINEAR	1	-19	18.30	699	3.87	3.64	14.7	3.91	8.56	DO
P/2004 VR_8	LONEOS	16	0	17.60	699	3.28	2.34	6.6	3.20	5.90	JF
			0	17.87	644	3.28	2.34	6.6		6.29	
P/2004 WR_9	LINEAR	15	0	18.60	704	1.98	1.04	11.9	1.95	1.38	JF
C/2004 RG_{113}	LINEAR	75	-18	19.70	704	3.02	3.21	18.4	2.31	4.19	DO
			0	19.34	704	2.87	2.86	20.3		4.26	
162P/	Siding Spring	33	0	13.88	I05	1.28	0.48	44.7	1.23	4.22	JF
160P/	LINEAR	43	0	19.30	704	2.21	1.40	20.3	2.10	1.64	JF
			7	18.00	699	2.19	1.33	18.4		2.11	
C/2004 K3	LINEAR	13	0	19.52	704	1.22	0.58	55.9	1.15	0.47	DO
			1	19.48	704	1.21	0.58	56.5		0.48	
			2	19.07	854	1.21	0.57	57.0		0.51	
			2	19.57	926	1.21	0.57	57.0		0.38	
C/2004 HV_{60}	Spacewatch	13	1	21.80	291	3.29	2.30	3.7	3.34	1.10	DN
P/2004 EW_{38}	Catalina-LINEAR	31	-76	19.98	704	1.83	1.64	32.4	2.20	1.30	JF
			-50	19.88	704	1.89	1.44	30.8		1.22	
			-50	19.20	699	1.89	1.44	30.8		1.27	
			0	20.03	703	2.06	1.17	16.2		0.77	
			2	19.90	704	2.07	1.17	15.3		0.93	
C/2004 DZ_{61}	Catalina-LINEAR	27	-1	19.10	703	2.32	1.48	16.0	2.18	1.68	DO
			1	18.10	A50	2.31	1.44	15.2		2.39	
C/2004 D1	NEAT	3	-57	19.80	704	7.62	6.74	3.6	7.32	17.90	DN
P/2004 CB	LINEAR	56	2	18.00	673	1.22	0.49	50.5	0.91	0.64	JF
P/2004 DO_{29}	Spacewatch-LINEAR	28	-6	19.10	699	4.32	3.37	4.1	4.26	5.41	JF
P/2003 HT_{15}	LINEAR	59	-77	20.73	608	2.71	2.29	20.6	4.86	2.61	JF
P/2003 QX_{29}	NEAT	1	-405	19.47	644	4.31	3.40	6.7	4.57	5.75	JF
P/2003 SQ_{215}	NEAT-LONEOS	117	-6	19.60	644	2.79	1.87	10.1	2.37	2.01	JF
			0	19.10	644	2.76	1.88	12.1		2.57	
C/2003 WT_{42}	LINEAR	40	2	18.80	691	8.15	7.18	1.5	7.95	31.32	DN
P/2003 WC_7	LINEAR-Catalina	44	29	17.80	703	1.75	1.23	33.1	1.66	2.25	JF
159P/	LONEOS	45	0	18.80	699	3.73	2.80	6.2	3.69	4.59	JF
			5	19.43	644	3.73	2.77	4.9		4.03	
P/2003 UY_{275}	LINEAR	32	20	19.07	644	2.20	1.24	7.5	2.26	1.30	JF
C/2002 X1	LINEAR	2	-287	20.67	644	5.56	4.66	4.7	2.95	5.70	DN
P/2002 LZ_{11}	LINEAR	511	53	18.57	608	2.53	2.47	23.4	2.78	7.31	JF
			133	17.40	699	2.74	1.81	9.7		4.33	
C/2002 V2	LINEAR	2	-671	19.45	608	8.77	7.87	2.8	2.51	42.67	DN
C/2002 VQ_{94}	LINEAR	290	1	18.67	649	10.02	9.16	3.0	8.84	43.44	DO
			1	18.80	711	10.02	9.16	3.0		39.98	
			1	18.60	926	10.02	9.16	3.0		45.69	
			-16	19.13	644	10.22	9.60	4.6		38.66	
C/2002 T7	LINEAR	14	2	17.20	649	6.87	6.44	7.7	6.76	44.17	DN
P/2002 T6	NEAT-LINEAR	23	0	20.37	644	3.84	2.86	2.8	3.77	2.68	JF
			-6	20.30	644	3.86	2.89	4.4		2.89	
C/2002 L9	NEAT	18	0	17.70	644	8.21	7.36	4.1	8.15	51.67	DN
			2	17.60	644	8.20	7.34	3.9		53.71	

Table 31 (continued):

Comet		ΔT_{dis}	ΔT_{obs}	m	obs	r_h [AU]	Δ [AU]	β [°]	r_h^*	R_N [km]	DC
P/2002 JN_{16}	LINEAR	8	-25	18.90	644	2.01	1.09	15.9	1.90	1.23	JF
P/2002 BV	Yeung	104	1	19.03	691	2.27	2.32	24.7	2.28	3.37	JF
			-827	20.70	691	4.78	3.84	4.4		4.38	
			-821	20.90	691	4.78	3.81	2.9		3.86	
C/2002 J5	LINEAR	1	-282	20.70	608	7.87	6.88	1.7	6.70	18.25	DN
P/2002 EJ_{57}	LINEAR	49	0	18.80	644	2.72	1.76	6.4	2.85	2.55	JF
			-25	19.50	644	2.68	1.70	3.9		1.69	
			-17	19.30	644	2.69	1.70	0.7		1.68	
C/2002 B2	LINEAR	11	1	18.07	649	3.89	3.40	13.4	3.88	9.40	DN
C/2002 A2	LINEAR	3	-21	18.43	644	4.71	3.78	4.2	4.71	10.90	JF
158P/	LINEAR	805	12	20.30	644	4.61	3.68	5.2	4.64	4.46	JF
			420	20.30	644	4.60	3.69	5.6		4.48	
			435	19.57	644	4.60	3.83	8.5		6.75	
P/2001 WF_2	LONEOS	91	0	18.90	699	1.39	0.43	17.0	1.00	0.28	JF
C/2001 OG_{108}	LONEOS	167	0	18.70	699	3.26	2.98	18.0	1.41	5.07	HT
			1	19.13	644	3.25	2.96	18.0		4.98	
			3	18.70	649	3.23	2.90	18.1		5.22	
			4	18.13	649	3.22	2.88	18.1		6.72	
			26	19.17	608	3.09	2.56	17.7		6.65	
			34	17.80	644	2.90	2.14	15.2		5.76	
			53	16.80	699	2.70	1.77	9.8		5.51	
			63	16.57	644	2.59	1.62	7.2		6.30	
			81	17.87	608	2.40	1.47	11.9		5.09	
			87	16.20	699	2.32	1.45	15.1		5.40	
C/2001 RX_{14}	LINEAR	38	-13	18.70	699	5.66	5.12	9.1	5.24	13.81	DN
			-13	19.27	644	5.66	5.12	9.1		12.83	
			8	18.27	644	5.49	4.70	7.0		17.67	
			9	18.20	699	5.48	4.68	6.8		14.98	
C/2001 G1	LONEOS	1	-93	18.93	608	8.41	8.33	6.7	8.31	58.54	DN
C/2001 A2	LINEAR	13	0	17.80	699	1.76	1.08	30.4	2.28	1.69	DN
150P/	LONEOS	80	0	17.20	699	2.08	1.45	25.4	2.24	3.37	JF
			22	16.67	854	1.98	1.17	21.3		3.68	
148P/	Anderson-LINEAR	61	2	18.50	699	2.57	1.58	3.7	2.24	1.98	JF
			7	18.60	699	2.54	1.54	2.4		1.77	
C/2000 SV_{74}	LINEAR	25	12	16.20	699	6.07	5.09	2.1	5.98	41.81	DN
C/2000 OF_8	Spacewatch	36	0	20.88	691	4.56	3.57	3.6	4.26	3.53	DN
			1	21.03	691	4.55	3.56	3.4		3.27	
P/1999 XN_{120}	Catalina	84	-26	18.38	703	3.37	2.40	4.3	3.30	4.82	JF
			-23	18.10	699	3.37	2.39	3.4		4.68	
P/1999 DN_3	Korlevic-Juric	84	33	17.60	699	3.95	2.96	2.5	3.97	8.39	JF
			50	17.60	699	3.96	2.97	2.5		8.44	
P/1998 VS_{24}	LINEAR	55	-14	18.50	699	3.41	2.49	7.8	3.41	4.37	JF
139P/	Vaisala-Oterma	18	7	17.40	699	3.39	2.41	1.9	3.40	6.32	JF
P/1998 QP_{54}	LONEOS-Tucker	17	0	17.10	699	1.92	1.02	18.9	3.42	2.15	JF
			1	17.30	699	1.92	1.01	18.5		1.94	

ing heliocentric distance, r_h, since a comet is likely to be more active closer to the Sun. Therefore, it was studied whether such an increase of nuclear radii with r_h can be found. This test was possible for only five comets, the observations of which cover a range in heliocentric distance of more than 0.4 AU. Their nuclear radius versus heliocentric distance is shown in Fig. 58. The data for comet P/2003 SQ_{215} show an increase in nucleus radius with decreasing r_h. Thus, for this comet it cannot be excluded that it has already been active at the time of first observation and the derived nucleus radius is therefore an upper limit only. For the other comets in Fig. 58, no clear trend is obvious. For comet C/2001 OG_{108}, the two displayed values around 2.2 AU where obtained when cometary activity was detected. Because of the large photometric uncertainty, the photometry is not sensitive to coma contributions as long as the activity is weak.

Clearly, a larger number of magnitude estimates for the comets in this study would result if all available magnitude determinations were to be included instead of only those from observers that passed the photometric analysis discussed above. In this case, the

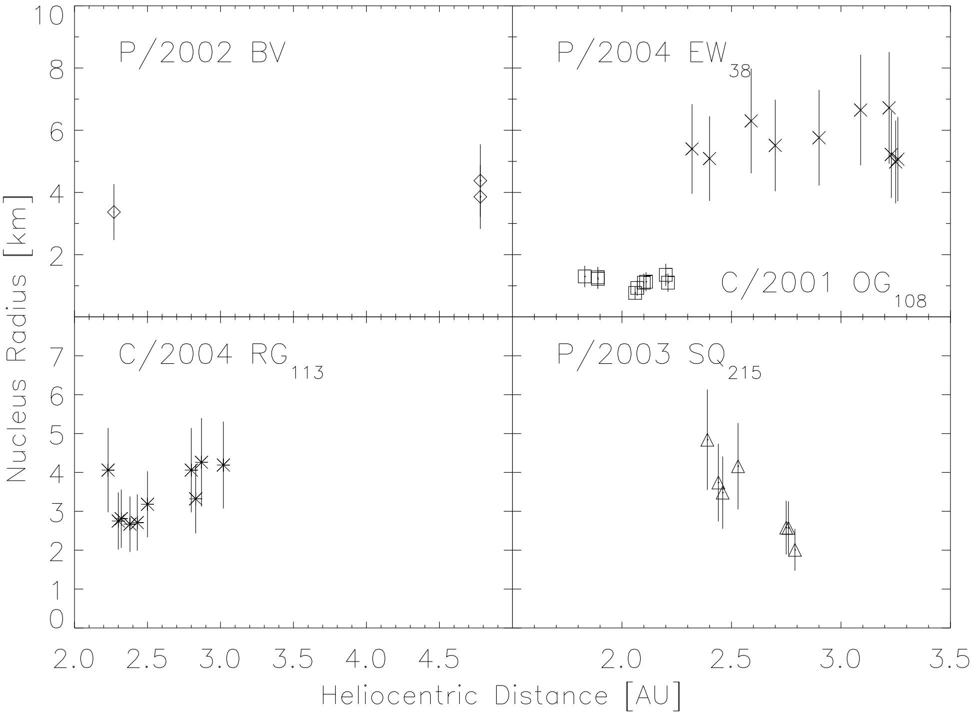

Figure 58: Nucleus radius versus heliocentric distance for five comets from the dataset.

scatter of the data points becomes larger. Examples of lightcurves including all available magnitude values are given in Fig. 59 to Fig. 62. The displayed data points are normalized to 1 AU of heliocentric and geocentric distance, but are not corrected for different phase angles. The phase angles for each data point are included in the Figures. For objects without cometary activity, the lightcurves would be constant. The lightcurves of the comets in the dataset range from those containing clear periods of cometary activity (Fig. 59) to those with no significant impact of the observed activity on the lightcurve within the large scatter (Fig. 60). Other lightcurves are inconclusive since the scatter of the data points is too large to decide whether the increase in the lightcurve starts with the detection of activity or if a general trend is present for all observations (Fig. 61). For some comets, activity was detected during a strong decrease in the phase angle (Fig. 62). Since at smaller phase angles, the brightness of the dust coma should be larger, the activity could have been present during previous observations but could have remained undetected.

The largest nuclear radii were determined for long-period comets at large geocentric distances. Since the spatial resolution of the cometary coma decreases with increasing geocentric distance, activity would be more difficult to detect at larger geocentric distances. In order to limit the influence of the reduced spatial resolution, a minimum time period of 10 days between the time of discovery of the object and its activity is applied. Objects like C/2002 VQ_{94} with 290 days between the object discovery and the discovery of activity are examples that long period comets can indeed remain inactive for a long time.

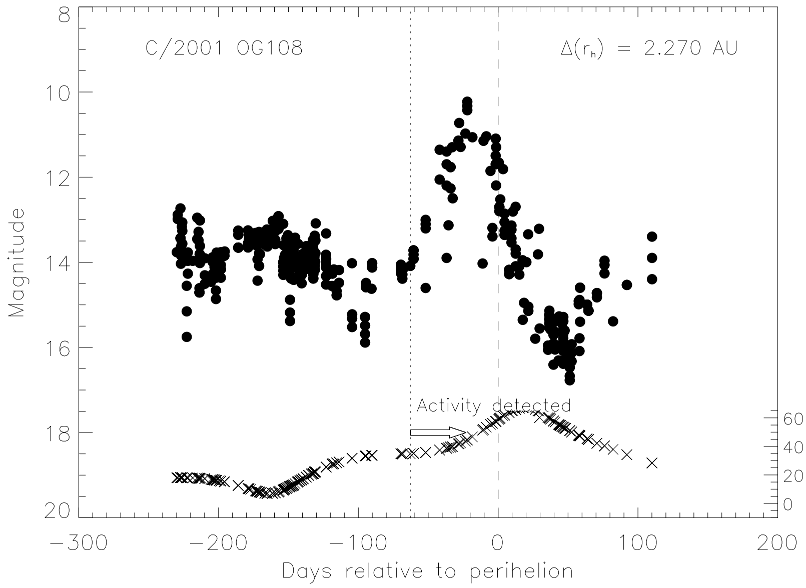

Figure 59: Magnitudes (black circles) from various observers corrected for the heliocentric and the geocentric distance versus time for comet C/2001 OG_{108}. The phase angles (crosses) for each data point are presented in the lower part of the diagram with a scale to the right (in degrees). The time of detection of activity is indicated. $\Delta(r_h)$ shows the range of the heliocentric distance covered by the data points.

Activity was then detected at $r_h = 8.84$ AU. Nevertheless, the lower spatial resolution at large geocentric distances always remains a limiting factor in ground-based observations. If the long-period comets included here were indeed affected by undetected activity, the derived radii would be only upper limits.

For one cometary nucleus in the dataset analysed in this work, C/2001 OG_{108}, albedo and size measurements are available which can be compared with the result derived in this work. Abell *et al.* (2005) give an albedo of 0.043 ± 0.010 and a mean radius of (7.6 ± 1.0) km, derived from simultaneous optical and infrared observations. This value for the radius is slightly larger than the value of (5.67 ± 1.53) km derived in this work. The difference in albedo is small, but a different correction for the phase angle was used, which led to the somewhat larger value for the nuclear radius.

Even without information on the point spread function of the observed object, objects with cometary activity can be identified since their brightness varies not with r_h^{-2}, but with a smaller exponent. Thus, additional observations of the comets in the dataset used could help to estimate the influence of the cometary activity on the determined nuclear sizes. Because of the large uncertainty in the magnitudes, a sufficiently large difference in heliocentric distance compared to the value at the date of the observation is necessary. Compared to the uncertainty of 0.58^{mag}, an increase of the heliocentric distance by a factor of 2 or larger is required to discriminate between the absence of activity and activity varying with r_h^{-2} (meaning a total variation in brightness with r_h^{-4}). Tab. 33 lists all

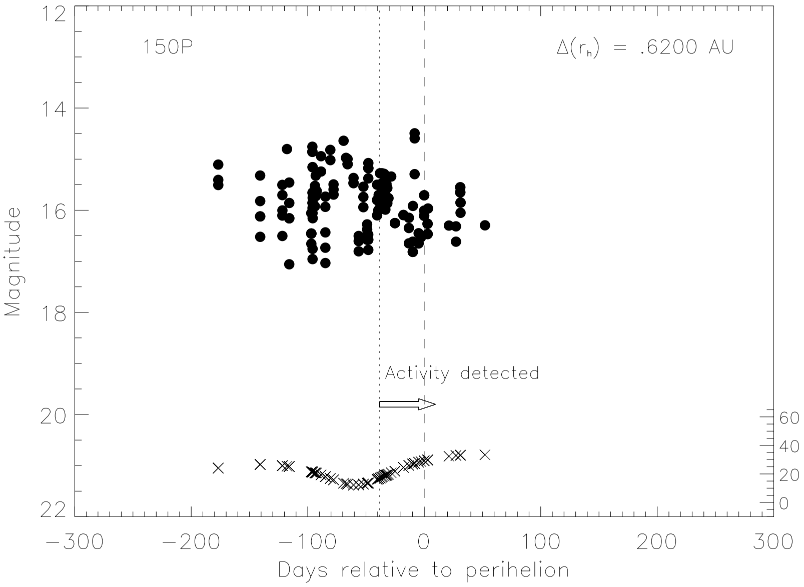

Figure 60: As for Fig. 59, but for comet 150P.

comets in the dataset for which the heliocentric distance on April 1, 2007 (the beginning of ESO observing period 78) is at least twice its value at the time of the observations used for the nuclear size determination. Tab. 33 shows the nuclear sizes of these comets, the heliocentric distance at the time of the observation used for the radius determination and the heliocentric distance on April 1, 2007. Two values for the magnitude of the comets are shown for April 1, 2007, one assuming that the nuclear radius is correct and no influence of activity on the observations is present, the other assumes an activity varying with r_h^{-2}. The magnitudes are determined for zero phase angle and would have to be adapted to the actual observing geometry for observations in the future. Since the change in heliocentric distance is large and comets in the dataset may be on poorly determined heliocentric orbits, the area in the sky (in squarearcsec) that is covered by the 3σ error ellipse is also listed. The values are computed using the HORIZONS ephemeris service and represent the area in the sky that has to be covered by observations to ensure that a potential non-detection of the comet is not caused by a poor pointing of the telescope but indeed by an unexpected fast fading of the target.

Four comets that are suitable for searching for the influence of activity are printed in bold in Tab. 33. These comets have expected magnitudes, both assuming activity and no activity, that are accessible with medium to large telescopes within reasonable exposure times, and the 3σ ellipse of these comets are within the typical field of view of a telescope (around 6' × 6' for VLT/FORS or ESO 3.6m/EFOSC2). Unfortunately, only one of the comets with a very large nuclear radius (C/2000 SV_{74} with a nuclear radius determined to be 41.81 km) is among the subset of comets suitable for future observations. Photometry of this comet could allow the observer to confirm the presence of large long-period comets.

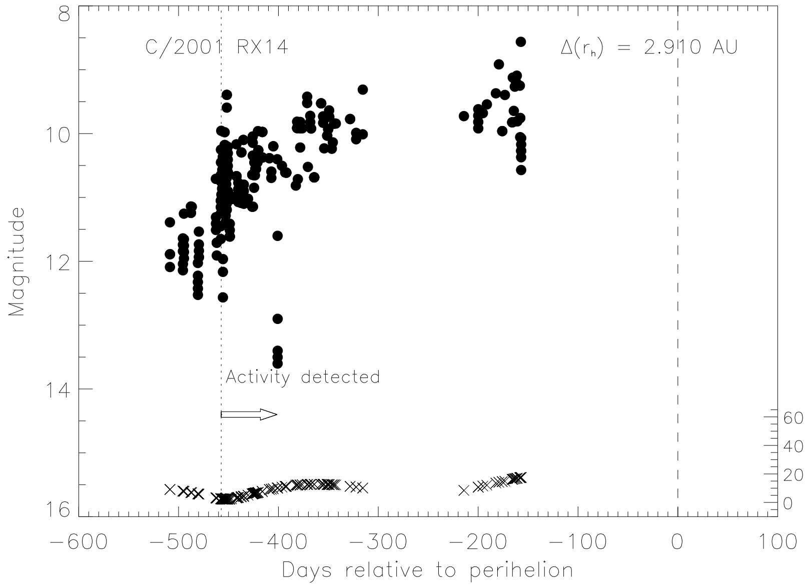

Figure 61: As for Fig. 59, but for comet C/2001 RX_{14}.

Furthermore, studying only the comets from the subset highlighted in Tab. 33 places a constraint upon the applicability of the described method of nuclear size determination.

13.6 Comparison of the Size Distributions

In Fig. 64, the size distributions for the long-period and the short-period comets in the presented dataset are plotted. The histograms show the number of comets with nuclear sizes within intervals of 2 km, normalized to the total number of comets. For comparison, the size distribution derived by Meech *et al.* (2004) is shown. Their dataset includes 11 Jupiter family comets and one Halley type comet (109P/Swift-Tuttle, the largest nucleus in this dataset).

For long-period comets, nuclei with all sizes up to 60 km exist, while for short-period comets, only nuclear radii smaller than 11 km are present in the dataset. That large long period comet nuclei exist has already been suggested by observations of comet C/1995 O1 Hale-Bopp, for which the nuclear radius estimates are 20 - 35 km (Altenhoff *et al.* (1999), Sekanina (1999)). If such large objects existed among the short-period comets, they would be easy to discover. Therefore, the lack of large nuclei among the short-period comets is probably real and not an observational selection effect.

The nuclear size distribution of short-period comets shows a peak at small sizes while among the long-period comets in the analysed dataset this peak is far less distinct (see Fig. 64). A large fraction of the newly discovered long-period comets have perihelion distances beyond the orbit of Jupiter, and thus small nuclei are more difficult to discover for these objects than for short-period comets. The lack of small-sized long-period comets could therefore be an observational selection effect, and the nearly equally-distributed

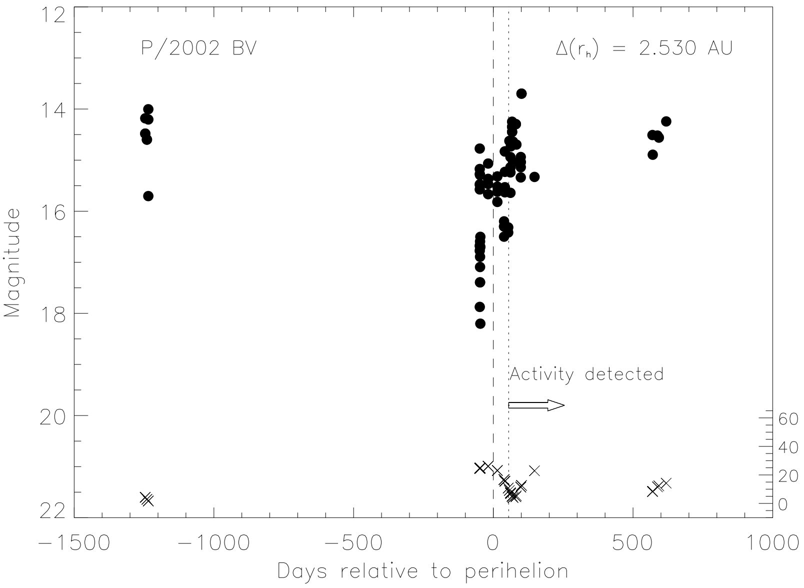

Figure 62: As for Fig. 59, but for comet P/2002 BV.

sizes seen in the upper panel of Fig. 64 may not reflect the true size distribution. In order to estimate that effect, the analysis was repeated for long-period comets with perihelion distances inside the orbit of Jupiter (i.e. $q < 5.2\,\mathrm{AU}$). These long-period comets penetrate the inner solar system in the same range as short period comets. Furthermore, the perihelion distances of short-period and these long-period comets are distributed roughly homogenously in the heliocentric distance range of 0.5 AU and 5 AU (see Tab. 31). Since the mechanism that drives the sudden onset of activity of the comets in the dataset is unknown, it is assumed here that there is no correlation between the heliocentric distance at which the activity starts and the size of the nucleus.

In total, 14 long-period comets with perihelion distances inside Jupiter's orbit have been compared to the size distribution of the short-period comets (Fig. 65). Now, the size distribution of the long-period comets indeed shows a more distinct peak at smaller sizes. This fact indicates that observational selection effects indeed could bias the size distribution of long-period comets towards larger sizes. However, large nuclei are also present in this data subset. The total number of objects is too small to definitely conclude whether a large number of small long-period comet nuclei exist or not. Nevertheless, the data clearly show that the size distribution of long-period comets is significantly extended to large sizes of tens of kilometers, which is not found for short-period comets.

The cumulative size distributions for long-period and short-period comet nuclei were fitted by a law of the form:

$$N_R = \beta\, R_N^{-\alpha} \tag{163}$$

where N_R is the number of comets with nuclear sizes larger than R_N and α and β are fit parameters. In Fig. 63, the normalized cumulative size distributions for short-period and long-period comets are shown, together with a power law fit. Within the nuclear size interval of 2 km and 5 km, as used by Meech *et al.* (2004), one obtains $\alpha = 0.77 \pm 0.24$ for the short period comets. For the long period comets, $\alpha = 0.31 \pm 0.05$ is obtained in an interval between 2 km and 40 km.

If only the long-period comets with perihelion distances inside Jupiter's orbit are taken into account, the slope of the cumulative size distribution reaches $\alpha = 0.52 \pm 0.10$, i.e. similar to the slope of the short-period comets in our dataset. Therefore, it cannot be ruled out that the difference in the slopes is caused by a selection effect towards larger long-period comets.

The slopes derived for short-period comets in the dataset used here are significantly smaller than those found by Meech *et al.* (2004) over the same size interval. Meech *et al.* (2004) give $\alpha = 1.91 \pm 0.06$. Their data set is a combination of ground-based observations and published nuclear sizes derived from HST measurements (e.g. Lamy *et al.* (2000)), which include very small radii. Using only nuclear radii determined in by their ground-based observations, corresponding to 12 comets, $\alpha = 1.22 \pm 0.19$ is obtained. Tancredi *et al.* (2006) published nuclear size estimates for 105 Jupiter family comets. In this dataset the nuclear size determinations of 27 comets were classified as quality 1 or 2 (out of 4 quality classes in their work). From these comets they derive $\alpha = 2.20 \pm 0.14$, while from all 105 comets $\alpha = 2.40 \pm 0.08$. Lowry *et al.* (2003) give a value of $\alpha = 1.6 \pm 0.1$ from the analysis of 32 Jupiter family comets. Comparing the values of the slopes of the cumulative size distribution found in the literature, they seem to depend strongly on the selected dataset and are thus, at the present time, not well-constrained. The future analysis of a larger, representative and homogeneous dataset is mandatory for a more secure determination of the size distributions. Nevertheless, the result of this work imply that the available nuclear size distributions for short period-comets are not consistent with the size distribution obtained for long-period comets.

For long-period comets, no estimates of the size distribution have yet been published. Nevertheless, for five comets of this type, nuclear radii have been determined, ranging from 0.37 km (C/1983 J1) to approximately 30 km (C/1995 O1). A summary is presented in Tab. 32. This dataset is somewhat affected by bias effects, since most of the comets were studied because of their prominent apparition in the sky. The apparent brightness can be caused either by a strong cometary activity due to a large nucleus (e.g. comet C/1995 O1 Hale-Bopp), or by a close approach to Earth. This was the case for comets Hyakutake, IRAS-Araki-Alcock and Sugano-Saigusa-Fujikawa (see Tab. 32). The correlation between the minimum geocentric distance of the comets and their nuclear sizes is obvious, so this dataset cannot be regarded as representative. Nevertheless, the large radius of comet C/1995 O1 Hale-Bopp confirms the existence of large long-period comets.

Meech *et al.* (2004) selected long period-comets based on their well documented lightcurves hence derived upper limits for five comets, all below 13 km. From the size distribution for long-period comets derived in this chapter of the presented work, it follows that about 54% of the comets should be larger than the mean upper limit of 8.2 km from Meech *et al.* (2004). If only the long-period comets with perihelion inside Jupiter's orbit are taken into account, 37% of the comets are still larger than this detection limit. It is unlikely that five comets arbitrarily chosen are all beyond the detection limit. An explanation for this could be that the comets studies by Meech *et al.* (2004) have a higher content of volatile material and thus are more active than the comets with unusual variations in activity studied in this work. If the behaviour in activity of the comets in the dataset of this work is caused by a low fraction of ices, small nuclei remain undetected, while small nuclei with high ice content develop significant activity that makes the observations of the objects possible.

A possible reason for the disagreement of the nuclear size distributions could be an observational selection effect. The observed magnitude distribution of a cometary population, $m_{obs}(a, e, i, H)$, can be related to the true distribution, $m_{true}(a, e, i, H)$, by the equation (Whitman et al. 2006)

$$m_{obs}(a, e, i, H)\,\mathrm{d}a\,\mathrm{d}e\,\mathrm{d}i\,\mathrm{d}H = B(a, e, i, H) \cdot m_{true}(a, e, i, H)\,\mathrm{d}a\,\mathrm{d}e\,\mathrm{d}i\,\mathrm{d}H\ . \tag{164}$$

Here, a, e, i and H denote the semi-major axes, the eccentricity, inclination and absolute magnitude of a comet, respectively. The function $B(a, e, i, H)$ is the observational bias function, that gives the fraction of comets having the orbital parameters a, e, i and the absolute magnitude H, that are discovered by the sky surveys. If it is furthermore assumed that the value of H is independent from the orbital parameters of a comet, the orbital elements and the absolute magnitude can be separated into $m_{true}(a, e, i, H)$:

$$m_{true}(a, e, i, H) = f(a, e, i) \cdot g(H)\ . \tag{165}$$

If the bias function $B(a, e, i, H)$ and the true distribution of comets in the space of orbital elements, $f(a, e, i)$, are known, it would therefore be possible to determine the true distribution of absolute magnitudes H hence the nuclear radii. For the determination of the bias function $B(a, e, i, H)$, detailed simulations of the large survey programs were performed by Robert Jedicke, and were described in the publication by Whitman *et al.* (2006). The true distribution of Jupiter family comets in orbital space, $f(a, e, i)$ was modelled by Bottke *et al.* (2002). Unfortunately, the space of orbital elements a, e and i covered by this modelling does not include a significant fraction of comets from the dataset used in the presented work. Only three Jupiter family comets of the dataset have orbital elements for which the functions B and f are known. Therefore, an influence of the observational selection effect upon the determined nucleus size distribution cannot be ruled out in this work. Additional modelling of the detection propabilities of survey programs and the distribution of comets in orbital space could open the possibility to correct for observational bias effects in future.

Since the detection probability for smaller and thus fainter comets is lower, one would expect that the observational selection effect would lead to a less steep size distribution.

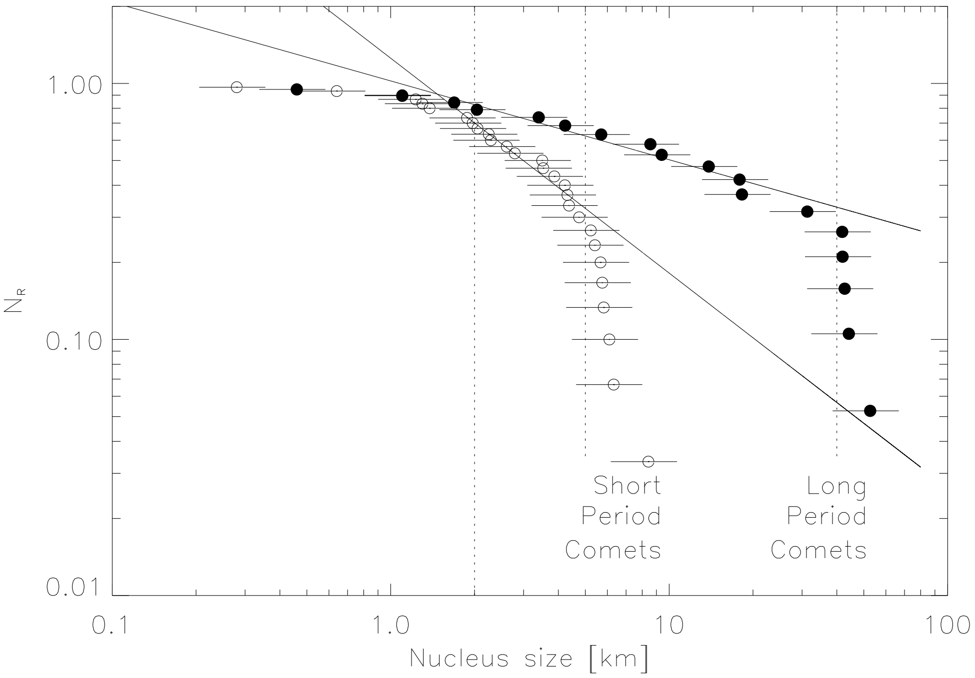

Figure 63: Normalized cumulative size distributions, N_R, for the short-period (open circles) and long-period (filled circles) comets in the dataset analysed in this work. The straight lines show power law fits to the data. For the short-period comets, the fit was done between nuclear radii between 2 km and 5 km, for the long-period comets, it was done between radii of 2 km and 40 km, as indicated by the dotted lines.

13.7 Discussion of Possible Activity Mechanisms

The cause of the sudden onset of the activity of comets which until then appeared asteroidal is not understood. Some mechanisms that could cause the development of activity are now discussed.

1) *Variation of the heliocentric distance.* Increasing solar irradiation as the comet approaches the Sun causes cometary activity. It is, however, difficult to understand how the continuous decrease in heliocentric distances could cause a sudden increase in cometary activity over a small range of r_h. For the majority of comets in the presented dataset the relative change in r_h between the discovery of the object and the discovery of its activity was small (compare column r_h and r_h^* of Tab. 31). Furthermore, some comets in the dataset showed activity only after their perihelion passage. This explanation for the observed steep onset of cometary activity therefore seems unlikely.

2) *Depletion in hypervolatile species.* If late-developing comets were depleted in hypervolatile species such as CO, significant activity would be expected only at helicentric

Table 32: Overview of nuclear sizes, R_N of long-period comets. Additionally, the minimum geocentric distance (Δ_m) and the corresponding date or the perihelion distance, q is shown. For Meech et al. *(2004), the 3σ upper limits for R_N are listed.*

Comet	R_N [km]	Ref.	remarks	
C/1983 H1 IRAS-Araki-Alcock	3.5	Meech *et al.* (2004)	$\Delta_m = 0.0312$ AU	1983 May 11
C/1991 L3 Levy	8.2	Meech *et al.* (2004)	$\Delta_m = 1.2709$ AU	1991 Jun 17
C/1995 O1 Hale-Bopp	30.0	Fernández (2002)	$\Delta_m = 1.3152$ AU	1997 Mar 22
C/1996 B2 Hyakutake	2.1	Harmon *et al.* (1997)	$\Delta_m = 0.1018$ AU	1996 Mar 25
C/1983 J1 Sugano-Saigusa-Fujikawa	0.37	Hanner *et al.* (1987)	$\Delta_m = 0.0628$ AU	1983 Jun 12
C/1987 H1 Shoemaker	< 5.3	Meech *et al.* (2004)	q = 5.464 AU	(IAUC 4395)
C/1988 B1 Shoemaker	< 7.4	Meech *et al.* (2004)	q = 5.026 AU	(IAUC 4585)
C/1987 F1 Torres	< 7.8	Meech *et al.* (2004)	q = 3.624 AU	(IAUC 4394)
C/1984 K1 Shoemaker	< 7.7	Meech *et al.* (2004)	q = 2.853 AU	(IAUC 3949)
C/1983 O1 Cernis	< 12.6	Meech *et al.* (2004)	q = 3.318 AU	(IAUC 3852)

distances where water sublimates efficiently, i.e. inside approximately 3 AU. In this case, the comets in the analysed dataset would be compositionally different from other comets. This mechanism would imply an accumulation of activity discoveries arround $r_h \approx 3$ AU. Indeed, the number of comets showing activity peaks between 2 AU and 3 AU, as can be seen in Fig. 66, where the number of comets of different dynamical types are plotted versus the heliocentric distance where activity was observed for the first time. Nevertheless, since the changes in heliocentric distance between the discovery of the objects and their activity is small, this distribution basically reproduces the frequency of discovery versus heliocentric distance and is therefore not conclusive. Furthermore, the distances at which cometary activity starts range from approximately 1 AU up to values as high as 8 AU. Therefore, a depletion in hypervolatile species appears unlikely to be the reason for the observed development of cometary activity with time.

3) *Phase transition between amorphous and crystalline ice.* If it is assumed that hypervolatile species such as CO are trapped in amorphous water ice before the comet approaches the inner solar system, sublimation and thus cometary activity could be inhibited. After a phase transition to crystalline ice, the hypervolatile species could be released and activity can begin. Such a phase transition would be expected to happen at heliocentric distances around 6−10 AU, assuming that the phase transition to crystalline ice becomes significant at approximately 120 K (Schmitt *et al.*, 1989). When such a comet approaches the inner solar system another time, it could be depleated in hypervolatile species and activity would occur only in the region of water sublimation. If such

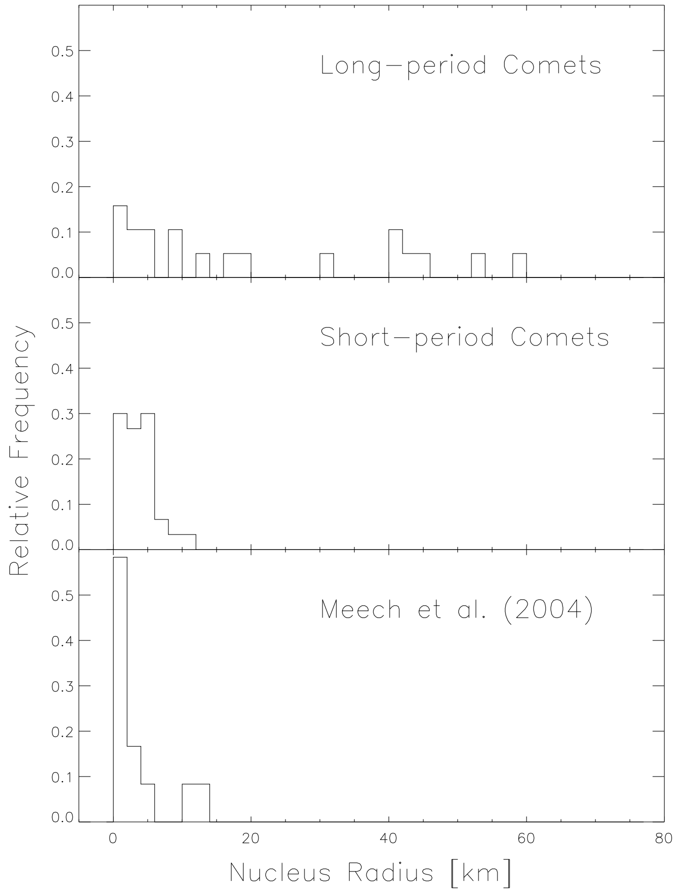

Figure 64: Histograms of the nuclear size distributions of long- and short-period comets. For comparison, the size distribution taken from Meech et al. *(2004) is shown. This size distribution contains 11 Jupiter family comets and one Halley type comet.*

a scenario causes the behavior in activity observed for the comets in the dataset of this work, one would expect the dynamically new long-period comets to show their activity at large heliocentric distances around 8 AU, where the phase transition of water ice occurs, while dynamically old long-period comets should start activity around 3 AU, where water starts to sublimate. In Fig. 66, the heliocentric distances at which the observed activity starts are shown in a histogram for both new and old long-period comets. It can be seen that no clear spatial separation of the heliocentric distances of activity onset of dynamically old and new comets is present. Therefore, this mechanism cannot explain the late occurance of cometary activity. It is also difficult to understand how a similar scenario would work for short-period comets.

4) *Isolated regions of activity.* The sudden increase in cometary activity can be caused by isolated active regions on rotating nuclei. Because of interaction between the orbital evolution, the orientation of the spin axis and the cometographic locations of active regions, icy surfaces could be exposed to sunlight only on certain parts of a cometary orbit around the Sun. Sudden illumination could then cause a steep increase in activity. This

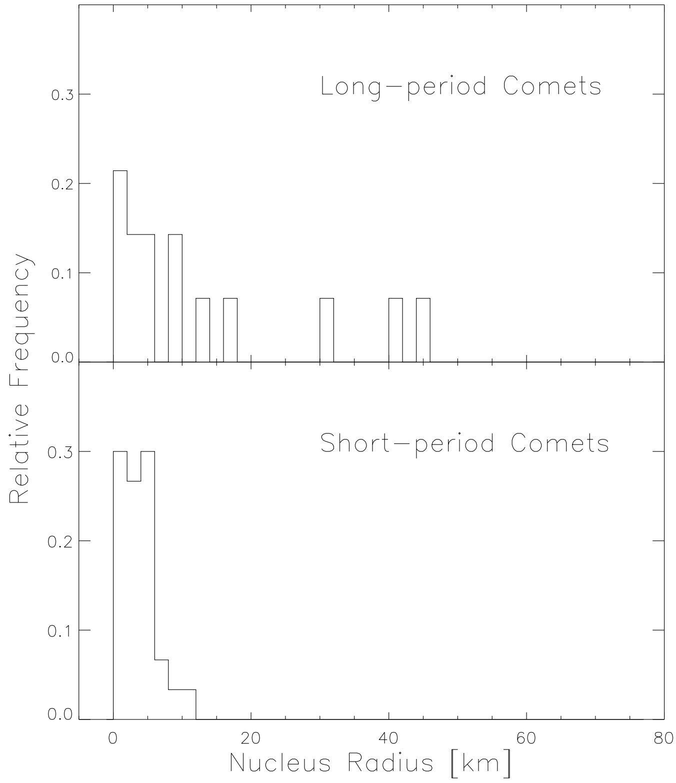

Figure 65: Histograms of the nuclear size distributions of long- and short-period comets with perihelion distances less than 5.2 AU. The sample of long period comets contains 14 objects, that one of short-period comets contains 29 objects.

scenario may offer a possible explanation for the observed activity evolution of the comets treated in this work.

There may be other mechanisms causing the sudden onset of cometary activity, but the discussion is limited here, because the purpose of this chapter is simply to derive nucleus sizes. A deeper study of the causes of sudden activity onsets should be the subject of further investigations.

13.8 Discussion and Conclusions

The size distribution of short period comets peaks at small nuclear sizes and no short-period comet with a nucleus size larger than 11 km is present in the dataset analysed in this work. This result is in agreement with previous findings published in the literature. The nuclear sizes of 19 long-period comets in the dataset cover the full range of nuclear radii from approximately 0.5 km to 50 km. Only a weak peak of the nuclear size distribution is observed at small sizes, which may in part be caused by observational selection effects favouring observations of larger objects. However, large cometary nuclei were found in the dataset analysed, which cannot be explained by an observational bias.

The exponent of a cumulative size distribution function for short-period comets in the

Table 33: Comets in the dataset for which the heliocentric distance on April 1, 2007, (denoted r_h^b*) is more than twice its value at the time of observation without activity (denoted* r_h^a*).* R_N *means the derived nuclear radius of the comet. The column denoted with* m_a *shows the magnitude on April 1, 2007, assuming that the derived nuclear radius is correct and no activity is present. The column labeled* m_b *shows the magnitude for the same date but assuming an activity scaling with* r_h^{-2}*. Both values are computed for zero phase angle. F shows the area in the sky (in arcs*^{2}*) with a 3*σ *probability of containing the comet. Suitable candidates for future observations are shown in bold.*

Comet		R_N [km]	r_h^a [AU]	r_h^b [AU]	m_a	m_b	F [sqarcs]
C/2004 X2	**LINEAR**	**8.56**	**3.87**	**8.45**	**21.80**	**23.49**	**1450.9**
P/2004 WR$_{9}$	LINEAR	1.38	1.98	6.26	24.27	26.77	108.8
C/2004 RG$_{113}$	LINEAR	4.23	3.02	7.66	22.87	24.95	4.4
162P/	**Siding Spring**	**4.22**	**1.28**	**4.83**	**20.50**	**23.38**	**0.3**
160P/	LINEAR	1.88	2.21	5.25	22.85	24.73	27.6
C/2004 K3	LINEAR	0.46	1.22	9.83	28.96	33.50	1246.5
C/2004 HV$_{60}$	Spacewatch	1.10	3.29	9.67	26.97	29.38	1.2
P/2004 EW$_{38}$	Catalina-LINEAR	1.10	2.07	5.38	24.68	26.88	456.1
C/2004 DZ$_{61}$	Catalina-LINEAR	2.04	2.32	9.37	25.69	28.72	6.5
P/2004 CB	LINEAR	0.64	1.22	4.84	25.44	28.43	13.5
P/2003 HT$_{15}$	LINEAR	2.61	2.71	6.35	23.50	25.35	1200.5
P/2003 SQ$_{215}$	NEAT-LONEOS	2.29	2.79	6.83	23.50	25.46	862.8
P/2003 WC$_{7}$	LINEAR-Catalina	2.25	1.75	7.32	23.92	27.03	194.7
P/2003 UY$_{275}$	LINEAR	1.30	2.20	5.61	23.78	25.82	4780.1
C/2002 X1	LINEAR	5.70	5.56	11.50	24.19	25.77	0.39
P/2002 T6	NEAT-LINEAR	2.79	2.89	8.08	23.83	25.44	13.1
P/2002 JN$_{16}$	LINEAR	1.23	2.01	4.43	23.14	24.85	451.5
P/2002 EJ$_{57}$	LINEAR	1.97	2.72	9.35	25.61	28.31	4086.8
C/2002 B2	LINEAR	9.40	3.89	13.57	23.86	26.57	5974.8
C/2002 A2	LINEAR	10.90	4.71	11.67	22.59	24.56	16.8
C/2001 RX$_{14}$	LINEAR	14.82	5.66	12.89	22.50	24.32	0.5
150P/	**LONEOS**	**3.53**	**2.08**	**4.83**	**21.67**	**23.41**	**3.9**
C/2000 SV$_{74}$	**LINEAR**	**41.81**	**6.07**	**13.61**	**20.35**	**22.10**	**0.4**
C/2000 OF$_{8}$	Spacewatch	3.40	4.56	16.04	26.70	29.43	51.16

size range 2 km to 5 km is $\alpha = 0.77 \pm 0.24$, and thus at the lower end of values for α available from other nucleus size datasets in the literature. Again, this may be caused by an observational selection effect in the dataset. For the nuclear size distribution of long-period comets between 2 km and 40 km, an exponent of $\alpha = 0.31 \pm 0.05$ was derived,

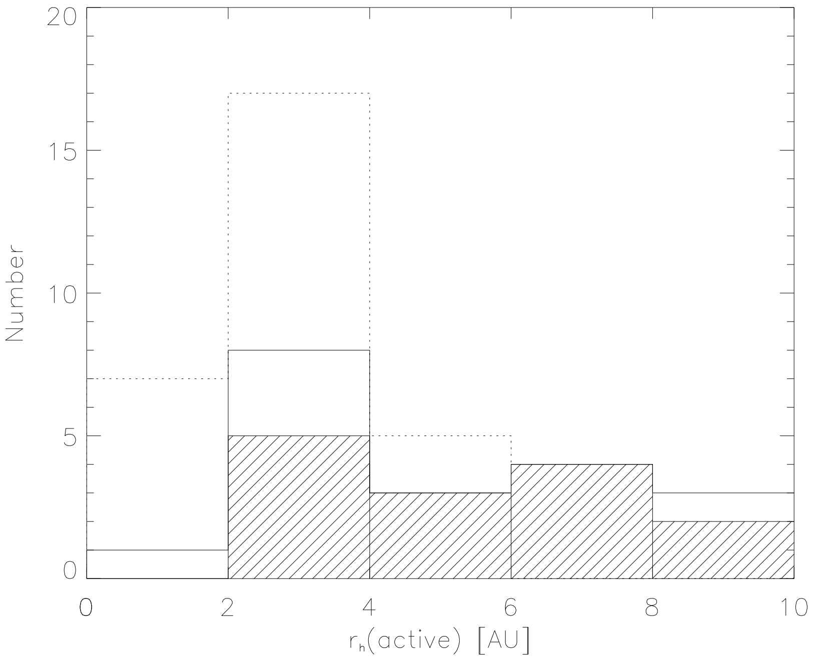

Figure 66: The number of comets versus the heliocentric distance, at which cometary activity was observed for the first time. The columns with solid lines show the number of long-period comets, where the shaded part is the fraction of dynamically new comets. The columns with dotted lines indicate the number of the short-period comets in the dataset analysed in this work.

significantly smaller than for short-period comets.

The mechanism causing the sudden increase in the cometary activity remains uncertain. Observations suggest that both short-period and long-period comets show such a behavior. The long-period comets in the dataset of this work therefore are different from more "typical" long-period comets. The latter show an activity that has a dependency r_h^{-2} upon the heliocentric distance, e.g. comet Hale-Bopp (Biver *et al.*, 2002). In the dataset used here, comets with nuclear sizes in the same range as for comet Hale-Bopp are present, and they were observed at similar heliocentric distances as Hale-Bopp at the time of its discovery (approx. 7.2 AU in July 1995). Also while comet Hale-Bopp was between 11^{mag} and 10^{mag} at the time of discovery and featured a coma diameter of approximately $1'$, large comets studied in this work are inactive. This indicates differences in the nuclear properties of the different comets. Furtheremore, dynamically new comets are present in the dataset of this work, which are likely to enter the inner solar system for the first time. The differences between the cometary nuclei could already be present in the Oort cloud. This implies that such differences in the nucleus properties could mean a variation in the ice content, e.g. a high dust to gas ratio in the nucleus, or only minor ice present between large areas of non-volatile material.

14 Summary and Outlook

14.1 Summary

14.1.1 Results of the Coma Chemistry Modelling

Within this work, a model for the chemistry in cometary comae was realized. The one-dimesional model assumes spherical symmetry of the coma and takes three fluids moving with a common hydrodynamical velocity into account. The three fluids, consisting of the neutral species, the ionic species, and the electrons, are coupled via mass and energy exchange. Unlike the widely-used Haser model, this approach makes it possible to include various chemical reaction types, such as electron impact reactions, two-body collision reactions, and photochemistry into account. The negligence of magnetic fields restricts the model to the study of neutral species.

Results published in literature that were obtained with other models for the cometary coma were used as test cases for the presented model. A satisfying quantitative agreement with results obtained for comet C/1996 B2 Hyakutake with a model by Rodgers and Charnley (1998) was found. A good qualitative agreement with results obtained for comet C/1995 O1 Hale-Bopp by Helbert (2002) was obtained. It was shown that the presented model is suitable to reproduce the observed C_3 and C_2 column density profiles of comet Hale-Bopp at large heliocentric distances. However, a quantitative deviation between the results obtained with the model presented in this work and obtained by Helbert (2002) remain unexplained.

The model for the chemistry in the cometary coma was used to reproduce column density profiles of the radicals C_3 and C_2 observed in the comae of the comets C/2001 Q4 NEAT, C/2002 T7 LINEAR, and 9P/Tempel 1 at heliocentric distances between 1.0 AU and 1.5 AU. The reaction network by Helbert (2002) did not allow for a satisfying fit of the observed C_3 column density profiles. This is in part caused by an overestimate of the electron impact reactions. The corresponding electron rate coefficients were updated from the literature, leading to lower reaction rates. Furthermore, the additional parent species C_4H_2 and HC_3N were taken into consideration, making it necessary to estimate the reaction rates of a number of photoreactions. With the two parent species C_3H_4 and C_4H_2, a satisfying fit of the observed C_3 column density profiles for all three comets studied was possible. The required amount of the parent C_4H_2 to reproduce the observed C_3 column density profiles was in the order of about 0.14% to 0.25% of the water production rate. However, no simultaneous fitting of the C_2 column density profiles was possible assuming C_2H_2 and HC_3N as additional potential C_2 parent species. C_2H_6 turned out to be neglegible as a parent species of C_2 and its abundance cannot be constrained from observations of C_2 column density profiles at projected nucleocentric distances less than about 10^6 km.

Since no acceptable fit of the observed C_3 column density profiles with C_3H_4 as the sole C_3 parent species was possible, C_3H_4 is probably not the only parent of C_3, at least at heliocentric distances close to 1 AU. C_4H_2 would provide an additional parent species with which the C_3 column density profiles can be reproduced. However, this parent species, together with the photoreaction rates assumed in this work, is not in agreement with the observed C_2 column density profiles. The large number of involved parent species and reactions with poorly known reaction rates do not allow for a deeper analysis of the C_3 and C_2 formation in cometary comae. For a more detailed analysis, more detailed knowlegde of the photoreaction pathways, especially of C_4H_2, HC_3N and their photodissociation products, are very desirable to obtain more constraints on the formation mechanism.

14.1.2 Results for Comet 67P/Churyumov-Gerasimenko

The comparison of the CN Haser production rate and the Afρ parameter obtained from observations performed in February 1996 with corresponding values published in the literature from the 1982 perihelion passage showed no significant change in activity of comet 67P/Churyumov-Gerasimenko between the 1982 and the 1996 perihelion passages. A comparison of visual magnitudes of that comet during the 1982, the 1996, and the 2002 perihelion passages revealed the same lightcurve with an asymmetry with respect to the perihelion, with a steep increase in activity shortly after perihelion. Thus, the activity of comet 67P/Churyumov-Gerasimenko appears very stable from perihelion passage to perihelion passage.

The analysis of images obtained in March 2003 revealed two dust jets in the coma with constant position between March 7 and March 31, 2003. These structures are interpreted as edges of a cone resulting from dust set free from a single active surface area on the nucleus surface. This interpretation suggests an inclination of the projected nucleus rotation axis with respect to the comets orbital plane of about 40° in March 2003.

The dust production of comet 67P/Churyumov-Gerasimenko was determined from OH production rates and Afρ parameters published in the literature. The results suggest comet 67P/Churyumov-Gerasimenko to be a very dusty comet, with a dust-to-water mass ratio in the coma of about 4.8. The dust production rates determined in this work are higher compared to values from other publications. The difference can be explained by a more realistic determination of dust parameters such as the dust velocity and the maximum particle size in the coma done in this work. A study of the dusty gas dynamics in the coma, applying standard parameters on the dust size distribution, showed that even a dust-to-gas mass ratio as high as 8.5 is still neglegible for the determination of the dust and gas production rates.

Based on the maximum dust production rate determined from the data of the 1981 perihelion passage, the total area flux of the dust in a distance of 20 km from the nucleus of $9.1 \cdot 10^{-6}\ \mathrm{m}^2\,(\mathrm{m}^2\,\mathrm{s})^{-1}$ was determined. This value represents the maximum dust flux that the Rosetta orbiter spacecraft will be exposed to shortly after the perihelion passage of comet 67P/Churyumov-Gerasimenko.

14.1.3 Results for Comet 9P/Tempel 1

Long-slit spectra of comet 9P/Tempel 1 around the Deep Impact event were analysed. No new gas emission bands were observed after the impact event. An expanding gas cloud was observed after impact, and its mean projected expansion velocity of (1.23 ± 0.12) km s^{-1} for CN and (1.17 ± 0.14) km s^{-1} for C_2 was measured. This velocity was derived from the position of the outermost detectable part of the CN and C_2 cloud with time. The velocities of the center of the clouds were determined to (0.63 ± 0.04) km s^{-1} and (0.75 ± 0.04) km s^{-1}, respectively.

Based on a Haser-like model for the formation and destruction of the radicals CN, C_2, and C_3, the numbers of parent molecules released by the impact event were determined. The derived numbers are $(3.48 \pm 0.87) \cdot 10^{29}$ for the CN parent species, $(5.20 \pm 1.48) \cdot 10^{29}$ for the C_2 parent species, and $(0.66 \pm 0.48) \cdot 10^{29}$ for the C_3 parent species, respectively. The abundances of the C_2 and C_3 parent species with respect to the CN parent species in the impact cloud were in agreement with the values for the pre-impact and post-impact coma of comet 9P/Tempel 1. No indications for compositional differences of the impact cloud compared to the undisturbed coma were found.

The Haser gas production rates for CN, C_2, C_3, and NH_2 five and six days after the impact event are in agreement with the gas production rates two and one days before impact. No influence of the impact event upon the gas production rates on the timescale of days was observed.

A variation of the gas emission band brightness of CN, C_2, C_3, and NH_2 in the inner coma with the rotational phase of the nucleus was observed. The variations suggest the presence of at least two located active surface areas on the nucleus of comet 9P/Tempel 1. The variation of activity of the four species studied are in agreement at all rotational phases with the exception of the CN activity at rotational phases of 0.6 to 0.7 with respect to the impact time. At these phases, the CN emission brightness in the innermost coma is lower compared to the brightness of the other species. This result provides one of the to date best indications for a compositional difference between different parts of the surface of a cometary nucleus.

14.1.4 Results from the Nuclear Size Determination

From the analysis of survey observations, the nuclear radii of 28 Jupiter family comets, 19 long-period comets, and one Halley type comet were determined. The radii of the long-period comets range from 0.5 km to about 50 km, while the largest Jupiter family comet in the datset has a nuclear radius of about 11 km. This result cannot be explained by an observational selection effect, since large Jupiter family comets should be more easily to discover than large long-period comets. On the size interval from 2 km to 5 km the slope of the nucleus size frequency distribution of 0.77 ± 0.24 for the Jupiter family comets was derived. For long-period comets, the slope between radii of 2 km and 40 km was determined to 0.31 ± 0.05. However, observational bias effects could not be removed from the dataset. An observational bias towards the detection of large long-period cometary nuclei could cause the size distribution of these comets to be artificially flattened. A more extensive modelling of the discovery probability of cometary nuclei by survey programs is required to eliminate such observational bias.

Furthermore, the influence of undetected activity of the comets in the analysed dataset could not be sufficiently estimated. Therefore, all derived nuclear radii remain strictly speaking upper limits. From the analysed dataset, four comets were selected that provide good conditions to determine the contribution of undetected activity to the observed brightness and they are thus suitable candidates for testing the presented method of nucleus size determination. Future observations of these four comets provide the opportunity to decide whether nuclear radii of comets can be determined from survey observations. If the results obtained by the presented method turn out to be reliable, it will be possible for the first time to determine the size distribution of long-period comets.

14.2 Outlook

If the proposed further observations should confirm the possibility of determining the comet nucleus sizes from survey observations, use could be made from the upcoming next gerneration sky surveys. The ground based sky survey project PAN STARRS (Kaiser and Pan-STARRS Team, 2005), that sould become operational in late 2006, is expected to increase the number of discovered comets per year dramatically. Thus, the number of comets suitable for the determination of the nuclear size could rise within the next years, reaching numbers that provide a reliable basis for staticics. The ESA space mission GAIA (Perryman, 2005) is intended to scan the whole sky in average about 100 times between the years 2011 and 2016. Since this mission includes a photometric capability, it could also provide a homogenious photometric dataset of a large number of comets.

Since comet 9P/Tempel 1 did not show any indications of long-term effects induced by the Deep Impact experiment, no need for further observations of this comet arises in this respect. Nevertheless, a more detailed analysis of the radial gas emission profiles of the impact cloud is still missing. This analysis requires the treatment of the chemical reactions in a non-steady gas flow with sublimating icy grains, and thus lies outside the scope of this work. However, such extensive modelling of the post-impact phenomena could in combination with the available observations provide deeper insights into the physical and chemical composition of comet 9P/Tempel 1.

The available dataset on comet 67P/Churyumov-Gerasimenko is still poor. Before the arrival of the Rosetta spacecraft in 2014, comet 67P/Churyumov-Gerasimenko will have a perihelion passage in 2008 under a good observing geometry. A study of the comet during that perihelion passage should also include the study of the CN, C_3, and C_2 activity. Since comet 67P/Churyumov-Gerasimenko is classified as depleated in C_3 (A'Hearn *et al.*, 1995), the analysis of the C_3 and C_2 emissions of that comet are also suitable to invesitigate in detail how the depleation is correlated to the abundances of the parent species of C_3 and C_2.

For the correlation of the chemical classification of comets with the cometary formation regions, the dataset has to be significantly extended. The recent discovery of three main belt objects showing cometary activity (Hsieh and Jewitt, 2006) provides in principle an elegant approach in this respect. Since the three objects are on typical and stable orbits in the main belt, it is assumed that they are still in a region close to their original formation region. This formation region is at smaller heliocentric distance than the assumed formation region of classical comets. Possible differences in the composition of volatiles of active main belt objects and classical comets therefore could be more easily related to the formation regions. Unfortunately, the active main belt objects are very faint ($> 20^{\mathrm{mag}}$ at opposition), and thus not suitable for ground-based spectroscopy. Therefore, among other science objectives (Hsieh and Jewitt, 2006), the investigation of the abundances of hydrocarbons, i.e. C_2H_2 and C_3H_4, in the volatiles of that bodies would make them interesting targets for a future space mission.

References

Abell, P. A., Fernández, Y. R., Pravec, P., French, L. M., Farnham, T. L., Gaffey, M. J., Hardersen, P. S., Kušnirák, P., Šarounová, L., Sheppard, S. S., and Narayan, G. (2005). Physical characteristics of Comet Nucleus C/2001 OG_{108} (LONEOS). *Icarus*, **179**, 174–194.

A'Hearn, M. F., Schleicher, D. G., Millis, R. L., Feldman, P. D., and Thompson, D. T. (1984). Comet Bowell 1980b. *Astronomical Journal*, **89**, 579–591.

A'Hearn, M. F., Millis, R. L., Schleicher, D. G., Osip, D. J., and Birch, P. V. (1995). The ensemble properties of comets: Results from narrowband photometry of 85 comets, 1976-1992. *Icarus*, **118**, 223–270.

A'Hearn, M. F., Belton, M. J. S., Delamere, W. A., Kissel, J., Klaasen, K. P., McFadden, L. A., Meech, K. J., Melosh, H. J., Schultz, P. H., Sunshine, J. M., Thomas, P. C., Veverka, J., Yeomans, D. K., Baca, M. W., Busko, I., Crockett, C. J., Collins, S. M., Desnoyer, M., Eberhardy, C. A., Ernst, C. M., Farnham, T. L., Feaga, L., Groussin, O., Hampton, D., Ipatov, S. I., Li, J.-Y., Lindler, D., Lisse, C. M., Mastrodemos, N., Owen, W. M., Richardson, J. E., Wellnitz, D. D., and White, R. L. (2005). Deep Impact: Excavating Comet Tempel 1. *Science*, **310**, 258–264.

Alman, D. A., Ruzic, D. N., and Brooks, J. N. (2000). A hydrocarbon reaction model for low temperature hydrogen plasmas and an application to the Joint European Torus. *Physics of Plasmas*, **7**, 1421–1432.

Altenhoff, W. J., Bieging, J. H., Butler, B., Butner, H. M., Chini, R., Haslam, C. G. T., Kreysa, E., Martin, R. N., Mauersberger, R., McMullin, J., Muders, D., Peters, W. L., Schmidt, J., Schraml, J. B., Sievers, A., Stumpff, P., Thum, C., von Kap-Herr, A., Wiesemeyer, H., Wink, J. E., and Zylka, R. (1999). Coordinated radio continuum observations of comets Hyakutake and Hale-Bopp from 22 to 860 GHz. *Astronomy and Astrophysics*, **348**, 1020–1034.

Ashihara, O. (1975). The Electron Energy Loss Rates by Polar Molecules. In *Report 530*, volume 40, page 10. Inst. Space Science and Aeronautical Science, University of Tokyo.

Bader, G. and Deuflhard, P. (1983). A Semi-Implicit Mid-Point Rule for Stiff Systems of Ordinary Differential Equations. *Numer. Math.*, **41**, 373–398.

Biver, N., Bockelée-Morvan, D., Colom, P., Crovisier, J., Henry, F., Lellouch, E., Winnberg, A., Johansson, L. E. B., Gunnarsson, M., Rickman, H., Rantakyrö, F., Davies, J. K., Dent, W. R. F., Paubert, G., Moreno, R., Wink, J., Despois, D., Benford, D. J., Gardner, M., Lis, D. C., Mehringer, D., Phillips, T. G., and Rauer, H.

(2002). The 1995 2002 Long-Term Monitoring of Comet C/1995 O1 (HALE BOPP) at Radio Wavelength. *Earth Moon and Planets*, **90**, 5–14.

Biver, N., Bockelee-Morvan, D., Colom, P., Crovisier, J., Lecacheux, A., and Paubert, G. (2005). Comet 9P/Tempel. *IAU circular*, **8538**, 1.

Bockelee-Morvan, D. and Crovisier, J. (2003). Lessons of Comet Hale-Bopp for Coma Chemistry: Observations and Theory. In H. Boehnhardt, M. Combi, M. R. Kidger, and R. Schulz, editors, *Cometray Science after Hale-Bopp Invited Papers*, pages 53–71. Kluwer Academic Publishers.

Bottke, W. F., Morbidelli, A., Jedicke, R., Petit, J.-M., Levison, H. F., Michel, P., and Metcalfe, T. S. (2002). Debiased Orbital and Absolute Magnitude Distribution of the Near-Earth Objects. *Icarus*, **156**, 399–433.

Buratti, B., Hicks, M., Soderblom, L., Britt, D., Boice, D., Brown, R., Nelson, R., Oberst, J., Owen, T., Sandel, B., Stern, S. A., Thomas, N., and Yelle, R. (2002). The nucleus of 19/P Borrelly as revealed by Deep Space 1. In B. Warmbein, editor, *ESA SP-500: Asteroids, Comets, and Meteors: ACM 2002*, pages 545–547.

Burki, G., Rufener, F., Burnet, M., Richard, C., Blecha, A., and Bratschi, P. (1995). The atmospheric extinction at the E.S.O. La Silla observatory. *Astronomy and Astrophysics Supplement Series*, **112**, 383.

Chang Hung-Chhiao (1958). *Chung-Kuo Ku Li Hsi I.* Peking.

Clark, B. E., Veverka, J., Helfenstein, P., Thomas, P. C., Bell, J. F., Harch, A., Robinson, M. S., Murchie, S. L., McFadden, L. A., and Chapman, C. R. (1999). NEAR Photometry of Asteroid 253 Mathilde. *Icarus*, **140**, 53–65.

Clark, B. E., Helfenstein, P., Bell, J. F., Peterson, C., Veverka, J., Izenberg, N. I., Domingue, D., Wellnitz, D., and McFadden, L. (2002). NEAR Infrared Spectrometer Photometry of Asteroid 433 Eros. *Icarus*, **155**, 189–204.

Cochran, A. L. (1985). A re-evaluation of the Haser model scale lengths for comets. *Astronomical Journal*, **90**, 2609–2614.

Cochran, A. L., Barker, E. S., Ramseyer, T. F., and Storrs, A. D. (1992). The McDonald Observatory Faint Comet Survey - Gas production in 17 comets. *Icarus*, **98**, 151–162.

Combi, M. R., Reinard, A. A., Bertaux, J.-L., Quemerais, E., and Mäkinen, T. (2000). SOHO/SWAN Observations of the Structure and Evolution of the Hydrogen Lyman-α Coma of Comet Hale-Bopp (1995 O1). *Icarus*, **144**, 191–202.

Connors, K. A., editor (1990). *Chemical Kinetics.* VCH, Weinheim.

Cravens, T. E. and Korosmezey, A. (1986). Vibrational and rotational cooling of electrons by water vapor. *Planetary and Space Science*, **34**, 961–970.

Cremonese, G., Huebner, W. F., Rauer, H., and Boice, D. C. (2002). Neutral sodium tails in comets. *Advances in Space Research*, **29**, 1187–1197.

Crifo, J. F., Fulle, M., Kömle, N. I., and Szego, K. (2004). Nucleus-coma structural relationships: lessons from physical models. *Comets II*, pages 471–503.

Davidsson, B. J. R. and Gutiérrez, P. J. (2004a). Estimating the Nucleus Bulk Density of Comet 81P/Wild 2. *AAS/Division for Planetary Sciences Meeting Abstracts*, **36**, 21.06.

Davidsson, B. J. R. and Gutiérrez, P. J. (2004b). Estimating the nucleus density of Comet 19P/Borrelly. *Icarus*, **168**, 392–408.

Delahodde, C. E., Meech, K. J., Hainaut, O. R., and Dotto, E. (2001). Detailed phase function of comet 28P/Neujmin 1. *Astronomy and Astrophysics*, **376**, 672–685.

Despois, D. (2005). Observations of molecules in comets. In D. C. Lis, G. A. Blake, and E. Herbst, editors, *IAU Symposium No. 231, Astrochemistry Throughout the Universe: Recent Successes and Current Challenges*, page 257.

Deuflhard, P. (1983). Order and Stepsize Control in Extrapolation Methods. *Numer. Math.*, **41**, 399–422.

Divine, N. (1981). A simple radiation model of cometary dust for P/Halley. In B. Battrick and E. Swallow, editors, *ESA SP-174: The Comet Halley. Dust and Gas Environment*, pages 47–53.

Dones, L., Weissman, P. R., Levison, H. F., and Duncan, M. J. (2004). Oort cloud formation and dynamics. *Comets II*, pages 153–174.

Draine, B. T. (1980). Interstellar shock waves with magnetic precursors. *Astrophysical Journal*, **241**, 1021–1038.

Draine, B. T. (1986). Multicomponent, reacting MHD flows. *Monthly Notes of the Royal Astronomical Society*, **220**, 133–148.

Dybczyński, P. A. (2001). Dynamical history of the observed long-period comets. *Astronomy and Astrophysics*, **375**, 643–650.

Emel'yanenko, V. V., Asher, D. J., and Bailey, M. E. (2005). Centaurs from the Oort cloud and the origin of Jupiter-family comets. *Monthly Notes of the Royal Astronomical Society*, **361**, 1345–1351.

Fanale, F. P. and Salvail, J. R. (1984). An idealized short-period comet model - Surface insolation, H2O flux, dust flux, and mantle evolution. *Icarus*, **60**, 476–511.

Feaga, L. M., A'Hearn, M. F., Sunshine, J. M., Groussin, O., and Deep Impact Science Team (2006). Asymmetry of Gaseous CO2 and H2O in the Inner Coma of Comet Tempel 1. In S. Mackwell and E. Stansbery, editors, *37th Annual Lunar and Planetary Science Conference*, page 2149.

Feldman, P. D., Weaver, H. A., Christian, D., Combi, M. R., Krasnopolsky, V., Lisse, C. M., Mumma, M. J., Shemansky, D. E., and Stern, S. A. (2004a). FUSE Observations of Comet C/2001 Q4 (NEAT). *Bulletin of the American Astronomical Society*, **36**, 1121.

Feldman, P. D., Cochran, A. L., and Combi, M. R. (2004b). Spectroscopic investigations of fragment species in the coma. *Comets II*, pages 425–447.

Feldman, P. D., Lupu, R. E., McCandliss, S. R., Weaver, H. A., A'Hearn, M. F., Belton, M. J. S., and Meech, K. J. (2006). Carbon Monoxide in Comet 9P/Tempel 1 before and after the Deep Impact Encounter. *Astrophysical Journal Letters*, **647**, L61–L64.

Fernández, J. A., Gallardo, T., and Brunini, A. (2004). The scattered disk population as a source of Oort cloud comets: evaluation of its current and past role in populating the Oort cloud. *Icarus*, **172**, 372–381.

Fernández, Y. R. (2002). The Nucleus of Comet Hale-Bopp (C/1995 O1): Size and Activity. *Earth Moon and Planets*, **89**, 3–25.

Fink, U., Combi, M. R., and Disanti, M. A. (1991). Comet P/Halley - Spatial distributions and scale lengths for C2, CN, NH2, and H2O. *Astrophysical Journal*, **383**, 356–371.

Flower, D. R., Pineau des Forets, G., and Hartquist, T. W. (1985). Theoretical studies of interstellar molecular shocks. I - General formulation and effects of the ion-molecule chemistry. *Monthly Notes of the Royal Astronomical Society*, **216**, 775–794.

French, L. M. (2002). Pre-Activity BVRI Colors of High-Inclination Comet C/2001 OG108 (LONEOS). *Bulletin of the American Astronomical Society*, **34**, 868.

Friedel, D. N., Remijan, A. J., Snyder, L. E., A'Hearn, M. F., Blake, G. A., de Pater, I., Dickel, H. R., Forster, J. R., Hogerheijde, M. R., Kraybill, C., Looney, L. W., Palmer, P., and Wright, M. C. H. (2005). BIMA Array Detections of HCN in Comets LINEAR (C/2002 T7) and NEAT (C/2001 Q4). *Astrophysical Journal*, **630**, 623–630.

Fulle, M. (2004). Motion of cometary dust. *Comets II*, pages 565–575.

Fulle, M., Barbieri, C., Cremonese, G., Rauer, H., Weiler, M., Milani, G., and Ligustri, R. (2004). The dust environment of comet 67P/Churyumov-Gerasimenko. *Astronomy and Astrophysics*, **422**, 357–368.

Gail, H.-P. (2002). Radial mixing in protoplanetary accretion disks. III. Carbon dust oxidation and abundance of hydrocarbons in comets. *Astronomy and Astrophysics*, **390**, 253–265.

Gear, C. W. (1971). *Numerical Initial-Value Problems in Ordinary Differential Equations*. Englewood Cliffs, Prentice-Hall.

Glicker, S. and Okabe, H. (1987). Photochemistry of Diacetylene. *Journal of Physical Chemistry*, **91**, 437–440.

Gomes, R. S., Morbidelli, A., and Levison, H. F. (2004). Planetary migration in a planetesimal disk: why did Neptune stop at 30 AU? *Icarus*, **170**, 492–507.

Greenberg, J. M., Mizutani, H., and Yamamoto, T. (1995). A new derivation of the tensile strength of cometary nuclei: Application to comet Shoemaker-Levy 9. *Astronomy and Astrophysics*, **295**, L35–L38.

Groussin, O., A'Hearn, M. F., Li, J.-Y., Thomas, P. C., Sunshine, J. M., Lisse, C. M., Delamere, A., and Deep Impact Science Team (2006). Temperature of the Nucleus of Comet Tempel 1. In S. Mackwell and E. Stansbery, editors, *37th Annual Lunar and Planetary Science Conference*, page 1297.

Haken, H. and Wolf, H. C., editors (2006). *Molekülphysik und Quantenchemie*. Springer.

Halpern, J. B., Miller, G. E., and Okabe, H. (1988). The UV Photochemistry of Cyanoacetylene. *Journal of Photochemistry and Photobiology*, **42**, 63–72.

Halpern, J. B., Petway, L., Lu, R., Jackson, M., and McCrary, V. R. (1990). Photochemistry of Cyano- and Dicyanoacetylene at 193 nm. *Journal of Physical Chemistry*, **94**, 1869–1873.

Hamuy, M., Walker, A. R., Suntzeff, N. B., Gigoux, P., Heathcote, S. R., and Phillips, M. M. (1992). Southern spectrophotometric standards. *Publications of the Astronomical Society of the Pacific*, **104**, 533–552.

Hamuy, M., Suntzeff, N. B., Heathcote, S. R., Walker, A. R., Gigoux, P., and Phillips, M. M. (1994). Southern spectrophotometric standards, 2. *Publications of the Astronomical Society of the Pacific*, **106**, 566–589.

Hanner, M. S., Tedesco, E., Tokunaga, A. T., Veeder, G. J., Lester, D. F., Witteborn, F. C., Bregman, J. D., Gradie, J., and Lebofsky, L. (1985). The dust coma of periodic Comet Churyumov-Gerasimenko (1982 VIII). *Icarus*, **64**, 11–19.

Hanner, M. S., Newburn, R. L., Spinrad, H., and Veeder, G. J. (1987). Comet Sugano-Saigusa-Fujikawa (1983V) - A small, puzzling comet. *Astronomical Journal*, **94**, 1081–1087.

Hanner, M. S., Gehrz, R. D., Harker, D. E., Hayward, T. L., Lynch, D. K., Mason, C. C., Russell, R. W., Williams, D. M., Wooden, D. H., and Woodward, C. E. (1999). Thermal Emission from the Dust Coma of Comet Hale-Bopp and the Composition of the Silicate Grains. *Earth Moon and Planets*, **79**, 247–264.

Harmon, J. K., Ostro, S. J., Benner, L. A. M., Rosema, K. D., Jurgens, R. F., Winkler, R., Yeomans, D. K., Choate, D., Cormier, R., Giorgini, J. D., Mitchell, D. L., Chodas, P. W., Rose, R., Kelley, D., Slade, M. A., and Thomas, M. L. (1997). Radar Detection of the Nucleus and Coma of Comet Hyakutake (C/1996 B2). *Science*, **278**, 1921.

Haser, L. (1957). Distribution d'intensite dans la tete d'une comete. *Bulletin de la Societe Royale des Sciences de Liege*, **43**, 740–750.

Helbert, J. (2002). *Studying the longterm evolution of gas activity in the coma of comet C/1995 O1 Hale-Bopp, with a special focus on the chemistry of carbon bearing molecules.* Ph.D. thesis, Freie Universität Berlin.

Helbert, J., Rauer, H., Boice, D. C., and Huebner, W. F. (2005). The chemistry of C_2 and C_3 in the coma of Comet C/1995 O1 (Hale-Bopp) at heliocentric distances $r_h < 2.9$ AU. *Astronomy and Astrophysics*, **442**, 1107–1120.

Hills, J. G. (1981). Comet showers and the steady-state infall of comets from the Oort cloud. *Astronomical Journal*, **86**, 1730–1740.

Hindmarsh, A. C. (1983). *Scientific Computing*, page 55. North-Holland, Amsterdam.

Ho, P. Y. (1962). Ancient and mediaeval observations of comets and novae in Chinese sources. *Vistas in Astronomy*, **5**, 127–225.

Howell, E. S., Lovell, A. J., and Schloerb, F. P. (2004). Comet C/2002 T7 (LINEAR). *IAU circular*, **8329**, 2.

Hsieh, H. H. and Jewitt, D. (2006). A Population of Comets in the Main Asteroid Belt. *Science*, **312**, 561–563.

Huebner, W. F., Keady, J. J., and Lyon, S. P. (1992). Solar photo rates for planetary atmospheres and atmospheric pollutants. *Astrophysics and Space Science*, **195**, 1–289.

Hutsemékers, D., Manfroid, J., Jehin, E., Arpigny, C., Cochran, A., Schulz, R., Stüwe, J. A., and Zucconi, J.-M. (2005). Isotopic abundances of carbon and nitrogen in Jupiter-family and Oort Cloud comets. *Astronomy and Astrophysics*, **440**, L21–L24.

Jehin, E., Manfroid, J., Hutsemékers, D., Cochran, A. L., Arpigny, C., Jackson, W. M., Rauer, H., Schulz, R., and Zucconi, J.-M. (2006). Deep Impact: High-Resolution Optical Spectroscopy with the ESO VLT and the Keck I Telescope. *Astrophysical Journal Letters*, **641**, L145–L148.

Jessberger, E. K. and Kissel, J. (1991). Chemical properties of cometary dust and a note on carbon isotopes. In R. L. Newburn, Jr., M. Neugebauer, and J. Rahe, editors, *ASSL Vol. 167: IAU Colloq. 116: Comets in the post-Halley era*, pages 1075–1092.

Jewitt, D. and Meech, K. J. (1986). Cometary grain scattering versus wavelength, or 'What color is comet dust'? *Astrophysical Journal*, **310**, 937–952.

Jockers, K. (1997). Observations Of Scattered Light From Cometary Dust And Their Interpretation. *Earth Moon and Planets*, **79**, 221–245.

Jorda, L. (1995). *Atmosphères cométaires: interprétation des observations dans le visible et comparaison avec les observations radio*. Ph.D. thesis, Observatoire de Paris-Meudon.

Kührt, E. (1999). H2O-Activity of Comet Hale-Bopp. *Space Science Reviews*, **90**, 75–82.

Kaiser, N. and Pan-STARRS Team (2005). The Pan-STARRS Survey Telescope Project. *Bulletin of the American Astronomical Society*, **37**, 1409.

Kawakita, H. and Watanabe, J.-i. (2002). Revised Fluorescence Efficiencies of Cometary NH_2: Ammonia Abundance in Comets. *Astrophysical Journal Letters*, **572**, L177–L180.

Kinochita, K., editor (2004). *Comet Orbit Homepage*. http://www9.ocn.ne.jp/ comets/0067p.htm.

Kitamura, Y. (1986). Axisymmetric dusty gas jet in the inner coma of a comet. *Icarus*, **66**, 241–257.

Knollenberg, J. (1993). *Modellrechnungen zur Staubverteilung in der inneren Koma von Kometen unter spezieller Berücksichtigung der HMC-Daten der Giotto-Mission*. Ph.D. thesis, Georg-August-Universität zu Göttingen.

Krasnopol'Skii, V. A. (1991). C3 and CN parents in Comet P/Halley. *Astronomy and Astrophysics*, **245**, 310–315.

Krishna Swamy, K. S. (1991). Heliocentric variation of dust production in comets inferred from infrared observations. *Astronomy and Astrophysics*, **241**, 260–266.

Kumar, D. and Huber, J. R. (1976). Emission Excitation Spectra and Photochemistry of the 3820 Å Band System of Propynal. *Chemical Physics Letters*, **38**, 537–542.

Küppers, M., Bertini, I., Fornasier, S., Gutierrez, P. J., Hviid, S. F., Jorda, L., Keller, H. U., Knollenberg, J., Koschny, D., Kramm, R., Lara, L.-M., Sierks, H., Thomas, N., Barbieri, C., Lamy, P., Rickman, H., Rodrigo, R., A'Hearn, M. F., Angrilli, F., Bailey, M. E., Barthol, P., Barucci, M. A., Bertaux, J.-L., Burns, J. A., Cremonese, G., Curdt, W., De Cecco, M., Debei, S., Fulle, M., Gliem, F., Ip, W.-H., Kührt, E., Llebaria, A., Lopez Moreno, J. J., Marzari, F., Naletto, G., Sabau, L., Sanz Andrés, A., Sivan, J. P., Tondello, G., and Wenzel, K.-P. (2005). A large dust/ice ratio in the nucleus of comet 9P/Tempel 1. *Nature*, **437**, 987–990.

Kurucz, R. L., Furenlid, I., Brault, J., and Testerman, L. (1984). *Solar Flux Atlas from 296 to 1300 nm*. Tech. rept. National Solar Observatory, Sunspot, New Mexico.

Lamy, P. L., Toth, I., Weaver, H. A., Delahodde, C., Jorda, L., and A'Hearn, M. F. (2000). The nucleus of 13 short-period comets. *Bulletin of the American Astronomical Society*, **32**, 1061.

Lamy, P. L., Toth, I., Jorda, L., Groussin, O., A'Hearn, M. F., and Weaver, H. A. (2002). The Nucleus of Comet 22P/Kopff and Its Inner Coma. *Icarus*, **156**, 442–455.

Lamy, P. L., Toth, I., Weaver, H., Jorda, L., and Kaasalainen, M. (2003). The Nucleus of Comet 67P/Churyumov-Gerasimenko, the New Target of the Rosetta Mission. *AAS/Division for Planetary Sciences Meeting Abstracts*, **35**, 30.04.

Lamy, P. L., Toth, I., Fernandez, Y. R., and Weaver, H. A. (2004). The sizes, shapes, albedos, and colors of cometary nuclei. *Comets II*, pages 223–264.

Landau, L. D. and Lifschitz, E. M., editors (1991). *Lehrbuch der theoretischen Physik, Band 6: Hydrodynamik*. Harri Deutsch.

Lemaitre, G., Kohler, D., Lacroix, D., Meunier, J. P., and Vin, A. (1990). Reflective aspherized grating spectrographs for the Haute-Provence and Nanjing observatories - MARLYs and CARELEC. *Astronomy and Astrophysics*, **228**, 546–558.

Lena, P., Lebrun, F., and Mingnard, F. (1998). Observational Astrophysics. *A&A Library*.

Levison, H. F. (1996). Comet Taxonomy. In T. Rettig and J. M. Hahn, editors, *ASP Conf. Ser. 107: Completing the Inventory of the Solar System*, pages 173–191.

Levison, H. F. and Morbidelli, A. (2003). The formation of the Kuiper belt by the outward transport of bodies during Neptune's migration. *Nature*, **426**, 419–421.

Lowry, S. C., Fitzsimmons, A., and Collander-Brown, S. (2003). CCD photometry of distant comets. III. Ensemble properties of Jupiter-family comets. *Astronomy and Astrophysics*, **397**, 329–343.

Mallama, A., Wang, D., and Howard, R. A. (2002). Photometry of Mercury from SOHO/LASCO and Earth. The Phase Function from 2 to 170 deg. *Icarus*, **155**, 253–264.

Marconi, M. L. and Mendis, D. A. (1983). The atmosphere of a dirty-clathrate cometary nucleus - A two-phase, multifluid model. *Astrophysical Journal*, **273**, 381–396.

Marconi, M. L. and Mendis, D. A. (1986). The electron density and temperature in the tail of Comet Giacobini-Zinner. *Geophysical Research Letters*, **13**, 405.

Marsden, B. G. (2005). Sungrazing Comets. *Annual Review of Astronomy and Astrophysics*, **43**, 75–102.

Meech, K. J., Hainaut, O. R., and Marsden, B. G. (2004). Comet nucleus size distributions from HST and Keck telescopes. *Icarus*, **170**, 463–491.

Meech, K. J., Ageorges, N., A'Hearn, M. F., Arpigny, C., Ates, A., Aycock, J., Bagnulo, S., Bailey, J., Barber, R., Barrera, L., Barrena, R., Bauer, J. M., Belton, M. J. S., Bensch, F., Bhattacharya, B., Biver, N., Blake, G., Bockelée-Morvan, D., Boehnhardt, H., Bonev, B. P., Bonev, T., Buie, M. W., Burton, M. G., Butner, H. M., Cabanac, R., Campbell, R., Campins, H., Capria, M. T., Carroll, T., Chaffee, F., Charnley, S. B., Cleis, R., Coates, A., Cochran, A., Colom, P., Conrad, A., Coulson, I. M., Crovisier, J., deBuizer, J., Dekany, R., de Léon, J., Dello Russo, N., Delsanti, A., DiSanti, M., Drummond, J., Dundon, L., Etzel, P. B., Farnham, T. L., Feldman, P., Fernández, Y. R., Filipovic, M. D., Fisher, R. S., Fitzsimmons, A., Fong, D., Fugate, R., Fujiwara, H., Fujiyoshi, T., Furusho, R., Fuse, T., Gibb, E., Groussin, O., Gulkis, S., Gurwell, M., Hadamcik, E., Hainaut, O., Harker, D., Harrington, D., Harwit, M., Hasegawa, S., Hergenrother, C. W., Hirst, P., Hodapp, K., Honda, M., Howell, E. S., Hutsemékers, D., Iono, D., Ip, W.-H., Jackson, W., Jehin, E., Jiang, Z. J., Jones, G. H., Jones, P. A., Kadono, T., Kamath, U. W., Käufl, H. U., Kasuga, T., Kawakita, H., Kelley, M. S., Kerber, F., Kidger, M., Kinoshita, D., Knight, M., Lara, L., Larson, S. M., Lederer, S., Lee, C.-F., Levasseur-Regourd, A. C., Li, J. Y., Li, Q.-S., Licandro, J., Lin, Z.-Y., Lisse, C. M., LoCurto, G., Lovell, A. J., Lowry, S. C., Lyke, J., Lynch, D., Ma, J., Magee-Sauer, K., Maheswar, G., Manfroid, J., Marco, O., Martin, P., Melnick, G., Miller, S., Miyata, T., Moriarty-Schieven, G. H., Moskovitz, N., Mueller, B. E. A., Mumma, M. J., Muneer, S., Neufeld, D. A., Ootsubo, T., Osip, D., Pandea, S. K., Pantin, E., Paterno-Mahler, R., Patten, B., Penprase, B. E., Peck, A., Petitpas, G., Pinilla-Alonso, N., Pittichova, J., Pompei, E., Prabhu, T. P., Qi, C., Rao, R., Rauer, H., Reitsema, H., Rodgers, S. D., Rodriguez, P., Ruane, R., Ruch, G., Rujopakarn, W., Sahu, D. K., Sako, S., Sakon, I., Samarasinha, N., Sarkissian, J. M., Saviane, I., Schirmer, M., Schultz, P., Schulz, R., Seitzer, P., Sekiguchi, T., Selman, F., Serra-Ricart, M., Sharp, R., Snell, R. L., Snodgrass, C., Stallard, T., Stecklein, G., Sterken, C., Stüwe, J. A., Sugita, S., Sumner, M., Suntzeff, N., Swaters, R., Takakuwa, S., Takato, N., Thomas-Osip, J., Thompson, E., Tokunaga, A. T., Tozzi, G. P., Tran, H., Troy, M., Trujillo, C., Van Cleve, J., Vasundhara, R., Vazquez, R., Vilas, F., Villanueva, G., von Braun, K., Vora, P., Wainscoat, R. J., Walsh, K., Watanabe, J., Weaver, H. A., Weaver, W., Weiler, M., Weissman, P. R., Welsh, W. F., Wilner, D., Wolk, S., Womack, M., Wooden, D., Woodney, L. M., Woodward, C., Wu, Z.-Y., Wu, J.-H., Yamashita, T., Yang, B., Yang, Y.-B., Yokogawa, S., Zook, A. C., Zauderer, A., Zhao, X., Zhou, X., and Zucconi, J.-M. (2005). Deep Impact: Observations from a Worldwide Earth-Based Campaign. *Science*, **310**, 265–269.

Morbidelli, A., Brown, M. E., and Levison, H. F. (2003). The Kuiper Belt and its Primordial Sculpting. *Earth Moon and Planets*, **92**, 1–27.

Mumma, M. J., DiSanti, M. A., Magee-Sauer, K., Bonev, B. P., Villanueva, G. L., Kawakita, H., Dello Russo, N., Gibb, E. L., Blake, G. A., Lyke, J. E., Campbell, R. D., Aycock, J., Conrad, A., and Hill, G. M. (2005). Parent Volatiles in Comet 9P/Tempel 1: Before and After Impact. *Science*, **310**, 270–274.

Murray, C. D. and Dermott, S. F. (2000). *Solar System Dynamics*. Cambridge University Press.

Nakano, S. and Tsumura, M. (2005). Comet C/1995 O1 (Hale-Bopp). *IAU circular*, **8490**, 4.

Neubauer, F. M. (1991). The Magnetic Field Structure of the Cometary Plasma Environment. In R. L. Newburn, Jr., M. Neugebauer, and J. Rahe, editors, *ASSL Vol. 167: IAU Colloq. 116: Comets in the post-Halley era*, pages 1107–1124.

Newburn, R. L. and Spinrad, H. (1985). Spectrophotometry of seventeen comets. II - The continuum. *Astronomical Journal*, **90**, 2591–2608.

Okabe, H. (1981). Photochemistry of Acetylene at 1470 Å. *Journal of Chemical Physics*, **75**, 2772–2778.

Oke, J. B. (1990). Faint spectrophotometric standard stars. *Astronomical Journal*, **99**, 1621–1631.

Osip, D. J., Schleicher, D. G., and Millis, R. L. (1992). Comets - Groundbased observations of spacecraft mission candidates. *Icarus*, **98**, 115–124.

Patat, F. (2003). UBVRI night sky brightness during sunspot maximum at ESO-Paranal. *Astronomy and Astrophysics*, **400**, 1183–1198.

Perryman, M. A. C. (2005). Overview of the Gaia Mission. In P. K. Seidelmann and A. K. B. Monet, editors, *ASP Conf. Ser. 338: Astrometry in the Age of the Next Generation of Large Telescopes*, page 3.

Prialnik, D., Benkhoff, J., and Podolak, M. (2004). Modeling the structure and activity of comet nuclei. *Comets II*, pages 359–387.

Probstein, R. F. (1969). The Dusty Gasdynamics of Comet Heads. In *Problems of Hydrodynamics and Continuum Mechanics*, pages 568–583.

Rauer, H., Helbert, J., Arpigny, C., Benkhoff, J., Bockelée-Morvan, D., Boehnhardt, H., Colas, F., Crovisier, J., Hainaut, O., Jorda, L., Kueppers, M., Manfroid, J., and Thomas, N. (2003). Long-term optical spectrophotometric monitoring of comet C/1995 O1 (Hale-Bopp). *Astronomy and Astrophysics*, **397**, 1109–1122.

Remijan, A. J., Friedel, D. N., de Pater, I., Hogerheijde, M. R., Snyder, L. E., A'Hearn, M. F., Blake, G. A., Dickel, H. R., Forster, J. R., Kraybill, C., Looney, L. W., Palmer, P., and Wright, M. C. H. (2006). A BIMA Array Survey of Molecules in Comets LINEAR (C/2002 T7) and NEAT (C/2001 Q4). *Astrophysical Journal*, **643**, 567–572.

Rivkin, A. S., Binzel, R. P., and Bus, S. J. (2005). Constraining near-Earth object albedos using near-infrared spectroscopy. *Icarus*, **175**, 175–180.

Rodgers, S. D. and Charnley, S. B. (1998). HNC and HCN in Comets. *Astrophysical Journal Letters*, **501**, L227.

Rodgers, S. D. and Charnley, S. B. (2002). A model of the chemistry in cometary comae: deuterated molecules. *Monthly Notes of the Royal Astronomical Society*, **330**, 660–674.

Rodgers, S. D. and Charnley, S. B. (2005). Suprathermal chemical reactions driven by fast hydrogen atoms in cometary comae. *Monthly Notes of the Royal Astronomical Society*, **356**, 1542–1548.

Rodgers, S. D., Charnley, S. B., Huebner, W. F., and Boice, D. C. (2004). Physical processes and chemical reactions in cometary comae. *Comets II*, pages 505–522.

Romon-Martin, J., Delahodde, C., Barucci, M. A., de Bergh, C., and Peixinho, N. (2003). Photometric and spectroscopic observations of (2060) Chiron at the ESO Very Large Telescope. *Astronomy and Astrophysics*, **400**, 369–373.

Russell, H. N. (1916). On the Albedo of the Planets and Their Satellites. *Astrophysical Journal*, **43**, 173.

Sagdeev, R. Z., Elyasberg, P. E., and Moroz, V. I. (1988). Is the nucleus of Comet Halley a low density body? *Nature*, **331**, 240–242.

Schleicher, D. G. (1983). *The fluorescence of cometary OH and CN.* Ph.D. thesis, Maryland Univ., College Park.

Schleicher, D. G., Barnes, K. L., and Baugh, N. F. (2006). Photometry and Imaging Results for Comet 9P/Tempel 1 and Deep Impact: Gas Production Rates, Postimpact Light Curves, and Ejecta Plume Morphology. *Astronomical Journal*, **131**, 1130–1137.

Schmidt, H. U., Wegmann, R., Huebner, W. F., and Boice, D. C. (1988). Cometary gas and plasma flow with detailed chemistry. *Computer Physics Communications*, **49**, 17–59.

Schmitt, B., Espinasse, S., Grim, R. J. A., Greenberg, J. M., and Klinger, J. (1989). Laboratory studies of cometary ice analogues. In J. J. Hunt and T. D. Guyenne, editors, *ESA SP-302: Physics and Mechanics of Cometary Materials*, pages 65–69.

Sekanina, Z. (1999). A Determination of The Nuclear Size of Comet Hale-Bopp (C/1995 O1). *Earth Moon and Planets*, **77**, 147–153.

Seki, K., He, M., and Okabe, H. (1996). Photochemistry of Cyanoacetylene at 193.3 nm. *Journal of Physical Chemistry*, **100**, 5349–5353.

Stoer, J. and Bulirsch, R., editors (2000). *Numerische Mathematik 2.* Springer.

Storrs, A. D., Cochran, A. L., and Barker, E. S. (1992). Spectrophotometry of the continuum in 18 comets. *Icarus*, **98**, 163–178.

Sunshine, J. M., A'Hearn, M. F., Groussin, O., Li, J.-Y., Belton, M. J. S., Delamere, W. A., Kissel, J., Klaasen, K. P., McFadden, L. A., Meech, K. J., Melosh, H. J., Schultz, P. H., Thomas, P. C., Veverka, J., Yeomans, D. K., Busko, I. C., Desnoyer, M., Farnham, T. L., Feaga, L. M., Hampton, D. L., Lindler, D. J., Lisse, C. M., and Wellnitz, D. D. (2006). Exposed Water Ice Deposits on the Surface of Comet 9P/Tempel 1. *Science*, **311**, 1453–1455.

Swings, P. (1965). Cometary Spectra. (George Darwin Lecture). *Quarterly Journal of the Royal Astronomical Society*, **6**, 28.

Tancredi, G., Fernández, J. A., Rickman, H., and Licandro, J. (2006). Nuclear magnitudes and the size distribution of Jupiter family comets. *Icarus*, **182**, 527–549.

Tozzi, G. P., Boehnhardt, H., and Curto, G. L. (2003). Imaging and spectroscopy of comet C/2001 Q4 (NEAT) at 8.6 AU from the Sun. *Astronomy and Astrophysics*, **398**, L41–L44.

Weaver, H. A., A'Hearn, M. F., Arpigny, C., Combi, M. R., Feldman, P. D., Festou, M. C., and Tozzi, G.-P. (2004). Detection of Deuterium Emission from C/2001 Q4 (NEAT). *Bulletin of the American Astronomical Society*, **36**, 1120.

Wedler, G., editor (2004). *Lehrbuch der Physikalischen Chemie*. Wiley-VCH.

Weiler, M., Rauer, H., Knollenberg, J., Jorda, L., and Helbert, J. (2003). The dust activity of comet C/1995 O1 (Hale-Bopp) between 3 AU and 13 AU from the Sun. *Astronomy and Astrophysics*, **403**, 313–322.

Whipple, F. L. (1950). A comet model. I. The acceleration of Comet Encke. *Astrophysical Journal*, **111**, 375–394.

Whipple, F. L. (1951). A Comet Model. II. Physical Relations for Comets and Meteors. *Astrophysical Journal*, **113**, 464.

Whipple, F. L. (1955). A Comet Model. III. The Zodiacal Light. *Astrophysical Journal*, **121**, 750.

Whitman, K., Morbidelli, A., and Jedicke, R. (2006). The size frequency distribution of dormant Jupiter family comets. *Icarus*, **183**, 101–114.

Woodall, J., Agundez, M., Markwick-Kemper, A. J., and Millar, T. J. (2006). The UMIST Database for Astrochemistry 2005. *submitted to Astronomy and Astrophysics*.

Appendix A Chemical Reaction Network

This Appendix lists all chemical reactions included in the reaction network used in this work. γ denotes a photon and A, B, C list the Arrhenius coefficients of the reaction according to equation (77). A is given in $[10^{-6}\,\mathrm{s}^{-1}]$ in case of photoreactions, and $[10^{-6}\,\mathrm{cm}^3\,\mathrm{s}^{-1}]$ for all other reactions types. ΔE is the excess energy per reaction, given in $[\,\mathrm{eV}\,]$. Photoreactions for which the influence of optical density was computed by integration over the wavelength-dependend rate coefficients are indicated by †. The reactions are sorted according to their type, charge exchange reactions are included as a special case in the neutral−ion rearrangement reactions. The rate coefficients and excess energies were taken from Schmidt *et al.* (1988), Huebner *et al.* (1992), Helbert (2002), and Woodall *et al.* (2006). For some reactions, the Arrhenius coefficients were estimated in this work as discussed in chaper 8. In cases were the different sources give different rate coefficients for the same reaction, the value from the most recent reference is applied.

Photodissociation Reactions

Reaction									*A*	*B*	*C*	ΔE
H_2O	+	γ	→	H	+	OH			$10.3000^\dagger$	0.00000	0.00000	3.41000
H_2O	+	γ	→	H	+	H	+	O	$0.75500^\dagger$	0.00000	0.00000	0.70000
CO	+	γ	→	C	+	O			$0.28100^\dagger$	0.00000	0.00000	2.56000
H_2CO	+	γ	→	H_2	+	CO			$116.000^\dagger$	0.00000	0.00000	2.07000
H_2CO	+	γ	→	H	+	HCO			$66.4000^\dagger$	0.00000	0.00000	0.39000
CH_3OH	+	γ	→	H_2CO	+	H_2			$10.2000^\dagger$	0.00000	0.00000	7.45000
CH_3OH	+	γ	→	CH_3	+	OH			$0.55800^\dagger$	0.00000	0.00000	4.96000
CS_2	+	γ	→	CS	+	S			2030.00	0.00000	0.00000	1.52000
H_2S	+	γ	→	HS	+	H			320.000	0.00000	0.00000	2.14000
NH_3	+	γ	→	NH	+	H_2			$3.95000^\dagger$	0.00000	0.00000	1.72000
CO_2	+	γ	→	CO	+	O			$0.01710^\dagger$	0.00000	0.00000	1.69000
NH_2	+	γ	→	NH	+	H			$2.15000^\dagger$	0.00000	0.00000	6.38000
H_2CO	+	γ	→	CO	+	H	+	H	$32.0000^\dagger$	0.00000	0.00000	3.03000
NH	+	γ	→	N	+	H			10.0000	0.00000	0.00000	0.00000
C_2H_4	+	γ	→	C_2H_2	+	H_2			$23.6000^\dagger$	0.00000	0.00000	6.21000
NH_3	+	γ	→	NH_2	+	H			$170.000^\dagger$	0.00000	0.00000	1.84000
HCN	+	γ	→	CN	+	H			$12.6000^\dagger$	0.00000	0.00000	3.82000
CN	+	γ	→	C	+	N			$3.17000^\dagger$	0.00000	0.00000	7.41000
C_2H_2	+	γ	→	C_2H	+	H			$10.2000^\dagger$	0.00000	0.00000	3.16000
C_2H	+	γ	→	C_2	+	H			30.0000	0.00000	0.00000	3.00000
C_2	+	γ	→	C	+	C			$0.10300^\dagger$	0.00000	0.00000	3.62000
C_2H_6	+	γ	→	C_2H_4	+	H_2			$3.67000^\dagger$	0.00000	0.00000	8.96000
CH_2	+	γ	→	CH	+	H			20.0000	0.00000	0.00000	3.00000
HCO	+	γ	→	CO	+	H			40.0000	0.00000	0.00000	3.00000
NH_3	+	γ	→	NH	+	H	+	H	$1.99000^\dagger$	0.00000	0.00000	2.10000
C_2H_2	+	γ	→	C_2	+	H_2			$2.74000^\dagger$	0.00000	0.00000	3.07000
CH_4	+	γ	→	CH_2	+	H_2			$3.96000^\dagger$	0.00000	0.00000	5.29000
CH	+	γ	→	C	+	H			$9200.00^\dagger$	0.00000	0.00000	0.45000
OH	+	γ	→	O	+	H			$6.54000^\dagger$	0.00000	0.00000	1.27000
C_2H_4	+	γ	→	C_2H_2	+	H	+	H	$22.9000^\dagger$	0.00000	0.00000	1.67000
C_2H_6	+	γ	→	CH_3	+	CH_3			$0.88000^\dagger$	0.00000	0.00000	7.38000
C_2H_6	+	γ	→	C_2H_5	+	H			$3.28000^\dagger$	0.00000	0.00000	6.78000
C_2H_6	+	γ	→	CH_2	+	CH_4			$2.22000^\dagger$	0.00000	0.00000	6.14000
C_2H_5	+	γ	→	C_2H_2	+	H_2	+	H	1.00000	0.00000	0.00000	0.00000
HNCO	+	γ	→	NH	+	CO			14.9000	0.00000	0.00000	5.10000
HNCO	+	γ	→	H	+	NCO			13.8000	0.00000	0.00000	4.05000
OH	+	γ	→	O_{1s}	+	H			$0.06710^\dagger$	0.00000	0.00000	9.80000
OH	+	γ	→	O_{1d}	+	H			$0.63500^\dagger$	0.00000	0.00000	7.90000
SO_2	+	γ	→	S	+	O_2			50.9000	0.00000	0.00000	0.75000
C_2H_4	+	γ	→	CH_2	+	CH_2			60.0000	0.00000	0.00000	0.00000
C_3H_3	+	γ	→	C_3H_2	+	H			1820.00	0.00000	0.00000	0.00000
C_3H_4	+	γ	→	C_3H_3	+	H			133.000	0.00000	0.00000	0.00000
C_3H_4	+	γ	→	C_3H_2	+	H_2			29.6000	0.00000	0.00000	0.00000
C_3H_2	+	γ	→	C_3	+	H_2			0.95000	0.00000	0.00000	0.00000
CH_4	+	γ	→	CH_3	+	H			$0.26400^\dagger$	0.00000	0.00000	6.52000
CH_4	+	γ	→	CH_2	+	H	+	H	$2.14000^\dagger$	0.00000	0.00000	0.83000
CH_4	+	γ	→	CH	+	H_2	+	H	$0.63900^\dagger$	0.00000	0.00000	1.72000
CH	+	γ	→	C_{1d}	+	H			$5.12000^\dagger$	0.00000	0.00000	3.60000

Photodissociation Reactions (continued)

Reaction	A	B	C	ΔE
$CH_3CN + \gamma \rightarrow CH_3 + CN$	50.0000	0.00000	0.00000	2.00000
$NH_2CH_3 + \gamma \rightarrow NH_2 + CH_3$	30.0000	0.00000	0.00000	1.00000
$HC_3N + \gamma \rightarrow CN + C_2H$	39.2000	0.00000	0.00000	2.65000
$H_2 + \gamma \rightarrow H + H$	0.04800	0.00000	0.00000	8.23000
$CO + \gamma \rightarrow C_{1d} + O_{1d}$	$0.03460^\dagger$	0.00000	0.00000	2.29000
$N_2 + \gamma \rightarrow N + N$	0.66100	0.00000	0.00000	3.38000
$O_2 + \gamma \rightarrow O + O$	0.14500	0.00000	0.00000	4.39000
$O_2 + \gamma \rightarrow O + O_{1d}$	4.05000	0.00000	0.00000	1.33000
$O_2 + \gamma \rightarrow O_{1s} + O_{1s}$	0.03900	0.00000	0.00000	0.74000
$CO_{3p} + \gamma \rightarrow C + O$	72.0000	0.00000	0.00000	2.20000
$NO + \gamma \rightarrow N + O$	2.20000	0.00000	0.00000	1.84000
$C_3 + \gamma \rightarrow C_2 + C$	20.0000	0.00000	0.00000	0.00000
$H_2O + \gamma \rightarrow O_{1d} + H_2$	$0.59700^\dagger$	0.00000	0.00000	3.84000
$HNC + \gamma \rightarrow CN + H$	20.0000	0.00000	0.00000	3.00000
$CO_2 + \gamma \rightarrow CO + O_{1d}$	$0.92400^\dagger$	0.00000	0.00000	4.34000
$CO_2 + \gamma \rightarrow CO_{3p} + O$	$0.28200^\dagger$	0.00000	0.00000	1.99000
$H_2CO + \gamma \rightarrow CO_{1p} + H_2$	1.63000	0.00000	0.00000	2.10000
$H_2CO + \gamma \rightarrow CO_{3p} + H_2$	1.63000	0.00000	0.00000	2.10000
$H_2CO + \gamma \rightarrow CO_{3d} + H_2$	1.63000	0.00000	0.00000	2.10000
$H_2CO + \gamma \rightarrow CO_{3s} + H_2$	1.63000	0.00000	0.00000	2.10000
$H_2CO_2 + \gamma \rightarrow CO_2 + H_2$	316.000	0.00000	0.00000	4.75000
$H_2CO_2 + \gamma \rightarrow OH + HCO$	564.000	0.00000	0.00000	1.76000
$SO + \gamma \rightarrow S + O$	620.000	0.00000	0.00000	0.62000
$OCS + \gamma \rightarrow CO + S$	15.3000	0.00000	0.00000	2.72000
$OCS + \gamma \rightarrow CO + S_{1d}$	49.9000	0.00000	0.00000	1.96000
$OCS + \gamma \rightarrow CO + S_{1s}$	30.1000	0.00000	0.00000	2.13000
$OCS + \gamma \rightarrow CS + O$	0.06920	0.00000	0.00000	0.13000
$OCS + \gamma \rightarrow CS + O_{1d}$	6.34000	0.00000	0.00000	0.85000
$SO_2 + \gamma \rightarrow SO + O$	159.000	0.00000	0.00000	0.44000
$CS_2 + \gamma \rightarrow CS + S_{1d}$	892.000	0.00000	0.00000	0.50000
$H_2CS + \gamma \rightarrow CS + H_2$	$1.00 \cdot 10^{-5}$	0.00000	0.00000	0.00000
$C_4H_2 + \gamma \rightarrow C_3 + CH_2$	64.7000	0.00000	0.00000	0.00000
$C_4H_2 + \gamma \rightarrow C_4H + H$	66.2000	0.00000	0.00000	0.00000
$C_4H_2 + \gamma \rightarrow C_2H_2 + C_2$	13.9000	0.00000	0.00000	0.00000
$C_4H_2 + \gamma \rightarrow C_2H + C_2H$	9.58000	0.00000	0.00000	0.00000
$C_4H + \gamma \rightarrow C_2H + C_2$	30.0000	0.00000	0.00000	0.00000
$C_4H + \gamma \rightarrow C_4 + H$	30.0000	0.00000	0.00000	0.00000
$C_4 + \gamma \rightarrow C_3 + C$	100.000	0.00000	0.00000	0.00000
$C_4 + \gamma \rightarrow C_2 + C_2$	100.000	0.00000	0.00000	0.00000
$HC_3N + \gamma \rightarrow C_2H + CN$	0.03390	0.00000	0.00000	0.00000
$HC_3N + \gamma \rightarrow C_3N + H$	10.3000	0.00000	0.00000	0.00000
$C_3N + \gamma \rightarrow C_2 + CN$	0.72000	0.00000	0.00000	0.00000

Photoionisation Reactions

Reaction	A	B	C	ΔE
$C_2 + \gamma \rightarrow C_2^+ + e^-$	$0.908000^\dagger$	0.00000	0.00000	6.76000
$CO + \gamma \rightarrow CO^+ + e^-$	$0.380000^\dagger$	0.00000	0.00000	14.0000
$CO_2 + \gamma \rightarrow CO_2^+ + e^-$	$0.655000^\dagger$	0.00000	0.00000	16.9000
$C_2H_6 + \gamma \rightarrow C_2H_6^+ + e^-$	$0.486000^\dagger$	0.00000	0.00000	9.98000
$OH + \gamma \rightarrow OH^+ + e^-$	$0.247000^\dagger$	0.00000	0.00000	19.1000
$HCN + \gamma \rightarrow HCN^+ + e^-$	$0.451000^\dagger$	0.00000	0.00000	11.2000
$C_2H_2 + \gamma \rightarrow C_2H_2^+ + e^-$	$0.780000^\dagger$	0.00000	0.00000	5.06000
$C_2H_4 + \gamma \rightarrow C_2H_4^+ + e^-$	$0.580000^\dagger$	0.00000	0.00000	7.26000
$CH_4 + \gamma \rightarrow CH_4^+ + e^-$	$0.358000^\dagger$	0.00000	0.00000	5.45000
$CH_2 + \gamma \rightarrow CH_2^+ + e^-$	1.000000	0.00000	0.00000	0.00000
$CH + \gamma \rightarrow CH^+ + e^-$	$0.758000^\dagger$	0.00000	0.00000	6.35000
$H + \gamma \rightarrow H^+ + e^-$	0.073100	0.00000	0.00000	3.50000
$C + \gamma \rightarrow C^+ + e^-$	0.410000	0.00000	0.00000	5.90000
$C_{1d} + \gamma \rightarrow C^+ + e^-$	3.580000	0.00000	0.00000	1.00000
$N + \gamma \rightarrow N^+ + e^-$	0.185000	0.00000	0.00000	14.9000
$O + \gamma \rightarrow O^+ + e^-$	0.212000	0.00000	0.00000	21.6000
$O_{1d} + \gamma \rightarrow O^+ + e^-$	0.182000	0.00000	0.00000	21.6000
$O_{1s} + \gamma \rightarrow O^+ + e^-$	0.196000	0.00000	0.00000	18.9000
$H_2 + \gamma \rightarrow H_2^+ + e^-$	0.054100	0.00000	0.00000	6.56000
$O_2 + \gamma \rightarrow O_2^+ + e^-$	0.464000	0.00000	0.00000	15.9000
$CO_{3p} + \gamma \rightarrow CO^+ + e^-$	8.580000	0.00000	0.00000	2.20000
$N_2 + \gamma \rightarrow N_2^+ + e^-$	0.352000	0.00000	0.00000	17.8000
$NO + \gamma \rightarrow NO^+ + e^-$	1.280000	0.00000	0.00000	8.23000
$H_2O + \gamma \rightarrow H_2O^+ + e^-$	$0.331000^\dagger$	0.00000	0.00000	12.4000
$NH_3 + \gamma \rightarrow NH_3^+ + e^-$	$0.610000^\dagger$	0.00000	0.00000	5.77000
$H_2CO + \gamma \rightarrow H_2CO^+ + e^-$	$0.403000^\dagger$	0.00000	0.00000	3.19000
$H_2CO_2 + \gamma \rightarrow H_2CO_2^+ + e^-$	0.911000	0.00000	0.00000	3.89000
$S + \gamma \rightarrow S^+ + e^-$	1.070000	0.00000	0.00000	6.30000
$S_{1s} + \gamma \rightarrow S^+ + e^-$	1.050000	0.00000	0.00000	5.42000
$S_{1d} + \gamma \rightarrow S^+ + e^-$	1.080000	0.00000	0.00000	6.21000
$SO + \gamma \rightarrow SO^+ + e^-$	0.870000	0.00000	0.00000	9.80000
$H_2S + \gamma \rightarrow H_2S^+ + e^-$	0.564000	0.00000	0.00000	2.18000
$OCS + \gamma \rightarrow OCS^+ + e^-$	0.237000	0.00000	0.00000	1.50000
$SO_2 + \gamma \rightarrow SO_2^+ + e^-$	1.060000	0.00000	0.00000	12.0000
$CS_2 + \gamma \rightarrow CS_2^+ + e^-$	0.550000	0.00000	0.00000	2.41000

Photodissociative Ionisations

Reaction	A	B	C	ΔE
$H_2S + \gamma \rightarrow S^+ + H_2 + e^-$	0.147000	0.00000	0.00000	6.86000
$H_2S + \gamma \rightarrow HS^+ + H + e^-$	0.072600	0.00000	0.00000	12.0000
$CO_2 + \gamma \rightarrow C^+ + O_2 + e^-$	$0.028900^{\dagger}$	0.00000	0.00000	30.2000
$C_2H_2 + \gamma \rightarrow C_2H^+ + H + e^-$	$0.074300^{\dagger}$	0.00000	0.00000	15.9000
$C_2H_4 + \gamma \rightarrow C_2H_3^+ + H + e^-$	$0.226000^{\dagger}$	0.00000	0.00000	13.1000
$C_2H_4 + \gamma \rightarrow C_2H_2^+ + H_2 + e^-$	$0.197000^{\dagger}$	0.00000	0.00000	12.4000
$CH_4 + \gamma \rightarrow CH_3^+ + H + e^-$	$0.198000^{\dagger}$	0.00000	0.00000	8.01000
$CH_4 + \gamma \rightarrow CH_2^+ + H_2 + e^-$	$0.020800^{\dagger}$	0.00000	0.00000	19.6000
$CH_4 + \gamma \rightarrow H^+ + CH_3 + e^-$	$0.009120^{\dagger}$	0.00000	0.00000	27.0000
$H_2 + \gamma \rightarrow H^+ + H + e^-$	0.009520	0.00000	0.00000	24.8000
$N_2 + \gamma \rightarrow N^+ + N + e^-$	0.015000	0.00000	0.00000	28.9000
$O_2 + \gamma \rightarrow O^+ + O + e^-$	0.110000	0.00000	0.00000	23.8000
$CO + \gamma \rightarrow C^+ + O + e^-$	$0.029400^{\dagger}$	0.00000	0.00000	26.4000
$CO + \gamma \rightarrow O^+ + C + e^-$	$0.024200^{\dagger}$	0.00000	0.00000	26.0000
$CO_{3p} + \gamma \rightarrow C^+ + O + e^-$	0.024000	0.00000	0.00000	32.0000
$CO_{3p} + \gamma \rightarrow O^+ + C + e^-$	0.021000	0.00000	0.00000	32.6000
$NO + \gamma \rightarrow O^+ + N + e^-$	0.001810	0.00000	0.00000	18.6000
$NO + \gamma \rightarrow N^+ + O + e^-$	0.031800	0.00000	0.00000	25.2000
$H_2O + \gamma \rightarrow OH^+ + H + e^-$	$0.055400^{\dagger}$	0.00000	0.00000	18.6000
$H_2O + \gamma \rightarrow O^+ + H_2 + e^-$	$0.005850^{\dagger}$	0.00000	0.00000	36.5000
$H_2O + \gamma \rightarrow H^+ + OH + e^-$	$0.013100^{\dagger}$	0.00000	0.00000	25.0000
$CO_2 + \gamma \rightarrow CO^+ + O + e^-$	$0.050200^{\dagger}$	0.00000	0.00000	27.1000
$CO_2 + \gamma \rightarrow O^+ + CO + e^-$	$0.063800^{\dagger}$	0.00000	0.00000	27.9000
$H_2CO + \gamma \rightarrow CHO^+ + H + e^-$	$0.196000^{\dagger}$	0.00000	0.00000	7.34000
$H_2CO + \gamma \rightarrow CO^+ + H_2 + e^-$	$0.121000^{\dagger}$	0.00000	0.00000	28.5000
$NH_3 + \gamma \rightarrow NH_2^+ + H + e^-$	$0.177000^{\dagger}$	0.00000	0.00000	11.3000
$NH_3 + \gamma \rightarrow NH^+ + H_2 + e^-$	$0.006920^{\dagger}$	0.00000	0.00000	26.2000
$NH_3 + \gamma \rightarrow H^+ + NH_2 + e^-$	$0.003330^{\dagger}$	0.00000	0.00000	20.3000
$H_2CO_2 + \gamma \rightarrow CHO^+ + OH + e^-$	0.282000	0.00000	0.00000	21.4000
$OCS + \gamma \rightarrow S^+ + CO + e^-$	0.008660	0.00000	0.00000	57.5000
$OCS + \gamma \rightarrow CO^+ + S + e^-$	0.002040	0.00000	0.00000	62.1000
$OCS + \gamma \rightarrow CS^+ + O + e^-$	0.000273	0.00000	0.00000	56.6000
$OCS + \gamma \rightarrow O^+ + CS + e^-$	0.000184	0.00000	0.00000	61.6000
$OCS + \gamma \rightarrow C^+ + SO + e^-$	0.000558	0.00000	0.00000	61.0000
$CS_2 + \gamma \rightarrow S^+ + CS + e^-$	0.011900	0.00000	0.00000	53.4000
$CS_2 + \gamma \rightarrow CS^+ + S + e^-$	0.007750	0.00000	0.00000	51.3000
$CS_2 + \gamma \rightarrow S_2^+ + C + e^-$	0.000345	0.00000	0.00000	48.4000
$CS_2 + \gamma \rightarrow C^+ + S_2 + e^-$	0.001170	0.00000	0.00000	50.2000
$CH_4 + \gamma \rightarrow CH^+ + H_2 + H + e^-$	$0.004210^{\dagger}$	0.00000	0.00000	27.8000
$CO_2 + \gamma \rightarrow C^+ + O + O + e^-$	0.028900	0.00000	0.00000	30.2000
$NH_3 + \gamma \rightarrow N^+ + H_2 + H + e^-$	$0.003250^{\dagger}$	0.00000	0.00000	29.5000

Neutral–Neutral Rearrangements

Reaction									A	B	C	ΔE
C_2H_3	+	H_2	→	C_2H_4	+	H			$5.00 \cdot 10^{-6}$	0.00000	3200.00	0.00000
C_2H_3	+	H	→	C_2H_2	+	H_2			$3.32 \cdot 10^{-5}$	0.00000	0.00000	0.00000
CH_2	+	CH_2	→	C_2H_2	+	H_2			0.002630	0.00000	6013.00	0.00000
CH_2	+	CH_3	→	C_2H_4	+	H			$5.00 \cdot 10^{-5}$	0.00000	0.00000	0.00000
CH	+	CH_4	→	C_2H_4	+	H			0.000105	−1.04000	36.0000	0.00000
C	+	C_3H_4	→	C_4H_2	+	H_2			0.000400	0.00000	0.00000	0.00000
C_{1d}	+	CH_4	→	C_2H_2	+	H_2			$3.20 \cdot 10^{-5}$	0.00000	0.00000	0.00000
CH_2	+	N	→	HCN	+	H			$3.95 \cdot 10^{-5}$	0.17000	0.00000	0.00000
O_{1d}	+	CH_4	→	CH_3	+	OH			0.000120	0.00000	0.00000	0.00000
CH_4	+	H_2	→	CH_3	+	H	+	H_2	0.330000	0.00000	44035.0	0.00000
CH_4	+	H	→	CH_3	+	H	+	H	0.330000	0.00000	44035.0	0.00000
O_{1d}	+	CO_2	→	CO_2	+	O			0.000120	0.00000	0.00000	0.00000
O_{1d}	+	CO	→	CO	+	O			0.000550	0.00000	625.000	0.00000
O_{1d}	+	N_2	→	N_2	+	O			$2.30 \cdot 10^{-5}$	0.00000	0.00000	0.00000
O_{1d}	+	O_2	→	O_2	+	O			$5.30 \cdot 10^{-5}$	0.00000	0.00000	0.00000
O_{1s}	+	O_2	→	O_2	+	O			$4.90 \cdot 10^{-6}$	0.00000	870.900	0.00000
O_{1s}	+	N_2	→	N_2	+	O			$1.00 \cdot 10^{-11}$	0.00000	0.00000	0.00000
O_{1s}	+	O	→	O	+	O			$2.00 \cdot 10^{-8}$	0.00000	0.00000	0.00000
O_2	+	H	→	O	+	O	+	H	0.006000	0.00000	52300.0	0.00000
CH	+	H	→	C	+	H	+	H	0.006000	0.00000	40200.0	0.00000
CO	+	H	→	C	+	O	+	H	0.006000	0.00000	129000.	0.00000
NO	+	H	→	N	+	O	+	H	670.0000	−1.50000	75500.0	0.00000
N_2	+	H	→	N	+	N	+	H	6700.000	−1.60000	113200.	0.00000
OH	+	H	→	O	+	H	+	H	0.006000	0.00000	50900.0	0.00000
H_2	+	H	→	H	+	H	+	H	0.467000	−1.00000	55000.0	0.00000
H_2O	+	H	→	OH	+	H	+	H	0.005800	0.00000	52900.0	0.00000
HCO	+	H	→	CO	+	H	+	H	0.000960	0.00000	8350.00	0.00000
NH_3	+	H	→	NH_2	+	H	+	H	0.015000	0.00000	42400.0	0.00000
H_2CO	+	H	→	HCO	+	H	+	H	0.600000	0.00000	43680.0	0.00000
O_2	+	H_2	→	O	+	O	+	H_2	0.006000	0.00000	52300.0	0.00000
CH	+	H_2	→	C	+	H	+	H_2	0.006000	0.00000	40200.0	0.00000
CO	+	H_2	→	C	+	O	+	H_2	0.006000	0.00000	129000.	0.00000
NO	+	H_2	→	N	+	O	+	H_2	670.0000	−1.50000	75500.0	0.00000
N_2	+	H_2	→	N	+	N	+	H_2	6700.000	−1.60000	113200.	0.00000
OH	+	H_2	→	O	+	H	+	H_2	0.006000	0.00000	50900.0	0.00000
H_2O	+	H_2	→	OH	+	H	+	H_2	0.005800	0.00000	52900.0	0.00000
HCO	+	H_2	→	CO	+	H	+	H_2	0.000960	0.00000	8350.00	0.00000
NH_3	+	H_2	→	NH_2	+	H	+	H_2	0.015000	0.00000	42400.0	0.00000
H_2CO	+	H_2	→	HCO	+	H	+	H_2	0.006000	0.00000	43680.0	0.00000
C	+	OH	→	CO	+	H			$1.00 \cdot 10^{-4}$	0.00000	0.00000	0.00000
O	+	CH_3	→	H_2CO	+	H			0.000130	0.00000	0.00000	0.00000
O	+	CH_2	→	CH	+	OH			0.000498	0.00000	6000.00	0.00000
O	+	CH_2	→	HCO	+	H			$5.01 \cdot 10^{-5}$	0.00000	0.00000	0.00000
O	+	HCO	→	CO	+	OH			$5.00 \cdot 10^{-5}$	0.00000	0.00000	0.00000
O	+	HCO	→	CO_2	+	H			$5.00 \cdot 10^{-5}$	0.00000	0.00000	0.00000
HCO	+	H	→	CO	+	H_2			0.000200	0.00000	0.00000	0.00000
O	+	OH	→	H	+	O_2			$4.15 \cdot 10^{-5}$	0.00000	0.00000	0.70000
N	+	NH	→	N_2	+	H			$4.98 \cdot 10^{-5}$	0.00000	0.00000	0.00000

Neutral−Neutral Rearrangements (continued)

Reaction							A	B	C	ΔE
NH	+	C	→	CN	+	H	0.000120	0.50000	0.00000	0.00000
CH	+	N	→	CN	+	H	0.000166	−0.09000	0.00000	0.00000
NH	+	O	→	NO	+	H	0.000116	0.00000	0.00000	0.00000
NH_2	+	O	→	OH	+	NH	$1.39 \cdot 10^{-5}$	0.00000	40.0000	0.00000
NH_2	+	O	→	HNO	+	H	$4.56 \cdot 10^{-5}$	0.00000	−10.0000	0.00000
NO	+	N	→	N_2	+	O	$3.75 \cdot 10^{-5}$	0.00000	26.0000	3.20000
C	+	O_2	→	CO	+	O	$3.30 \cdot 10^{-5}$	0.00000	0.00000	0.00000
C	+	NO	→	CN	+	O	$6.00 \cdot 10^{-5}$	−0.16000	0.00000	0.00000
N	+	OH	→	NO	+	H	$5.81 \cdot 10^{-5}$	0.00000	0.00000	0.00000
OH	+	OH	→	O	+	H_2O	$1.65 \cdot 10^{-6}$	1.14000	50.0000	0.700000
CO	+	OH	→	CO_2	+	H	$2.81 \cdot 10^{-7}$	0.00000	176.000	0.00000
CH	+	O	→	CO	+	H	$4.00 \cdot 10^{-5}$	0.00000	0.00000	0.00000
CH	+	C	→	C_2	+	H	$6.59 \cdot 10^{-5}$	0.00000	0.00000	0.00000
C_2	+	O	→	CO	+	C	$3.00 \cdot 10^{-5}$	0.00000	0.00000	0.00000
CN	+	O_2	→	NCO	+	O	$1.86 \cdot 10^{-5}$	−0.13000	−40.0000	0.00000
CH	+	H	→	C	+	H_2	0.000131	0.00000	80.0000	0.00000
O_{1d}	+	NH_3	→	NH_2	+	OH	0.000340	0.00000	0.00000	0.00000
O_{1d}	+	CH_4	→	H_2CO	+	H_2	0.000130	0.00000	0.00000	0.00000
O_{1d}	+	H_2O	→	OH	+	OH	0.000210	0.00000	0.00000	1.30000
O_{1d}	+	H_2	→	OH	+	H	0.000130	0.00000	0.00000	0.00000
C_{1d}	+	H_2	→	CH	+	H	$4.15 \cdot 10^{-5}$	0.00000	0.00000	0.00000
C_{1d}	+	NO	→	CN	+	O	$9.20 \cdot 10^{-5}$	0.00000	0.00000	0.00000
S	+	O_2	→	SO	+	O	$4.74 \cdot 10^{-7}$	1.41000	−439.000	0.00000
CH	+	S	→	CS	+	H	$5.00 \cdot 10^{-5}$	0.00000	0.00000	0.00000
OH	+	S	→	SO	+	H	$6.60 \cdot 10^{-5}$	0.00000	0.00000	0.00000
HS	+	O	→	SO	+	H	$8.25 \cdot 10^{-5}$	0.17000	−254.000	0.00000
HS	+	N	→	NS	+	H	$1.00 \cdot 10^{-4}$	0.00000	0.00000	0.00000
CS	+	O	→	CO	+	S	0.000248	−0.65000	783.000	0.00000
SO	+	N	→	NO	+	S	$1.73 \cdot 10^{-5}$	0.50000	750.000	0.00000
SO	+	OH	→	SO_2	+	H	$8.60 \cdot 10^{-5}$	0.50000	0.00000	0.00000
CH_3	+	S	→	H_2CS	+	H	0.000140	0.00000	0.00000	0.00000
SO	+	C	→	CO	+	S	$3.50 \cdot 10^{-5}$	0.00000	0.00000	0.00000
SO	+	C	→	CS	+	O	$3.50 \cdot 10^{-5}$	0.00000	0.00000	0.00000

Neutral−Ion Rearrangements

Reaction							A	B	C	ΔE
NH_4^+	+	H_2O	→	NH_4^+	+	H_2O	$1.00 \cdot 10^{-4}$	0.50000	0.00000	0.00000
H_3O^+	+	H_2O	→	H_3O^+	+	H_2O	$1.00 \cdot 10^{-4}$	0.50000	0.00000	0.00000
H_3O^+	+	CO_2	→	H_3O^+	+	CO_2	$1.00 \cdot 10^{-4}$	0.50000	0.00000	0.00000
H_3O^+	+	CO	→	H_3O^+	+	CO	$1.00 \cdot 10^{-4}$	0.50000	0.00000	0.00000
$C_2H_6^+$	+	C_2H_4	→	$C_2H_4^+$	+	C_2H_6	0.001150	0.00000	0.00000	0.00000
$C_2H_6^+$	+	NH_3	→	NH_3^+	+	C_2H_6	0.000624	0.00000	0.00000	0.00000
$C_2H_6^+$	+	CH_3	→	CH_3^+	+	C_2H_6	0.001000	0.00000	0.00000	0.00000
$C_2H_4^+$	+	NH_3	→	NH_3^+	+	C_2H_4	0.001800	0.00000	0.00000	0.00000
$C_2H_4^+$	+	CH_3	→	CH_3^+	+	C_2H_4	0.001000	0.00000	0.00000	0.00000
$C_2H_2^+$	+	C_2H_4	→	$C_2H_4^+$	+	C_2H_2	0.000414	0.00000	0.00000	0.00000
$C_2H_2^+$	+	C_3H_4	→	$C_3H_4^+$	+	C_2H_2	0.000500	0.00000	0.00000	0.00000
$C_2H_2^+$	+	NH_3	→	NH_3^+	+	C_2H_2	0.002140	0.00000	0.00000	0.00000
$C_2H_2^+$	+	H_2CO	→	H_2CO^+	+	C_2H_2	0.000860	0.00000	0.00000	0.00000
$C_2H_2^+$	+	H_2S	→	H_2S^+	+	C_2H_2	0.002200	0.00000	0.00000	0.00000
C_2H^+	+	S	→	S^+	+	C_2H	0.001200	0.00000	0.00000	0.00000
CH_4^+	+	C_2H_2	→	$C_2H_2^+$	+	CH_4	0.001130	0.00000	0.00000	0.00000
CH_4^+	+	C_2H_4	→	$C_2H_4^+$	+	CH_4	0.001380	0.00000	0.00000	0.00000
CH_4^+	+	NH_3	→	NH_3^+	+	CH_4	0.001650	0.00000	0.00000	0.00000
CH_4^+	+	O_2	→	O_2^+	+	CH_4	0.000390	0.00000	0.00000	0.00000
H_2^+	+	C_2H_6	→	$C_2H_6^+$	+	H_2	0.000294	0.00000	0.00000	0.00000
H_2^+	+	C_2H_4	→	$C_2H_4^+$	+	H_2	0.002210	0.00000	0.00000	0.00000
H_2^+	+	C_2H_2	→	$C_2H_2^+$	+	H_2	0.004820	0.00000	0.00000	0.00000
H_2^+	+	CH_4	→	CH_4^+	+	H_2	0.001400	0.00000	0.00000	0.00000
H^+	+	C_3H_4	→	$C_3H_4^+$	+	H	0.002000	0.00000	0.00000	0.00000
H^+	+	CH_4	→	CH_4^+	+	H	0.001500	0.00000	0.00000	0.00000
C^+	+	C_3H_4	→	$C_3H_4^+$	+	C	0.000570	0.00000	0.00000	0.00000
N_2^+	+	CH_4	→	CH_4^+	+	N_2	0.000165	0.00000	0.00000	0.00000
OH^+	+	CH_4	→	CH_4^+	+	OH	0.000966	0.00000	0.00000	0.00000
CO^+	+	CH_4	→	CH_4^+	+	CO	0.000793	0.00000	0.00000	0.00000
CO_2^+	+	CH_4	→	CH_4^+	+	CO_2	0.000550	0.00000	0.00000	0.00000
C^+	+	CH	→	CH^+	+	C	0.000380	0.00000	0.00000	0.00000
$C_3H_5^+$	+	C_6H_6	→	$C_6H_7^+$	+	C_3H_4	0.000115	0.00000	0.00000	0.00000
$C_3H_4^+$	+	C_3H_4	→	$C_6H_7^+$	+	H	0.000750	0.00000	0.00000	0.00000
C_4H^+	+	C_3H_4	→	$C_7H_4^+$	+	H	0.001200	0.00000	0.00000	0.00000
$C_4H_2^+$	+	C_3H_4	→	$C_7H_4^+$	+	H_2	0.001000	0.00000	0.00000	0.00000
$C_4H_3^+$	+	C_3H_4	→	$C_7H_5^+$	+	H_2	0.001000	0.00000	0.00000	0.00000
$C_5H_2^+$	+	C_3H_4	→	$C_8H_4^+$	+	H_2	0.001000	0.00000	0.00000	0.00000
$C_6H_2^+$	+	C_3H_4	→	$C_9H_4^+$	+	H_2	0.001100	0.00000	0.00000	0.00000
$C_3H_3^+$	+	C_3H_4	→	$C_6H_5^+$	+	H_2	0.001000	0.00000	0.00000	0.00000
$C_3H_2^+$	+	C_3H_4	→	$H_2C_3H^+$	+	C_3H_3	0.000300	0.00000	0.00000	0.00000
$C_3H_2^+$	+	C_3H_4	→	$C_6H_4^+$	+	H_2	0.000300	0.00000	0.00000	0.00000
C_3^+	+	H_2	→	C_3H^+	+	H	0.000240	0.00000	0.00000	0.00000
$C_2H_6^+$	+	C_2H_6	→	$C_3H_8^+$	+	CH_4	$7.98 \cdot 10^{-6}$	0.00000	0.00000	0.00000
$C_2H_6^+$	+	C_2H_2	→	$C_3H_5^+$	+	CH_3	0.000819	0.00000	0.00000	0.00000
$C_2H_6^+$	+	C_2H_2	→	$C_4H_7^+$	+	H	0.000129	0.00000	0.00000	0.00000
$C_2H_6^+$	+	C_2H_2	→	$C_2H_5^+$	+	C_2H_3	0.000222	0.00000	0.00000	0.00000
$C_2H_6^+$	+	H_2O	→	H_3O^+	+	C_2H_5	0.002950	0.00000	0.00000	0.00000
$C_2H_6^+$	+	NH_3	→	NH_4^+	+	C_2H_5	0.001610	0.00000	0.00000	0.00000

Neutral–Ion Rearrangements (continued)

Reaction							A	B	C	ΔE
$C_2H_6^+$	+	H_2CO	→	CH_2OH^+	+	C_2H_5	0.001000	0.00000	0.00000	0.00000
$C_2H_6^+$	+	HCN	→	H_2CN^+	+	C_2H_5	0.001000	0.00000	0.00000	0.00000
$C_2H_5^+$	+	C_2H_2	→	$C_3H_3^+$	+	CH_4	$6.84 \cdot 10^{-5}$	0.00000	0.00000	0.00000
$C_2H_5^+$	+	C_2H_2	→	$C_4H_5^+$	+	H_2	0.000122	0.00000	0.00000	0.00000
$C_2H_5^+$	+	C_2H_4	→	$C_3H_5^+$	+	CH_4	0.000390	0.00000	0.00000	0.00000
$C_2H_5^+$	+	H_2O	→	H_3O^+	+	C_2H_4	0.001400	0.00000	0.00000	0.00000
$C_2H_5^+$	+	NH_3	→	NH_4^+	+	C_2H_4	0.002100	0.00000	0.00000	0.00000
$C_2H_5^+$	+	H_2CO	→	CH_2OH^+	+	C_2H_4	0.001000	0.00000	0.00000	0.00000
$C_2H_5^+$	+	HCN	→	H_2CN^+	+	C_2H_4	0.001000	0.00000	0.00000	0.00000
$C_2H_5^+$	+	CH_3	→	$C_2H_4^+$	+	CH_4	0.000500	0.00000	0.00000	0.00000
$C_2H_4^+$	+	C_3H_4	→	$C_4H_5^+$	+	CH_3	0.000800	0.00000	0.00000	0.00000
$C_2H_4^+$	+	C_2H_4	→	$C_3H_5^+$	+	CH_3	0.000711	0.00000	0.00000	0.00000
$C_2H_4^+$	+	C_2H_4	→	$C_4H_7^+$	+	H	$7.90 \cdot 10^{-5}$	0.00000	0.00000	0.00000
$C_2H_4^+$	+	C_2H_2	→	$C_3H_3^+$	+	CH_3	0.000632	0.00000	0.00000	0.00000
$C_2H_4^+$	+	C_2H_2	→	$C_4H_5^+$	+	H	0.000193	0.00000	0.00000	0.00000
$C_2H_4^+$	+	NH_3	→	NH_4^+	+	C_2H_3	0.001940	0.00000	0.00000	0.00000
$C_2H_3^+$	+	C_3H_4	→	$C_3H_5^+$	+	C_2H_2	0.000500	0.00000	0.00000	0.00000
$C_2H_3^+$	+	C_3H_4	→	$C_5H_5^+$	+	H_2	0.000500	0.00000	0.00000	0.00000
$C_2H_3^+$	+	C_2H_6	→	$C_2H_5^+$	+	C_2H_4	0.000291	0.00000	0.00000	0.00000
$C_2H_3^+$	+	C_2H_6	→	$C_3H_5^+$	+	CH_4	0.000248	0.00000	0.00000	0.00000
$C_2H_3^+$	+	C_2H_6	→	$C_4H_7^+$	+	H_2	$8.10 \cdot 10^{-5}$	0.00000	0.00000	0.00000
$C_2H_3^+$	+	C_2H_4	→	$C_2H_5^+$	+	C_2H_2	0.000890	0.00000	0.00000	0.00000
$C_2H_3^+$	+	C_2H_2	→	$C_4H_3^+$	+	H_2	0.000720	0.00000	0.00000	0.00000
$C_2H_3^+$	+	H_2O	→	H_3O^+	+	C_2H_2	0.001110	0.00000	0.00000	0.00000
$C_2H_3^+$	+	NH_3	→	NH_4^+	+	C_2H_2	0.002500	0.00000	0.00000	0.00000
$C_2H_3^+$	+	H_2CO	→	CH_2OH^+	+	C_2H_2	0.001000	0.00000	0.00000	0.00000
$C_2H_3^+$	+	HCN	→	H_2CN^+	+	C_2H_2	0.001000	0.00000	0.00000	0.00000
$C_2H_3^+$	+	H_2S	→	H_3S^+	+	C_2H_2	0.000840	0.00000	0.00000	0.00000
$C_2H_3^+$	+	CH_4	→	$C_3H_5^+$	+	H_2	0.000200	0.00000	0.00000	0.00000
$C_2H_2^+$	+	C_3H_4	→	$C_5H_4^+$	+	H_2	0.000500	0.00000	0.00000	0.00000
$C_2H_2^+$	+	C_3H_4	→	$C_5H_5^+$	+	H	0.000500	0.00000	0.00000	0.00000
$C_2H_2^+$	+	C_2H_2	→	$C_4H_2^+$	+	H_2	0.000490	0.00000	0.00000	0.00000
$C_2H_2^+$	+	C_2H_2	→	$C_4H_3^+$	+	H	0.000910	0.00000	0.00000	0.00000
$C_2H_2^+$	+	C_2H_6	→	$C_2H_4^+$	+	C_2H_4	0.000263	0.00000	0.00000	0.00000
$C_2H_2^+$	+	C_2H_6	→	$C_2H_5^+$	+	C_2H_3	0.000131	0.00000	0.00000	0.00000
$C_2H_2^+$	+	C_2H_6	→	$C_3H_5^+$	+	CH_3	0.000788	0.00000	0.00000	0.00000
$C_2H_2^+$	+	C_2H_6	→	$C_4H_7^+$	+	H	0.000131	0.00000	0.00000	0.00000
$C_2H_2^+$	+	C_2H_4	→	$C_3H_3^+$	+	CH_3	0.000507	0.00000	0.00000	0.00000
$C_2H_2^+$	+	C_2H_4	→	$C_4H_5^+$	+	H	0.000317	0.00000	0.00000	0.00000
$C_2H_2^+$	+	H_2CO	→	HCO^+	+	C_2H_3	0.000538	0.00000	0.00000	0.00000
$C_2H_2^+$	+	CH_4	→	$C_3H_4^+$	+	H_2	0.000176	0.00000	0.00000	0.00000
$C_2H_2^+$	+	CH_4	→	$C_3H_5^+$	+	H	0.000664	0.00000	0.00000	0.00000
C_2H^+	+	CH_4	→	$C_2H_2^+$	+	CH_3	0.000374	0.00000	0.00000	0.00000
C_2H^+	+	CH_4	→	$C_3H_3^+$	+	H_2	0.000374	0.00000	0.00000	0.00000
C_2H^+	+	CH_4	→	$C_3H_4^+$	+	H	0.000132	0.00000	0.00000	0.00000
C_2H^+	+	NH_3	→	NH_4^+	+	C_2	0.000500	0.00000	0.00000	0.00000
C_2H^+	+	H_2CO	→	CH_2OH^+	+	C_2	0.001000	0.00000	0.00000	0.00000
C_2H^+	+	HCN	→	H_2CN^+	+	C_2	0.001000	0.00000	0.00000	0.00000

Neutral–Ion Rearrangements (continued)

Reaction							A	B	C	ΔE
C_2H^+	+	H_2	→	$C_2H_2^+$	+	H	0.001100	0.00000	0.00000	0.00000
C_2^+	+	CH_4	→	$C_3H_2^+$	+	H_2	0.000574	0.00000	0.00000	0.00000
C_2^+	+	CH_4	→	C_2H^+	+	CH_3	0.000238	0.00000	0.00000	0.00000
C_2^+	+	CH_4	→	$C_3H_3^+$	+	H	0.000210	0.00000	0.00000	0.00000
C_2^+	+	CH_4	→	$C_2H_2^+$	+	CH_2	1.820000	0.00000	0.00000	0.00000
C_2^+	+	H_2	→	C_2H^+	+	H	0.001100	0.00000	0.00000	0.00000
C^+	+	C_3H_4	→	$C_2H_2^+$	+	C_2H_2	0.000190	0.00000	0.00000	0.00000
C^+	+	C_3H_4	→	$H_2C_3H^+$	+	CH	0.000380	0.00000	0.00000	0.00000
C^+	+	C_3H_4	→	$C_2H_3^+$	+	C_2H	0.000190	0.00000	0.00000	0.00000
C^+	+	C_3H_4	→	$C_4H_2^+$	+	H_2	0.000570	0.00000	0.00000	0.00000
C^+	+	CH_4	→	$C_2H_3^+$	+	H	0.001100	0.00000	0.00000	0.00000
C^+	+	CH_4	→	$C_2H_2^+$	+	H_2	0.000400	0.00000	0.00000	0.00000
C^+	+	CH_2	→	C_2H^+	+	H	0.000550	0.00000	0.00000	0.00000
C^+	+	CH_3	→	$C_2H_2^+$	+	H	0.001300	0.00000	0.00000	0.00000
C^+	+	C_2H	→	C_3^+	+	H	0.001000	0.00000	0.00000	0.00000
CH_5^+	+	CH_3	→	$C_2H_6^+$	+	H_2	0.000500	0.00000	0.00000	0.00000
CH_4^+	+	C_2H_2	→	$C_2H_3^+$	+	CH_3	0.001230	0.00000	0.00000	0.00000
CH_4^+	+	C_2H_4	→	$C_2H_5^+$	+	CH_3	0.000423	0.00000	0.00000	0.00000
CH_4^+	+	CH_4	→	CH_5^+	+	CH_3	0.001500	0.00000	0.00000	0.00000
CH_3^+	+	C_2H_2	→	$C_3H_3^+$	+	H_2	0.001150	0.00000	0.00000	0.00000
CH_3^+	+	C_2H_4	→	$C_2H_3^+$	+	CH_4	0.000350	0.00000	0.00000	0.00000
CH_3^+	+	C_2H_4	→	$C_3H_5^+$	+	H_2	0.000524	0.00000	0.00000	0.00000
CH_3^+	+	C_2H_6	→	$C_2H_5^+$	+	CH_4	0.001480	0.00000	0.00000	0.00000
CH_3^+	+	CH_4	→	$C_2H_5^+$	+	H_2	0.001200	0.00000	0.00000	0.00000
CH_3^+	+	NH_3	→	NH_4^+	+	CH_2	0.000304	0.00000	0.00000	0.00000
CH_3^+	+	H_2CO	→	HCO^+	+	CH_4	0.001600	0.00000	0.00000	0.00000
CH_3^+	+	C	→	C_2H^+	+	H_2	0.001200	0.00000	0.00000	0.00000
CH_2^+	+	CH_4	→	$C_2H_5^+$	+	H	0.000360	0.00000	0.00000	0.00000
CH_2^+	+	CH_4	→	$C_2H_4^+$	+	H_2	0.000840	0.00000	0.00000	0.00000
CH^+	+	H_2O	→	HCO^+	+	H_2	0.002900	0.00000	0.00000	0.00000
CH^+	+	H_2O	→	H_2CO^+	+	H	0.000580	0.00000	0.00000	0.00000
CH^+	+	H_2O	→	H_3O^+	+	C	0.000580	0.00000	0.00000	0.00000
CH^+	+	CO_2	→	HCO^+	+	CO	0.001600	0.00000	0.00000	0.00000
CH^+	+	NH_3	→	H_2CN^+	+	H_2	0.001840	0.00000	0.00000	0.00000
CH^+	+	NH_3	→	NH_4^+	+	C	0.000405	0.00000	0.00000	0.00000
CH^+	+	CH_4	→	$C_2H_4^+$	+	H	$6.50 \cdot 10^{-5}$	0.00000	0.00000	0.00000
CH^+	+	CH_4	→	$C_2H_3^+$	+	H_2	0.001090	0.00000	0.00000	0.00000
CH^+	+	H_2CO	→	CH_2OH^+	+	C	0.000960	0.00000	0.00000	0.00000
CH^+	+	HCN	→	H_2CN^+	+	C	0.001800	0.00000	0.00000	0.00000
CH^+	+	C_2H_2	→	$C_2H_3^+$	+	C	0.001000	0.00000	0.00000	0.00000
CH^+	+	C_2H_4	→	$C_2H_5^+$	+	C	0.001000	0.00000	0.00000	0.00000
CH^+	+	HCO	→	H_2CO^+	+	C	0.001000	0.00000	0.00000	0.00000
CH^+	+	NH_2	→	NH_3^+	+	C	0.001000	0.00000	0.00000	0.00000
CH^+	+	H_2	→	CH_2^+	+	H	0.001200	0.00000	0.00000	0.00000
H_3O^+	+	C_2H_3	→	$C_2H_4^+$	+	H_2O	0.002000	0.00000	0.00000	0.00000
H_3O^+	+	C_3H_4	→	$C_3H_5^+$	+	H_2O	0.002000	0.00000	0.00000	0.00000
H_2O^+	+	C_2H_2	→	$C_2H_3^+$	+	OH	0.001000	0.00000	0.00000	0.00000
H_2O^+	+	C_2H_4	→	$C_2H_5^+$	+	OH	0.001000	0.00000	0.00000	0.00000

Neutral–Ion Rearrangements (continued)

Reaction							A	B	C	ΔE
H_2O^+	+	C_2	→	C_2H^+	+	OH	0.000470	0.00000	0.00000	0.00000
OH^+	+	C_2H_5	→	$C_2H_6^+$	+	O	0.001000	0.00000	0.00000	0.00000
H_2^+	+	C_2H_2	→	$C_2H_3^+$	+	H	0.000480	0.00000	0.00000	0.00000
H_2^+	+	CH_4	→	CH_5^+	+	H	0.000114	0.00000	0.00000	0.00000
H_3^+	+	C_2H_2	→	$C_2H_3^+$	+	H_2	0.003500	0.00000	0.00000	0.00000
H_3^+	+	C_2H_4	→	$C_2H_5^+$	+	H_2	0.001150	0.00000	0.00000	0.00000
H_3^+	+	C_3H_4	→	$C_3H_5^+$	+	H_2	0.006750	0.00000	0.00000	0.00000
H_3^+	+	C	→	CH^+	+	H_2	0.002000	0.00000	0.00000	0.00000
H_3^+	+	CH_4	→	CH_5^+	+	H_2	0.002400	0.00000	0.00000	0.00000
H_2^+	+	C	→	CH^+	+	H	0.002400	0.00000	0.00000	0.00000
H^+	+	CH_4	→	CH_3^+	+	H_2	0.002300	0.00000	0.00000	0.00000
H_2CO^+	+	C_2H_4	→	$C_2H_5^+$	+	HCO	0.001000	0.00000	0.00000	0.00000
H_2CO^+	+	C_2	→	C_2H^+	+	HCO	0.000820	0.00000	0.00000	0.00000
HCO^+	+	C_2H_2	→	$C_2H_3^+$	+	CO	0.001400	0.00000	0.00000	0.00000
HCO^+	+	C_2H_4	→	$C_2H_5^+$	+	CO	0.001400	0.00000	0.00000	0.00000
HCO^+	+	C_3H_4	→	$C_3H_5^+$	+	CO	0.001400	0.00000	0.00000	0.00000
HCO^+	+	C_2H	→	$C_2H_2^+$	+	CO	0.000780	0.00000	0.00000	0.00000
NH_4^+	+	CO	→	NH_4^+	+	CO	$1.00 \cdot 10^{-4}$	0.50000	0.00000	0.00000
NH_4^+	+	CO_2	→	NH_4^+	+	CO_2	$1.00 \cdot 10^{-4}$	0.50000	0.00000	0.00000
H_2CO^+	+	CO_2	→	H_2CO^+	+	CO_2	$1.00 \cdot 10^{-4}$	0.50000	0.00000	0.00000
H_2CO^+	+	CO	→	H_2CO^+	+	CO	$1.00 \cdot 10^{-4}$	0.50000	0.00000	0.00000
H^+	+	H_2O	→	H_2O^+	+	H	0.006900	0.00000	0.00000	0.00000
H^+	+	NH_3	→	NH_3^+	+	H	0.003700	0.00000	0.00000	0.00000
H^+	+	OH	→	OH^+	+	H	0.002100	0.00000	0.00000	0.00000
H^+	+	O	→	O^+	+	H	0.000796	−0.15500	215.000	0.00000
H^+	+	NO	→	NO^+	+	H	0.002900	0.00000	0.00000	0.00000
H^+	+	O_2	→	O_2^+	+	H	0.002000	0.00000	0.00000	0.00000
H^+	+	H_2CO	→	H_2CO^+	+	H	0.002960	0.00000	0.00000	0.00000
H_2^+	+	H_2O	→	H_2O^+	+	H_2	0.003900	0.00000	0.00000	0.00000
H_2^+	+	NH_3	→	NH_3^+	+	H_2	0.005700	0.00000	0.00000	0.00000
H_2^+	+	CO	→	CO^+	+	H_2	0.000644	0.00000	0.00000	0.00000
H_2^+	+	O_2	→	O_2^+	+	H_2	0.000800	0.00000	0.00000	0.00000
C^+	+	NH_3	→	NH_3^+	+	C	0.005060	0.00000	0.00000	0.00000
C^+	+	H_2CO	→	H_2CO^+	+	C	0.000780	0.00000	0.00000	0.00000
C^+	+	NO	→	NO^+	+	C	0.000520	0.00000	0.00000	0.00000
CH^+	+	NH_3	→	NH_3^+	+	CH	0.000459	0.00000	0.00000	0.00000
CH_3^+	+	NO	→	NO^+	+	CH_3	0.001000	0.00000	0.00000	0.00000
N^+	+	H_2O	→	H_2O^+	+	N	0.002800	0.00000	0.00000	0.00000
N^+	+	CO_2	→	CO_2^+	+	N	0.000750	0.00000	0.00000	0.00000
N^+	+	CH_4	→	CH_4^+	+	N	$2.80 \cdot 10^{-5}$	0.00000	0.00000	0.00000
N^+	+	CO	→	CO^+	+	N	0.000825	0.00000	0.00000	0.00000
N^+	+	O_2	→	O_2^+	+	N	0.000311	0.00000	0.00000	0.00000
N^+	+	NO	→	NO^+	+	N	0.000451	0.00000	0.00000	0.00000
N^+	+	O	→	O^+	+	N	$1.00 \cdot 10^{-6}$	0.00000	0.00000	0.00000
NH^+	+	NH_3	→	NH_3^+	+	NH	0.001800	0.00000	0.00000	0.00000
NH_2^+	+	NH_3	→	NH_3^+	+	NH_2	0.000690	0.00000	0.00000	0.00000
O^+	+	H_2O	→	H_2O^+	+	O	0.003200	0.00000	0.00000	0.00000
O^+	+	NH_3	→	NH_3^+	+	O	0.001200	0.00000	0.00000	0.00000

Neutral–Ion Rearrangements (continued)

Reaction							A	B	C	ΔE
O^+	+	CH_4	→	CH_4^+	+	O	0.000890	0.00000	0.00000	0.00000
O^+	+	OH	→	OH^+	+	O	0.000360	0.00000	0.00000	0.00000
O^+	+	O_2	→	O_2^+	+	O	$1.90 \cdot 10^{-5}$	0.00000	0.00000	0.00000
O^+	+	H	→	H^+	+	O	0.000566	0.36000	−8.60000	0.00000
OH^+	+	H_2O	→	H_2O^+	+	OH	0.001590	0.00000	0.00000	0.00000
OH^+	+	NH_3	→	NH_3^+	+	OH	0.001200	0.00000	0.00000	0.00000
OH^+	+	H_2CO	→	H_2CO^+	+	OH	0.000744	0.00000	0.00000	0.00000
OH^+	+	O_2	→	O_2^+	+	OH	0.000590	0.00000	0.00000	0.00000
H_2O^+	+	NH_3	→	NH_3^+	+	H_2O	0.002210	0.00000	0.00000	0.00000
H_2O^+	+	H_2CO	→	H_2CO^+	+	H_2O	0.001410	0.00000	0.00000	0.00000
H_2O^+	+	O_2	→	O_2^+	+	H_2O	0.000460	0.00000	0.00000	0.00000
N_2^+	+	H_2O	→	H_2O^+	+	N_2	0.002340	0.00000	0.00000	0.00000
N_2^+	+	CO_2	→	CO_2^+	+	N_2	0.000770	0.00000	0.00000	0.00000
N_2^+	+	NH_3	→	NH_3^+	+	N_2	0.001900	0.00000	0.00000	0.00000
N_2^+	+	CO	→	CO^+	+	N_2	$7.40 \cdot 10^{-5}$	0.00000	0.00000	0.00000
N_2^+	+	O	→	O^+	+	N_2	$1.00 \cdot 10^{-5}$	0.00000	0.00000	0.00000
N_2^+	+	H	→	H^+	+	N_2	0.000120	0.00000	0.00000	0.00000
N_2^+	+	O_2	→	O_2^+	+	N_2	$5.00 \cdot 10^{-5}$	0.00000	0.00000	0.00000
N_2^+	+	NO	→	NO^+	+	N_2	0.000440	0.00000	0.00000	0.00000
O_2^+	+	NH_3	→	NH_3^+	+	O_2	0.002000	0.00000	0.00000	0.00000
O_2^+	+	NO	→	NO^+	+	O_2	0.000460	0.00000	0.00000	0.00000
O_2^+	+	C	→	C^+	+	O_2	$5.20 \cdot 10^{-5}$	0.00000	0.00000	0.00000
CO^+	+	H_2O	→	H_2O^+	+	CO	0.001720	0.00000	0.00000	0.00000
CO^+	+	CO_2	→	CO_2^+	+	CO	0.001000	0.00000	0.00000	0.00000
CO^+	+	NH_3	→	NH_3^+	+	CO	0.002020	0.00000	0.00000	0.00000
CO^+	+	H_2CO	→	H_2CO^+	+	CO	0.001350	0.00000	0.00000	0.00000
CO^+	+	H_2CO_2	→	$H_2CO_2^+$	+	CO	0.003000	0.00000	0.00000	0.00000
CO^+	+	HCN	→	HCN^+	+	CO	0.003400	0.00000	0.00000	0.00000
CO^+	+	OH	→	OH^+	+	CO	0.000310	0.00000	0.00000	0.00000
CO^+	+	NO	→	NO^+	+	CO	0.000330	0.00000	0.00000	0.00000
CO^+	+	O_2	→	O_2^+	+	CO	0.000120	0.00000	0.00000	0.00000
CO^+	+	O	→	O^+	+	CO	0.000140	0.00000	0.00000	0.00000
CO^+	+	H	→	H^+	+	CO	0.000750	0.00000	0.00000	0.00000
H_2CO^+	+	NH_3	→	NH_3^+	+	H_2CO	0.000425	0.00000	0.00000	0.00000
CO_2^+	+	H	→	H^+	+	CO_2	0.000110	0.00000	0.00000	0.00000
CO_2^+	+	H_2O	→	H_2O^+	+	CO_2	0.002040	0.00000	0.00000	0.00000
CO_2^+	+	NH_3	→	NH_3^+	+	CO_2	0.001900	0.00000	0.00000	0.00000
CO_2^+	+	OH	→	OH^+	+	CO_2	0.000300	0.00000	0.00000	0.00000
CO_2^+	+	O	→	O^+	+	CO_2	$9.62 \cdot 10^{-5}$	0.00000	0.00000	0.00000
CO_2^+	+	O_2	→	O_2^+	+	CO_2	$5.30 \cdot 10^{-5}$	0.00000	0.00000	0.00000
CO_2^+	+	NO	→	NO^+	+	CO_2	0.000120	0.00000	0.00000	0.00000
H^+	+	S	→	S^+	+	H	0.001300	0.00000	0.00000	0.00000
H^+	+	HS	→	HS^+	+	H	0.001600	0.00000	0.00000	0.00000
H^+	+	CS	→	CS^+	+	H	0.004900	0.00000	0.00000	0.00000
H^+	+	NS	→	NS^+	+	H	0.004700	0.00000	0.00000	0.00000
H^+	+	SO	→	SO^+	+	H	0.003200	0.00000	0.00000	0.00000
H^+	+	H_2S	→	H_2S^+	+	H	0.005280	0.00000	0.00000	0.00000
H^+	+	H_2CS	→	H_2CS^+	+	H	0.004700	0.00000	0.00000	0.00000

Neutral–Ion Rearrangements (continued)

Reaction							A	B	C	ΔE
C^+	+	S	→	S^+	+	C	0.001500	0.00000	0.00000	0.00000
C^+	+	CS	→	CS^+	+	C	0.001600	0.00000	0.00000	0.00000
C^+	+	SO	→	SO^+	+	C	0.000260	0.00000	0.00000	0.00000
C^+	+	NS	→	NS^+	+	C	0.000760	0.00000	0.00000	0.00000
C^+	+	H_2S	→	H_2S^+	+	C	0.000600	0.00000	0.00000	0.00000
O^+	+	H_2S	→	H_2S^+	+	O	0.001360	0.00000	0.00000	0.00000
S^+	+	NO	→	NO^+	+	S	0.000370	0.00000	0.00000	0.00000
S^+	+	HCO	→	CHO^+	+	S	0.000360	0.00000	0.00000	0.00000
S^+	+	NH_3	→	NH_3^+	+	S	0.001440	0.00000	0.00000	0.00000
H_2^+	+	H_2S	→	H_2S^+	+	H_2	0.002700	0.00000	0.00000	0.00000
C_2^+	+	S	→	S^+	+	C_2	0.000580	0.00000	0.00000	0.00000
N_2^+	+	S	→	S^+	+	N_2	0.001100	0.00000	0.00000	0.00000
O_2^+	+	S	→	S^+	+	O_2	0.000540	0.00000	0.00000	0.00000
O_2^+	+	H_2S	→	H_2S^+	+	O_2	0.001400	0.00000	0.00000	0.00000
CH^+	+	S	→	S^+	+	CH	0.000470	0.00000	0.00000	0.00000
NH^+	+	S	→	S^+	+	NH	0.000690	0.00000	0.00000	0.00000
OH^+	+	S	→	S^+	+	OH	0.000430	0.00000	0.00000	0.00000
CO^+	+	S	→	S^+	+	CO	0.001100	0.00000	0.00000	0.00000
CN^+	+	S	→	S^+	+	CN	0.001100	0.00000	0.00000	0.00000
HS^+	+	S	→	S^+	+	HS	0.000970	0.00000	0.00000	0.00000
HS^+	+	H_2S	→	H_2S^+	+	HS	0.000450	0.00000	0.00000	0.00000
HS^+	+	NH_3	→	NH_3^+	+	HS	0.000525	0.00000	0.00000	0.00000
SO^+	+	NH_3	→	NH_3^+	+	SO	0.001300	0.00000	0.00000	0.00000
NH_2^+	+	S	→	S^+	+	NH_2	0.000440	0.00000	0.00000	0.00000
NH_2^+	+	H_2S	→	H_2S^+	+	NH_2	0.000720	0.00000	0.00000	0.00000
H_2O^+	+	H_2S	→	H_2S^+	+	H_2O	0.000972	0.00000	0.00000	0.00000
H_2O^+	+	S	→	S^+	+	H_2O	0.000430	0.00000	0.00000	0.00000
HCN^+	+	S	→	S^+	+	HCN	0.000570	0.00000	0.00000	0.00000
H_2S^+	+	S	→	S^+	+	H_2S	0.001100	0.00000	0.00000	0.00000
H_2S^+	+	NO	→	NO^+	+	H_2S	0.000370	0.00000	0.00000	0.00000
H_2S^+	+	HCO	→	CHO^+	+	H_2S	0.000700	0.00000	0.00000	0.00000
H_2S^+	+	NH_3	→	NH_3^+	+	H_2S	0.000340	0.00000	0.00000	0.00000
H_2CO^+	+	H_2S	→	H_2S^+	+	H_2CO	0.000550	0.00000	0.00000	0.00000
CH_4^+	+	H_2S	→	H_2S^+	+	CH_4	0.000945	0.00000	0.00000	0.00000
H^+	+	CO_2	→	CHO^+	+	O	0.003000	0.00000	0.00000	0.00000
H_2^+	+	H_2O	→	H_3O^+	+	H	0.003400	0.00000	0.00000	0.00000
H_2^+	+	H_2	→	H_3^+	+	H	0.002080	0.00000	0.00000	0.00000
H_2^+	+	N	→	NH^+	+	H	0.001900	0.00000	0.00000	0.00000
H_2^+	+	O	→	OH^+	+	H	0.001500	0.00000	0.00000	0.00000
H_2^+	+	CO	→	CHO^+	+	H	0.002160	0.00000	0.00000	0.00000
H_2^+	+	O_2	→	O_2H^+	+	H	0.001900	0.00000	0.00000	0.00000
H_2^+	+	N_2	→	N_2H^+	+	H	0.002000	0.00000	0.00000	0.00000
H_3^+	+	H_2O	→	H_3O^+	+	H_2	0.005900	0.00000	0.00000	0.00000
H_3^+	+	CO_2	→	CO_2H^+	+	H_2	0.002000	0.00000	0.00000	0.00000
H_3^+	+	NH_3	→	NH_4^+	+	H_2	0.004390	0.00000	0.00000	0.00000
H_3^+	+	O	→	OH^+	+	H_2	0.000840	0.00000	0.00000	0.00000
H_3^+	+	OH	→	H_2O^+	+	H_2	0.001300	0.00000	0.00000	0.00000
H_3^+	+	CO	→	CHO^+	+	H_2	$2.70 \cdot 10^{-5}$	0.00000	0.00000	0.00000

Neutral–Ion Rearrangements (continued)

Reaction							A	B	C	ΔE
H_3^+	+	O_2	→	O_2H^+	+	H_2	0.000930	0.00000	100.000	0.00000
H_3^+	+	H_2CO	→	CH_2OH^+	+	H_2	0.002000	0.00000	0.00000	0.00000
H_3^+	+	HCN	→	H_2CN^+	+	H_2	0.008000	0.00000	0.00000	0.00000
H_3^+	+	HCO	→	H_2CO^+	+	H_2	0.001700	0.00000	0.00000	0.00000
H_3^+	+	NO	→	HNO^+	+	H_2	0.001100	0.00000	0.00000	0.00000
H_3^+	+	N_2	→	N_2H^+	+	H_2	0.001700	0.00000	0.00000	0.00000
H_3^+	+	CN	→	HCN^+	+	H_2	0.002000	0.00000	0.00000	0.00000
C^+	+	H_2O	→	CHO^+	+	H	0.001800	0.00000	0.00000	0.00000
C^+	+	CO_2	→	CO^+	+	CO	0.001100	0.00000	0.00000	0.00000
C^+	+	NH_3	→	HCN^+	+	H_2	$7.00 \cdot 10^{-5}$	0.00000	0.00000	0.00000
C^+	+	NH_3	→	H_2CN^+	+	H	0.001080	0.00000	0.00000	0.00000
C^+	+	NH	→	H^+	+	CN	0.001000	0.00000	0.00000	0.00000
C^+	+	NH	→	CN^+	+	H	0.000780	0.00000	0.00000	0.00000
C^+	+	NH_2	→	H^+	+	HCN	0.001000	0.00000	0.00000	0.00000
C^+	+	NH_2	→	HCN^+	+	H	0.001100	0.00000	0.00000	0.00000
C^+	+	OH	→	CO^+	+	H	0.000770	0.00000	0.00000	0.00000
C^+	+	OH	→	H^+	+	CO	0.001000	0.00000	0.00000	0.00000
C^+	+	CH	→	C_2^+	+	H	0.000380	0.00000	0.00000	0.00000
C^+	+	H_2CO	→	CH_2^+	+	CO	0.002340	0.00000	0.00000	0.00000
C^+	+	H_2CO	→	CHO^+	+	CH	0.000920	0.00000	0.00000	0.00000
C^+	+	O_2	→	CO^+	+	O	0.000380	0.00000	0.00000	0.00000
C^+	+	O_2	→	O^+	+	CO	0.000620	0.00000	0.00000	0.00000
C^+	+	HCN	→	C_2N^+	+	H	0.003200	0.00000	0.00000	0.00000
CH^+	+	N	→	CN^+	+	H	0.000190	0.00000	0.00000	0.00000
CH^+	+	O	→	CO^+	+	H	0.000350	0.00000	0.00000	0.00000
CH^+	+	O_2	→	CHO^+	+	O	0.000970	0.00000	0.00000	0.00000
CH^+	+	O_2	→	O^+	+	HCO	$1.00 \cdot 10^{-5}$	0.00000	0.00000	0.00000
CH^+	+	O_2	→	CO^+	+	OH	$1.00 \cdot 10^{-5}$	0.00000	0.00000	0.00000
CH_2^+	+	H_2O	→	CH_2OH^+	+	H	0.001200	0.00000	0.00000	0.00000
CH_2^+	+	CO_2	→	H_2CO^+	+	CO	0.001600	0.00000	0.00000	0.00000
CH_2^+	+	NH_3	→	NH_4^+	+	CH	0.001260	0.00000	0.00000	0.00000
CH_2^+	+	NH_3	→	CH_4N^+	+	H	0.001540	0.00000	0.00000	0.00000
CH_2^+	+	H_2	→	CH_3^+	+	H	0.001600	0.00000	0.00000	0.00000
CH_2^+	+	O	→	CHO^+	+	H	0.001000	0.00000	0.00000	0.00000
CH_2^+	+	O_2	→	CHO^+	+	OH	0.000910	0.00000	0.00000	0.00000
CH_2^+	+	O_2	→	H_2CO^+	+	O	0.000182	0.00000	0.00000	0.00000
CH_3^+	+	NH_3	→	CH_4N^+	+	H_2	0.001300	0.00000	0.00000	0.00000
CH_3^+	+	N	→	H_2CN^+	+	H	$3.35 \cdot 10^{-5}$	0.00000	0.00000	0.00000
CH_3^+	+	N	→	HCN^+	+	H_2	$3.35 \cdot 10^{-5}$	0.00000	0.00000	0.00000
CH_3^+	+	O	→	CHO^+	+	H_2	0.000440	0.00000	0.00000	0.00000
CH_3^+	+	O_2	→	CHO^+	+	H_2O	$4.30 \cdot 10^{-5}$	0.00000	0.00000	0.00000
CH_4^+	+	H_2O	→	H_3O^+	+	CH_3	0.002600	0.00000	0.00000	0.00000
CH_4^+	+	CO_2	→	CO_2H^+	+	CH_3	0.001200	0.00000	0.00000	0.00000
CH_4^+	+	NH_3	→	CH_5^+	+	NH_2	$6.40 \cdot 10^{-5}$	0.00000	0.00000	0.00000
CH_4^+	+	NH_3	→	NH_4^+	+	CH_3	0.001150	0.00000	0.00000	0.00000
CH_4^+	+	H_2	→	CH_5^+	+	H	$4.10 \cdot 10^{-5}$	0.00000	0.00000	0.00000
CH_4^+	+	O	→	H_2CO^+	+	H_2	0.001000	0.00000	0.00000	0.00000
CH_4^+	+	CO	→	CH_3CO^+	+	H	$7.02 \cdot 10^{-5}$	0.00000	0.00000	0.00000

Neutral–Ion Rearrangements (continued)

Reaction							A	B	C	ΔE
CH_4^+	+	CO	→	CHO^+	+	CH_3	0.000710	0.00000	0.00000	0.00000
CH_5^+	+	H_2O	→	H_3O^+	+	CH_4	0.003700	0.00000	0.00000	0.00000
CH_5^+	+	NH_3	→	NH_4^+	+	CH_4	0.002500	0.00000	0.00000	0.00000
CH_5^+	+	CO	→	CHO^+	+	CH_4	0.001000	0.00000	0.00000	0.00000
N^+	+	H_2	→	NH^+	+	H	0.001000	0.00000	85.0000	0.00000
N^+	+	CO	→	NO^+	+	C	0.000145	0.00000	0.00000	0.00000
N^+	+	NH	→	N_2^+	+	H	0.000370	0.00000	0.00000	0.00000
N^+	+	O_2	→	O^+	+	NO	$3.66 \cdot 10^{-5}$	0.00000	0.00000	0.00000
N^+	+	O_2	→	NO^+	+	O	0.000263	0.00000	0.00000	0.00000
N^+	+	NO	→	N_2^+	+	O	$7.90 \cdot 10^{-5}$	0.00000	0.00000	0.00000
NH^+	+	H_2O	→	H_3O^+	+	N	0.001050	0.00000	0.00000	0.00000
NH^+	+	NH_3	→	NH_4^+	+	N	0.000600	0.00000	0.00000	0.00000
NH^+	+	H_2	→	NH_2^+	+	H	0.001280	0.00000	0.00000	0.00000
NH_2^+	+	H_2O	→	H_3O^+	+	NH	0.002760	0.00000	0.00000	0.00000
NH_2^+	+	H_2O	→	NH_4^+	+	O	0.000145	0.00000	0.00000	0.00000
NH_2^+	+	H_2O	→	NH_3^+	+	OH	$1.00 \cdot 10^{-4}$	0.00000	0.00000	0.00000
NH_2^+	+	NH_3	→	NH_4^+	+	NH	0.001610	0.00000	0.00000	0.00000
NH_2^+	+	H_2	→	NH_3^+	+	H	0.000270	0.00000	0.00000	0.00000
NH_3^+	+	H_2O	→	NH_4^+	+	OH	0.000110	0.00000	0.00000	0.00000
NH_3^+	+	NH_3	→	NH_4^+	+	NH_2	0.002200	0.00000	0.00000	0.00000
NH_3^+	+	CH_4	→	NH_4^+	+	CH_3	0.000480	0.00000	0.00000	0.00000
NH_3^+	+	OH	→	NH_4^+	+	O	0.000700	0.00000	0.00000	0.00000
NH_3^+	+	H_2	→	NH_4^+	+	H	$1.00 \cdot 10^{-7}$	0.00000	0.00000	0.00000
NH_3^+	+	H_2CO	→	NH_4^+	+	HCO	0.001100	0.00000	0.00000	0.00000
NH_3^+	+	CH_2	→	CH_3^+	+	NH_2	0.000960	0.00000	0.00000	0.00000
O^+	+	CO_2	→	O_2^+	+	CO	0.000940	0.00000	0.00000	0.00000
O^+	+	CH_4	→	CH_3^+	+	OH	0.000110	0.00000	0.00000	0.00000
O^+	+	H_2	→	OH^+	+	H	0.001700	0.00000	0.00000	0.00000
O^+	+	OH	→	H^+	+	O_2	$2.70 \cdot 10^{-5}$	0.130000	0.00000	0.00000
O^+	+	N_2	→	NO^+	+	N	$1.20 \cdot 10^{-6}$	−1.00000	0.00000	0.00000
OH^+	+	H_2O	→	H_3O^+	+	O	0.001300	0.00000	0.00000	1.80000
OH^+	+	NH_3	→	NH_4^+	+	O	0.001200	0.00000	0.00000	0.00000
OH^+	+	CH_4	→	H_3O^+	+	CH_2	0.001310	0.00000	0.00000	0.00000
OH^+	+	H_2CO	→	CH_2OH^+	+	O	0.001120	0.00000	0.00000	0.00000
OH^+	+	CO_2	→	CO_2H^+	+	O	0.001440	0.00000	0.00000	0.00000
OH^+	+	HCN	→	H_2CN^+	+	O	0.001000	0.00000	0.00000	0.00000
OH^+	+	CO	→	CHO^+	+	O	$2.00 \cdot 10^{-5}$	0.00000	0.00000	0.00000
OH^+	+	N_2	→	N_2H^+	+	O	0.000190	0.00000	0.00000	0.00000
OH^+	+	OH	→	H_2O^+	+	O	0.000700	0.00000	0.00000	0.00000
OH^+	+	H_2	→	H_2O^+	+	H	0.001010	0.00000	0.00000	1.20000
OH^+	+	C	→	CO^+	+	H	0.001000	0.00000	0.00000	0.00000
OH^+	+	C	→	CH^+	+	O	0.001200	0.00000	0.00000	0.00000
H_2O^+	+	H_2O	→	H_3O^+	+	OH	0.002100	0.00000	0.00000	1.10000
H_2O^+	+	NH_3	→	NH_4^+	+	OH	0.000945	0.00000	0.00000	0.00000
H_2O^+	+	CH_4	→	H_3O^+	+	CH_3	0.001400	0.00000	0.00000	0.00000
H_2O^+	+	H_2CO	→	CH_2OH^+	+	OH	0.000662	0.00000	0.00000	0.00000
H_2O^+	+	HCN	→	H_2CN^+	+	OH	0.001000	0.00000	0.00000	0.00000
H_2O^+	+	CO	→	CHO^+	+	OH	0.000252	0.30900	180.000	0.00000

Neutral–Ion Rearrangements (continued)

Reaction							A	B	C	ΔE
H_2O^+	+	HCO	→	H_2CO^+	+	OH	0.000280	0.00000	0.00000	0.00000
H_2O^+	+	NH_2	→	NH_3^+	+	OH	0.000490	0.00000	0.00000	0.00000
H_2O^+	+	CH_2	→	CH_3^+	+	OH	0.000470	0.00000	0.00000	0.00000
H_2O^+	+	CH	→	CH_2^+	+	OH	0.000340	0.00000	0.00000	0.00000
H_2O^+	+	C	→	CH^+	+	OH	0.001100	0.00000	0.00000	0.00000
H_2O^+	+	H_2	→	H_3O^+	+	H	0.000640	0.00000	0.00000	1.80000
H_3O^+	+	NH_3	→	NH_4^+	+	H_2O	0.002200	0.00000	0.00000	0.00000
H_3O^+	+	H_2CO	→	CH_2OH^+	+	H_2O	0.001100	0.00000	0.00000	0.00000
H_3O^+	+	HCN	→	H_2CN^+	+	H_2O	0.001000	0.00000	0.00000	0.00000
H_3O^+	+	NH_2	→	NH_3^+	+	H_2O	0.000970	0.00000	0.00000	0.00000
H_3O^+	+	CH_2	→	CH_3^+	+	H_2O	0.000940	0.00000	0.00000	0.00000
H_3O^+	+	CH	→	CH_2^+	+	H_2O	0.000680	0.00000	0.00000	0.00000
H_3O^+	+	C	→	CHO^+	+	H_2	0.002000	0.00000	0.00000	0.00000
$C_2H_2^+$	+	H_2O	→	H_3O^+	+	C_2H	0.000220	0.00000	0.00000	0.00000
$C_2H_2^+$	+	NH_3	→	NH_4^+	+	C_2H	0.000961	0.00000	0.00000	0.00000
$C_2H_2^+$	+	H_2CO	→	CH_2OH^+	+	C_2H	0.000409	0.00000	0.00000	0.00000
$C_2H_2^+$	+	H_2CO	→	$C_3H_3O^+$	+	H	$6.50 \cdot 10^{-5}$	0.00000	0.00000	0.00000
$C_2H_2^+$	+	H_2CO	→	$C_2H_4^+$	+	CO	0.000280	0.00000	0.00000	0.00000
$C_2H_2^+$	+	HCN	→	H_2CN^+	+	C_2H	$2.20 \cdot 10^{-5}$	0.00000	0.00000	0.00000
$C_2H_2^+$	+	HCN	→	$C_3H_2N^+$	+	H	$3.10 \cdot 10^{-5}$	0.00000	0.00000	0.00000
$C_2H_4^+$	+	H	→	$C_2H_3^+$	+	H_2	0.000300	0.00000	0.00000	0.00000
$C_2H_6^+$	+	H	→	$C_2H_5^+$	+	H_2	$1.00 \cdot 10^{-4}$	0.00000	0.00000	0.00000
N_2^+	+	H_2O	→	N_2H^+	+	OH	0.000462	0.00000	0.00000	0.00000
N_2^+	+	NH_3	→	N_2H^+	+	NH_2	$2.10 \cdot 10^{-5}$	0.00000	0.00000	0.00000
N_2^+	+	H_2	→	N_2H^+	+	H	0.001730	0.00000	0.00000	0.00000
N_2^+	+	O	→	NO^+	+	N	0.000130	0.00000	0.00000	0.00000
N_2H^+	+	H_2O	→	H_3O^+	+	N_2	0.002600	0.00000	0.00000	0.00000
N_2H^+	+	CO_2	→	CO_2H^+	+	N_2	0.000920	0.00000	0.00000	0.00000
N_2H^+	+	NH_3	→	NH_4^+	+	N_2	0.002300	0.00000	0.00000	0.00000
N_2H^+	+	CH_4	→	CH_5^+	+	N_2	0.000890	0.00000	0.00000	0.00000
N_2H^+	+	CO	→	CHO^+	+	N_2	0.000880	0.00000	0.00000	0.00000
N_2H^+	+	O	→	OH^+	+	N_2	0.000140	0.00000	0.00000	0.00000
O_2^+	+	N	→	NO^+	+	O	0.000180	0.00000	0.00000	0.00000
O_2H^+	+	H_2	→	H_3^+	+	O_2	0.000640	0.00000	0.00000	0.00000
CO^+	+	H_2O	→	CHO^+	+	OH	0.000884	0.00000	0.00000	0.00000
CO^+	+	NH_3	→	CHO^+	+	NH_2	$4.20 \cdot 10^{-5}$	0.00000	0.00000	0.00000
CO^+	+	CH_4	→	CHO^+	+	CH_3	0.000210	0.00000	0.00000	0.00000
CO^+	+	CH_4	→	CH_3CO^+	+	H	$5.20 \cdot 10^{-5}$	0.00000	0.00000	0.00000
CO^+	+	H_2CO	→	CHO^+	+	HCO	0.001000	0.00000	0.00000	0.00000
CO^+	+	HCN	→	CHO^+	+	CN	0.000500	0.00000	0.00000	0.00000
CO^+	+	H_2	→	CHO^+	+	H	0.000750	0.00000	0.00000	0.00000
CHO^+	+	H_2O	→	H_3O^+	+	CO	0.003200	0.00000	0.00000	0.00000
CHO^+	+	NH_3	→	NH_4^+	+	CO	0.002600	0.00000	0.00000	0.00000
CHO^+	+	OH	→	CO_2H^+	+	H	0.001000	0.00000	0.00000	0.00000
CHO^+	+	OH	→	H_2O^+	+	CO	0.001000	0.00000	0.00000	0.00000
CHO^+	+	NH_2	→	NH_3^+	+	CO	0.001000	0.00000	0.00000	0.00000
CHO^+	+	H_2CO	→	CH_2OH^+	+	CO	0.001000	0.00000	0.00000	0.00000
CHO^+	+	HCN	→	H_2CN^+	+	CO	0.001140	0.00000	0.00000	0.00000

Neutral–Ion Rearrangements (continued)

Reaction							A	B	C	ΔE
CHO^+	+	HCO	→	H_2CO^+	+	CO	0.001000	0.00000	0.00000	0.00000
CHO^+	+	CH_2	→	CH_3^+	+	CO	0.001000	0.00000	0.00000	0.00000
CHO^+	+	CH	→	CH_2^+	+	CO	0.001000	0.00000	0.00000	0.00000
CHO^+	+	NH	→	NH_2^+	+	CO	0.001000	0.00000	1007.00	0.00000
CHO^+	+	C	→	CH^+	+	CO	0.001000	0.00000	0.00000	0.00000
H_2CO^+	+	H_2O	→	H_3O^+	+	HCO	0.002600	0.00000	0.00000	0.00000
H_2CO^+	+	H_2CO	→	CH_2OH^+	+	HCO	0.001000	0.00000	0.00000	0.00000
H_2CO^+	+	NH_3	→	NH_4^+	+	HCO	0.001280	0.00000	0.00000	0.00000
H_2CO^+	+	HCN	→	H_2CN^+	+	HCO	0.001400	0.00000	0.00000	0.00000
H_2CO^+	+	CH	→	CH_2^+	+	HCO	0.000310	0.00000	0.00000	0.00000
H_2CO^+	+	CH_2	→	CH_3^+	+	HCO	0.000430	0.00000	0.00000	0.00000
H_2CO^+	+	NH_2	→	NH_3^+	+	HCO	0.000880	0.00000	0.00000	0.00000
CH_2OH^+	+	H_2O	→	H_3O^+	+	H_2CO	0.002000	0.00000	648.800	0.00000
CH_2OH^+	+	NH_3	→	NH_4^+	+	H_2CO	0.002300	0.00000	0.00000	0.00000
CH_2OH^+	+	HCN	→	H_2CN^+	+	H_2CO	0.001000	0.00000	0.00000	0.00000
CH_2OH^+	+	CH	→	CH_2^+	+	H_2CO	0.001000	0.00000	0.00000	0.00000
CH_2OH^+	+	CH_2	→	CH_3^+	+	H_2CO	0.001000	0.00000	0.00000	0.00000
CH_2OH^+	+	NH_2	→	NH_3^+	+	H_2CO	0.001000	0.00000	0.00000	0.00000
CN^+	+	CH_4	→	CH_2CN^+	+	H_2	0.001000	0.00000	0.00000	0.00000
CN^+	+	H_2	→	HCN^+	+	H	0.001000	0.00000	0.00000	0.00000
HCN^+	+	H_2	→	H_2CN^+	+	H	0.000900	0.00000	0.00000	0.00000
H_2CN^+	+	NH_3	→	NH_4^+	+	HNC	0.001100	0.00000	0.00000	0.00000
H_2CN^+	+	NH_3	→	NH_4^+	+	HCN	0.001100	0.00000	0.00000	0.00000
CO_2^+	+	H_2O	→	CO_2H^+	+	OH	0.000756	0.00000	0.00000	0.00000
CO_2^+	+	CH_4	→	CO_2H^+	+	CH_3	0.000550	0.00000	0.00000	0.00000
CO_2^+	+	H_2	→	CO_2H^+	+	H	0.000950	0.00000	0.00000	0.00000
CO_2^+	+	H	→	CHO^+	+	O	0.000290	0.00000	0.00000	0.00000
CO_2^+	+	O	→	O_2^+	+	CO	0.000164	0.00000	0.00000	0.00000
CO_2H^+	+	H_2O	→	H_3O^+	+	CO_2	0.002300	0.00000	0.00000	0.00000
CO_2H^+	+	NH_3	→	NH_4^+	+	CO_2	0.001000	0.00000	0.00000	0.00000
CO_2H^+	+	CH_4	→	CH_5^+	+	CO_2	0.000780	0.00000	0.00000	0.00000
CO_2H^+	+	H_2CO	→	CH_2OH^+	+	CO_2	0.001000	0.00000	0.00000	0.00000
CO_2H^+	+	HCN	→	H_2CN^+	+	CO_2	0.001000	0.00000	0.00000	0.00000
CO_2H^+	+	CH_2	→	CH_3^+	+	CO_2	0.001000	0.00000	0.00000	0.00000
CO_2H^+	+	CO	→	CHO^+	+	CO_2	0.001000	0.00000	0.00000	0.00000
H^+	+	HS	→	S^+	+	H_2	0.001600	0.00000	0.00000	0.00000
H^+	+	OCS	→	HS^+	+	CO	0.002100	0.00000	0.00000	0.00000
C^+	+	HS	→	CS^+	+	H	0.001100	0.00000	0.00000	0.00000
C^+	+	SO	→	S^+	+	CO	0.000260	0.00000	0.00000	0.00000
C^+	+	SO	→	CS^+	+	O	0.000260	0.00000	0.00000	0.00000
C^+	+	SO	→	CO^+	+	S	0.000260	0.00000	0.00000	0.00000
C^+	+	OCS	→	CO^+	+	CS	0.000930	0.00000	0.00000	0.00000
C^+	+	OCS	→	CS^+	+	CO	0.001600	0.00000	0.00000	0.00000
C^+	+	SO_2	→	SO^+	+	CO	0.002300	0.00000	0.00000	0.00000
C^+	+	H_2CS	→	CH_2^+	+	CS	0.001500	0.00000	0.00000	0.00000
C^+	+	NS	→	CS^+	+	N	0.000760	0.00000	0.00000	0.00000
C^+	+	H_2S	→	HCS^+	+	H	0.001400	0.00000	0.00000	0.00000
S^+	+	C_2	→	CS^+	+	C	0.000810	0.00000	0.00000	0.00000

Neutral–Ion Rearrangements (continued)

Reaction							A	B	C	ΔE
S^+	+	CH	→	CS^+	+	H	0.000620	0.00000	0.00000	0.00000
S^+	+	NH	→	NS^+	+	H	0.000630	0.00000	0.00000	0.00000
S^+	+	OH	→	SO^+	+	H	0.000610	0.00000	0.00000	0.00000
S^+	+	CH_2	→	HCS^+	+	H	$1.00 \cdot 10^{-5}$	0.00000	0.00000	0.00000
S^+	+	HCO	→	HS^+	+	CO	0.000360	0.00000	0.00000	0.00000
S^+	+	H_2CO	→	H_2S^+	+	CO	0.000335	0.00000	0.00000	0.00000
S^+	+	NH_3	→	NH_2^+	+	HS	$7.00 \cdot 10^{-5}$	0.00000	0.00000	0.00000
S^+	+	CH_3	→	H_2CS^+	+	H	$1.00 \cdot 10^{-5}$	0.00000	0.00000	0.00000
S^+	+	CH_4	→	H_3CS^+	+	H	0.000380	0.00000	0.00000	0.00000
C_2^+	+	S	→	CS^+	+	C	0.000580	0.00000	0.00000	0.00000
O_2^+	+	S	→	SO^+	+	O	0.000540	0.00000	0.00000	0.00000
CH^+	+	S	→	HS^+	+	C	0.000470	0.00000	0.00000	0.00000
CH^+	+	S	→	CS^+	+	H	0.000470	0.00000	0.00000	0.00000
CH^+	+	H_2S	→	HCS^+	+	H_2	0.001470	0.00000	0.00000	0.00000
NH^+	+	S	→	NS^+	+	H	0.000690	0.00000	0.00000	0.00000
NH^+	+	S	→	HS^+	+	N	0.000690	0.00000	0.00000	0.00000
OH^+	+	S	→	SO^+	+	H	0.000430	0.00000	0.00000	0.00000
OH^+	+	S	→	HS^+	+	O	0.000430	0.00000	0.00000	0.00000
OH^+	+	H_2S	→	H_3S^+	+	O	0.000820	0.00000	0.00000	0.00000
CO^+	+	SO_2	→	SO^+	+	CO_2	0.001700	0.00000	0.00000	0.00000
HS^+	+	C	→	CS^+	+	H	0.000990	0.00000	0.00000	0.00000
HS^+	+	N	→	NS^+	+	H	0.000740	0.00000	0.00000	0.00000
HS^+	+	O	→	SO^+	+	H	0.000290	0.00000	0.00000	0.00000
HS^+	+	O	→	S^+	+	OH	0.000290	0.00000	0.00000	0.00000
HS^+	+	CH	→	CH_2^+	+	S	0.000580	0.00000	0.00000	0.00000
HS^+	+	H_2O	→	H_3O^+	+	S	0.000780	0.00000	0.00000	0.00000
HS^+	+	HCN	→	H_2CN^+	+	S	0.000890	0.00000	0.00000	0.00000
HS^+	+	H_2S	→	H_3S^+	+	S	0.000470	0.00000	0.00000	0.00000
HS^+	+	NH_3	→	NH_4^+	+	S	0.000975	0.00000	0.00000	0.00000
HS^+	+	CH_4	→	H_3CS^+	+	H_2	0.000220	0.00000	0.00000	0.00000
CS^+	+	O	→	CO^+	+	S	$6.00 \cdot 10^{-5}$	0.00000	0.00000	0.00000
CS^+	+	H_2	→	HCS^+	+	H	0.000450	0.00000	0.00000	0.00000
SO^+	+	N	→	NS^+	+	O	$5.00 \cdot 10^{-5}$	0.00000	0.00000	0.00000
NS^+	+	O	→	NO^+	+	S	0.000610	0.00000	0.00000	0.00000
H_3^+	+	S	→	HS^+	+	H_2	0.002600	0.00000	0.00000	0.00000
H_3^+	+	HS	→	H_2S^+	+	H_2	0.001900	0.00000	0.00000	0.00000
H_3^+	+	CS	→	HCS^+	+	H_2	0.002900	0.00000	0.00000	0.00000
H_3^+	+	NS	→	HNS^+	+	H_2	0.002800	0.00000	0.00000	0.00000
H_3^+	+	SO	→	HSO^+	+	H_2	0.001900	0.00000	0.00000	0.00000
H_3^+	+	H_2S	→	H_3S^+	+	H_2	0.003700	0.00000	0.00000	0.00000
H_3^+	+	OCS	→	$HOCS^+$	+	H_2	0.001900	0.00000	0.00000	0.00000
H_3^+	+	H_2CS	→	H_3CS^+	+	H_2	0.002800	0.00000	0.00000	0.00000
CH_2^+	+	S	→	HCS^+	+	H	0.001400	0.00000	0.00000	0.00000
CH_2^+	+	H_2S	→	H_3CS^+	+	H	0.001840	0.00000	0.00000	0.00000
NH_2^+	+	S	→	HNS^+	+	H	0.000440	0.00000	0.00000	0.00000
NH_2^+	+	S	→	HS^+	+	NH	0.000440	0.00000	0.00000	0.00000
NH_2^+	+	H_2S	→	H_3S^+	+	NH	0.000270	0.00000	0.00000	0.00000
H_2O^+	+	S	→	HSO^+	+	H	0.000430	0.00000	0.00000	0.00000

Neutral–Ion Rearrangements (continued)

Reaction	*A*	*B*	*C*	Δ*E*
$H_2O^+ + S \rightarrow HS^+ + OH$	0.000430	0.00000	0.00000	0.00000
$H_2O^+ + H_2S \rightarrow H_3S^+ + OH$	0.000774	0.00000	0.00000	0.00000
$H_2O^+ + H_2S \rightarrow H_3O^+ + HS$	0.000540	0.00000	0.00000	0.00000
$CHO^+ + HS \rightarrow H_2S^+ + CO$	0.000820	0.00000	0.00000	0.00000
$CHO^+ + CS \rightarrow HCS^+ + CO$	0.001200	0.00000	0.00000	0.00000
$CHO^+ + NS \rightarrow HNS^+ + CO$	0.001100	0.00000	0.00000	0.00000
$CHO^+ + SO \rightarrow HSO^+ + CO$	0.000750	0.00000	0.00000	0.00000
$CHO^+ + H_2S \rightarrow H_3S^+ + CO$	0.001100	0.00000	0.00000	0.00000
$CHO^+ + OCS \rightarrow HOCS^+ + CO$	0.001300	0.00000	0.00000	0.00000
$CHO^+ + H_2CS \rightarrow H_3CS^+ + CO$	0.001100	0.00000	0.00000	0.00000
$HCN^+ + S \rightarrow HS^+ + CN$	0.000570	0.00000	0.00000	0.00000
$HNO^+ + S \rightarrow HS^+ + NO$	0.001100	0.00000	0.00000	0.00000
$N_2H^+ + S \rightarrow HS^+ + N_2$	0.001100	0.00000	0.00000	0.00000
$O_2H^+ + S \rightarrow HS^+ + O_2$	0.001100	0.00000	0.00000	0.00000
$H_2S^+ + C \rightarrow HCS^+ + H$	0.001000	0.00000	0.00000	0.00000
$H_2S^+ + N \rightarrow NS^+ + H_2$	0.000790	0.00000	0.00000	0.00000
$H_2S^+ + O \rightarrow HS^+ + OH$	0.000310	0.00000	0.00000	0.00000
$H_2S^+ + O \rightarrow SO^+ + H_2$	0.000310	0.00000	0.00000	0.00000
$H_2S^+ + H_2O \rightarrow H_3O^+ + HS$	0.000810	0.00000	0.00000	0.00000
$H_2S^+ + H_2S \rightarrow H_3S^+ + HS$	0.001000	0.00000	0.00000	0.00000
$H_2S^+ + NH_3 \rightarrow NH_4^+ + HS$	0.001360	0.00000	0.00000	0.00000
$NH_3^+ + H_2S \rightarrow NH_4^+ + HS$	0.001300	0.00000	0.00000	0.00000
$NH_3^+ + H_2S \rightarrow H_3S^+ + NH_2$	0.000110	0.00000	0.00000	0.00000
$H_2CO^+ + S \rightarrow HS^+ + HCO$	0.000550	0.00000	0.00000	0.00000
$CH_3^+ + S \rightarrow HCS^+ + H_2$	0.001400	0.00000	0.00000	0.00000
$CH_3^+ + HS \rightarrow H_2CS^+ + H_2$	0.001000	0.00000	0.00000	0.00000
$CH_3^+ + SO \rightarrow HOCS^+ + H_2$	0.000950	0.00000	0.00000	0.00000
$CH_3^+ + H_2S \rightarrow H_3CS^+ + H_2$	0.001300	0.00000	0.00000	0.00000
$C_2H_2^+ + H_2S \rightarrow C_2H_3^+ + HS$	$4.60 \cdot 10^{-5}$	0.00000	0.00000	0.00000
$C_2H_2^+ + H_2S \rightarrow H_3S^+ + C_2H$	$4.60 \cdot 10^{-5}$	0.00000	0.00000	0.00000
$CH_4^+ + H_2S \rightarrow CH_5^+ + HS$	$9.00 \cdot 10^{-5}$	0.00000	0.00000	0.00000
$CH_4^+ + H_2S \rightarrow H_3S^+ + CH_3$	0.001160	0.00000	0.00000	0.00000
$CH_5^+ + S \rightarrow HS^+ + CH_4$	0.001300	0.00000	0.00000	0.00000
$HCS^+ + O \rightarrow CHO^+ + S$	0.001000	0.00000	0.00000	0.00000
$HCS^+ + O \rightarrow OCS^+ + H$	$5.00 \cdot 10^{-6}$	0.00000	0.00000	0.00000
$S^+ + O_2 \rightarrow O^+ + SO$	$2.00 \cdot 10^{-5}$	0.00000	0.00000	0.00000
$C_2H_2^+ + C_2H_6 \rightarrow C_3H_3^+ + CH_3 + H_2$	$8.80 \cdot 10^{-5}$	0.00000	0.00000	0.00000
$C_2H_2^+ + C_2H_6 \rightarrow C_4H_5^+ + H_2 + H$	$7.30 \cdot 10^{-5}$	0.00000	0.00000	0.00000
$C_2^+ + CH_4 \rightarrow C_3H^+ + H_2 + H$	0.000196	0.00000	0.00000	0.00000
$CH_4^+ + C_2H_2 \rightarrow C_3H_3^+ + H_2 + H$	0.000151	0.00000	0.00000	0.00000
$CH_4^+ + C_2H_4 \rightarrow C_3H_5^+ + H_2 + H$	$5.50 \cdot 10^{-5}$	0.00000	0.00000	0.00000
$CH_4^+ + C_2H_6 \rightarrow C_2H_4^+ + CH_4 + H_2$	0.001910	0.00000	0.00000	0.00000
$CH_3^+ + C_2H_4 \rightarrow C_3H_3^+ + H_2 + H_2$	$4.60 \cdot 10^{-5}$	0.00000	0.00000	0.00000
$CH_3^+ + C_2H_6 \rightarrow C_3H_5^+ + H_2 + H_2$	0.000157	0.00000	0.00000	0.00000
$CH_2^+ + CH_4 \rightarrow C_2H_3^+ + H_2 + H$	0.000264	0.00000	0.00000	0.00000
$CH_2^+ + CH_4 \rightarrow C_2H_2^+ + H_2 + H_2$	0.000144	0.00000	0.00000	0.00000
$CH^+ + CH_4 \rightarrow C_2H_2^+ + H_2 + H$	0.000143	0.00000	0.00000	0.00000
$H_2^+ + C_2H_4 \rightarrow C_2H_3^+ + H_2 + H$	0.001810	0.00000	0.00000	0.00000

Neutral–Ion Rearrangements (continued)

Reaction											A	B	C	ΔE
H_2^+	+	C_2H_4	→	$C_2H_2^+$	+	H_2	+	H_2			0.000882	0.00000	0.00000	0.00000
H_2^+	+	C_2H_6	→	$C_2H_5^+$	+	H_2	+	H			$1.37 \cdot 10^{-9}$	0.00000	0.00000	0.00000
H_2^+	+	C_2H_6	→	$C_2H_4^+$	+	H_2	+	H_2			0.002350	0.00000	0.00000	0.00000
H_2^+	+	CH_4	→	CH_3^+	+	H_2	+	H			0.002300	0.00000	0.00000	0.00000
H_3^+	+	C_2H_4	→	$C_2H_3^+$	+	H_2	+	H_2			0.001150	0.00000	0.00000	0.00000
H_3^+	+	C_2H_6	→	$C_2H_5^+$	+	H_2	+	H_2			0.003400	0.00000	0.00000	0.00000
H_3^+	+	C_3H_4	→	$H_2C_3H^+$	+	H_2	+	H_2			0.002250	0.00000	0.00000	0.00000
N^+	+	CH_4	→	CH_3^+	+	N	+	H			0.000470	0.00000	0.00000	0.00000
N^+	+	CH_4	→	H_2CN^+	+	H	+	H			0.000432	0.00000	0.00000	0.00000
N^+	+	CH_4	→	HCN^+	+	H_2	+	H			$5.60 \cdot 10^{-5}$	0.00000	0.00000	0.00000
N_2^+	+	CH_4	→	CH_3^+	+	H	+	N_2			0.000930	0.00000	0.00000	0.00000
N_2^+	+	CH_4	→	CH_2^+	+	H_2	+	N_2			$7.00 \cdot 10^{-5}$	0.00000	0.00000	0.00000
H_2^+	+	H_2S	→	HS^+	+	H	+	H_2			0.000860	0.00000	0.00000	0.00000
H_2^+	+	H_2S	→	S^+	+	H_2	+	H_2			0.000770	0.00000	0.00000	0.00000
CH_2^+	+	H_2S	→	HCS^+	+	H_2	+	H			0.000230	0.00000	0.00000	0.00000
H_2^+	+	C_2H_6	→	$C_2H_3^+$	+	H_2	+	H_2	+	H	0.000686	0.00000	0.00000	0.00000
H_2^+	+	C_2H_6	→	$C_2H_2^+$	+	H_2	+	H_2	+	H_2	0.000196	0.00000	0.00000	0.00000

Electron Impact Excitation

Reaction							A	B	C	ΔE
CO	+	e^-	$\rightarrow$	CO_{1p}	+	e^-	0.004460	0.20300	94940.0	−8.10000
CO	+	e^-	$\rightarrow$	CO_{3p}	+	e^-	0.163000	−0.41800	83840.0	−6.00000
CO	+	e^-	$\rightarrow$	CO_{3s}	+	e^-	0.002890	0.10700	91000.0	−6.90000
CO	+	e^-	$\rightarrow$	CO_{3d}	+	e^-	0.000822	−0.04000	99850.0	−7.70000

Electron Impact Ionisation

Reaction									A	B	C	ΔE
C_2H_4	+	e^-	$\rightarrow$	$C_2H_4^+$	+	e^-	+	e^-	$3.88 \cdot 10^{-6}$	1.62000	77820.0	0.00000
CH_4	+	e^-	$\rightarrow$	CH_4^+	+	e^-	+	e^-	$3.75 \cdot 10^{-7}$	1.91000	65960.0	0.00000
H	+	e^-	$\rightarrow$	H^+	+	e^-	+	e^-	$5.80 \cdot 10^{-5}$	0.50000	158000.	−13.6000
H_2	+	e^-	$\rightarrow$	H_2^+	+	e^-	+	e^-	0.000943	0.50000	179100.	−15.4300
C	+	e^-	$\rightarrow$	C^+	+	e^-	+	e^-	0.000350	0.40000	131000.	−11.2600
C_2	+	e^-	$\rightarrow$	C_2^+	+	e^-	+	e^-	0.000943	0.50000	143900.	−12.4000
N	+	e^-	$\rightarrow$	N^+	+	e^-	+	e^-	0.000110	0.44000	168000.	−14.5300
N_2	+	e^-	$\rightarrow$	N_2^+	+	e^-	+	e^-	$4.02 \cdot 10^{-7}$	1.34000	105900.	−15.5800
O	+	e^-	$\rightarrow$	O^+	+	e^-	+	e^-	0.001270	0.57000	158200.	−13.6200
O_2	+	e^-	$\rightarrow$	O_2^+	+	e^-	+	e^-	0.000320	0.79000	155700.	−12.0600
CO	+	e^-	$\rightarrow$	CO^+	+	e^-	+	e^-	0.000705	0.72000	172100.	−14.0100
CO_2	+	e^-	$\rightarrow$	CO_2^+	+	e^-	+	e^-	$5.13 \cdot 10^{-6}$	1.24000	107700.	−13.7900
H_2O	+	e^-	$\rightarrow$	H_2O^+	+	e^-	+	e^-	$5.34 \cdot 10^{-5}$	0.97000	897400.	−12.6000
NH_3	+	e^-	$\rightarrow$	NH_3^+	+	e^-	+	e^-	0.000943	0.50000	117900.	−10.1600
NO	+	e^-	$\rightarrow$	NO^+	+	e^-	+	e^-	$5.90 \cdot 10^{-5}$	1.10000	110400.	−9.25000
C_3H_4	+	e^-	$\rightarrow$	$C_3H_4^+$	+	e^-	+	e^-	0.000170	0.77000	115105.	0.00000
C_3H_3	+	e^-	$\rightarrow$	$C_3H_3^+$	+	e^-	+	e^-	0.000160	0.76700	115143.	0.00000
C_3H_2	+	e^-	$\rightarrow$	$C_3H_2^+$	+	e^-	+	e^-	0.000480	0.76300	115182.	0.00000
C_3H	+	e^-	$\rightarrow$	C_3H^+	+	e^-	+	e^-	0.000750	0.76900	115114.	0.00000
C_2H	+	e^-	$\rightarrow$	C_2H^+	+	e^-	+	e^-	0.000350	0.75400	115257.	0.00000
C_2H_2	+	e^-	$\rightarrow$	$C_2H_2^+$	+	e^-	+	e^-	0.000360	0.75400	115267.	0.00000
C_2H_3	+	e^-	$\rightarrow$	$C_3H_3^+$	+	e^-	+	e^-	0.000120	0.77100	115064.	0.00000
C_2H_4	+	e^-	$\rightarrow$	$C_2H_4^+$	+	e^-	+	e^-	0.000120	0.77300	115054.	0.00000
C_2H_5	+	e^-	$\rightarrow$	$C_2H_5^+$	+	e^-	+	e^-	0.000140	0.77000	115088.	0.00000
C_2H_6	+	e^-	$\rightarrow$	$C_2H_6^+$	+	e^-	+	e^-	0.000160	0.76500	115138.	0.00000

Electron Impact Dissociation

Reaction	A	B	C	ΔE
$C_3H_4 + e^- \rightarrow C_3 + H_2 + H_2 + e^-$	0.038000	0.50000	40618.0	0.00000
$C_2H_2 + e^- \rightarrow C_2H + H + e^-$	0.019000	0.50000	62400.0	0.00000
$C_2H_2 + e^- \rightarrow C_2 + H_2 + e^-$	0.019000	0.50000	71700.0	0.00000
$CH_4 + e^- \rightarrow CH_3 + H + e^-$	0.000943	0.50000	51989.0	0.00000
$H_2 + e^- \rightarrow H + H + e^-$	0.003220	0.35000	102000.	−4.48000
$C_2 + e^- \rightarrow C + C + e^-$	0.000943	0.50000	70905.0	−6.11000
$N_2 + e^- \rightarrow N + N + e^-$	0.000103	1.00000	122300.	−9.76000
$O_2 + e^- \rightarrow O + O + e^-$	0.000943	0.50000	59417.0	−5.12000
$CO_2 + e^- \rightarrow CO + O + e^-$	0.000943	0.50000	63246.0	−5.45000
$CO + e^- \rightarrow C + O + e^-$	0.000943	0.50000	128700.	−11.0900
$CO_2 + e^- \rightarrow CO_{1p} + O + e^-$	0.000943	0.50000	157200.	−13.5500
$CO_2 + e^- \rightarrow CO_{3p} + O + e^-$	0.000943	0.50000	133000.	−11.4600
$H_2O + e^- \rightarrow H_2 + O_{1d} + e^-$	0.000943	0.50000	81234.0	−7.00000
$H_2O + e^- \rightarrow OH + H + e^-$	0.000943	0.50000	59301.0	−5.11000
$NH_3 + e^- \rightarrow NH_2 + H + e^-$	0.000943	0.50000	51409.0	−4.43000
$NH_3 + e^- \rightarrow H_2 + NH + e^-$	0.000943	0.50000	64291.0	−5.54000
$H_2CO + e^- \rightarrow HCO + H + e^-$	0.019000	0.50000	43100.0	−3.70000
$H_2CO + e^- \rightarrow CO + H + H + e^-$	0.019000	0.50000	52300.0	−4.50000
$HCN + e^- \rightarrow CN + H + e^-$	0.038000	0.50000	74900.0	−6.50000
$CH_3CN + e^- \rightarrow CH_3 + CN + e^-$	0.038000	0.50000	55704.0	−4.80000
$NH_2CH_3 + e^- \rightarrow NH_2 + CH_3 + e^-$	0.038000	0.50000	51990.0	−4.50000
$C_3H_4 + e^- \rightarrow C_3H_3 + H + e^-$	0.004800	0.59500	115847.	0.00000
$C_3H_3 + e^- \rightarrow C_3H_2 + H + e^-$	0.004560	0.59500	115800.	0.00000
$C_3H_3 + e^- \rightarrow C_3H + H + H + e^-$	0.009780	0.36900	116800.	0.00000
$C_3H_2 + e^- \rightarrow C_3H + H + e^-$	0.006450	0.59600	115800.	0.00000
$C_3H + e^- \rightarrow 3\,C + H + e^-$	0.006220	0.59100	115900.	0.00000
$C_2H + e^- \rightarrow C + C + H + e^-$	0.003960	0.59800	115818.	0.00000
$C_2H_3 + e^- \rightarrow C_2 + H_2 + H + e^-$	0.003240	0.59000	115903.	0.00000
$C_2H_3 + e^- \rightarrow C_2 + 3\,H + e^-$	0.006890	0.36600	116796.	0.00000
$C_2H_4 + e^- \rightarrow C_2 + H_2 + 2\,H + e^-$	0.007670	0.36200	116831.	0.00000

Radiative Recombination

Reaction	A	B	C	ΔE
$CH^+ + e^- \rightarrow CH$	0.000105	0.00000	0.00000	0.00000
$H^+ + e^- \rightarrow H$	$3.50 \cdot 10^{-6}$	−0.70000	0.00000	0.00000
$C^+ + e^- \rightarrow C$	$3.50 \cdot 10^{-6}$	−0.70000	0.00000	0.00000
$N^+ + e^- \rightarrow N$	$3.50 \cdot 10^{-6}$	−0.70000	0.00000	0.00000
$O^+ + e^- \rightarrow O$	$3.50 \cdot 10^{-6}$	−0.70000	0.00000	0.00000
$O_2^+ + e^- \rightarrow O_2$	$4.00 \cdot 10^{-6}$	−0.70000	0.00000	0.00000
$S^+ + e^- \rightarrow S$	$3.90 \cdot 10^{-6}$	−0.63000	0.00000	0.00000
$H_2S^+ + e^- \rightarrow H_2S$	0.000110	−0.70000	0.00000	0.00000
$H_2CS^+ + e^- \rightarrow H_2CS$	0.000110	−0.70000	0.00000	0.00000

Dissociative Recombination

Reaction	A	B	C	ΔE
$C_4H_5^+ + e^- \rightarrow C_3H_4 + CH$	0.150000	−0.50000	0.00000	0.00000
$C_4H_2^+ + e^- \rightarrow C_2H + C_2H$	0.250000	−0.50000	0.00000	0.00000
$C_2H_6^+ + e^- \rightarrow C_2H_4 + H_2$	1.900000	−0.50000	0.00000	10.2300
$C_2H_4^+ + e^- \rightarrow C_2H_2 + H_2$	0.033600	−0.76000	0.00000	8.79000
$C_2H_3^+ + e^- \rightarrow C_2H_2 + H$	0.950000	−0.50000	0.00000	4.00000
$C_2H_2^+ + e^- \rightarrow C_2H + H$	0.090000	−0.50000	0.00000	6.04000
$C_2H^+ + e^- \rightarrow C_2 + H$	0.116000	−0.76000	0.00000	4.00000
$C_3H_5^+ + e^- \rightarrow C_3H_4 + H$	0.150000	−0.50000	0.00000	0.00000
$C_3H^+ + e^- \rightarrow C_3 + H$	0.150000	−0.50000	0.00000	3.00000
$CH_5^+ + e^- \rightarrow CH_4 + H$	0.014000	−0.52000	0.00000	1.00000
$CH_4^+ + e^- \rightarrow CH_3 + H$	0.175000	−0.50000	0.00000	8.64000
$CH_4^+ + e^- \rightarrow CH_2 + H_2$	0.120000	−0.50000	0.00000	7.90000
$CH_3^+ + e^- \rightarrow CH_2 + H$	0.077500	−0.50000	0.00000	3.00000
$CH^+ + e^- \rightarrow C + H$	0.150000	−0.42000	0.00000	7.15000
$H_2^+ + e^- \rightarrow H + H$	0.016000	−0.43000	0.00000	10.9500
$H_3^+ + e^- \rightarrow H_2 + H$	0.023400	−0.52000	0.00000	6.00000
$CH_2^+ + e^- \rightarrow CH + H$	0.160000	−0.60000	0.00000	5.00000
$CH_3^+ + e^- \rightarrow CH + H_2$	0.195000	−0.50000	0.00000	3.00000
$NH^+ + e^- \rightarrow N + H$	0.046000	−0.50000	0.00000	9.34000
$NH_2^+ + e^- \rightarrow NH + H$	0.300000	−0.50000	0.00000	9.00000
$NH_3^+ + e^- \rightarrow NH_2 + H$	0.155000	−0.50000	0.00000	5.73000
$NH_3^+ + e^- \rightarrow NH + H_2$	0.100000	−0.50000	0.00000	4.62000
$NH_4^+ + e^- \rightarrow NH_3 + H$	0.117000	−0.50000	0.00000	3.00000
$OH^+ + e^- \rightarrow O + H$	0.037500	−0.50000	0.00000	8.97000
$H_2O^+ + e^- \rightarrow OH + H$	0.086000	−0.50000	0.00000	7.49000
$H_2O^+ + e^- \rightarrow O + H_2$	0.039000	−0.50000	0.00000	3.63000
$H_2O^+ + e^- \rightarrow O_{1d} + H_2$	0.076000	−0.50000	0.00000	5.60000
$H_3O^+ + e^- \rightarrow H_2O + H$	0.108000	−0.50000	0.00000	1.00000
$H_3O^+ + e^- \rightarrow OH + H_2$	0.060200	−0.50000	0.00000	1.00000
$C_2^+ + e^- \rightarrow C + C$	0.300000	−0.50000	0.00000	6.29000
$C_2H_2^+ + e^- \rightarrow C_2 + H_2$	0.295000	−0.50000	0.00000	5.24000
$C_3^+ + e^- \rightarrow C_2 + C$	0.300000	−0.50000	0.00000	3.00000
$N_2^+ + e^- \rightarrow N + N$	0.170000	−0.30000	0.00000	5.82000
$N_2H^+ + e^- \rightarrow N_2 + H$	0.760000	−0.50000	0.00000	1.00000
$O_2^+ + e^- \rightarrow O + O$	0.195000	−0.70000	0.00000	6.94000
$O_2H^+ + e^- \rightarrow O_2 + H$	0.300000	−0.50000	0.00000	4.00000
$CHO^+ + e^- \rightarrow CO + H$	0.110000	−1.00000	0.00000	1.00000
$CO^+ + e^- \rightarrow C + O$	0.200000	−0.48000	0.00000	2.90000
$CO^+ + e^- \rightarrow C_{1d} + O_{1d}$	0.250000	−0.50000	0.00000	6.17000
$CH_2OH^+ + e^- \rightarrow H_2CO + H$	0.320000	−0.50000	0.00000	1.00000
$CN^+ + e^- \rightarrow C + N$	0.180000	−0.50000	0.00000	6.20000
$HCN^+ + e^- \rightarrow CN + H$	0.200000	−0.50000	0.00000	8.30000
$H_2CN^+ + e^- \rightarrow HCN + H$	0.213000	−0.50000	0.00000	3.00000
$H_2CN^+ + e^- \rightarrow HNC + H$	0.213000	−0.50000	0.00000	3.00000
$NO^+ + e^- \rightarrow N + O$	0.430000	−0.37000	0.00000	2.76000
$CO_2^+ + e^- \rightarrow CO + O$	0.380000	−0.50000	0.00000	8.34000
$CO_2^+ + e^- \rightarrow CO_{3p} + O$	0.087900	−0.50000	0.00000	2.33000
$CO_2^+ + e^- \rightarrow CO + O_{1d}$	0.292000	−0.50000	0.00000	6.37000

Dissociative Recombination (continued)

Reaction									A	B	C	ΔE
CO_2H^+	+	e^-	→	CO_2	+	H			0.060000	−0.64000	0.00000	1.00000
HS^+	+	e^-	→	S	+	H			0.200000	−0.50000	0.00000	0.00000
CS^+	+	e^-	→	C	+	S			0.200000	−0.50000	0.00000	0.00000
SO^+	+	e^-	→	S	+	O			0.200000	−0.50000	0.00000	0.00000
NS^+	+	e^-	→	N	+	S			0.200000	−0.50000	0.00000	0.00000
H_2S^+	+	e^-	→	HS	+	H			0.150000	−0.50000	0.00000	0.00000
HCS^+	+	e^-	→	CS	+	H			0.184000	−0.57000	0.00000	0.00000
HSO^+	+	e^-	→	SO	+	H			0.200000	−0.50000	0.00000	0.00000
HNS^+	+	e^-	→	NS	+	H			0.300000	−0.50000	0.00000	0.00000
H_3S^+	+	e^-	→	H_2S	+	H			0.185000	−0.50000	0.00000	0.00000
$HOCS^+$	+	e^-	→	OH	+	CS			0.200000	−0.50000	0.00000	0.00000
$HOCS^+$	+	e^-	→	OCS	+	H			0.200000	−0.50000	0.00000	0.00000
H_3CS^+	+	e^-	→	H_2CS	+	H			0.300000	−0.50000	0.00000	0.00000
$C_2H_5^+$	+	e^-	→	C_2H_2	+	H_2	+	H	0.081200	−0.79000	0.00000	10.0000
CH_4^+	+	e^-	→	CH_2	+	H	+	H	0.175000	−0.50000	0.00000	3.74000
CH_4^+	+	e^-	→	CH	+	H_2	+	H	0.120000	−0.50000	0.00000	4.07000
H_3^+	+	e^-	→	H	+	H	+	H	0.043600	−0.52000	0.00000	11.0000
CH_3^+	+	e^-	→	CH	+	H	+	H	0.200000	−0.40000	0.00000	7.00000
NH_3^+	+	e^-	→	NH	+	H	+	H	0.155000	−0.50000	0.00000	1.73000
NH_4^+	+	e^-	→	NH_2	+	H	+	H	0.130000	−0.50000	0.00000	6.00000
H_3O^+	+	e^-	→	OH	+	H	+	H	0.258000	−0.50000	0.00000	5.00000
$C_3H_2^+$	+	e^-	→	C_3	+	H	+	H	0.060000	−0.50000	0.00000	5.00000
$C_3H_4^+$	+	e^-	→	C_3	+	H_2	+	H_2	0.500000	−0.50000	0.00000	3.00000
$H_2CO_2^+$	+	e^-	→	CO	+	OH	+	H	0.200000	−0.50000	0.00000	8.00000
H_2CO^+	+	e^-	→	CO	+	H	+	H	0.500000	−0.50000	0.00000	6.35000
H_2CN^+	+	e^-	→	CN	+	H	+	H	0.213000	−0.50000	0.00000	5.00000
CO_2H^+	+	e^-	→	CO	+	O	+	H	0.810000	−0.64000	0.00000	7.00000
CH_4N^+	+	e^-	→	HCN	+	H_2	+	H	0.300000	−0.50000	0.00000	3.00000
CH_4N^+	+	e^-	→	CN	+	H_2	+	H_2	0.030000	−0.50000	0.00000	6.00000
H_2S^+	+	e^-	→	S	+	H	+	H	0.150000	−0.50000	0.00000	0.00000
H_3S^+	+	e^-	→	HS	+	H	+	H	0.185000	−0.50000	0.00000	0.00000
H_2CS^+	+	e^-	→	CS	+	H	+	H	0.300000	−0.50000	0.00000	0.00000
H_3CS^+	+	e^-	→	CS	+	H	+	H_2	0.300000	−0.50000	0.00000	0.00000
$C_2H_5^+$	+	e^-	→	C_2H_3	+	H_2			0.300000	−0.50000	0.00000	0.00000
$C_2H_3^+$	+	e^-	→	C_2H	+	H_2			0.057500	−1.38000	0.00000	0.00000
$C_2H_3^+$	+	e^-	→	C_2H	+	H	+	H	0.565000	−1.38000	0.00000	0.00000
$C_2H_3^+$	+	e^-	→	C_2H	+	H_2			0.300000	−1.38000	0.00000	0.00000
$C_2H_3^+$	+	e^-	→	C_2	+	H	+	H_2	0.028700	−1.38000	0.00000	0.00000
$C_2H_3^+$	+	e^-	→	CH_3	+	C			0.005750	−1.38000	0.00000	0.00000
$C_2H_3^+$	+	e^-	→	CH_2	+	CH			0.002870	−1.38000	0.00000	0.00000
$C_2H_2^+$	+	e^-	→	C_2	+	H	+	H	0.141000	−0.50000	0.00000	0.00000
$C_2H_2^+$	+	e^-	→	CH	+	CH			0.141000	−0.50000	0.00000	0.00000
C_2H^+	+	e^-	→	C	+	C	+	H	0.289000	−0.50000	0.00000	0.00000
C_2H^+	+	e^-	→	CH	+	H			0.289000	−0.50000	0.00000	0.00000
$C_3H_4^+$	+	e^-	→	C_3H_3	+	H			0.342000	−0.50000	0.00000	0.00000
$C_3H_4^+$	+	e^-	→	C_3H_2	+	H_2			0.342000	−0.50000	0.00000	0.00000
$C_3H_3^+$	+	e^-	→	C_3H_2	+	H			0.342000	−0.50000	0.00000	0.00000
$C_3H_3^+$	+	e^-	→	C_3H	+	H_2			0.342000	−0.50000	0.00000	0.00000

Dissociative Recombination (continued)

Reaction							*A*	*B*	*C*	Δ*E*
$C_3H_2^+$	+	e^-	→	C_2	+	CH_2	0.030000	−0.50000	0.00000	0.00000
$C_3H_2^+$	+	e^-	→	C_3	+	H_2	0.060000	−0.50000	0.00000	0.00000
$C_3H_2^+$	+	e^-	→	C_2H_2	+	C	0.030000	−0.50000	0.00000	0.00000
$C_3H_2^+$	+	e^-	→	C_3H	+	H	0.342000	−0.50000	0.00000	0.00000
$C_3H_2^+$	+	e^-	→	C_2H	+	CH	0.342000	−0.50000	0.00000	0.00000
C_3H+	+	e^-	→	C_2H	+	C	0.228000	−0.50000	0.00000	0.00000
C_3H+	+	e^-	→	CH	+	2 C	0.228000	−0.50000	0.00000	0.00000
C_3H+	+	e^-	→	3 C	+	H	0.228000	−0.50000	0.00000	0.00000

Dissociative Ionisation

Reaction											*A*	*B*	*C*	Δ*E*
N_2	+	e^-	→	N^+	+	N	+	e^-	+	e^-	$2.34 \cdot 10^{-9}$	2.34000	125300.	−24.2900
O_2	+	e^-	→	O^+	+	O	+	e^-	+	e^-	$1.58 \cdot 10^{-8}$	2.09000	981900.	−21.1900
CO	+	e^-	→	C^+	+	O	+	e^-	+	e^-	$3.47 \cdot 10^{-6}$	1.05500	72640.0	−22.3500
CO_2	+	e^-	→	O^+	+	CO	+	e^-	+	e^-	$8.97 \cdot 10^{-6}$	1.09000	271500.	−19.0700
CO_2	+	e^-	→	CO^+	+	O	+	e^-	+	e^-	$8.97 \cdot 10^{-6}$	1.09000	271500.	−19.4700
H_2O	+	e^-	→	OH^+	+	H	+	e^-	+	e^-	$5.03 \cdot 10^{-7}$	1.45000	106300.	−18.1200
H_2O	+	e^-	→	H^+	+	OH	+	e^-	+	e^-	$1.14 \cdot 10^{-7}$	2.02000	99600.0	−18.7200
H_2O	+	e^-	→	H_2^+	+	O	+	e^-	+	e^-	$1.63 \cdot 10^{-6}$	0.63000	117100.	−20.5300
H_2O	+	e^-	→	O^+	+	H_2	+	e^-	+	e^-	$8.53 \cdot 10^{-10}$	2.00000	97080.0	−18.6500
NO	+	e^-	→	N^+	+	O	+	e^-	+	e^-	$1.03 \cdot 10^{-6}$	1.42000	248900.	−21.2900
NO	+	e^-	→	O^+	+	N	+	e^-	+	e^-	$1.03 \cdot 10^{-6}$	1.42000	248900.	−27.9900
C_3H_4	+	e^-	→	$C_3H_3^+$	+	H	+	2 e^-			0.000160	0.72900	138478.	0.00000
C_3H_4	+	e^-	→	$C_3H_2^+$	+	2 H	+	2 e^-			0.000760	0.73600	138386.	0.00000
C_3H_3	+	e^-	→	$C_3H_2^+$	+	H	+	2 e^-			0.000150	0.73000	138460.	0.00000
C_3H_3	+	e^-	→	C_3H^+	+	2 H	+	2 e^-			0.000720	0.73700	138370.	0.00000
C_3H_2	+	e^-	→	C_3H^+	+	H	+	2 e^-			0.000420	0.73500	138396.	0.00000
C_2H	+	e^-	→	C^+	+	C	+	H	+	2 e^-	0.000320	0.73400	138369.	0.00000
C_2H_2	+	e^-	→	C_2H^+	+	H	+	2 e^-			0.000300	0.73800	138330.	0.00000
C_2H_3	+	e^-	→	$C_2H_2^+$	+	H	+	2 e^-			0.000110	0.73100	138414.	0.00000
C_2H_3	+	e^-	→	C_2H^+	+	H_2	+	2 e^-			0.000590	0.72500	138491.	0.00000
C_2H_4	+	e^-	→	$C_2H_3^+$	+	H	+	2 e^-			0.000110	0.73300	138403.	0.00000
C_2H_4	+	e^-	→	$C_2H_2^+$	+	H_2	+	2 e^-			0.000600	0.72700	138486.	0.00000
C_2H_5	+	e^-	→	$C_2H_4^+$	+	H	+	2 e^-			0.000130	0.73000	138444.	0.00000
C_2H_5	+	e^-	→	$C_2H_3^+$	+	H_2	+	2 e^-			0.000610	0.73800	138346.	0.00000
C_2H_6	+	e^-	→	$C_2H_5^+$	+	H	+	2 e^-			0.000140	0.72800	138446.	0.00000
C_2H_6	+	e^-	→	$C_2H_4^+$	+	H_2	+	2 e^-			0.000690	0.73600	138361.	0.00000

Radiative Deexcitation

Reaction					A	B	C	ΔE
O_{1d}	$\rightarrow$	O	+	γ	6800.00	0.00000	0.00000	0.00000
O_{1s}	$\rightarrow$	O_{1d}	+	γ	$1.34 \cdot 10^{6}$	0.00000	0.00000	0.00000
S_{1d}	$\rightarrow$	S	+	γ	36000.0	0.00000	0.00000	0.00000
S_{1s}	$\rightarrow$	S_{1d}	+	γ	$1.78 \cdot 10^{6}$	0.00000	0.00000	0.00000
S_{1s}	$\rightarrow$	S	+	γ	$3.57 \cdot 10^{5}$	0.00000	0.00000	0.00000
C_{1d}	$\rightarrow$	C	+	γ	340.000	0.00000	0.00000	0.00000
CO_{1p}	$\rightarrow$	CO	+	γ	$9.70 \cdot 10^{13}$	0.00000	0.00000	0.00000
CO_{3p}	$\rightarrow$	CO	+	γ	$1.26 \cdot 10^{8}$	0.00000	0.00000	0.00000
CO_{3s}	$\rightarrow$	CO	+	γ	$1.00 \cdot 10^{11}$	0.00000	0.00000	0.00000
CO_{3d}	$\rightarrow$	CO	+	γ	10.0000	0.00000	0.00000	0.00000
CO_{3s}	$\rightarrow$	CO_{3p}	+	γ	$1.00 \cdot 10^{11}$	0.00000	0.00000	0.00000
CO_{3d}	$\rightarrow$	CO_{3p}	+	γ	$2.37 \cdot 10^{11}$	0.00000	0.00000	0.00000

Neutral−Neutral Ionisation

Reaction							A	B	C	ΔE
CH	+	O	$\rightarrow$	CHO^{+}	+	e^{-}	$2.00 \cdot 10^{-5}$	0.44000	00000.0	0.00000

Appendix B List of Used IAU Circulars

This Appendix lists all circulars of the International Astronomical Union (IAUC) that contain the discovery observations and the first detection of cometary activity used in chapter 13 of this work. Additional observations were taken from the Extended Computer Service of the Minor Planet Center and are available for download by the Minor Planet Center (`http://cfa-www.harvard.edu`).

Comet Designation	IAUC No.	Date of Issue	Comet Designation	IAUC No.	Date of Issue
C/2004 X2	8450	10. Dec 2004	C/2002 T7	8003	29. Oct 2002
P/2004 VR_8	8451	10. Dec 2004	P/2002 T6	8002	29. Oct 2002
P/2004 WR_9	8448	8. Dec 2004	C/2002 L9	7931	2. Jul 2002
C/2004 RG_{113}	8444	23. Nov 2004	P/2002 JN_{16}	7907	22. May 2002
162P	8436	12. Nov 2004	P/2002 BV	7896	9. May 2002
160P	8408	23. Sep 2004	C/2002 J5	7904	18. May 2002
C/2004 K3	8350	11. Jun 2004	P/2002 EJ_{57}	7890	2. May 2002
C/2004 HV_{60}	8337	9. May 2004	C/2002 B2	7821	6. Feb 2002
P/2004 EW_{38}	8322	15. Apr 2004	C/2002 A2	7788	11. Jan 2002
C/2004 DZ_{61}	8321	14. Apr 2004	158P	8244	28. Nov 2003
C/2004 D1	8294	27. Feb 2004	P/2001 WF_2	7827	13. Feb 2002
P/2004 CB	8314	31. Mar 2004	C/2001 OG_{108}	7814	2. Feb 2002
P/2004 DO_{29}	8305	16. Mar 2004	C/2001 RX_{14}	7739	25. Oct 2001
P/2003 HT_{15}	8156	25. Jun 2003	C/2001 G1	7606	2. Apr 2001
P/2003 QX_{29}	8192	2. Sep 2003	C/2001 A2	7564	16. Jan 2001
P/2003 SQ_{215}	8274	23. Jan 2004	150P	7584	17. Feb 2001
C/2003 WT_{42}	8270	16. Jan 2004	148P	7524	25. Nov 2000
P/2003 WC_7	8280	1. Feb 2004	C/2000 SV_{74}	7510	19. Oct 2000
159P	8248	3. Dec 2003	C/2000 OF_8	7484	31. Aug 2000
P/2003 UY_{275}	8247	2. Dec 2003	P/1999 XN_{120}	7370	29. Feb 2000
C/2002 X1	8028	7. Dec 2002	P/1999 DN_3	7167	14. May 1999
P/2002 LZ_{11}	8240	18. Nov 2003	P/1998 VS_{24}	7071	19. Dec 1998
C/2002 V2	8013	9. Nov 2002	139P	7064	7. Dec 1998
C/2002 VQ_{94}	8194	3. Sep 2003	P/1998 QP_{54}	7012	14. Sep 1998

Acknowledgements

I would like to acknowlegde the people whose support made this work possible.

I would like to thank Prof. Dr. Heike Rauer for supervising this thesis and supporting me in many ways.

With many discussions and with providing programme routines, Dr. Jörg Knollenberg supported this work. Therefore I would like to thank him.

I would like to thank Dr. John Lee Grenfell for reading the proofs and making many valuable suggestions.

The observations analysed within this work benefit from the support of Dr. Silvio Klose, Dr. Jochen Eislöffel, Dr. Emmanuël Jehin, Dr. Gian-Paolo Tozzi, and Prof. Dr. Chris Sterken, for which I am thankful.

I would like to thank Prof. Dr. Erwin Sedlmayr and Prof. Dr. Hans Joachim Eichler for giving me the opportunity to prepare this thesis.

With her language skills and her patience my wife Polina was a great help while working on this thesis. Therefore I would like to thank her deeply.